

Designing tools for point-of-care diagnostics and biosensing for low-resource settings

Dissertation

with the aim of achieving a doctoral degree (Dr. rer. nat.) at the

Faculty of Mathematics, Informatics and Natural Sciences

Department of Chemistry

University of Hamburg

Submitted by

Sujatha Kumar

Hamburg

2021

Reviewers:

Prof. Dr. Robert Blick

Prof. Dr. Markus Fischer

Examination committee:

Prof. Dr. Robert Blick

Prof. Dr. Markus Fischer

Prof. Dr. Wolfgang Parak

Prof. Dr. Wolfram Brune

Prof. Dr. Christian Betzel

Date of Disputation:

September 15, 2021

This work was conducted at University of Washington, Seattle WA, USA and University of Wisconsin, Madison WI, USA. Support for this work was provided with funding from Bill and Melinda Gates Foundation, Seattle WA, USA, Defense Advanced Research Projects Agency (DARPA), National Institutes of Health, (NIH), Defense Threat Reduction Agency (DTRA), and Madigan Army Hospital WA, USA.

-To my loving husband George Kumar and our wonderful boys

Vikram and Raj

*karmanyevadhikaraste ma phaleshu kadachana /
ma karmaphalaheturbhurma te sangostvakarmani //*

-Bhagavad Gita

Chapter 2 Verse 47

Language: Sanskrit

Translation-

You have a right to perform your prescribed duty, but you are not entitled to the fruits of your actions /

Never consider yourself to be the cause of results of your actions, nor be attached to inaction //

List of publications

Peer-reviewed publications

1. *Long-term dry storage of enzyme-based reagents for isothermal nucleic acid amplification in a porous matrix for use in point-of-care diagnostic devices*
Sujatha Kumar, Ryan Gallagher, Josh Bishop, Enos Kline, Josh Buser, Lisa Lafleur, Kamal Shah, Barry Lutz, and Paul Yager. *Analyst* 2020, 145, 6875-6886
2. *Long-term dry storage of an enzyme-based reagent system for ELISA in point-of-care devices.*
Sujatha Ramachandran, Elain Fu, Barry Lutz, and Paul Yager. *Analyst* 2014 21;139 (6):1456-62.
3. *A low cost point-of-care viscous sample preparation device for molecular diagnosis in the developing world; an example of microfluidic origami.*
Anupama Govindarajan, Sujatha Ramachandran, Genevieve Vigil, Paul Yager and Karl Bohringer. *Lab Chip* 2012, 12, 174-181
4. *Selective loading of kinesin-powered molecular shuttles with protein cargo and its application to biosensing.*
Sujatha Ramachandran, Karl-Heinz Ernst, George D. Bachand, Viola Vogel, and Henry Hess. *Small* 2006, 2(3), 330-334.
5. *Long-term storage of bionanodevices by freezing and lyophilization*
Raviraja Seetharam*, Yuuko Wada*, Sujatha Ramachandran*, Henry Hess and Peter Satir. *Lab Chip* 2006, 6, 1239-1242.
***equal author contribution.**
6. *Direct microwave transmission on single alpha-hemolysin pores.*
Sujatha Ramachandran, Daniel W. van der Weide and Robert H. Blick, *Applied Physics Letters*, 2011, 99, 093105.
7. *Radio frequency rectification on membrane bound pores.*
Sujatha Ramachandran, Robert H. Blick, and Daniel W. van der Weide, *Nanotechnology* 2010, 21, 075201.
8. *Radio-frequency response of single pores and artificial ion channels.*
Hyun S Kim, Sujatha Ramachandran, Eric Stava, Daniel W Van Der Weide, Robert H Blick. *New Journal Physics* 2011, 13, 093033.
9. *Current bursts in lipid bilayers initiated by colloidal quantum dots.*
Sujatha Ramachandran, George L Kumar, Robert H Blick, Daniel W Van Der Weide. *Applied Physics Letters* 2005, 86, 083901.

Conference proceedings

1. *A disposable integrated diagnostic device for blood acquisition, sample processing, lysis, and detection of Ebola virus markers.*

Sujatha Kumar, Steven Bennett, Shichu Huang, Joshua Buser, and Paul Yager. *The 24 th International Conference on miniaturized systems for chemistry and life sciences (MicroTas)*, virtual conference 2020.

2. *A device for urine cell concentration, lysis, and nucleic acid amplification for Chlamydia detection at the point of care.*

Steven Bennett, Sujatha Kumar, Erin Heiniger, and Paul Yager. *The 24 th International Conference on miniaturized systems for chemistry and life sciences (MicroTas)*, virtual conference 2020.

3. *Integrated assay and sample processing: a paper-based device for IgM detection.*

Sujatha Ramachandran, Jacqueline Peltier, Jennifer Osborn, Carly Holstein, Barry Lutz, Elain Fu, and Paul Yager. *MicroTas*, Okinawa, Japan, 2012.

Other publications related to this work:

1. *Two-Fluorophore Mobile Phone Imaging of Bplexed Real-Time NAATs Overcomes Optical Artifacts in Highly Scattering Porous Media*

Kamal G. Shah, Sujatha Kumar, Vidhi Singh, Louise Hansen, Erin Heiniger, Joshua D. Bishop, Barry Lutz, and Paul Yager, *Analytical Chemistry*, 2020, 92, 19, 13066–13072.

2. *A rapid, instrument-free, sample-to-result nucleic acid amplification test.*

Lafleur LK, Bishop JD, Heiniger EK, Gallagher RP, Wheeler MD, Kauffman P, Zhang X, Kline EC, Buser JR, Kumar Sujatha, Byrnes SA, Vermeulen NM, Scarr NK, Belousov Y, Mahoney W, Toley BJ, Ladd PD, Lutz BR, Yager P, *Lab chip* 2016, 16(19):3777-87.

3. *A two-dimensional paper network format that enables simple multistep assays for use in low-resource settings in the context of malaria antigen detection*

Elain Fu, Tinny Liang, Paolo Spicar-Mihalic, Jared Houghtaling, Sujatha Ramachandran and Paul Yager, *Analytical Chemistry* 2012, 84, 4574-4579.

4. *A Rapid and Sensitive Method of Nucleic Acid Amplification for Point-of-Care Diagnosis.*

Toley BJ, Covelli I, Belousov Y, Ramachandran Sujatha, Kline E, Scarr N, Vermeulen N, Mahoney W, Lutz BR, Yager P, Isothermal Strand Displacement Amplification (iSDA): *Analyst* 2015, 140(22):7540-9

5. *Dissolvable fluidic time delays for programming multistep assays in instrument-free paper diagnostics,* Barry Lutz, Tinny Liang, Elain Fu, Sujatha Ramachandran, Peter Kauffman and Paul Yager, *Lab Chip*, 2013, 13, 2840-2847

6. *Understanding partial saturation in paper microfluidics enables alternative device architectures*

Joshua R. Buser, Samantha A. Byrnes, Caitlin E. Anderson, Arielle J. Howell, Peter C. Kauffman, Joshua D. Bishop, Maxwell H. Wheeler, Sujatha Kumar and Paul Yager, *Analytical methods* 2018, 11,336-345.

Patent applications:

1. *Long-term dry storage of enzyme-based reagents for isothermal nucleic acid amplification in a porous matrix for use in point-of-care diagnostic devices.* Sujatha Kumar and Paul Yager. US provisional patent application 63/066,687 (2020).
2. *Pathogen filtration apparatus system and method.* Paul Yager, Steven Bennett, Sujatha Kumar, Kamal Girish Shah, Erin K. Heiniger. International patent application number PCT/US2020/053761 (2020).
3. *Device and method for detection of pathogens in the home by amplification of their DNA or RNA.* Paul Yager, Steven Bennett, Erin K. Heiniger, and Sujatha Kumar. US patent application 63/039,859 (2020).
4. *Sequential delivery of fluid volumes and associated devices, systems, and methods.* JD Bishop, JR Buser, SA Byrnes, S Dharmaraja, E Fu, J Houghtaling, PC Kauffman, S Kumar, LK Lafleur, T Liang, BR Lutz, BJ Toley, MH Wheeler, P Yager, X Zhang. International Patent Application PCT/US2014/012618 (2014).
5. *Dry preservation of signal amplification reagents horseradish peroxidase-antibody and diaminbenzidine for use in point-of-care diagnostic devices.* Paul Yager, Elain Fu, Peter Kauffman, Barry Lutz, Sujatha Ramachandran, Karman Tandon. US provisional patent application NO: 61/609,667 (2012).

Table of contents

List of publications	i
Table of contents.....	iv
List of abbreviations	vi
Abstract.....	viii
Zusammenfassung.....	x
1 Introduction.....	1
1.1 Significance of the proposed work.....	1
1.2 Proposed solution.....	2
1.3 Outline of the thesis	4
2 Background.....	7
2.1 Low-cost paper-based point-of-care diagnostics for infectious diseases	7
2.2 Biomolecular motor-powered biosensing	13
2.3 Label-free biosensing.....	16
Part I: Low-cost paper-based point-of-care diagnostic devices for infectious diseases	22
3 Two-dimensional paper-network for multistep automated ELISA.....	23
3.1 Long-term dry storage of an enzyme-based reagent system for ELISA in point-of care devices*...	24
4 Two-dimensional paper networks for sample processing	32
4.1 Integrated assay and sample processing: paper-based device for IgM detection.....	33
4.2 A diagnostic device for sample processing, lysis, and detection of Ebola virus markers.....	39
4.3 A paper-based microfluidic origami device for nucleic acid extraction	49
5 Two-dimensional paper network for molecular diagnostics	58
5.1 Long-term dry storage of enzyme-based reagents for isothermal nucleic acid amplification*	59
5.2 A sample-to-result urinalysis device for chlamydia detection at point of care	72

Part II: Biomolecular motor-powered biosensing	76
6 Biomolecular motor-powered biosensing	77
6.1 Selective loading of kinesin-powered molecular shuttles with protein cargo*	78
6.2 Long-term storage of bionanodevices by freezing and lyophilization*	84
Part III: Label-free biosensing	89
7 Electronic interface to biological pores in lipid bilayer for label-free biosensing	90
7.1 Radio frequency rectification on membrane bound pores*	91
7.2 Direct microwave transmission on single alpha-hemolysin pores*	98
8 Interaction of quantum dots with lipid bilayer membrane	102
8.1 Current bursts in lipid bilayers initiated by colloidal quantum dots*	103
9 Discussion.....	107
9.1 Low-cost paper-based POC Dx for infectious diseases	107
9.2 Biomolecular motor-powered biosensing	110
9.3 Label-free biosensing	111
10. Bibliography	113
11. Appendix.....	124
11.1 Supporting information to chapter 3, section 3.1	124
11.2 Supporting information to chapter 5, section 5.1	125
11.3 Molecular mechanism of isothermal strand displacement amplification (iSDA)	128
11.4 Schematic of lateral flow detection for isothermal strand displacement amplification (iSDA) ...	130
11.5 Rapid, instrument-free, sample-to-result nucleic acid amplification test.....	131
11.6 Measurements using radiofrequency micro-strip transmission line.....	133
Risk and safety statement.....	138
Acknowledgments.....	140
Declaration upon oath	142

List of abbreviations

2DPN	2-Dimensional paper network
α -HL	Alpha-hemolysin
Ab	Antibody
AIDS	Acquired immunodeficiency syndrome
ALA	Alamethicin
AC	Alternate current
ASSURED	Affordable Sensitive Specific User-friendly, Rapid, Deliverable
ATP	Adenosine triphosphate
Au	Gold
β -CD	Beta-cyclodextrin
BSA	Bovine serum albumin
CFU	Colony forming unit
CT	Chlamydia trachomatis
DAB	Diaminobenzidine
DALY	Disability-adjusted life years
DC	Direct current
Dx	Diagnostics
ELISA	Enzyme-linked immunosorbent assay
FITC	Fluorescein isothiocyanate
GHz	Giga hertz
G Ω	Giga Ohm
GP	Glycoprotein
HIV	Human immunodeficiency virus
HRP	Horseradish peroxidase
IA	Immunoassay
IgG	Immunoglobulin G
IgM	Immunoglobulin M
iSDA	Isothermal strand displacement amplification
KHz	Kilo hertz
LFTs	Lateral flow tests
LOD	Limit of detection
LRS	Low-resource setting
μ F	Micro farad
μ PAD	Microfluidic paper-based analytical devices
MAD NAAT	Multiplexed autonomous disposable nucleic acid amplification test
MD NAAT	Multiplexed disposable nucleic acid amplification test
MHz	Mega hertz
MGB	Minor groove binder
MRSA	Methicillin-resistant staphylococcus aureus
NA	Nucleic acid
NAAT	Nucleic acid amplification test

PAGE	Polyacrylamide gel electrophoresis
POC	Point-of-care
RF	Radiofrequency
ROI	Region of interest
SA	Streptavidin
USB	Universal Serial Bus
TB	Tuberculosis
TL	Transmission line
VLP	Virus-like-particles
WHO	World health organization
QDs	Quantum dots

Abstract

Point-of-care and biosensing devices are in great demand to detect infectious and non-infectious diseases, especially in low-resource settings. Key technical challenges for successful instrument-free platforms are: 1) perform multistep assays, 2) ability to process different sample types, 3) incorporate sensitive detection methods, 4) dry storage and stability of reagents, 5) minimal user-steps for ease-of-use, 6) rapid detection time and, 7) low-cost for affordability. This thesis addressed these challenging tools with different approaches in three parts.

Part I: Low-cost paper-based point-of-care diagnostic devices for infectious diseases

First, a two-dimensional paper network (2DPN) device with onboard dry reagents that automated multistep ELISA in 15 minutes, with one user step, was designed and demonstrated for a malarial marker (Chapter 3). The dry reagents for ELISA in the porous matrix showed excellent long-term stability at high temperatures.

Next, three sample processing 2DPN devices were developed (Chapter 4): i) an integrated card for IgM detection that efficiently removed assay interfering IgG, ii) an integrated device with a user-friendly blood acquisition module that demonstrated plasma separation, lysis of Ebola virus-like particles, and detection of surface glycoprotein marker and, iii) a low-cost microfluidic "origami" device that extracted bacterial DNA from a viscous simulated sputum sample.

Finally, 2DPN for isothermal nucleic acid amplification for a MRSA DNA target in porous matrices was established (Chapter 5). A method for storing dry reagents for amplification and detection was developed with remarkable long-term stability. A sample-to-result test for a *Chlamydia trachomatis* target in the urine sample was demonstrated in a multiplexable, disposable NAAT device operated by a programmed USB-powered board with real-time fluorescence detection using a cellphone.

Part II: Biomolecular motor-powered biosensing

Using kinesin motor proteins as a power source for active transport of a "molecular shuttle" made up of functionalized microtubules, an immunoassay for a heart attack marker was demonstrated on a glass chip (Chapter 6). A fluorescence signal enhancement step was established. A method for long-term dry storage of the complex protein assemblies on a glass-chip was developed.

Part III: Label free biosensing

An electronic interface to biological pores in lipid bilayer using micro-coaxial probes to couple radiofrequency circuitry was developed as a fast readout technique for real-time sensing of single molecules (Chapter 7). Radiofrequency response to alamethicin ion channels and α -hemolysin (α -HL) pores were observed. The open-close state of the α -HL pore using β -cyclodextrin (β -CD), a channel blocker, was recorded by measuring changes in microwave-frequency transmission through the pore correlating simultaneously with conventional single-channel DC recordings.

Finally, the interaction of colloidal quantum dots (QDs) with an artificial lipid membrane was examined in an electric field using a planar lipid bilayer experimental setup (Chapter 8). Voltage-dependent current bursts were observed due to the presence of a large permanent dipole moment in the QDs. The formation of colloidal QD aggregates leading to pore formation is discussed.

Zusammenfassung

Behandlungsort- und Biosensorik-Geräte sind sehr gefragt zur Erkennung von infektiösen und nicht-infektiösen Krankheiten, besonders im ressourcenarmen Umfeld. Die wichtigsten technischen Herausforderungen für erfolgreiche gerätefreie Plattformen sind: 1) Durchführung von Mehrschritt-Assays, 2) Fähigkeit, verschiedene Probenotypen zu verarbeiten, 3) Einbindung empfindlicher Nachweismethoden, 4) trockene Lagerung und Stabilität der Reagenzien, 5) minimale Benutzerschnitte für eine einfache Bedienung, 6) schnelle Nachweiszeit und 7) erschwingliche Kosten. In dieser Abhandlung wurden diese anspruchsvollen Instrumente in drei Teilen mit unterschiedlichen Ansätzen behandelt.

Teil I: Kostengünstige papierbasierte Behandlungsort-Diagnosegeräte für Infektionskrankheiten

Zunächst wurde ein zweidimensionales Papiernetzwerk (2DPN) mit Onboard-Trockenreagenzien entwickelt und demonstriert, das einen mehrstufigen ELISA für einen Malariamarker in 15 Minuten und mit nur einem Bedienschritt automatisiert (Kapitel 3). Die Trockenreagenzien für den ELISA zeigten in der porösen Matrix eine ausgezeichnete Langzeitstabilität bei hohen Temperaturen.

Als nächstes wurden drei probenverarbeitende 2DPN-Geräte entwickelt (Kapitel 4): i) eine integrierte Karte für den IgM-Nachweis, der für den Assay störende IgG effizient entfernte, ii) ein integriertes Gerät mit einem benutzerfreundlichen Bluterfassungsmodul, das Plasmatrennung, Lyse von Ebola-Virus-ähnlichen Partikeln und den Nachweis von Oberflächenglykoprotein-Markern ermöglichte, und iii) ein kostengünstiges mikrofluidisches "Origami"-Gerät, das bakterielle DNA aus einer viskosen, simulierten Sputum-Probe extrahierte.

Schließlich wurde ein 2DPN für die isotherme Nukleinsäureamplifikation für ein MRSA-DNA-Ziel in porösen Matrices etabliert (Kapitel 5). Es wurde eine Methode zur Lagerung von Trockenreagenzien für die Amplifikation und den Nachweis mit bemerkenswerter Langzeitstabilität entwickelt. Ein „Sample-to-result“-Schnelltest für den Nachweis von *Chlamydia trachomatis* in der Urinprobe wurde in einem multiplexfähigen Einweg-NAAT-Gerät demonstriert, das von einer programmierten USB-betriebenen Platine mit Echtzeit-Fluoreszenznachweis über ein Mobiltelefon betrieben wird.

Teil II: Biomolekulare, motorbetriebene Biosensorik

Unter Verwendung von Kinesin-Motorproteinen als Antriebsquelle für den aktiven Transport eines “molekularen Shuttles“ aus funktionalisierten Mikrotubuli wurde ein Immunoassay für einen Herzinfarktmarker auf einem Glas-Chip demonstriert (Kapitel 6). Es wurde eine Fluoreszenzsignalverstärkung etabliert. Es wurde eine Methode zur trockenen Langzeitlagerung der komplexen Protein-Baugruppen auf einem Glaschip entwickelt.

Teil III: Etikettenfreie Biosensorik

Es wurde eine elektronische Schnittstelle zu biologischen Poren in Lipiddoppelschichten unter Verwendung von mikrokoaxialen Sonden zur Kopplung von Hochfrequenzschaltungen als schnelle Auslesetechnik für die Echtzeitabtastung von Einzelmolekülen entwickelt (Kapitel 7). Es wurde die Hochfrequenz-Antwort auf Alamethicin-Ionenkanäle und α -Hämolysin-Poren (α -HL) beobachtet. Der offene/geschlossene Zustand der α -HL-Pore unter Verwendung von β -Cyclodextrin (β -CD), einem Kanalblocker, wurde durch die Messung von Änderungen in der Mikrowellenfrequenzübertragung durch die Pore aufgezeichnet, die gleichzeitig mit konventionellen Einkanal-DC-Aufnahmen korrelierten.

Schließlich wurde die Wechselwirkung von kolloidalen Quantenpunkten (QDs) mit einer künstlichen Lipidmembran in einem elektrischen Feld unter Verwendung eines planaren Lipiddoppelschicht-Versuchsaufbaus untersucht (Kapitel 8). Aufgrund des Vorhandenseins eines großen permanenten Dipolmoments in den QDs wurden spannungsabhängige Stromstöße beobachtet. Es wird die Bildung von kolloidalen QD-Aggregaten, die zur Porenbildung führen, diskutiert.

Chapter 1

1 Introduction

1.1 Significance of the proposed work

At this very moment in the developing world, a child, a woman, or a man is dying from an infectious disease. Often, there is no diagnosis on which of the pathogens they contracted. The most common contagious diseases prevalent in the developing world, especially sub-Saharan Africa and Asia, are tuberculosis, malaria, dengue, typhoid, HIV/AIDS, and cholera, to name a few, and the innumerable emerging diseases caused by viruses such as Zika and Ebola. According to the World Health Organization (WHO), nearly 17 million people die worldwide every year due to infectious diseases. A 2010 Global Burden of Disease study led by the Institute for Health Metrics and Evaluation ranked lower respiratory infections, diarrhea, HIV/AIDS, and malaria in the top ten global disease burden causes. This burden accounts for an estimated 337 million DALYs (disability-adjusted life years) in total ¹ (Figure 1.1). One DALY equals one lost year of healthy life due to premature death and disability.

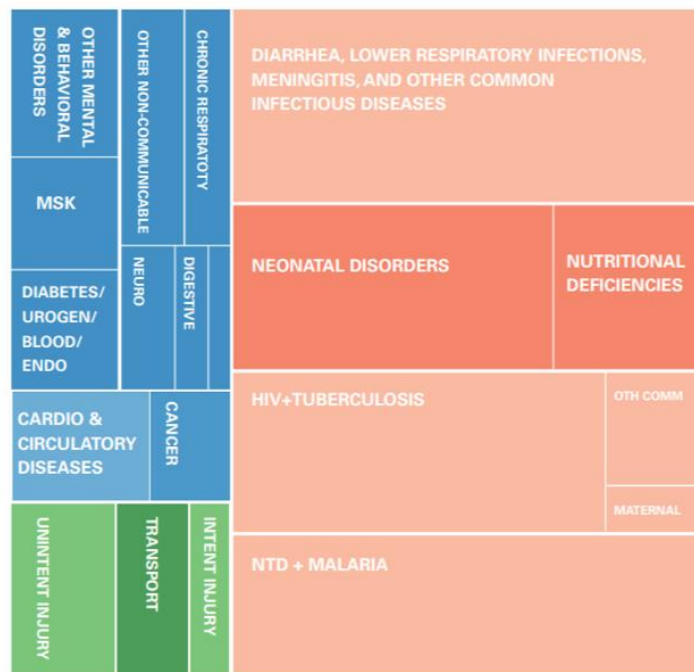


Figure 1.1. Causes of disability-adjusted life years (DALYs), both sexes, all ages, sub-Saharan Africa, 2010. (Reproduced from the 2010 Global Burden of Disease report)¹.

Many of these diseases could be prevented or cured if they could be accurately diagnosed in the first place. However, the disease burden is borne disproportionately by low-income countries with limited access to healthcare². There are millions for whom a visit to a clinic is miles away, or there is a lack of infrastructure like the ones available in the developed world. Such an infrastructure is a centralized lab that requires equipment running on electricity, cold storage of reagents, and trained personnel. For families living under a dollar per day, this would be simply unaffordable. The burden of these diseases, in turn, cripples the socioeconomic development of these nations. A timely diagnostic in such a resource-limited setting that is affordable is critical to containment of the disease, getting the right path to treatment, and preventing loss of life.

Besides, the recent outbreak of Covid 19 disease has sparked an urgent need to diagnose the virus at the point of care reliably. Diagnostics has become critical for tracking pathogen spread, understanding epidemiology, and suppress transmission.

1.2 Proposed solution

Point of care diagnostics for low resource settings

Point-of-care (POC) diagnostics (Dx) refers to medical testing at the time and place of patient care, either a doctor's office, near bedside in a hospital, or administered at home without having to wait days or even hours for sample transport and laboratory processing. It is also often referred to as extra laboratory testing done at the sample collection site without laboratory staff or facilities. The idea is to get results as soon as possible so the patients can receive treatment immediately. Especially for resource-limited settings where the infrastructure for laboratory-based testing is lacking, POC Dx can reduce costs tremendously and, in turn, would reduce hospital stay and eliminate the need for follow-up visits by the patient. Overall, POC Dx leads to disease management with economic benefits.

In the context of the diagnosis of infectious diseases, designing low-cost POC Dx devices is critical for low resource settings. The time-saving benefits, however, need to be weighed against the cost. Several studies have been conducted to evaluate POC tests' cost-benefit analysis, e.g., HIV screening³ TB diagnosis⁴, the Xpert MTB/RIF test⁵. Many commercial diagnostic tests such as the Cepheid GeneXpert and Alere i in the market offer sensitive platforms for pathogen detection.

However, they require multiple user steps, refrigeration, trained users, and need expensive consumables, thus rendering them unsuitable for low-resource settings.

The most commonly used rapid point-of-care tests, such as lateral flow tests (LFTs), have transformed disease testing in various community settings, hospitals, pharmacies, and homes worldwide ⁶. However, the World Health Organization (WHO) has imposed a stringent requirement for the diagnostic devices outlined by the ASSURED criteria, which stands for an **a**ffordable, **s**ensitive, **s**pecific, **u**ser-friendly, **r**apid and **r**obust, **e**quipment-free and **d**eliverable to the end-user ⁷. While there is no benchmark, the test's cost should be ideally \$1 for LFTs and about \$10 for molecular assays. The tests should minimize or avoid false negatives and have low false-positive rates. Sensitivity and specificity ensure accurate diagnosis and treatment and is vital to prevent the misuse of antibiotics, which has led to an increase in antibiotic resistance pathogens crisis in many countries ⁸. The device needs to be user-friendly, which can be performed in a few steps with minimal training. The test should be rapid, and results should be available in 15–60 minutes after sample collection and enable patient management and treatment during the same visit. Another critical challenge is the robustness of the test, which includes the stability of the dry reagents in POC devices, especially in countries where the ambient temperature could be as high as 45 °C.

Recently, two additional criteria, R for real-time connectivity and E for ease of specimen collection and environmental friendliness, were added to the original ASSURED to create a new acronym of REASSURED ⁹. Mobile phones can be used to power the POC test reaction, read results in real-time, and provide the required data to healthcare workers or decision-makers for effectively surveying and treating patients. Finally, the POC diagnostic test needs to be environmentally friendly and easily degradable without posing a risk to the health and the environment.

Simple lateral flow POC tests are available, but they are often qualitative and lack a sophisticated benchtop assay's sensitivity. Laboratory-based tests that are instrumented involve multiple steps and use reagents in cold storage such as ELISA or nucleic acid amplification test (NAAT) to improve sensitivity. Developing POC tests that use non-invasive specimens and perform concentration, purification, lysis, and target amplification are essential but challenging tasks.

1.3 Outline of the thesis

This dissertation, "Designing tools for point-of-care diagnostics and biosensing for low-resource settings," aims to bridge the gap by taking elements of the technologies used in a centralized laboratory and other innovations and merging it with POC Dx platforms for low-resource settings (LRS). The challenges include implementing multistep assays, sample processing, reagent dry storage and stability, signal enhancement for improving sensitivity, ease-of-use, rapid detection time, and low cost. The proposed solution is addressed in three parts with different approaches.

Part I: Low-cost paper-based point-of-care diagnostics for infectious diseases

Here, implementing the challenging tools for POC devices using low-cost paper-based materials is considered. Paper materials can move fluids by capillary action and perform a variety of functions. They can be skillfully cut and designed to different shapes to integrate challenging tools such as sample processing steps like filtration, concentration, plasma separation, lysis, nucleic acid extraction, and perform multistep immunoassays and molecular diagnostic assays. The porous matrices can store reagents in dry form and efficiently be rehydrated before use. The platforms can be made user-friendly and rapid, with minimal user activation steps and power consumption. The paper-based platforms can be safely disposed of.

Part II: Biomolecular motor-powered biosensing

Here, kinesin motor protein as a power source for active transport in a glass-chip device is considered for performing a multistep immunoassay. Antibody functionalized microtubules would transport biomarkers aided by the motor protein to the detection zone. This system would simplify the fluidic pathways without the need for pumps and valves typically used in microfluidic devices.

Part III: Label-free biosensing

Here, ion channels and pores embedded in the lipid bilayer for single molecule biosensing is considered. Radiofrequency waves in the MHz-GHz range for probing ion channel activity as a fast readout is explored for developing biosensing platforms.

Finally, the interaction of colloidal quantum dots (QDs) with the lipid bilayer to probe the living system as a tool is examined.

This thesis has six aims included in three parts, as illustrated in Figure 1.2.

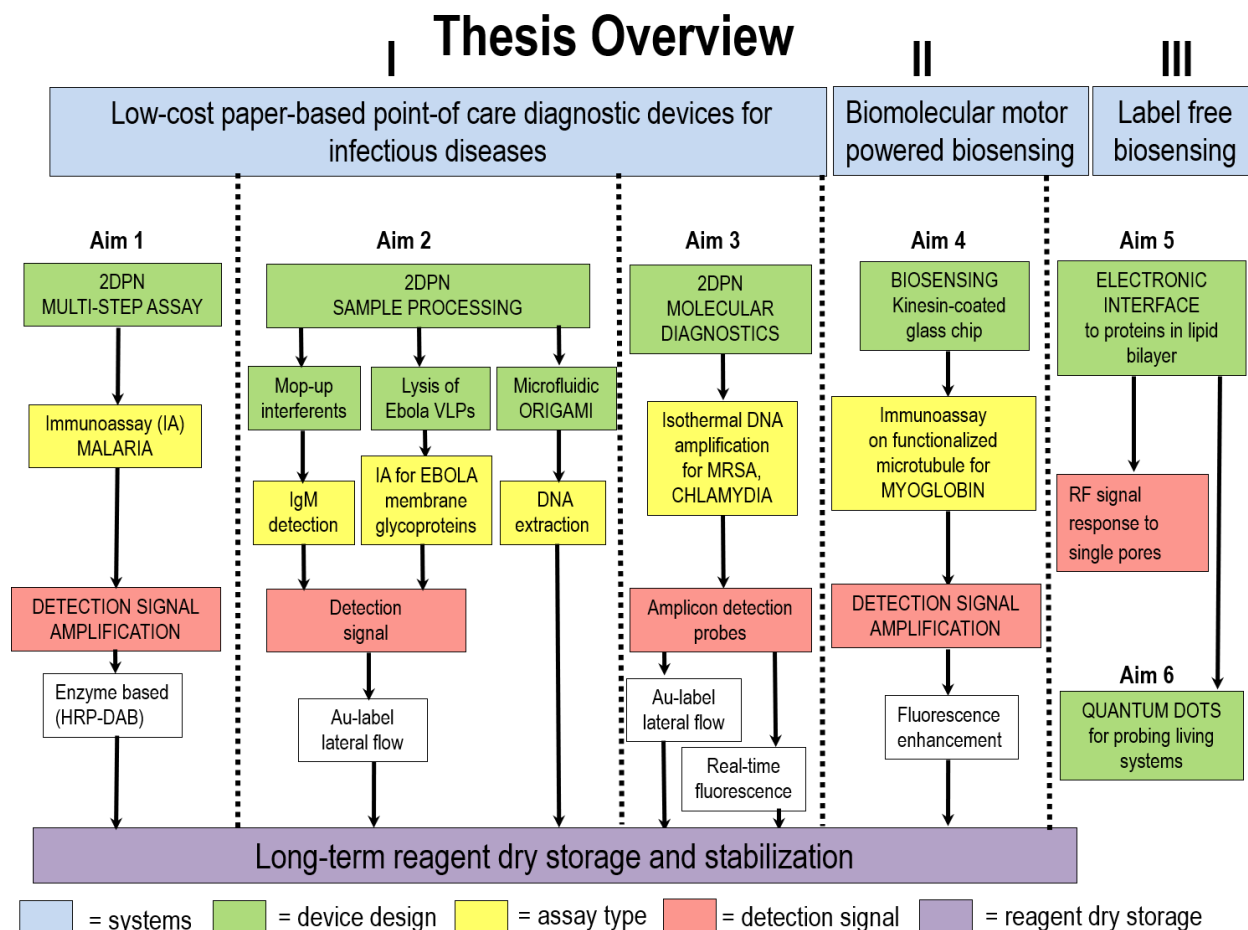


Figure 1.2 Thesis overview.

In chapter 2, the background information to the three parts of the thesis topic is given. For aims 1-3, paper fluidics' fundamental concepts for implementing the different challenging POC diagnostics tools are discussed. For aim 4, the background of adapting kinesin proteins for active transport in motor-powered biosensing nanodevices is presented. For aim 5, the need for an electronic interface using radiofrequency bandwidth to probe proteins in lipid bilayer as a mechanism for label-free biosensing is elucidated. For aim 6, the background information for the use of quantum dots to probe living systems is explained.

In chapter 3 (Aim1), a two-dimensional paper network (2DPN) POC device design for multistep immunoassay with an enzyme-based signal amplification method is presented. A method for long-

term dry storage of the ELISA reagents in the porous matrix is detailed. A 2DPN device that can perform an automated multistep ELISA with onboard dry reagents with one user-step activation for a malarial assay is demonstrated.

In chapter 4 (Aim 2), 2DPN devices for sample processing is presented. Three different sample processing devices are highlighted: 1) A 2DPN card with integrated assay and sample processing to remove upstream assay inhibiting IgG for IgM detection, 2) A 2DPN device with plasma separation and lysis capability for detection of membrane glycoprotein of Ebola virus-like-particles (VLPs) spiked into the blood, and 3) A paper-based microfluidic origami device for nucleic acid extraction from viscous samples.

In chapter 5 (Aim 3), a 2DPN for molecular diagnostics incorporating an isothermal nucleic acid (NA) amplification is presented. A method for long-term dry storage of amplification and detection reagents in the porous matrix is detailed. Two different ways to detect amplicons are described: 1) lateral flow detection with Au label, and 2) real-time fluorescence detection. Implementation of the 2DPN into an integrated POC NAAT device with onboard dry reagents with lateral flow detection and real-time fluorescence detection is discussed.

Chapter 6 (Aim 4) describes a kinesin motor-powered "molecular shuttle" for biosensing. A process for an *in-situ* assembly of antibody-functionalized microtubules for a sandwich immunoassay is demonstrated. A technique for enhancing the fluorescence signal by building multilayer structures using streptavidin-biotin linkages is described. A method for the long-term dry storage of the biosensor with complex protein assemblies on a glass-chip is presented.

In chapter 7 (Aim 5), an electronic interface using radiofrequency (RF) circuitry with biological pores in artificial lipid bilayer as a label-free sensor of single molecules is demonstrated. A micro-coax probe for direct RF transmission modulation in the presence of a single channel pore-blocking events in a lipid bilayer with simultaneous DC recording is presented.

In chapter 8 (Aim 6), the interaction of inorganic semiconductor colloidal quantum dots (QDs) with artificial lipid bilayer in an electric field is investigated. Pore formation with various sizes and the number of QDs in the lipid membrane is calculated.

In Chapter 9, discussion, and conclusions from all the aims are presented.

Chapter 2

2 Background

2.1 Low-cost paper-based point-of-care diagnostics for infectious diseases

Paper-based microfluidic POC devices

Since the 1990s, microfluidics platforms showed great promise for point-of-care diagnostics, leading to the miniaturization of laboratory-based instruments. The advantages were low sample volume, low reagent consumption, rapid detection time, and easy to use¹⁰⁻¹¹. However, the technology has many limiting factors, including complex fabrication, labor-intensive, high cost associated with syringe pumps to meter precise volume of fluid, and the ability to mass-produce.

Since the first demonstration of the Whiteside's group's paper-based biosensing in 2007,¹² paper microfluidic devices have become an attractive tool for POC Dx devices. There are several advantages for using a porous material, including 1) low-cost fabrication using materials such as nitrocellulose, cellulose, or glass fiber, compared to the materials used in conventional microfluidic devices, 2) fluid transport aided by the capillary action of the porous material instead of pumps, 3) dry reagents storage in the porous matrix, 4) portable and desirable for field-use especially in resource-limiting settings, 5) ease of production, and 6) disposable.

Lateral flow tests (LFTs), such as the one used in a pregnancy test is the earliest example of a paper-based POC platform (Figure 2.1). They are low-cost, simple to use, rapid, reagents stored in dry form, and equipment-free, especially advantageous in low-resource settings. Many LFTs for different analytes, including disease markers for pathogens¹³⁻¹⁴, contaminants in water supply¹⁵, and food safety¹⁷⁻¹⁸, have been developed.

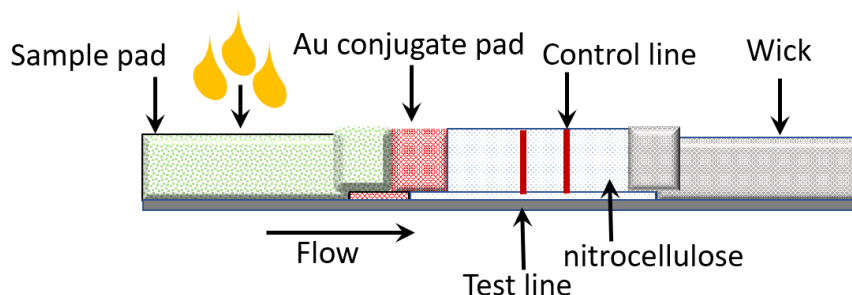


Figure 2.1. Schematic of a one-dimensional lateral flow test (LFT).

LFTs exist for use on various sample matrices, including whole blood ¹⁹, serum ²⁰, plasma ²¹, urine ²², sweat ²³, and saliva ²⁴. However, these LFTs are usually 1-dimensional, performing simple operations involving a single chemical delivery step, and hence the results are mostly qualitative lacking sensitivity. While LFTs fulfill the ASSURED criteria, they lack multiplexing and performing multiple sample and chemical processing steps. The following sections cover methods used to improve LFTs.

Multiplexing using paper-based devices

Laboratory-based assays often use multistep processes to achieve high performance. An example of a multistep assay is the ELISA. This method requires the sequential delivery of multiple reagents with many wash steps. Whiteside group introduced microfluidic paper-based analytical devices (μ PADS) in either 2D or 3D paper-based structures incorporating colorimetric assays to detect glucose and protein with multiplexing capability ^{12 25}. Since 2008, the Yager laboratory has focused on developing an ultra-low-cost point of care devices for pathogen identification using a two-dimensional porous network. There has been significant progress in developing tools to control fluid flow in paper-based systems to expand the capability to improve analytical sensitivity, rapid detection, and easy operation of using paper-based devices. Fu et al. manipulated the porous channel's width and length to slow down and speed up the advance of fluid within the channel under wet-out conditions ^{26 27}. Lutz et al. used dissolvable fluidic time delays for programming multistep assays in paper diagnostics ²⁸ (Figure 2.2).

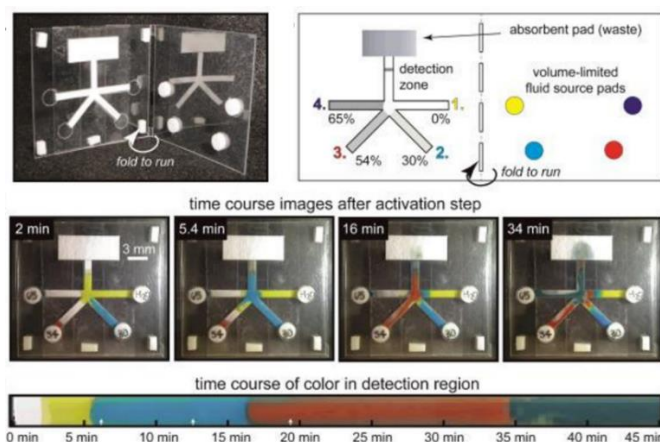


Figure 2.2 Paper fluidic device with timed sequential delivery with dissolvable sugar barriers as time delays. (Reproduced from *Lab Chip*, 2013,13, 2840-2847 with permission from the Royal Society of Chemistry).

Sucrose solutions ranging between 10-70% were dried on paper strips at different concentrations creating fluidic time delays spanning minutes to nearly an hour. A simple folding card format employing sugar delays was shown to automate a four-step fluidic process initiated by a single user activation step solution. The sugar barrier essentially functioned as valves.

Fu et al. presented a paper network with varying path lengths inlets to sequentially deliver multiple fluids to a downstream detection region of the device and demonstrated an immunoassay (Figure 2.3)²⁹.

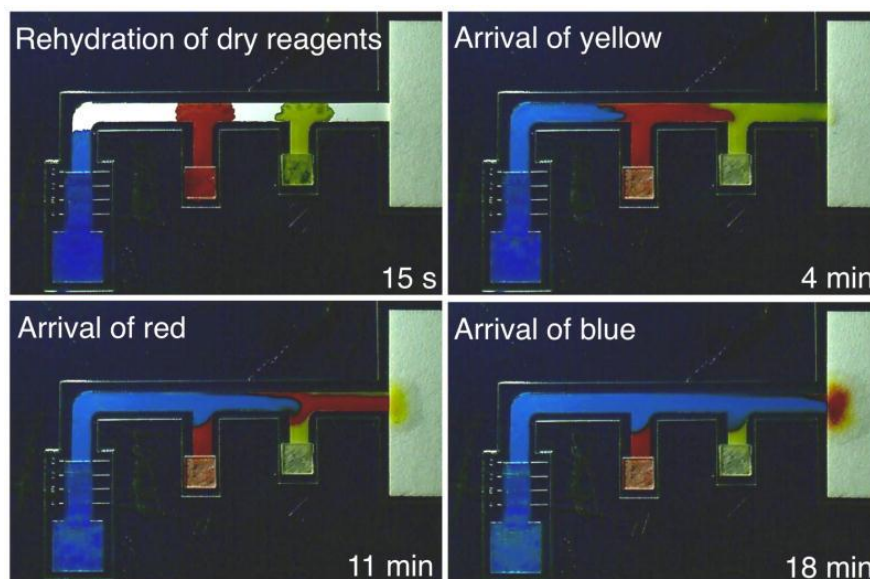


Figure 2.3. Demonstration of the multistep reagent delivery by 2DPN. (Reprinted with permission from *Anal. Chem.*, 2012, 84(1), 4574–4579 Copyright (2012) American Chemical Society).

Sample processing for POC

The process of diagnosing infectious diseases at the point of care is often complicated. The pathogens, whether viruses, bacteria, parasites, or fungi, or its markers, are present in various matrices such as blood, urine, nasal mucous, sputum, or saliva. They all require different sample processing steps such as separation of plasma from the blood for biomarker testing, filtration to concentrate the pathogens in urine, or extraction of DNA or RNA from these matrices, often inhibitory to the assays performed. Some samples need dilution to be more compatible with the assay. Applications that require upstream sample processing, such as removing blood cells and assay-interfering contaminants, require performing benchtop processes involving multiple steps

and centrifugation in a laboratory setting. These are, however, not practical for point-of-care (POC) settings. Yang et al. have used μ PADS for separating blood components and colorimetric detection of analytes in plasma³⁰. Brynes et al. developed methods for DNA purification and concentration system using linear polysaccharide chitosan in porous membrane substrates for POC applications^{31 32}. Brynes et al. also developed an integrated system for large volume sample preparation at the point of care for DNA purification from urinary pathogens using porous membrane³³.

Buser and colleagues used partial saturation properties of porous material to control fluid flow³⁴. They showed that in systems with multi-material porous networks, fluid transport is driven by material properties and saturation and pressure differentials at the junction of overlapping materials (Figure 2.4).

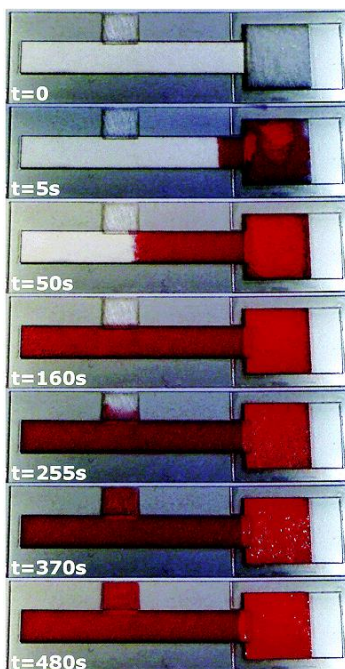


Figure. 2.4. Using partial saturation to control flow in a paperfluidic system. A red dye solution is added to the square glass fiber source pad, which drains into a strip of Fusion 5 membrane, referred to as the "primary membrane". An additional section of the glass fiber membrane is positioned partially down the Fusion 5 strip, referred to as the "secondary membrane". This glass fiber section will remain largely dry until the fluid has completely wet the length of Fusion 5 membrane (Reproduced with permission from *Anal. Methods*, 2019,11, 336-345 from the Royal Society of Chemistry).

Using the concept of partial saturation, they demonstrated its use for an automated parallel dilution system, and DNA extraction and concentration for milliliter sized samples³⁴.

Signal enhancement for POC

Simple LFTs are based on colorimetric detection based on Au, colored latex beads, or carbon nanoparticles. However, the clinical sensitivity and specificity must match assays performed by a centralized laboratory to use LFTs in infectious disease diagnosis effectively. Many signal enhancement methods are used in laboratory tests to improve sensitivity. ELISA is the most commonly used enzyme-based amplification of the signal. Many studies have shown improved sensitivity in LFTs using signal amplification, such as silver enhancement solution to improve 50-100-fold gain in the limit of detection (LOD)^{35 36} or 10-fold increase with enzyme-based amplification³⁷. These steps, however, were not integrated into the LFTs and had to be performed by users manually, involving many steps and handling of reagents, thus limiting the format for use in POC. Another method using quantum dots for fluorescence detection has been used to increase sensitivity but requires expensive optical instruments for detection^{38 39}.

Fu and colleagues used a gold enhancement solution to improve LOD by integrating rinse and amplification steps to a conventional LFT in a 2DPN format²⁷. This format incorporated dry reagents in a porous matrix and can be used by minimally trained users in POC low-resource settings (Figure 2.5).

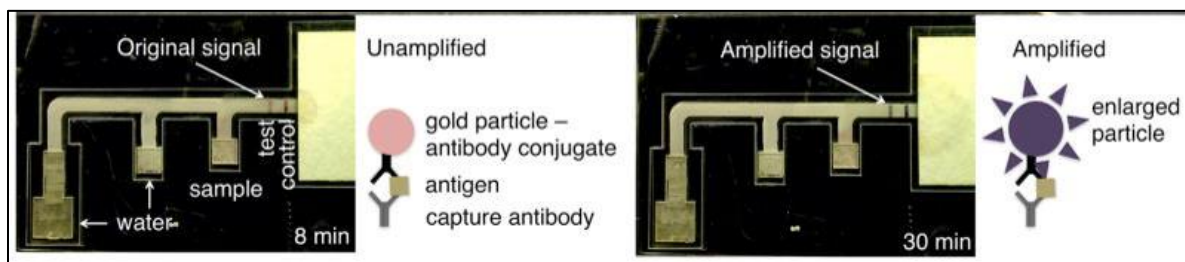


Figure 2.5. Easy-to-use 2DPN card format demonstrating amplified immunoassay using gold enhancement reagent. (Adapted with permission from *Anal. Chem.*, 2012, 84(1), 4574–4579) Copyright (2012) American Chemical Society).

Molecular diagnostics for POC

NAAT-based POC devices are rapidly growing for use in low-resource settings. They are the most sensitive approach to detecting pathogens via DNA or RNA amplification and have relatively rapid turnaround times (getting results on the same day) compared to microbiological cultures or ELISA^{40 41 42 43 44 45}. Unfortunately, while NAATs aimed at POC for bacterial and viral infectious disease diagnoses have been developed, they are instrumented and expensive because they either require thermal cycling and/or complicated optics for fluorescence readout^{46 47 48 49}. There has been progress towards developing isothermal amplification systems in miniaturized microfluidic devices that are easy to use and suitable for LRS, but often at high prices and with varying levels of automation^{50 51 52 53}. Paper fluidic devices have also been used for NAAT based testing as an inexpensive alternative to instrumented systems^{54 55 56}.

Dry reagents storage for POC

One of the key technical requirements for truly LRS-compatible POC systems is the device's robustness in different climates. The POC system requires the reagents to be stored dry. There are two main challenges. The first is the reagents' long-term stability at elevated temperatures, especially for use in places where the ambient temperature could be as high as 45 °C. The most promising approach is to store all reagents except simple buffers in dry form in a way that limits exposure to oxygen. The subsequent challenge is uniform rehydration of the reagents within the device to achieve optimal performance. Overcoming these challenges would circumvent the need for the "cold chain" (continuous refrigeration from the point of manufacture to the point of use), which is inconvenient in any diagnostic product and maybe too expensive and even unavailable in many LRS settings. The dry preservation of detection reagents and signal amplification reagents in a solid porous matrix could have high value for several applications with fluid connectivity, especially in paper-based POC devices and applicable to low-resource settings.

Chapter 3-5 describes the fabrication of different low-cost paper-based device designs incorporating tools for multistep assays, sample processing capabilities, signal enhancement, dry reagent storage, and the long-term stability for low-cost low-resource POC settings for both immunoassays and molecular diagnostics.

2.2 Biomolecular motor-powered biosensing

Biomolecular motors as nanoscale engines

Cellular transport utilizing motor proteins such as kinesin has provided great inspiration to scientists in implementing active transport mechanisms into biosensing devices. Molecular motors are a fascinating class of proteins that associate with the cytoskeleton of cells. They are involved in different functions such as intracellular transport, segregation of chromosomes during cell division, cell migration, cell signaling, and muscle contraction. They bind to the cytoskeletal filaments such as actin or microtubules and use the energy from ATP hydrolysis to move along it. One class of motor proteins is the kinesins that move along microtubules and play an essential role in intracellular transport carrying membrane-bound organelles such as secretory vesicles, Golgi stacks, and mitochondria to the appropriate location⁵⁷. Kinesin protein is made up of two head domains that attach to the microtubules and provide the motor function and a tail domain, which provide an attachment point for the cellular cargo to be transported. A schematic of the cargo transport by kinesin motor along the microtubule is represented in Figure 2.6.

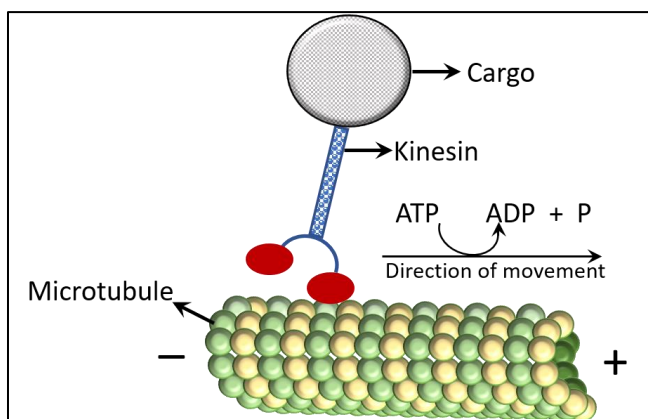


Figure 2.6. Kinesin motor protein walking on microtubule carrying a cargo powered by the hydrolysis of ATP.

Microtubules that form the cytoskeleton of the cell are hollow cylindrical structures made up of thousands of α and β tubulin monomers along which the kinesin motors move. The cellular transport by molecular motors is much faster than diffusion, move against the concentration gradient, and cover long distances such as anterograde and retrograde transport in neurons. Kinesin motors have been found to be highly efficient, generating a force of about 7 pN, and stepwise movement of 8 nm for each molecule of ATP hydrolysis^{58 59}. Thus, biomolecular motors can be

considered as nanoscale engines powering the movement of "cargos" along the cytoskeletal "tracks."

Kinesin motors and its application to nanodevices

The integration of biological nanomachines into micro-and nanodevices promises rapid advances in nanotechnology. This is because device development is not hampered by the lack of critical nanoscale components of human-made origin^{60 61 62}. A promising example of this hybrid approach is the utilization of kinesin motor proteins for the active transport of molecules in microfabricated devices. The molecular transport machinery of the cell has been integrated into many hybrid devices with kinesin as a power source for moving parts. Limberis and Stewart used a patterned microtubule device coupled with kinesin motors and showed the movement of a microchip⁶³. They suggest coupling kinesin to other microfabricated machine parts such as gears, rotors, and levers to function as switches or perhaps valves in microfluidic channels. For a successful device using biomolecular motor transport, the first step to consider is the function of motor proteins in a synthetic environment. A novel technique inverting the geometry, known as the *in vitro* inverted gliding motility assay, was developed⁶⁴. A schematic of kinesin coated glass aiding the movement of microtubules on the surface of the glass is shown in Figure 2.7.

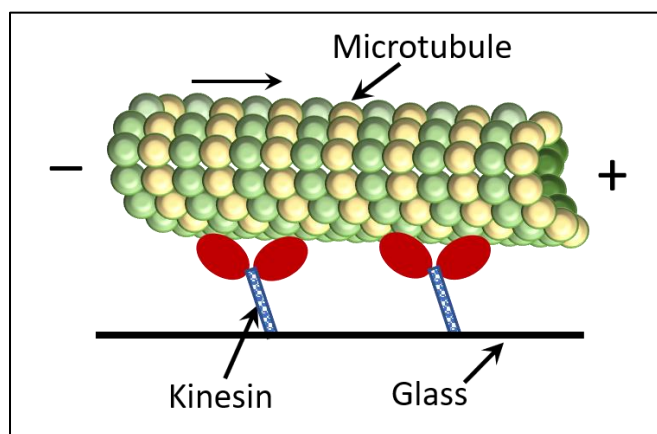


Figure 2.7. Inverted motility assay. Microtubules glide over the kinesin-coated glass surface.

Here, purified bovine brain kinesin motor protein along with casein was immobilized to a glass surface of a flow chamber with optimal coating density, and the ATP-dependent movement of individual microtubules was observed. There is a dynamic equilibrium between assembly and disassembly of microtubules in eukaryotic cells as needed and controlled by cell transport

regulation. For *in vitro* assays, purified tubulin from the bovine brain could easily be polymerized into microtubules and stabilized using taxol. Using the "inverted motility assay," many integrated devices were designed for studying transport by biomolecular motors in guided channels ^{65 66 67}. A stand-alone microfluidic device that can sort to concentrate bio-analyte molecules by using kinesin motors and microtubules as a chemo-mechanical transduction machine have been developed ⁶⁸. Thus, nanoscale biomolecular-motor-driven transport systems are a bioinspired alternative to pump-driven fluid flow or electroosmotic flow in microfluidic devices.

Molecular shuttles and motor-driven transport for analytical devices

The concept for a motor-driven analytical device is a "molecular shuttle," a nanoscale conveyor belt with stationary motors that move microtubule filament onto which the cargo is loaded ⁶⁷. Such a system involves the assembly of supramolecular structures and the manipulation of molecules in a liquid environment. For developing a biosensing device, it is essential to functionalize the microtubules for the capture and detection of specific analytes. Biology offers several receptor-ligand bonds that have been exploited for several assay development. One such bond is the streptavidin-biotin, which is known to have one of the strongest non-covalent interactions in nature. Using the biotin-streptavidin system, Diez *et al.* attached DNA to the microtubules to study stretching and movement using motor proteins ⁶⁹. Molecular shuttles with biotin linkage loaded with cargo have been constructed to move along motor protein-coated engineered paths. By using UV-induced release of caged ATP, the shuttle velocity could be controlled ⁷⁰. Direct crosslinking of antibodies to microtubules to capture the virus target was reported ⁷¹. A realization of "smart dust" biosensors powered by biomolecular motors has been reported by Bachand *et al.* ⁷². Thus, selective binding of protein analytes, viruses, or small molecules via the molecular shuttle can be designed for analytical detection.

Chapter 6 describes a "molecular shuttle" made up of antibody-functionalized microtubules and powered by kinesin motor protein and its application to biosensing. The long-term stability of the complex protein assembly is of great importance in designing biosensing devices.

2.3 Label-free biosensing

Developing label-free biosensors that can detect single molecules has become an important field of research in biology, physics, and chemistry. Biological pores and ion channels, which are in the nanoscale range, are excellent systems for developing single-molecule label-free sensors owing to the electrical nature of the detection signal.

Ion channels as bio-transistors

All biological cell membranes are generally impermeable to ions and act as insulators. They are functionally equivalent to a capacitor holding an enormous electrical charge. The membrane capacitance is in the order of $1 \mu\text{F}/\text{cm}^2$. Ion channels, which are made up of proteins, span across the hydrophobic cell membrane allowing the flux of specific ions, charged, or polar molecules from one side of the membrane. In nature, ion channels have diverse functions that range from maintaining cell homeostasis, cell signaling to activating, or killing cancer cells. Intercellular communication between cells like neurons and muscles relies on ion channels in the cell membrane, either voltage-gated, ligand-gated, or sensitive to mechanical stress.

Just like transistors that control current flow in electronic devices, ion channels control ionic current across the cell membrane. Thus, an ion channel can be regarded as a bio-transistor and as the most fundamental gating mechanism controlling the electric potential of cells. For the past few decades, electrophysiologists have been measuring ionic currents through single channels using the patch-clamp technique pioneered by Neher and Sakmann⁷³.

Patch clamping

The patch-clamp method relies on the formation of a micron-size contact with the cell membrane by means of an electrolyte filled glass pipet and isolating a membrane patch electrically by applying suction (Figure 2.8). Due to the strong glass-membrane adhesion, a $\text{G}\Omega$ seal is obtained. Voltage is then applied, forming a voltage clamp, and membrane current is measured. Currents fluxing through the ion channels in this patch flow into the pipette and can be recorded by an electrode that is connected to an extremely sensitive amplifier.

The patch-clamp technique allows the investigation of a single ion channel and is thus of special interest in the research of excitable cells such as neurons, cardiomyocytes, and muscle fibers.

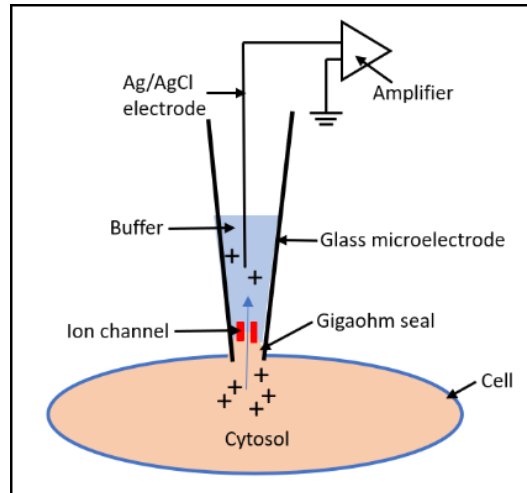


Figure 2.8. Patch-clamp technique. A glass pipette containing electrolyte solution is tightly sealed onto the cell membrane isolating a membrane patch. Currents fluxing through the channels in this patch is recorded by an electrode that is connected to a highly sensitive amplifier.

Planar lipid bilayer and ion channel measurement

While patch clamping has become a standard tool for studying ion channel behavior in cells, planar lipid membrane models have been developed as a method for studying reconstituted single ion channels in artificial bilayer^{74 75 76}. The system consists of two compartments of a chamber, traditionally made of Teflon, filled with electrolytes, and separated by a septum containing a tiny hole $\sim 100\text{-}200\ \mu\text{m}$ (Figure 2.9).

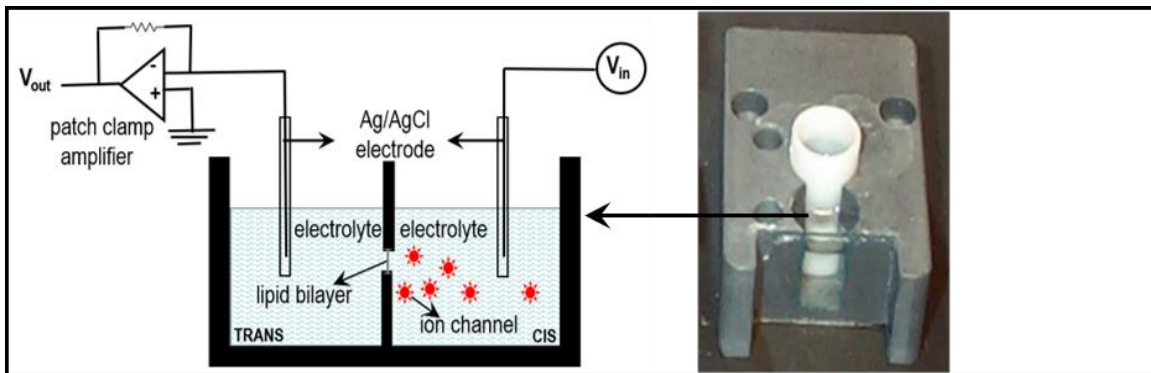


Figure 2.9. Schematic of planar lipid bilayer setup (left) and a picture of the chamber with two compartments (right).

A phospholipid solution is painted across the hole to form a lipid bilayer. Purified ion channels or pore-forming peptides are added to one side of the membrane and incorporated into the bilayer.

Using electrophysiological measurement, one can monitor ion channels' behavior at the single-molecule level in the artificial membranes. Many pore-forming peptides and proteins like gramicidin, alamethicin, and α -hemolysin have been used to study their behavior using the artificial lipid bilayer^{77 78 79}. Examples of traces of ion channel currents measured by planar lipid bilayer setup are shown in Figure 2.10.

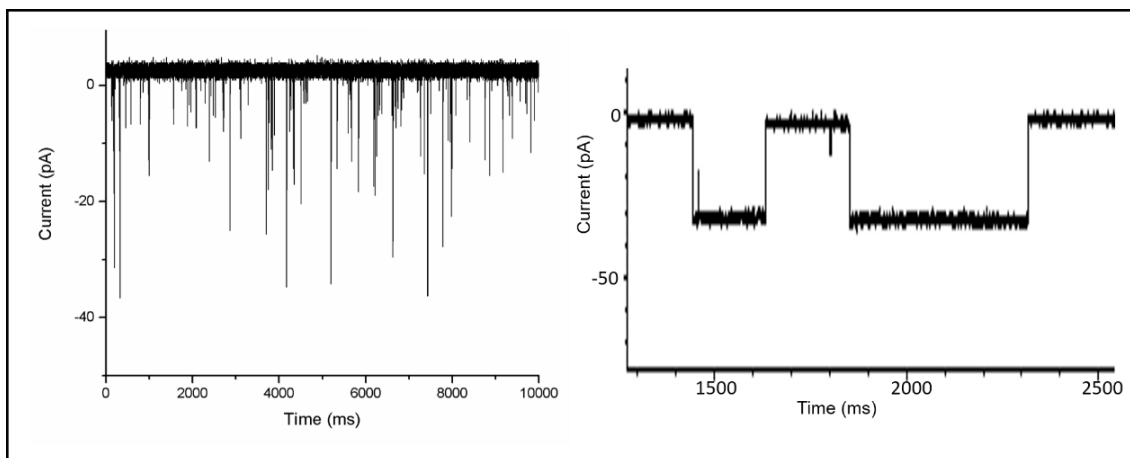


Figure 2.10. Examples of current trace for alamethicin (ALA) (left), and alpha-hemolysin (α -HL) with a channel blocker β -cyclodextrin (β -CD) (right) measured in a planar lipid bilayer setup under applied voltage bias.

Advances have also been made using a planar glass chip to record single-channel electrophysiology⁸⁰, including a 96-well high throughput planar bilayer device⁸¹.

Ion channels play a role in many diseases, referred to as channelopathies, including hypertension, epilepsy, cardiac arrhythmias, gastrointestinal, neuromuscular disorders, and pathological pain. Reconstitution of ion channels in artificial planar lipid bilayer enables researchers to understand how ion channels behave both in normal and disease states and how different drugs, ions, or other analytes can modify these conditions. By understanding the exact role that ion channels play in a particular disease, researchers might be able to find ways to affect the ion channel to alter the course of the disease.

Ion channels for biosensing platform

Many studies have exploited natural ligand-gated ion channels such as the glutamate receptor^{82 83} and nicotinic acetylcholine receptors as biosensing elements that are very selective for specific ligands. The binding of these ligands to the receptor site of the channel protein causes a transient conformational change leading to a measurable change in ion flux across the membrane. Thus, a single binding event results in an amplification of a signal, which is very appealing for biosensing platforms.

Bayley et al. developed stochastic nanopore sensing for measurements of the interaction kinetics and thermodynamics of protein complexes using α -hemolysin pores^{84 85}. Pores like gramicidin and α -hemolysin have been used for delivery of therapeutic agents, macromolecules, or nucleic acid into the cells^{86 87 88} and have been used in various sensing platforms^{89 90 91}. Biological pores and artificial pores have also been explored for many applications such as detection of single molecules⁹², sequencing of nucleic acid^{93 94}, detection of viruses^{95 96 97}, antibody-antigen interactions^{98 99 100}, the occurrence of chemical reactions^{101 102} and detection of nanoparticle^{103 104 105}.

There has been a report of ion channels' use as a diagnostic tool for the detection of bacteria, viruses, nucleic acids, and small molecules. Woodhouse et al.¹⁰⁶ described an ion-channel switch biosensor for direct measurement of molecular interactions at the surface of a tethered bilayer membrane through the change in electrical transduction of chemically modified gramicidin ion-channel. Using this molecular recognition tool, they measured a range of analytes, including bacteria, DNA, proteins, and drugs in complex biological matrices such as blood and sera. Using the same setup, Oh et al.¹⁰⁷ developed a rapid test for influenza A virus using specific antibodies attached to a gramicidin ion channel.

The most common approach in all these studies has been resistive-pulse sensing, where the transient change in current is monitored when a molecule passes through the pore. A general problem in all these methods is that the molecules translocate far too quickly to be detected, leaving the majority of the events undetected. Further, the amplitude and the width of these resistive-pulse signal needs to be above the noise to be detected and fully resolved. The signal bandwidth limits the time-resolution of changes in the current, while the noise helps determine the sensitivity of a given pore, and are thus two of the limiting factors for experiments that attempt to sense the tiny pulses and the short-lived signals in detecting a single molecule.

Hence, there are two challenges to achieve accurate and sensitive measurements: 1) the noise 2) the signal bandwidth.

Ultra-wide bandwidth frequencies for real-time kinetics of single ion channels

Traditionally, ionic current recordings on single-ion channels and pores are performed in the dc regime and are often hindered by the low temporal resolution of probing single-pore signals with bandwidths of some 10 kHz. This is due to large access resistances (R) and membrane capacitance (C), leading to low time constants $\tau=RC$, which translates into a very narrow range of frequencies or measurement bandwidth ($BW=1/\tau$), and hence a low temporal resolution. Several publications in the literature have addressed the noise and the signal bandwidth of the ion channel current recording in patch-clamp^{108 109} and planar bilayer^{110 111}. Uram et al. published a detailed study to predict noise and the signal bandwidth requirements of current recordings of different nanopore geometry in different synthetic membranes¹¹². Recently, new amplifiers for high-bandwidth (>100 kHz) current measurements have been developed^{113 114 115}. In these studies, the use of pores in membranes that are ultrathin (<10 nm thick) was used, which enhanced the signal/noise of the measurement and sub-microsecond temporal resolution^{116 117 118}.

While most biological signals cover a frequency range from DC to a few kHz, which corresponds to signal transduction time in milliseconds, the currents due to ion transport through the channels are in the order of pA to nA range. Applying a current-frequency relationship, periodic transportation of an elementary charge e with a well-defined frequency f , leads to a current given by the equation^{119 120 121}

$$I = e\tau^{-1} = ef$$

Where I is quantized current, e is electron charge equal to 1.6×10^{-19} coulombs, and τ is the time which translates to $1/f$. Solving for the applied f_{rf} (in the radiofrequency range), a few megahertz leads to a low current of a few picoamperes. Applying this to ion channel current in the pA to nA range, these values translate to frequencies in MHz to GHz range given by the equation: $I = N.q\tau_d^{-1} = N.qf_{rf}$ where N is the average number of the ions transported in the channel, τ_d the dwell time of the ions in the channel, and q the net charge. It is thus desirable to have circuitry available with the potential to deliver real-time information on ion channel operation in the nanosecond time scale. Using radiofrequency bandwidths of at least 1000 times greater than the current state-of-the-art patch-clamp technique would give us the high temporal resolution needed.

While RF dielectric spectroscopy of biological molecules has been reported ^{122 123 124}, the use of RF signals for direct investigation as a readout of ion channels has not been studied in great detail. There has been a report using 1 MHz frequency with a sub-microsecond measurement of DNA passing through a solid-state nanopore ¹¹⁵. There have been a few studies of the frequency response of alternating current through hemolysin pore ^{125 126}.

Chapter 7 describes a label-free biosensing method using an ultra-wide bandwidth electronics interface in the radio frequency range for real-time kinetics of single ion channels in a lipid bilayer. Using radio frequency as a readout method would give us the temporal resolution needed for probing the very fast open and closed states of the ion-channels. The development of such an electronic interface to nanopores will lead to diagnostic and therapeutic discipline applications.

Interaction of colloidal quantum dots with the lipid bilayer

Colloidal quantum dots (QDs) are chemically synthesized inorganic semiconductor nanocrystals. The most widely used QDs are the CdSe/ZnS (core/shell) nanocrystals coated with an outer hydrophilic shell ^{127 128}. QDs are typical > 10 nm in size, are highly fluorescent, showing size-dependent color, have a wide excitation wavelength range, have high quantum yield, and are resistant to photobleaching. QDs are the size of a typical protein, are water-soluble and biocompatible, and thus can be introduced into cells. The use of QDs for biological labeling was first reported by Alivisatos ¹²⁷, and Nie ¹²⁹. QDs coated with biological molecules like protein or DNA were not only used for molecular recognition ^{130 131}, but also for labeling specific cell compartments with different types of QDs ^{132 133}. Because many of the applications of QDs in cell biology involve interaction with the cell membranes, the behavior of QDs on a planar lipid bilayer model is of significant interest. The nanometer length scale of the QDs can sense and detect the state of biological systems and living organisms optically as well as electrically and can be expected to lead to entirely new types of biological sensors.

In chapter 8, a study of the interaction of the semiconductor colloidal quantum dots with a lipid bilayer as a method for probing living systems is described as a label free biosensing method.

Part I: Low-cost paper-based point-of-care diagnostic devices for infectious diseases

*Bada hua to kya hua, jaise ped khajoor
Panthi ko chhaaya nahi, phal laage ati door*

*- Kabir Das- mystic poet
15 th century
Language: Hindi*

Translation-

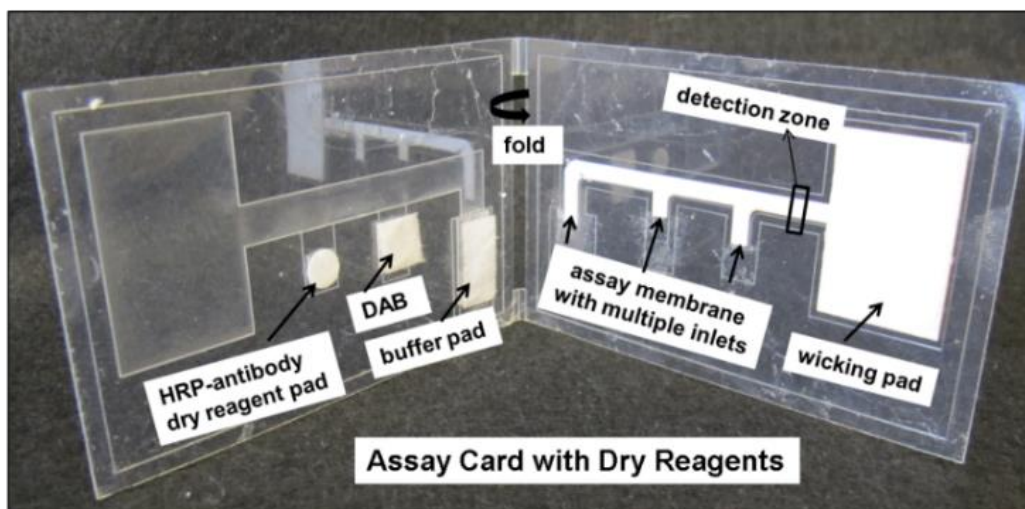
Of what use is eminence? like a date palm tree?

It neither offers shade to travelers, nor is its fruit easy to reach

Chapter 3

3 Two-dimensional paper-network for multistep automated ELISA*

This chapter is based on publication ¹³⁴. This paper describes an automated 2-dimensional paper-network (2DPN) device that performs multistep immunoassay with one user-activation step. The chapter starts with an introduction highlighting the need for compatible multistep assays, as well as sensitive detection methods for POC in resource-limited settings. An enzyme-based signal amplification such as the one used in ELISA was incorporated. A method for the long-term dry storage of ELISA reagents: horseradish peroxidase (HRP) conjugated antibody label and its colorimetric substrate diaminobenzidine (DAB) in a porous matrix is detailed. These dry reagents were incorporated into a 2DPN device made with nitrocellulose, glass fiber and cellulose in a plastic laminate foldable card that automated the multistep ELISA for the detection of a malarial biomarker. The results demonstrate the potential of signal amplification for enhanced sensitivity in low-cost POC devices for low-resource settings. Additional supporting information is given in **Appendix 11.1**.



Foldable 2DPN card for automated ELISA

Reproduced from *Analyst*, 2014, 21;139(6):1456-62 with permission from the Royal Society of Chemistry

3.1 Long-term dry storage of an enzyme-based reagent system for ELISA in point-of care devices*

Sujatha Ramachandran, Elain Fu, Barry Lutz, and Paul Yager

Reproduced from *Analyst*, 2014, 21;139(6):1456-62 with permission from the Royal Society of Chemistry.

I designed the experiment, conducted the work, and analyzed the data. Together with the other authors, I discussed the results, and I wrote the paper.

Long-term dry storage of an enzyme-based reagent system for ELISA in point-of-care devices†

Cite this: *Analyst*, 2014, **139**, 1456

Sujatha Ramachandran,* Elain Fu, Barry Lutz and Paul Yager

Lateral flow devices are commonly used for many point-of-care (POC) applications in low-resource settings. However, they lack the sensitivity needed for many analytes relevant in the diagnosis of diseases. One approach to achieve higher sensitivity is signal amplification, which is commonly used in laboratory assays, but uses reagents that require refrigeration and inherently requires multiple assay steps not normally compatible with POC settings. Enzyme-based signal amplification, such as the one used in ELISA, could greatly improve the limit of detection if it were translated to a format compatible with POC requirements. A signal-amplified POC device not only requires the reagents to be stored in a stable form, but also requires automation of the multiple sequential steps of signal amplification protocols. Here, we describe a method for the long-term dry storage of ELISA reagents: horseradish peroxidase (HRP) conjugated antibody label and its colorimetric substrate diaminobenzidine (DAB). The HRP conjugate retained ~80% enzymatic activity after dry storage at 45 °C for over 5 months. The DAB substrate was also stable at 45 °C and exhibited no detectable loss of activity over 3 months. These reagents were incorporated into a two-dimensional paper network (2DPN) device that automated the steps of ELISA for the detection of a malarial biomarker. These results demonstrate the potential of enzyme-based signal amplification for enhanced sensitivity in POC devices for low resource settings.

Received 12th December 2013
Accepted 26th January 2014

DOI: 10.1039/c3an02296j

www.rsc.org/analyst

Introduction

Point-of-care (POC) devices that are accurate, robust, low cost, rapid, easy-to-use, equipment-free and disposable are in great demand for the diagnosis of diseases in low-resource settings.^{1,2} Existing lateral flow tests (LFTs) are simple wicking-based devices that, typically, use colloidal gold for detection of proteins or antibodies and meet many of the requirements for low-resource settings. However, they lack the high sensitivity needed for many analytes and can lead to misdiagnosis.^{3,4} A main source of this lack of sensitivity arises from the fact that the most common visually-observable labels (*e.g.*, gold nanoparticle labels) are not particularly sensitive. Labels such as latex beads and carbon black have been substituted for gold in LFTs and been reported to have improved sensitivity.^{5,6} Fluorescent labels have been used for greater sensitivity,⁷ but at the expense of adding complexity and cost. Additionally, there have been reports of chemical signal amplification using silver and gold enhancement for overcoming sensitivity limitations.^{8,9} Enzyme-based signal amplification, for example, using the horseradish peroxidase (HRP) system commonly implemented in ELISA,

could greatly improve limits of detection (LOD) if it could be made compatible for use in POC devices. The two main challenges to this are (1) the long-term stability of the HRP conjugated antibody and its substrate and (2) the capability of the POC device to perform the sequential multistep processes needed for the enzyme-based signal amplification without added user steps.

Methods for stabilizing proteins and enzymes in dry form using sugars and sugar alcohols are widely used in the pharmaceutical industry. The most common method of making solid proteins is lyophilization.¹⁰ Trehalose, a non-reducing disaccharide can form protein-stabilizing glass and is the most common sugar used in the dry preservation of biomolecules.^{11–17} Transition metal ions formulated in sugars have been reported to stabilize enzymes.^{18–20} The stabilization of several enzymes including HRP, using a combination of sugar alcohols and cationic polymers or zinc ions was reported and have found application in extending the shelf-life of diagnostic alcohol kits.^{21,22} There have been reports on methods of stabilization of HRP immobilized onto various matrices like SiO₂²³ and polyacrylonitrile²⁴ for use in analytical systems as biosensors. One patent describes a method of freeze-drying peroxidases including HRP in glass tubes in the presence of polyvalent ions, most preferably ferrous ion, and long-term storage at 37 °C (US patent 4331761). However there have been no further reports incorporating these methods into a diagnostic device. We adapted the method described in this patent that uses ferrous

University of Washington, Department of Bioengineering, Seattle, Washington, USA.
E-mail: sujathar@u.washington.edu

† Electronic supplementary information (ESI) available. See DOI: 10.1039/c3an02296j

ions to stabilize the HRP for use in a diagnostic device. Several significant modifications were made in our system. First, we used trehalose instead of mannitol and sucrose in our reagents. Second, we chose vacuum-drying instead of lyophilization. And third, we used glass fiber pads for storing the reagents in contrast to storing in glass tubes. Finally, our reagents were stored at an elevated temperature of 45 °C as compared to 37 °C in the patent.

There have been a few reports on the incorporation of HRP enzyme-based signal amplification in a lateral-flow-like device.^{25–27} These methods combined the high sensitivity of the enzymatic amplification with the rapid lateral flow format; however they still required many timed user steps that make them less compatible with POC testing. In addition, these reports relied on fresh wet reagents and did not address the long-term stability of HRP or its substrates.

We recently reported on a two-dimensional paper network format (2DPNs) that uses shaped paper with multiple inlets to “program” automated multistep assays sequences while requiring only a single user activation step.²⁸ In this paper, we describe a method for the long-term elevated-temperature dry storage of reagents for enzyme-based signal amplification – antibodies conjugated to horseradish peroxidase (HRP) and the HRP substrate diaminobenzidine (DAB). Further, we incorporated the dry reagents into a 2DPN device and demonstrated an automated ELISA for detection of a malarial biomarker *Plasmodium falciparum* histidine rich protein 2 (*PfHRP2*) in a sandwich immunoassay. *PfHRP2* protein is secreted by the parasite into the host bloodstream and can be detected in serum, plasma and cerebrospinal fluids.^{29,30} The dry preservation of enzyme-based signal amplification reagents could have value for a number of applications that use enzyme-based systems targeting a variety of settings, ranging from the laboratory to a range of POC settings.

Experimental

Dry preservation of HRP conjugated antibody

A preservation formulation of HRP-conjugated anti-*PfHRP2* antibody (HRP-antibody) (Immunology Consultants Laboratory, Portland OR) at a concentration of 100 µg ml⁻¹ was prepared in a mixture containing a range of (0–0.2 M) FeSO₄-EDTA (Fe-EDTA), 4% trehalose (Sigma Aldrich, Saint Louis, MO), 0.1% bovine serum albumin (BSA) (Sigma Aldrich, Saint Louis, MO) in PBS. The FeSO₄ was prepared in water and premixed with an equimolar EDTA solution to prevent precipitation in PBS. The mixture was filtered through a 0.2 µm pore size filter. Polystyrene microtiter well strips (Thermo Electron Corporation, Milford MA) were coated with 2 mg ml⁻¹ BSA overnight, washed with water and dried. Glass fiber (grade 8964) (Ahlstrom, Helsinki, Finland) was laser cut (Universal Laser Systems, Scottsdale, AZ) to fit the wells of the polystyrene microtiter strip. The fluid capacity of each glass fiber pad was ~20 µl. Ten microliters of the HRP-antibody preservation mix was added to the glass fiber pads and dried at 30 °C under vacuum (Genevac Inc, Gardiner NY) for 2 hours. The microstrips were then sealed in triplicate using a Foodsaver® vacuum sealing system. The

samples were placed in a VaporLoc bag (LPS Industries, Moonache, NJ) with 2 grams of desiccant (Desiccare Inc, Pomona CA) per sample and stored at 45 °C for long-term storage.

Dry preservation of diaminobenzidine

Diaminobenzidine (DAB) tablets (Sigma Aldrich, Saint Louis, MO) were dissolved in water in acidic conditions by adding HCl to pH 2.0 and then raising the pH to 7.0 with NaOH to achieve a concentration of 2 mg ml⁻¹. Trehalose at a concentration of 4% was added to the DAB solution, and the solution was filtered through a 0.2 µm pore size filter. Glass fiber pads were placed in a polystyrene microtiter well strip, and 20 µl of the DAB mixture were added to each sample. The samples were dried, packaged and stored at conditions similar to those described above for the HRP-antibody.

Colorimetric assay for HRP preservation

A colorimetric assay using the 3,3',5,5 tetramethylbenzidine (TMB) substrate (KPL Inc, Gaithersburg, MD) was used for testing the HRP activity. The glass fiber pads containing the dry HRP-antibody were rehydrated with 100 µl PBS to 10 µg ml⁻¹ and vortexed for 1 minute. The samples were further diluted to a concentration of 200 ng ml⁻¹ and 10 µl was pipetted into a microtitre plate. A control sample of fresh HRP-antibody was used for comparison. One hundred microliters of TMB containing hydrogen peroxide was added to the plate and immediately placed in a VersaMax ELISA microplate reader (Molecular Devices LLC, Sunnyvale, CA). Kinetics of the TMB oxidation by HRP to its blue-colored singly-oxidized product was measured at 650 nm every 15 seconds over a period of 5 minutes. The initial rate of the reaction was calculated by taking the first 8 readings, and the percent activity was calculated relative to the fresh HRP-antibody.

Lateral flow assay for HRP-antibody preservation

A dipstick-style lateral flow assay format was used for demonstrating the dry preservation of the HRP-antibody. A nitrocellulose membrane (Millipore, Billerica, MA) was cut using a CO₂ laser cutting system (Universal Laser Systems, Scottsdale, AZ)³¹ into a “comb” structure consisting of multiple strips connected at the top. The assay used was a standard sandwich immunoassay for malarial antigen *Plasmodium falciparum* histidine rich protein 2 (*PfHRP2*). A murine antibody to *PfHRP2* (Immunology Consultants Laboratory, Portland, OR) was patterned (Scienion, Berlin, Germany) at a concentration of 1 mg ml⁻¹ onto the detection region of the nitrocellulose strip. A mock sample was created by adding 50 ng ml⁻¹ of the recombinant malaria protein *PfHRP2* (40 kD) (ImmunoDiagnostics Inc., Woburn, MA) to fetal bovine serum (Invitrogen, Carlsbad, CA). The glass fiber pads containing the dried HRP-antibody conjugate were rehydrated to a concentration of 10 µg ml⁻¹ in PBS pH 7.4 with Tween® 20 (PBST), vortexed for one minute, and used as the label in the sandwich assay. Fresh DAB prepared in PBST to a working concentration of 0.125 mg ml⁻¹ served as the substrate. Sodium percarbonate (Sigma

Aldrich, Saint Louis, MO) at a concentration of 0.025% was added fresh to the DAB solution as the source of hydrogen peroxide (H_2O_2). A fresh sample of HRP-antibody conjugate was used as a control. The nitrocellulose comb with a cellulose wicking pad at one end was placed vertically into a 96-well microtiter plate containing 30 μl of antigen for 4 minutes. This was followed by two transfers into 30 μl PBST wash buffer for 4 min each. The comb was then transferred to wells containing HRP-antibody at 10 $\mu\text{g ml}^{-1}$ for 4 min, followed by two more PBST washes. Finally, the comb was placed in 40 μl of DAB substrate for 6 minutes for the signal to develop at the detection zone. The assay membranes were then imaged wet using the procedure described below.

Lateral flow assay for DAB preservation

A dipstick format malarial assay, similar to the one used for the HRP preservation studies, was used to evaluate DAB preservation. Here, a fresh solution of secondary HRP-antibody conjugate at 10 $\mu\text{g ml}^{-1}$ was used as the label. The lateral flow assay procedure was similar to the one described above. At different times of dry storage, samples of dry DAB were removed and rehydrated to a working concentration of 0.125 mg ml^{-1} with 40 μl of PBST containing the H_2O_2 source in the form of sodium percarbonate at a concentration of 0.025% and vortexed for one minute. The assay membranes were imaged as described below. The percent activity retained after dry storage of DAB was calculated relative to that of the fresh DAB.

Automated 2DPN ELISA card

As previously reported, the 2DPN assay card design²⁸ was adapted for performing on-card ELISA using the dry reagents. The device was a nitrocellulose (Millipore, Billerica, MA) assay membrane cut into a three-inlet network using a CO_2 laser cutting system. The PfHRP2 antibody at a concentration of 1 mg ml^{-1} was patterned at the detection region of the membrane. The assay membrane along with a cellulose wicking pad (Millipore, Billerica, MA) was housed on one side of a folding Mylar (Fraylock, San Carlos, CA) laminate material. The glass fiber pads with dry HRP-antibody and DAB substrate (stored dry for 2 weeks at 45 °C) and buffer pad were placed on the opposite side of the laminate housing such that when the device was closed, each pad would make contact with the appropriate inlet of the assay membrane. Ten microliters of a known concentration of PfHRP2 antigen in FBS was added to the glass fiber pad containing HRP-antibody to rehydrate it to a concentration of 10 $\mu\text{g ml}^{-1}$. The dry DAB substrate pad was rehydrated with 40 μl of PBST containing hydrogen peroxide to give a concentration of 0.125 mg ml^{-1} . The buffer pad was filled with 80 μl of PBST. The assay card was folded to simultaneously initiate flow of each reagent sequentially through the detection zone. The membranes were scanned after 20 minutes, and signal was quantified as described below.

Image capture and quantification

Assay membranes were imaged with a flatbed scanner (ScanMaker i900, MicroTek International, Inc., Cerritos, CA USA) in

48-bit RGB mode at a resolution of 600 dpi. The intensities in the region of interest (ROI) were quantified using ImageJ³² by measuring mean green-channel intensity of each signal band and a background region within each strip. Each ROI was defined as a rectangular box around the detection line measuring 55 pixels \times 10 pixels. The signal from a region 30 pixels upstream from the detection zone was used as the background signal intensity. The assay signal was calculated as the background-subtracted intensity normalized to the full intensity range of the image.³³ For each concentration, $N = 3$ replicate measurements were performed. An estimate of the limit of detection (LOD) was obtained using $\text{LOD} = (3\sigma)/S$, where σ is the standard deviation of very low concentration measurements and S is the slope of the dose response curve in the linear region. In this case, the slope was taken over the lowest three concentrations and the standard deviation was calculated using the method of pooled variance (*i.e.* mean-centering each of the zero and lowest non-zero (6.25 ng ml^{-1}) concentration data sets and then calculating the standard deviation of the composite mean-centered data set). This procedure was motivated by the observation that the zero-concentration measurements had a much lower standard deviation than the lowest non-zero concentration measurements (this discrepancy may have been due to the modest number of replicates). In this case, the pooled variance may provide a more representative estimate of the LOD.

Results and discussion

Our goal in this study was to develop a method for the long-term dry preservation of the reagents used in ELISA (HRP-antibody and DAB substrate) and implement it in a lateral flow device. Glass fiber pads were chosen as a matrix for drying the reagents since they are convenient to handle during vacuum drying and provide a format appropriate for integration with our POC device.

We first tested the activity of the HRP enzyme in a colorimetric assay to determine the effects of long-term dry-storage at elevated temperature. We then tested the HRP-antibody function in a simple dipstick immunoassay using fresh DAB substrate to ensure that the preservatives did not interfere with the immunoassay. Next, we tested the stability of the dry-stored DAB substrate in the dipstick immunoassay using fresh HRP enzyme. Finally, we incorporated the dry reagents into an automated device and demonstrated ELISA in a simple card format.

Dry storage of enzyme (HRP) conjugated antibody

HRP conjugated to PfHRP2 antibody (HRP-antibody) was dried on glass fiber pads in the presence of Fe-EDTA, trehalose, and BSA. We believe that the BSA in the preservation formulation could serve as a sacrificial protein coating of the surface of the glass fiber matrix during the drying process and reduce the loss of HRP-antibody adsorption to the matrix. The HRP activity was determined by measuring the conversion of TMB substrate to a blue product in a colorimetric assay. Kinetic measurements

over a wide range of fresh HRP-antibody concentrations were performed in order to choose an HRP concentration in the linear measurement range for the assay (ESI Fig. S1†); an HRP concentration 200 ng ml^{-1} was chosen for the kinetic measurements so that the assay would be responsive to decreases in enzyme performance.

First, a range of Fe-EDTA concentrations (0–0.2 M) was tested to determine the optimal Fe-EDTA concentration that provides enzyme preservation without interfering with signal generation or target labeling. The HRP activity was quantified by colorimetric assay, and the percent activities for fresh and dried HRP-antibody were calculated relative to the fresh HRP-antibody control with no preservatives. There was no effect of Fe-EDTA concentration on the HRP activity for freshly prepared samples (Fig. 1a, gray bars). The optimum HRP activity in samples stored dry at 45°C for 3 days was achieved using concentrations of 0.005–0.02 M Fe-EDTA. Below and above this range Fe-EDTA resulted in a decrease in enzyme activity (Fig. 1a, white bars). A dipstick immunoassay using fresh DAB substrate was also performed to test for any interference of Fe-EDTA in the sandwich immunoassay. The dipstick assay results indicated that 0.005–0.02 M Fe-EDTA was the optimal range for enzyme stability (Fig. 1b). Concentrations greater than 0.02 M Fe-EDTA in the dry formulation gave weaker signals using both fresh and dry HRP-antibody, which suggests interference with the sandwich immunoassay. Hence, 0.01 M Fe-EDTA was chosen for the study of long-term dry stability of the HRP-antibody at elevated temperature.

Fig. 2a shows the HRP activity for dry storage over 5 months at 45°C . Enzyme activity was measured using TMB as the substrate relative to fresh HRP-antibody. The HRP-antibody dry-stored in the presence of Fe-EDTA, trehalose, and BSA retained 80% of the activity of the fresh control. In the presence of trehalose and BSA alone, the enzyme retained only 20% activity. The activity of HRP-antibody was also evaluated by a dipstick

sandwich immunoassay using fresh DAB as the substrate (Fig. 2b). The HRP-antibody was functional with signal intensity similar to the fresh HRP-antibody.

In our study, we found that adding FeSO_4 instead of Fe-EDTA complex reduced the enzyme activity to $\sim 40\%$ after 3 days of dry storage at 45°C , which indicates that the Fe-EDTA complex had a role in the preservation. Also, the FeSO_4 precipitated in the PBS buffer and adding equimolar concentration of EDTA prevented precipitation. Fe-EDTA alone without trehalose reduced the enzyme activity to $<20\%$ after one day of dry storage at 45°C . Also EDTA alone in presence of trehalose gave results similar to trehalose alone. In addition, the HRP sample stored in trehalose, which gave diminished activity, was tested by adding Fe-EDTA after rehydration. This experiment did not improve the HRP activity. In summary, the Fe-EDTA complex in the presence of trehalose had a stabilizing effect on HRP during dry storage at elevated temperature.

Dry preservation of substrate diaminobenzidine

Diaminobenzidine (DAB) has been a commonly-used substrate for HRP, especially in the field of immunocytochemistry. Advantages of DAB includes that it dissolves easily in aqueous media and the oxidized product self-precipitates; in the context of our assay this means that DAB deposits as a stationary signal at the detection line of the paper strip. In contrast, precipitation of the oxidized TMB product formed in ELISA requires addition of propriety precipitating components.

DAB substrate was dried in glass fiber pads in the presence of trehalose and stored at 45°C . The stability of DAB was evaluated using a dipstick immunoassay over a timescale of 3 months. First, the dipstick malarial assay using fresh reagents was used to determine the linear range for signal generation using DAB for testing its dry storage stability (such that loss in DAB activity would be detectable). The linear range of the assay was at

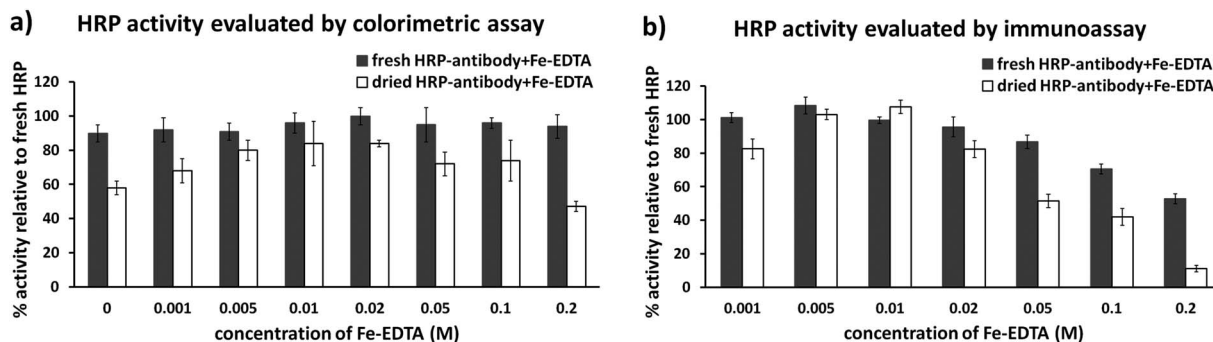


Fig. 1 Tests to determine optimal concentration of preservatives for the HRP-antibody. Dry storage conditions were 3 days at 45°C in presence of Fe-EDTA, 4% trehalose and 0.1% BSA. The fresh HRP condition tests for inhibition of HRP activity or immunoassay chemistry, and the dry HRP condition tests for additional effects on preservation of HRP-antibody performance. (a) Plot showing the effect of a range of Fe-EDTA concentrations on the activity of HRP determined by a colorimetric assay. The percentage activity was calculated relative to the fresh HRP without Fe-EDTA and trehalose. The enzyme activity was maintained for a wide range of Fe-EDTA concentrations for both fresh and dry-stored HRP-antibody with optimum range between 0.005 and 0.02 M Fe-EDTA for the dry-stored HRP antibody. (b) Plot showing the effect of a range of Fe-EDTA concentrations on performance of HRP-antibody measured in a full immunoassay. Note the consistency with data in (a) for the best range. Further, concentrations greater than 0.01 M Fe-EDTA in the dry stored HRP-antibody had an inhibitory effect on the sandwich assay.

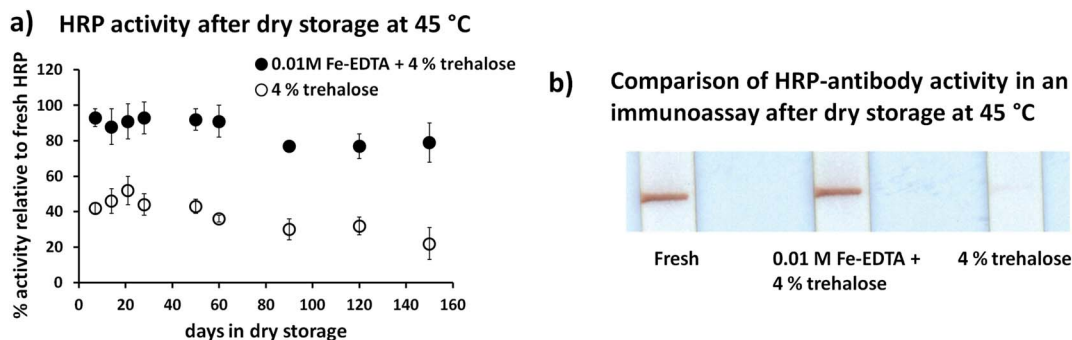


Fig. 2 Activity of HRP-antibody after dry storage. (a) Chart showing the HRP enzyme activity retained after dry storage at 45 °C at different time points as determined by colorimetry. The activity was compared to fresh reagent stored at 4 °C. The HRP enzyme in the presence of 0.01 M Fe-EDTA and 4% trehalose and 0.1% BSA retained ~80% activity after dry storage at 45 °C after 5 months. In the presence of 4% trehalose and 0.1% BSA the enzyme retained only 20% activity. (b) Images of a dipstick immunoassay using dry-stored (4 months, 45 °C) HRP-antibody and fresh DAB substrate and H₂O₂ in a malarial sandwich assay. The signal is seen as a brown precipitate due to oxidation of DAB by HRP in presence of hydrogen peroxide. The HRP-antibody shows excellent functionality upon rehydration when stored dry in the presence of Fe-EDTA, trehalose, and BSA whereas trehalose alone showed significantly diminished activity.

concentrations lower than 0.15 mg ml⁻¹, and thus a concentration of 0.125 mg ml⁻¹ of DAB was chosen for the dry storage study (ESI Fig. S2a†). One of the critical components in the enzyme-based immunoassay is H₂O₂, which is essential for oxidation of the substrate by HRP. For all the experiments in this study, we used sodium percarbonate, which generates H₂O₂ when it is dissolved in aqueous buffer. A concentration of 0.025% sodium percarbonate was chosen based on a study of the effect on H₂O₂ concentration on signal intensity in a dipstick assay (ESI Fig. S2b†).

Long-term stability study of DAB stored at 45 °C was tested in a dipstick immunoassay using fresh HRP-antibody. Fig. 3 shows that DAB was preserved with >90% activity for at least three months at 45 °C (Fig. 3a). We observed that adding trehalose had a suppressive effect on the auto-oxidation of DAB during dry storage compared to samples stored without trehalose (Fig. 3b). It was also necessary to store DAB in the dark to prevent photooxidation.

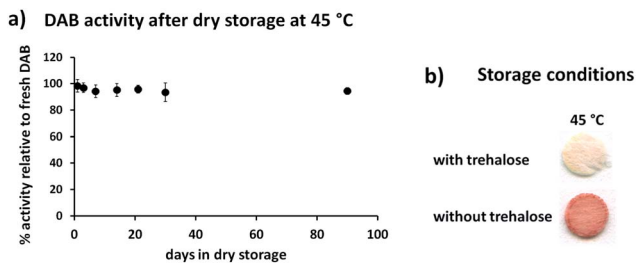


Fig. 3 (a) Plot showing percent DAB activity retained after dry storage as determined by a dipstick immunoassay. DAB substrate stored dry at 45 °C in the presence of 4% trehalose in a glass fiber pad was tested periodically for its functionality using fresh secondary HRP-antibody. The DAB substrate retained full functionality upon rehydration after 3 months of dry storage when compared to fresh DAB. (b) Samples of glass fiber pads containing dry DAB stored for one month with and without trehalose. Trehalose suppressed auto-oxidation of DAB during dry storage.

Automated ELISA in 2DPN device

A POC device with on-board dry reagents for enzymatic signal amplification could provide high sensitivity detection for low-resource settings. A previously reported 2DPN device²⁸ was adapted for demonstration of ELISA for the POC.

Fig. 4a shows a folding 2DPN device with integrated dry reagent pads that performs an automated ELISA for a malarial biomarker (*Pf*HRP antigen) with a single user activation step. Antigen-spiked sample was added to a pad containing dry HRP-antibody, PBST buffer containing sodium percarbonate was added to a pad containing dry DAB substrate, and PBST buffer was added to a buffer pad as a wash fluid. While on-device storage of sodium percarbonate was not done in this study, it is sold in a dry form that is stable at room temperature. The sodium percarbonate could be stored as a powder in the 2DPN device at a convenient location, and would generate H₂O₂ upon dissolution.

After two minutes to allow for reagent rehydration, the card was folded to initiate the sequential delivery of reagents through the detection zone. The antigen-antibody complex with the HRP-antibody label moved through the first inlet and across the detection zone, followed by the DAB substrate plus hydrogen peroxide from the second inlet, and finally a wash buffer from the third inlet. Fig. 4b shows an example result from an automated ELISA card. The signal from the DAB precipitate can be easily visualized by eye at the detection zone. This method of on-card enzyme signal amplification can also be quantified using a webcam or a flat-bed scanner. Fig. 4c shows images for an antigen dilution series and the corresponding dose response curve (Fig. 4d). The LOD using the 2DPN card for the malarial antigen was 6.5 ng ml⁻¹. The LOD is comparable to laboratory ELISA for *Pf*HRP2 of 4 ng ml⁻¹.³⁴ The *Pf*HRP2 levels in clinical blood samples can range from as low as 10 ng ml⁻¹ to as high as 10³ ng ml⁻¹.³⁵ Apart from diagnosing an active infection, the 2DPN card could also be used in the malaria elimination programs which aim to reduce parasite transmission in the population where higher sensitivities are required (P. LaBarre, personal communications).

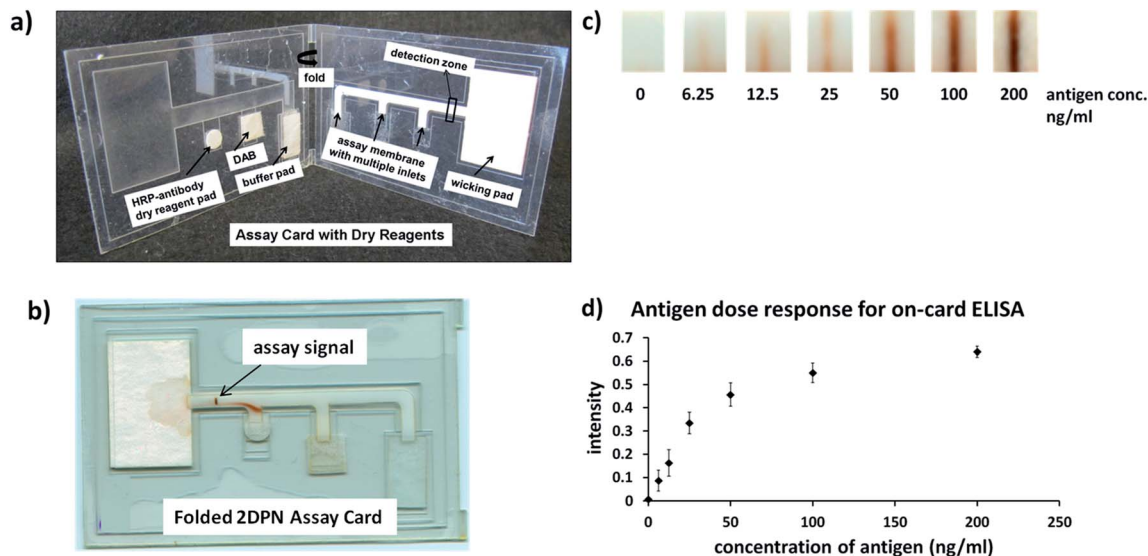


Fig. 4 2DPN device with incorporated dry reagents for automated ELISA. (a) Folding 2DPN device showing assay membrane on one side with three inlets for sequential reagent delivery, and glass fiber pads containing dry-preserved HRP labeled secondary antibody, DAB and buffer on the other side, assembled on a Mylar laminate material. Malarial antigen spiked in fetal bovine serum and buffer containing hydrogen peroxide is added to rehydrate the dry HRP-antibody and DAB respectively. The device is folded to simultaneously activate the reagent flow through the device. (b) Folded device showing malarial sandwich immunoassay signal development. A streak of DAB precipitate is seen near the first inlet. This is due to the two reagents (HRP-antibody and DAB substrate) flowing back to back. This however did not have a negative impact on the assay. Streaking could be eliminated by adding a wash step between the HRP-antibody and DAB delivery. (c) Images of the detection line for varying antigen concentration. (d) Dose response curve for the malarial antigen using 2DPN device with dry reagents.

Conclusion

We reported a method for dry preservation of reagents used in ELISA. We showed that an HRP-antibody conjugate and its substrate DAB retained a high level of activity after long-term dry storage at 45 °C. Our method for drying the reagents onto a glass fiber pad has the benefit of easy incorporation into POC devices, including conventional microfluidic³⁶ or paper-based devices.^{9,28} We used a simple vacuum-drying method over the time-consuming, cumbersome, and expensive lyophilization method. This method can be easily adapted for manufacturing in low-resource settings. Further, we have demonstrated an automated ELISA using a 2DPN device with dry reagents integrated into it. Future work will include adapting the device to accept a whole blood sample through use of a plasma extraction membrane that would separate the blood cells.^{36,37} In addition, we are also working on paper-fluidic valving tools to demonstrate the automated process of fluid delivery and metering in the 2DPN device.³⁸ Dry preservation of enzyme-based signal amplification reagents could be used for a variety of applications and has particular advantages for use in POC devices for enhanced sensitivity, portability, and ease-of-use in low resource settings.

Acknowledgements

Support for this project was provided through funding from NIH Grant no. 1RC1EB010593-01 and Grant no. 1R01A1096184-01. The content is solely the responsibility of the authors and does not necessarily represent the official views of the National

Institutes of Health. The authors thank Karman Tandon for contributions to preliminary work on HRP preservation.

References

- 1 P. Yager, G. J. Domingo and J. Gerdes, *Annu. Rev. Biomed. Eng.*, 2008, **10**, 107–144.
- 2 R. W. Peeling, P. G. Smith and P. M. M. Bossuyt, *Nat. Rev. Microbiol.*, 2006, S2–S6.
- 3 J. F. Drexler, A. Helmer, H. Kirberg, U. Reber, M. Panning, M. Muller, K. Hofling, B. Matz, C. Drosten and A. M. Eishubinger, *Emerging Infect. Dis.*, 2009, **15**, 1662–1664.
- 4 S. Skidmore, *Sexually Transmitted Infections*, 2010, **86**, 330.
- 5 T. Nareoja, M. Vehniainen, U. Lamminmaki, P. E. Hanninen and H. Harma, *J. Immunol. Methods*, 2009, **345**, 80–89.
- 6 E. M. Linares, L. T. Kubota, J. Michaelis and S. Thalhammer, *J. Immunol. Methods*, 2012, **375**, 264–270.
- 7 X. Xia, Y. Xu, X. Zhao and Q. Li, *Clin. Chem.*, 2009, **55**, 179–182.
- 8 I. H. Cho, S. M. Seo, E. H. Paek and S. H. Paek, *J. Chromatogr. B: Anal. Technol. Biomed. Life Sci.*, 2010, **878**, 271–277.
- 9 E. Fu, T. Liang, J. Houghtaling, S. Ramachandran, S. A. Ramsey, B. Lutz and P. Yager, *Anal. Chem.*, 2011, **83**, 7941–7946.
- 10 W. Wang, *Int. J. Pharm.*, 2000, **203**, 1–60.
- 11 S. Ohtake and Y. J. Wang, *J. Pharm. Sci.*, 2011, **100**, 2020–2053.
- 12 M. F. Mazzobre, M. D. Buera and J. Chirife, *Food Sci. Technol.*, 1997, **30**, 324–329.
- 13 M. E. Elias and A. M. Elias, *J. Mol. Liq.*, 1999, **83**, 303–310.

- 14 D. P. Miller, R. E. Anderson and J. J. de Pablo, *Pharm. Res.*, 1998, **15**, 1215–1221.
- 15 J. Buitink, I. J. van den Dries, F. A. Hoekstra, M. Alberda and M. A. Hemminga, *Biophys. J.*, 2000, **79**, 1119–1128.
- 16 K. I. Izutsu, S. Yoshioka and S. Kojima, *Pharm. Res.*, 1994, **11**, 995–999.
- 17 L. M. Crowe, D. S. Reid and J. H. Crowe, *Biophys. J.*, 1996, **71**, 2087–2093.
- 18 J. F. Carpenter and J. H. Crowe, *Cryobiology*, 1988, **25**, 459–470.
- 19 J. F. Carpenter, L. M. Crowe and J. H. Crowe, *Biochim. Biophys. Acta*, 1987, **923**, 109–115.
- 20 J. F. Carpenter, B. Martin, L. M. Crowe and J. H. Crowe, *Cryobiology*, 1987, **24**, 455–464.
- 21 T. D. Gibson, J. N. Hulbert and J. R. Woodward, *Anal. Chim. Acta*, 1993, **279**, 185–192.
- 22 T. D. Gibson, J. N. Hulbert, S. M. Parker, J. R. Woodward and I. J. Higgins, *Biosens. Bioelectron.*, 1992, **7**, 701–708.
- 23 S. Fornera, T. E. Balmer, B. Zhang, A. D. Schluter and P. Walde, *Macromol. Biosci.*, 2011, **11**, 1052–1067.
- 24 P. R. S. Leiriao, L. J. P. Fonseca, M. A. Taipa, J. M. S. Cabral and M. Mateus, *Appl. Biochem. Biotechnol.*, 2003, **110**, 1–10.
- 25 C. Zhang, Y. Zhang and S. Wang, *J. Agric. Food Chem.*, 2006, **54**, 2502–2507.
- 26 J. H. Cho, E. H. Paek, I. H. Cho and S. H. Paek, *Anal. Chem.*, 2005, **77**, 4091–4097.
- 27 J. H. Cho, S. M. Han, E. H. Paek, I. H. Cho and S. H. Paek, *Anal. Chem.*, 2006, **78**, 793–800.
- 28 E. Fu, T. Liang, P. Spicar-Mihalic, J. Houghtaling, S. Ramachandran and P. Yager, *Anal. Chem.*, 2012, **84**, 4574–4579.
- 29 E. P. Rock, K. Marsh, A. J. Saul, T. E. Wellems, D. W. Taylor, W. L. Maloy and R. J. Howard, *Parasitology*, 1987, **95**, 209–227.
- 30 C. Beadle, G. W. Long, W. R. Weiss, P. D. Mcelroy, S. M. Maret, A. J. Oloo and S. L. Hoffman, *Lancet*, 1994, **343**, 564–568.
- 31 P. Spicar-Mihalic, B. Toley, J. Houghtaling, T. Liang, P. Yager and E. Fu, *J. Micromech. Microeng.*, 2013, **23**, 067003.
- 32 W. S. Rasband, *ImageJ*, U. S. National Institutes of Health, Bethesda, Maryland, USA, <http://rsb.info.nih.gov/ij/>, 1997–2009.
- 33 D. Y. Stevens, C. R. Petri, J. L. Osborn, P. Spicar-Mihalic, K. G. McKenzie and P. Yager, *Lab Chip*, 2008, **8**, 2038–2045.
- 34 C. M. Kifude, H. G. Rajasekariah, D. J. Sullivan Jr, V. A. Stewart, E. Angov, S. K. Martin, C. L. Diggs and J. N. Waitumbi, *Clin. Vaccine Immunol.*, 2008, **15**, 1012–1018.
- 35 L. Manning, M. Laman, D. Stanisic, A. Rosanas-Urgell, C. Bona, D. Teine, P. Siba, I. Mueller and T. M. Davis, *Clin. Infect. Dis.*, 2011, **52**, 440–446.
- 36 L. Lafleur, D. Stevens, K. McKenzie, S. Ramachandran, P. Spicar-Mihalic, M. Singhal, A. Arjyal, J. Osborn, P. Kauffman, P. Yager and B. Lutz, *Lab Chip*, 2012, **12**, 1119–1127.
- 37 S. J. Vella, P. Beattie, R. Cademartiri, A. Laromaine, A. W. Martinez, S. T. Phillips, K. A. Mirica and G. M. Whitesides, *Anal. Chem.*, 2012, **84**, 2883–2891.
- 38 S. Dharmaraja, L. Lafleur, S. Byrnes, P. Kauffman, J. Buser, B. Toley, E. Fu, P. Yager and B. Lutz, *Proc. SPIE*, 2013, **8615**, 86150X.

Chapter 4

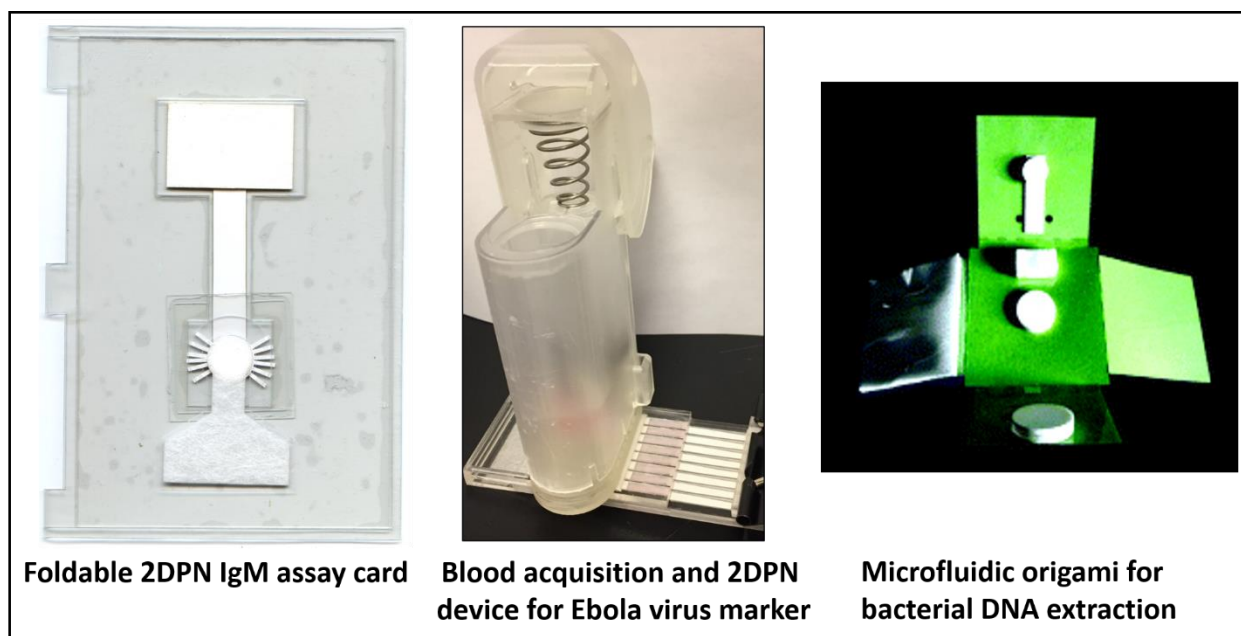
4 Two-dimensional paper networks for sample processing

This chapter has three sections describing three different 2DPN sample processing devices.

4.1 A 2DPN card with integrated assay and sample processing to remove upstream assay interfering IgG for IgM detection is based on a conference paper ¹³⁵.

4.2 A 2DPN device with plasma separation and lysis capability for detection of membrane glycoprotein of Ebola virus-like-particles (VLPs) spiked into the blood is based on a conference paper (Microtas 2020).

4.3 A paper-based microfluidic origami device for nucleic acid extraction from viscous samples is based on publication ¹³⁶.



4.1 Integrated assay and sample processing: paper-based device for IgM detection

This section is based on a conference proceeding¹³⁵ *Integrated assay and sample processing: paper-based device for IgM detection*.

Sujatha Ramachandran, Jacqueline Peltier, Jennifer Osborn, Carly Holstein, Barry Lutz, Elain Fu, and Paul Yager. *The 16th International Conference on miniaturized systems for chemistry and life sciences (MicroTas)*, Okinawa, Japan.

Abstract

Point-of-care (POC) devices that can perform multistep processes, are easy to use, and are inexpensive, are needed for use in limited-resource settings. We present an integrated paper-based device that performs an automated immunoassay for the detection of IgM antibodies with onboard sample processing. The device is a two-dimensional paper network (2DPN) consisting of protein-G coated nitrocellulose for flow-through removal of assay interfering IgG, integrated to a nitrocellulose membrane for lateral flow detection of IgM. The 2DPN is appropriate for POC settings with one user-activation step.

Introduction

Lateral flow diagnostic devices based on immunoassays are available; they involve a simple step of mixing and detection of the signal. However, applications that require upstream sample processing, such as removal of blood cells and assay-interfering contaminants, usually require performing benchtop processes involving multiple steps and centrifugation in a laboratory setting. These are not practical for point-of-care (POC) settings.

We are developing tools to automate sophisticated processes that can be incorporated into disposable devices for use at the POC. One such example is IgM immunoassay. Elevated disease-specific IgM in the blood is indicative of acute infection and thus is important in clinical diagnosis at the early stages of several diseases. However, the presence of disease-specific IgG in a sample can interfere with the IgM assay, causing false negatives (Figure 4.1) that lead to missed opportunities to treat patients with active disease. To prevent this erroneous result in IgM

immunoassays, IgG removal is necessary. The most common method for IgG depletion from a plasma sample is upstream capture by protein G, which has a specific affinity for human IgG.

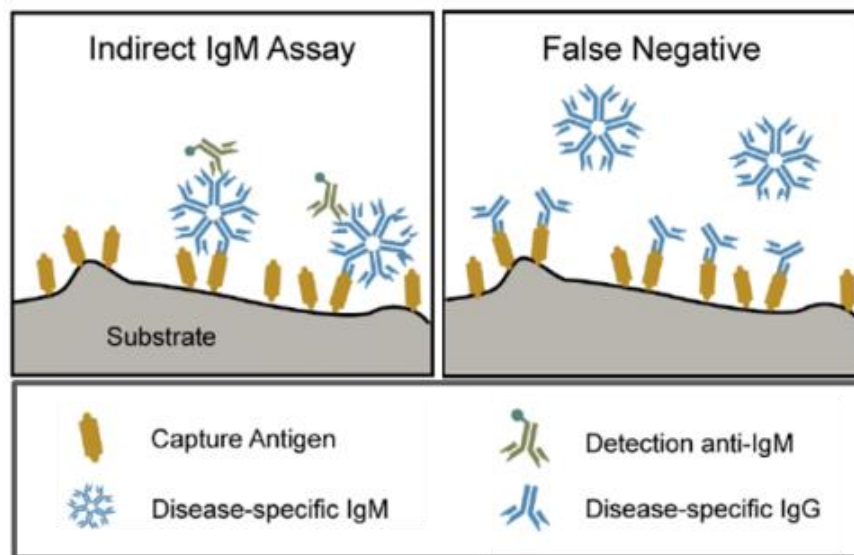


Figure 4.1. Schematics of the indirect IgM assay format and a potential interference mechanism in which disease-specific IgG causes false negatives. IgG "mop-up" would alleviate this problem (Image courtesy: Dean Stevens)

Previously, we reported on a conventional microfluidic platform consisting of an instrument and a microfluidic card that removed IgG using protein G-coated beads¹³⁷ before IgM detection. This platform, though automated, requires pumps to transport fluids through the microfluidic channels. We have also recently developed a two-dimensional paper network (2DPN) format that enables automated multistep reagent delivery without the use of pumps and have demonstrated a signal amplified antigen assay²⁹. Presented here, is the first demonstration of an automated IgM assay with integrated IgG removal in the 2DPN format, which can be used for POC serodiagnosis of infectious diseases.

Experimental setup

The integrated 2DPN IgM assay device consists of an IgG "mop-up" unit made up of a stack of nitrocellulose membranes (450 nm pore size) cut into circles with two projecting arms using a CO₂ laser cutting system. The membranes were incubated with 2 mg/ml protein G in citrate buffer (pH 5.0), washed, and dried in a desiccator. Six of the protein G-coated membranes were stacked with

the arms stuck on to a Mylar adhesive sheet to hold them together. The membrane stack was then placed directly in contact with a nitrocellulose assay membrane supported on a foldable Mylar laminate card with a cellulose wicking pad at the other end. A glass fiber conjugate pad for buffer supply was placed on the other side of the Mylar device. As a control, a BSA-coated membrane stack was similarly processed and assembled into a device.

For studying the efficiency of IgG removal, 7 μ l of Alexa 488 labeled IgG, at a level present in normal human blood (8 mg/ml), was added to the topmost membrane of the protein G/BSA-coated stack and incubated for 5 minutes. Buffer was added to the glass fiber pad, the adhesive layers of the Mylar card were exposed, and the card folded to activate the flow of the sample. Time-lapse images of the progression of the labeled IgG through the assay membrane to the wicking pad were recorded using a webcam. To quantify the output of fluorophore-labeled IgG, the wicking pads were removed from the card, soaked in buffer overnight, vortexed, and centrifuged to extract the label. The fluorescence signal was measured using a fluorimeter, and IgG depletion calculated and compared to the control.

As a proof-of-principle of integrated 2DPN IgM detection card with IgG depletion, a functional immunoassay was performed. Here, secondary anti-IgM and anti-IgG gold conjugates serving as labels for visible signal detection were dried in the presence of sugars in glass fiber pads and placed below the IgG removal stack in contact with the assay membrane. The assay membranes were striped with anti-IgM and anti-IgG for the capture of IgM and IgG, respectively. Normal human plasma was added to the protein G/BSA-coated membranes as the sample. The assay was completed within 30 minutes, and the gold signal was imaged using a flatbed scanner.

Results and discussion

Figure 4.2 shows the components of an integrated 2DPN IgM assay card. The key features of this design are a) the use of a stack of 450 nm pore-size nitrocellulose membranes coated with protein G for IgG "mop-up," b) integration of the IgG removal with IgM detection by overlaying the protein G-coated stack in direct contact with a lateral flow assay membrane and including glass fiber pad with dry secondary gold-labels, and c) housing of the paper networks and other components in a foldable Mylar and adhesive card.

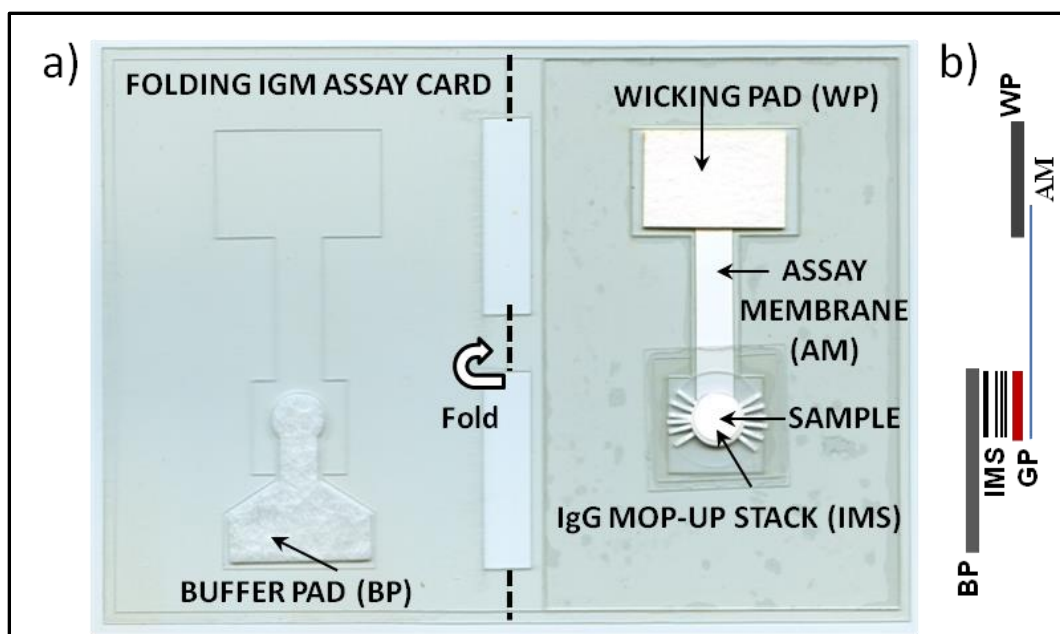


Figure 4.2. 2DPN IgM assay card. a) Foldable 2DPN IgM assay card with a stack of six nitrocellulose membranes coated with protein G for IgG "mop-up" overlaying the assay membrane via secondary gold label pad (GP). The assay is operated by adding a sample over the topmost layer of the stack and folding the card to bring the buffer pad in contact with the stack. b) Side-view of the layers.

The small pore size of the membrane for IgG removal provides a high surface area for the high capacity binding of the protein G and subsequent efficient removal of IgG present in the blood (~ 8 mg/ml). We used at least six protein G-coated membranes in the stack to ensure effective IgG removal. The device requires the addition of sample and buffer at the appropriate locations and then a folding step.

The sample flows vertically through the stack protein G stack allowing the binding of IgG to different layers and then laterally through the assay membrane to the detection zone for IgM detection. The advantage of a foldable card is that it can be easily closed for automated sample processing and immunoassay with one user-step activation.

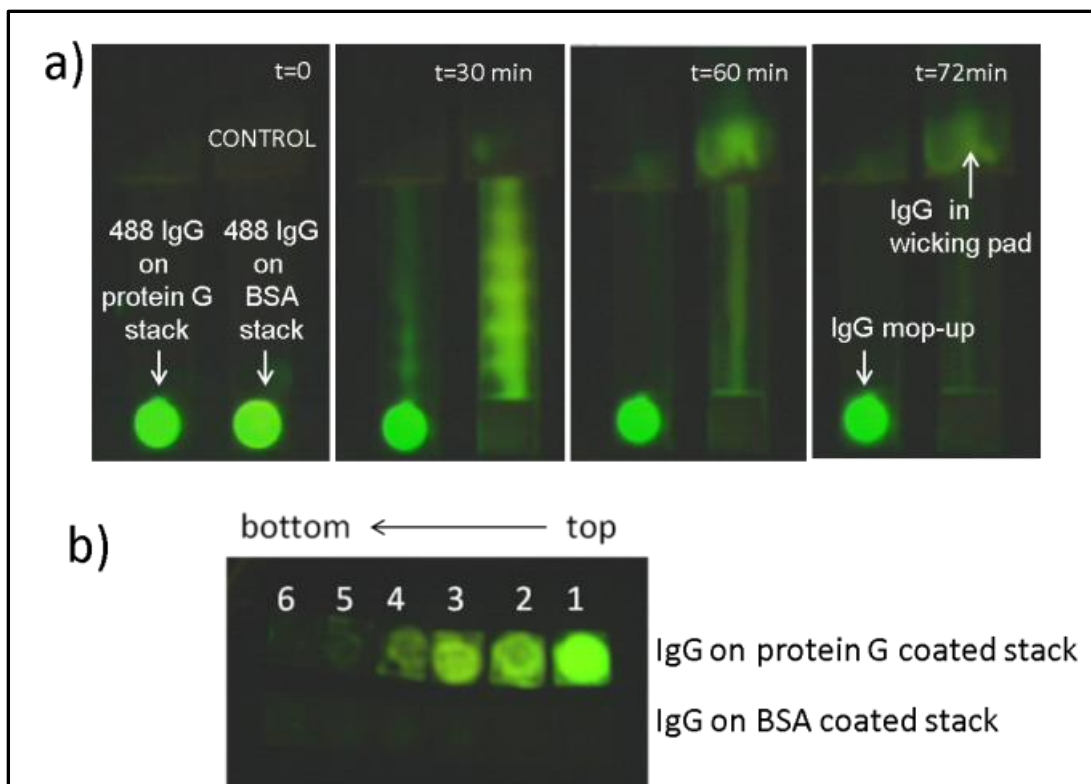


Figure 4.3. IgG "mop up" in 2DPN device. a) Time-lapse images of Alexa 488 labeled IgG flowing through the protein G-coated membrane stack in the 2DPN assay card. A BSA-coated membrane stack was used as a control. Arrows indicate successful IgG removal by the protein G-coated stack, whereas, in control, IgG collects in the wicking pad. b) Individual membranes from the protein G and BSA-coated membrane stacks indicate labeled IgG levels in each case.

Figure 4.3a) shows time-lapse images of Alexa 488-labeled IgG flowing through the device containing protein G/BSA-coated stack. The protein G-coated stack was successful in removing IgG, visualized as an intense signal at the region of the stack, whereas in the BSA-coated stack, the labeled IgG progressed through the device and was collected in the wicking pad. Figure 4.3 b) shows the images of individual membranes removed from the stack after a run. The different layers of the protein G stack show varying levels of bound IgG with decreasing intensity from top to the bottom of the stack. The BSA-coated membranes, on the other hand, did not significantly bind the labeled IgG. Using this device format, we obtained ~95 % efficiency in IgG removal with the protein G stack as determined by fluorimetry.

Figure 4.4 shows an image of a functional immunoassay performed using the integrated device to demonstrate IgG removal and IgM detection. IgG removal from human plasma by the protein G-coated stack was successful with the gold signal seen only for the IgM. As expected, the device with the control BSA-coated stack showed both the IgG and IgM signals. The total assay was completed in 30 minutes. Future work will integrate plasma separation, IgG removal, and the immunoassay into the 2DPN device for the serodiagnosis of diseases from a whole blood sample.

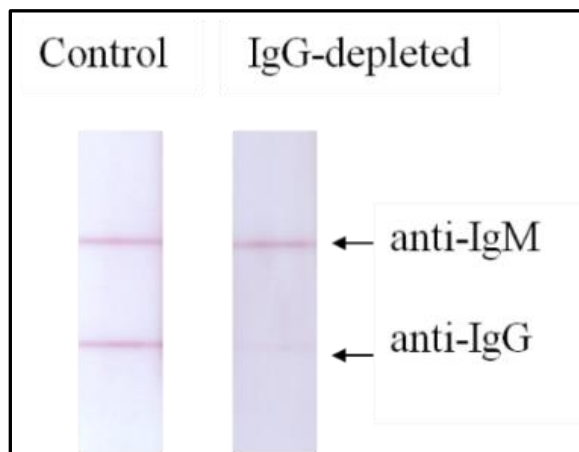


Figure 4.4. Scanned images of a functional IgM assay membrane showing IgG depletion and IgM capture. Normal human plasma flowing through the protein G-coated membrane stack showed signal only for IgM, indicating successful IgG "mop-up" (right), whereas BSA-coated membrane stack used as a control, showed signals for both IgG and IgM (left).

Conclusion

We have demonstrated an automated IgM assay with integrated IgG removal in a 2DPN device, which can be used for serodiagnosis of many infectious diseases. This device format, with one user activation step, can be used for removal of a variety of assay interferences and is rapid, inexpensive, and appropriate for use in low-resource POC settings.

4.2 A diagnostic device for sample processing, lysis, and detection of Ebola virus markers

This section is based on a conference proceeding *A disposable integrated diagnostic device for blood acquisition, sample processing, lysis, and detection of Ebola virus markers*.

Sujatha Kumar, Steven Bennett, Shichu Huang, Joshua Buser, and Paul Yager. *The 24 th International Conference on miniaturized systems for chemistry and life sciences (MicroTas)*, virtual conference (2020).

Abstract

We report a novel, disposable, instrument-free diagnostic device for Ebola virus disease (EVD) from a blood sample that could be operated from sample to result with minimal end-user steps at the point of care (POC) by medical personnel trained in safe interaction with Ebola patients. We demonstrated the proof-of-principle of the device using blood spiked with soluble glycoproteins and Ebola virus-like particles.

Introduction

POC devices for the detection of many infectious disease protein markers in blood require the acquisition of blood from either venous blood collected by a vacutainer or a finger stick, plasma separation to remove blood cells, and finally, detection of the markers by an immunoassay. The challenges for such clinical POC diagnostic devices (especially in resource-limited settings) include being low cost, rapid, robust, sensitive, and storing reagents in dry form.

A further challenge is to perform the above steps autonomously and safely with minimal user intervention. Based on the conclusions of a healthcare professional who had extensive experience working in West Africa during the 2014 Ebola epidemic, we believe that a vacutainer would be the most likely source for blood that needs to be used in the development of an Ebola diagnostic device. We earlier reported the development of a low-cost POC device using 2D-paper network (2DPN) that performs multistep assays with dry-stored reagents for enhanced sensitivity²⁹ and a swab-to-result autonomous disposable device for influenza diagnosis¹³⁸. There have been a few reports of rapid lateral flow POC tests for Ebola diagnostics, but none integrated the blood acquisition and sample processing steps^{139 140}.

Here, we report a novel, disposable, instrument-free diagnostic device for Ebola virus disease (EVD) from a blood sample that could be operated from sample to result with minimal end-user steps at the point of care (POC) by medical personnel trained in safe interaction with Ebola patients. We demonstrated the proof-of-principle of the device using blood spiked with soluble glycoproteins (sGP) and Ebola virus-like-particles (VLPs). The autonomous device has an integrated blood acquisition module that draws blood from a vacutainer, performs plasma separation, viral lysis, and detects Ebola protein markers by immunoassay. The device has the ability to perform 8-plex protein tests from a single blood sample.

Experimental setup

Assembly of 2DPN 8-channel lateral flow cartridge

A 2DPN 8-channel device containing a plasma separation stack, a cellulose collection pad, and Au label conjugate pad was built into the lateral flow (LF) cartridge. Figure 4.5 shows a model with different layers of the LF device and a fully assembled 8-channel LF cartridge.

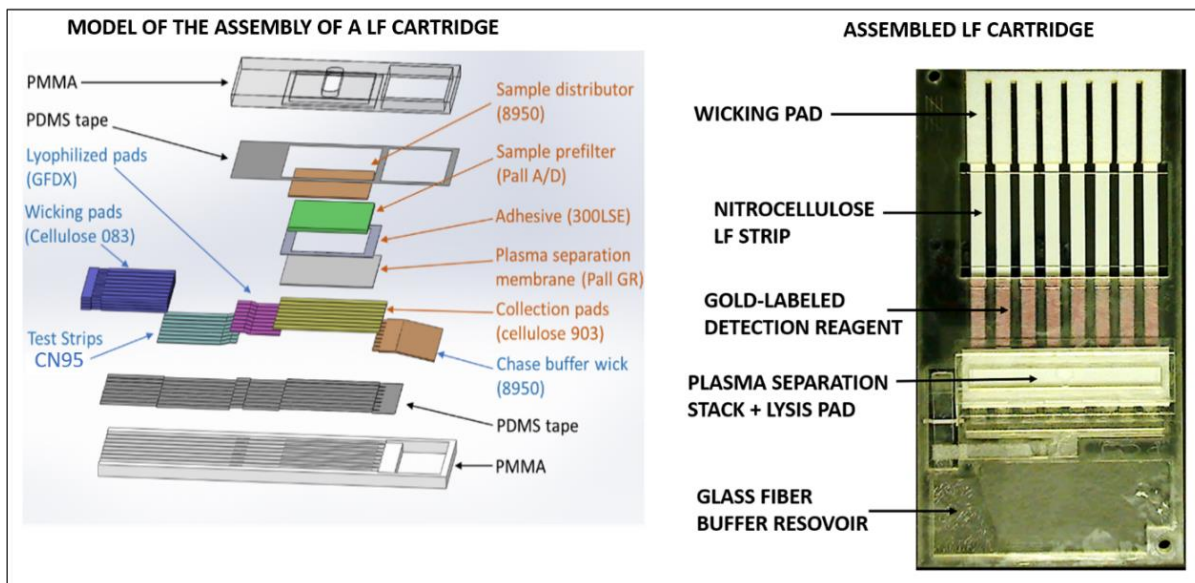


Figure 4.5. A model of the 8-channel LF cartridge with different layers (left) (Figure courtesy Steven Bennett). A fully assembled LF cartridge (right).

The plasma separation stack consists of a glass fiber (8950, Ahlstrom, Finland) that uniformly spreads the blood sample, a sample prefilter membrane (A/D, Pall corporations, NY, USA), a plasma separation membrane (Vivid membrane, Pall corporation, NY, USA), and a cellulose

collection pad (903, Cytiva, USA)). The plasma separation stack was layered overlapping the conjugate glass fiber pad (GFDX, Millipore Sigma, MA, USA) with Au-label on one side and a glass fiber wick (8950 Ahlstrom, Finland) on the other side. The conjugate pad, in turn, was placed overlapping a nitrocellulose membrane (Unisart® CN95, Sartorius, Germany), followed by a cellulose wicking pad. The entire stack is assembled in a PMMA tray secured with a PDMS tape (Valley industrial products, NY, USA).

Sandwich immunoassay for Ebola VLP GP 1/2 and limit of detection

Schematics of the sandwich immunoassay is shown in Figure 4.6. The nitrocellulose membranes were striped with 1mg/ml capture antibody mouse anti-GP1/2 KZ52 (Absolute Antibody Limited), which targets the GP1/2 base region of the Ebola viral membrane glycoprotein. Biotinylated detection antibodies rabbit anti-EBOV GP (IBT Bioservices) and streptavidin-coated Au label (Innova Biosciences, Cambridge, UK) were premixed in PBS buffer containing 8% trehalose and lyophilized in the conjugate pad.

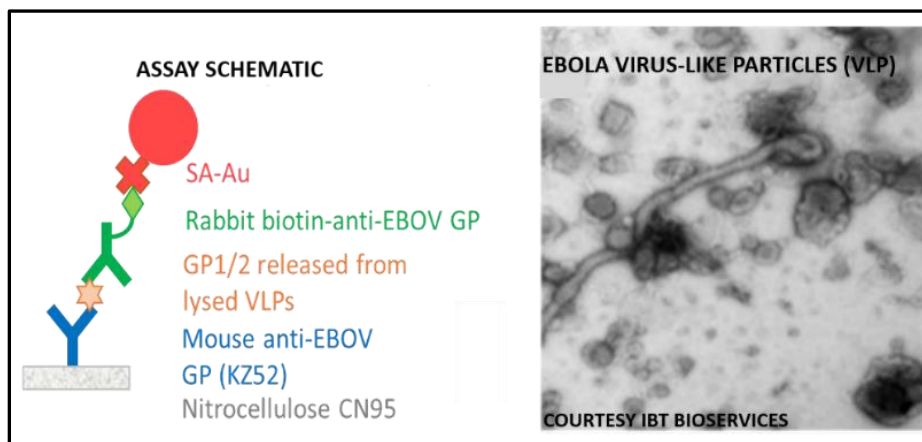


Figure 4.6. Schematic of the sandwich immunoassay for the detection of Ebola surface glycoprotein (left). Electron micrograph of Ebola virus-like particles (VLPs) (IBT Bioservices) (right).

A two-channel prototype device was built with the same layering of the 2DPN as the 8-channel device (Figure 4.5) to test the ability of plasma separation and the lysis of Ebola VLPs (IBT Bioservices, Rockville MD, USA). The plasma separation stack containing a lysis pad with 3% Tween 20 was placed in conjunction with the Au-labeled detection pad and the lateral flow capture membrane and enclosed in a laminate card. Ebola VLPs shown in Figure 4.6 (right) were supplied

as 1mg/ml. About 4 μ l of VLPs were spiked into the 100 μ l blood and applied to the plasma separation stack. After 4 minutes, PBS chase buffer for manually added to the buffer reservoir. As a control, we used a collection pad without Tween 20.

To determine the LOD, we used human plasma spiked with varying amounts of VLPs. A five-fold dilution series of VLP concentrations in plasma were tested in replicates of six. The amount of GP1/2 per VLP was estimated to be 106 μ g/ml by the manufacturer, IBT Bioservices, using ELISA. For the lysis of VLPs, 3% Tween-20 containing 1% (w/v) BSA was added to the cellulose 903 collection pad and dried at 37 °C. For comparison, we used recombinant GP 1/2 protein (IBT Bioservice, MD, USA). After the assay, all lateral flow detection strips were scanned wet using a flat-bed scanner at 600 ppi and signal quantified.

Blood acquisition module

A user-friendly blood acquisition module that meters a precise volume of blood (1 ml) was designed to safely and reproducibly draw blood from a vacutainer, mix blood with buffer, and deliver the fluid to an outlet that connects to the 2DPN plasma separation component located within an 8-channel device, The schematic of the device is shown in Figure 4.7. To operate the device, a vacutainer containing blood is inserted into the transfer device as shown in step1. The handle or the lever of the device is gently squeezed in step 2. When the lever rotates, it moves the syringe plunger up along the motion track, which draws blood from the inserted vacutainer. When the lever reaches its full rotation, it frees the syringe plunger from the motion track. The internal spring then forces the syringe plunger down, which dispenses the drawn blood from the syringe into the lateral flow cartridge. To test the function of the blood acquisition module and plasma separation through the 2DPN we spiked blood with 200 ng/ml of recombinant soluble glycoprotein (IBT Bioservices, MD, USA). The lateral flow nitrocellulose membranes were striped with human anti-sGP antibody BVBD (gift to David Baker). For detection, biotinylated human anti-sGP antibody (IBT Bioservices) and streptavidin-coated Au label were premixed in PBST buffer containing 4% trehalose, 1% (w/v) BSA, 0.05% (v/v) Tween-20, and stored dry in the conjugate pad. After the plasma rehydrated the conjugate, 2 ml of chase buffer was introduced to the 8-channel device to complete the LF detection. After 25 minutes of introduction of blood to the device, the Au-label signal was quantified across the 8 channels using a flat-bed scanner.

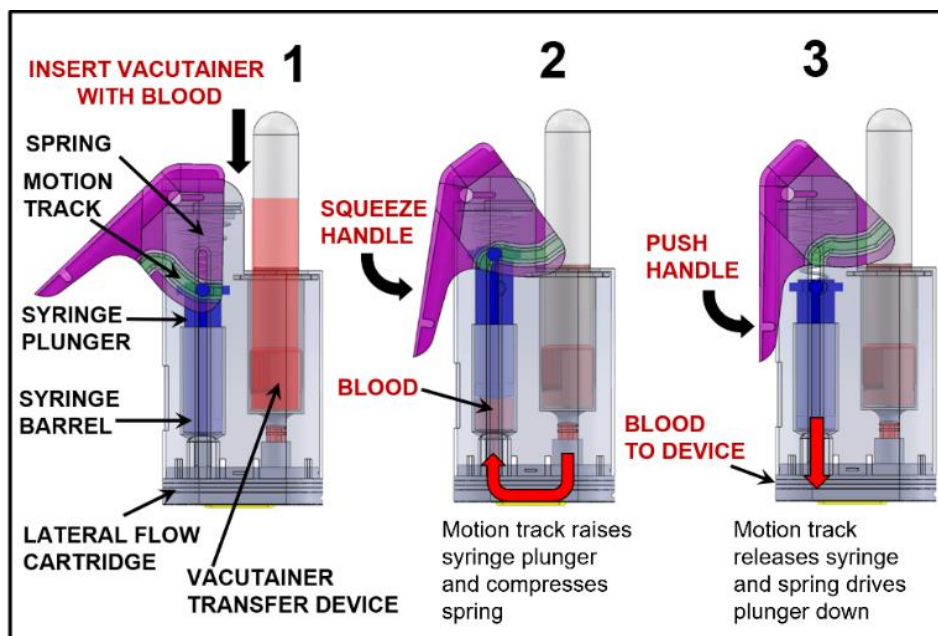


Figure 4.7. Schematic of the blood acquisition module showing user steps (1-3) to push blood from a vacutainer into an 8-channel device (Image courtesy: Steven Bennett). 1. Insert Vacutainer; 2. Pull lever to body of device to draw blood into the syringe; 3. Push handle further to deliver blood to 8 channel device lateral flow cartridge.

Results and discussion

The goal of this study was to develop a 2DPN device that can accept blood automatically from a vacutainer, separate blood plasma, lyse the Ebola virus, and detect protein markers. We obtained commercially available Ebola virus-like particles (VLPs) as our model system. The VLPs were 20 nm in width and up to 1000 nm long (Figure 4.6); they have structural proteins, nucleoprotein (NP), membrane surface glycoprotein (GP1/2), and matrix protein (VP40) without the non-structural proteins or genome. The VLPs are non-infectious, thus alleviating the need to work at a BSL4 facility. We chose the Ebola membrane trimeric glycoprotein (GP1/2) as the protein marker for our study to demonstrate the lysis capability of the 2DPN device. Antibodies directed to the KZ52 base region¹⁴¹ of the GP1/2 were selected for the sandwich immunoassay. Blood spiked with recombinant soluble glycoprotein (sGP) was used to demonstrate the blood acquisition module in a sample-to-result test of the integrated device.

First, we tested the plasma separation component of the 2DPN separately. Second, we tested the ability of the device to lyse the Ebola VLPs and release the membrane GP1/2 and detect signal by lateral flow detection in a prototype device. Third, we determined the LOD for the Ebola membrane GP1/2 using the 2DPN prototype device with plasma separation, lysis and lateral flow detection. Finally, we performed a proof-of-principle sample-to-result test with the blood acquisition module that delivered blood from a vacutainer to the integrated 2DPN device.

Demonstration of plasma separation and lysis of Ebola VLPs in the integrated 2DPN device

We first tested plasma separation using a miniature test fixture consisting of the same membrane stack as the 2DPN integrated device (Figure 4.8a) & b)).

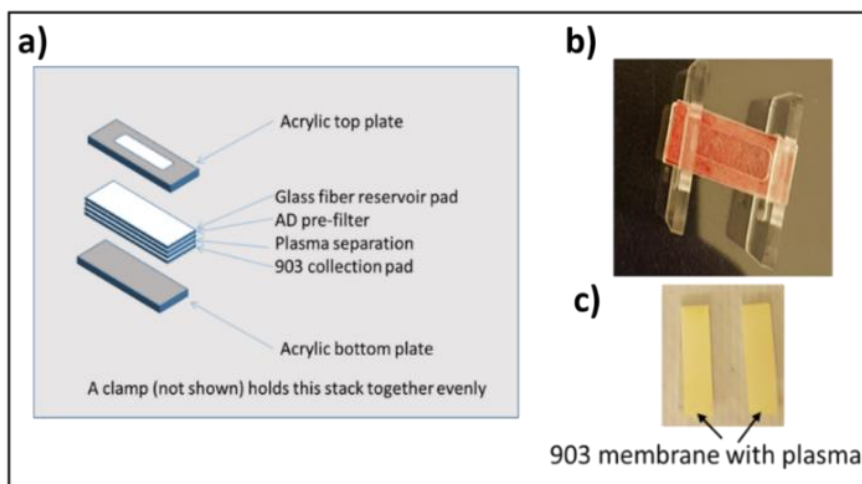


Figure 4.8. 2DPN plasma separation from blood. a) Component of the plasma separation stack assembled using a glass fiber reservoir pad, glass pre-filter, a Vivid plasma separation membrane and a 903 membrane. b) The membranes are held by acrylic plates on top and bottom and clamped together evenly. Blood was applied to the top glass fiber membrane. c) Clear plasma was consistently collected on to the cellulose 903-membrane using this device.

Blood was added to the topmost glass fiber pad. We found that human blood sample distributed evenly over the glass filter pad, filtered through the plasma separation membrane and clear plasma was consistently collected on to the 903 cellulose membrane using this device (Figure 4.8c)).

Next, we combined the plasma separation and the lateral flow component to demonstrate the lysis of Ebola VLPs in a two-channel prototype device (Figure 4.9).

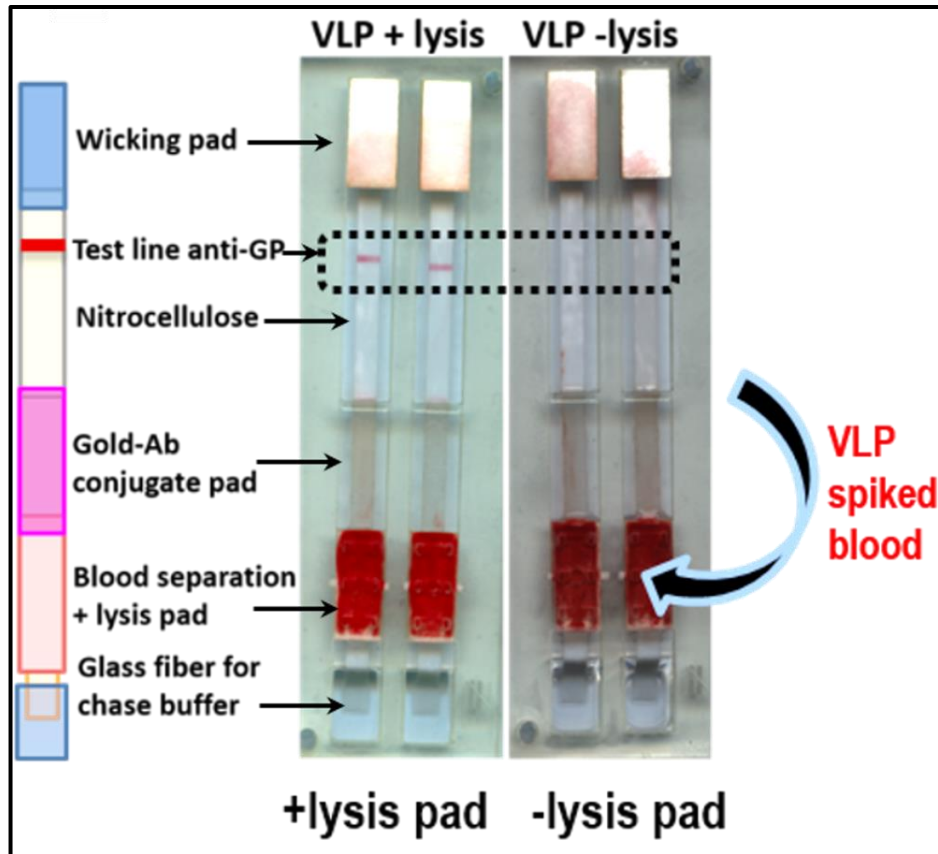


Figure 4.9. A 2-channel integrated prototype device consisting of plasma separation stack, dry lysis pad, dry detection reagents, and lateral flow strip. Blood spiked with Ebola VLPs was applied on to the plasma separation membrane and then chased with buffer. A strong detection signal for GP1/2 is seen at the test line. When VLPs were added to the pad without lysis reagent the signal was negative indicating that the GP1/2 base region was not exposed. VLPs.

In this device, the plasma collection cellulose membrane contained oven-dried 3% Tween 20 detergent as the lysing agent. Human blood spiked with Ebola VLPs was added to the plasma separation stack. After 4 minutes PBS chase buffer for manually added to complete lateral flow detection. The lysis reagent stored dry in the pad retained its ability to lyse VLPs in the plasma as seen by the intense Au signal at the capture line in the lateral flow membrane (Fig 4.9). The VLPs do not give any signal when no lysis reagent was added to the pad, as the targeted base region of the membrane bound GP1/2 is hidden and requires lysis for it to be exposed and detected by immunoassay. We were thus able to integrate plasma separation, viral lysis and lateral flow detection using 2DPN.

Limit of detection for Ebola VLP GP1/2 in the 2DPN device

Using the same 2DPN setup as above, we determined the LOD for samples spiked with Ebola VLPs and compared it with samples spiked in recombinant GP1/2. A five-fold dilution series of VLP concentrations were tested in replicates of six. The LOD of GP1/2 from VLPs detection was 1.8 ng and was comparable to the LOD with recombinant GP 1/2 at 2.6 ng. (Figure 4.10).

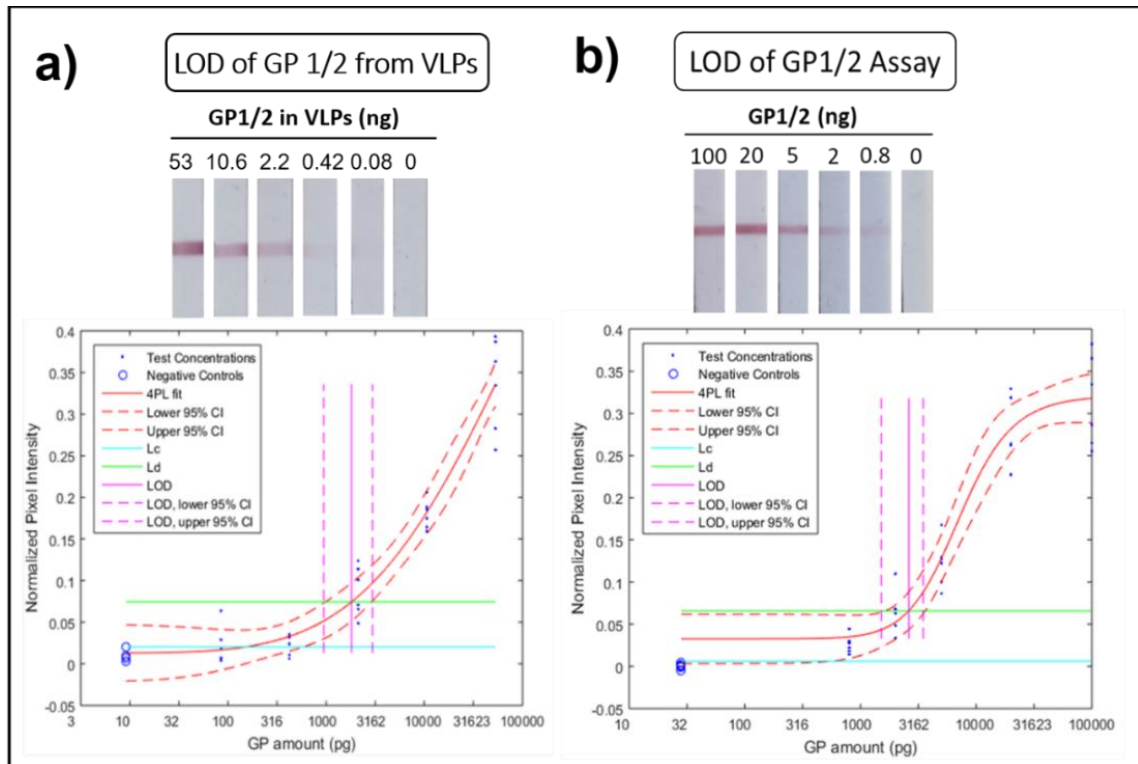


Figure 4.10. Limit of detection of Ebola glycoprotein markers in 2DPN device. a) Antibody-based capture assay in alpha prototype 2DPN for GP1/2 from VLPs with gold nanoparticle-based detection. LOD of GP1/2 from VLPs detection is 1.8 ng, with the 95% confidence interval being 0.944 to 2.965 ng. b) Antibody-based capture assay in alpha prototype 2DPN for recombinant GP1/2 with gold nanoparticle-based detection. LOD of GP1/2 detection is 2.6 ng, with the 95% confidence interval being 1.5160 to 3.4844 ng.

Integration of blood delivery, plasma extraction and immunoassay with 2DPN LF cartridge

Next, we integrated the blood acquisition module to the 8 channel 2DPN LF cartridge. The operation of the device with blood in vacutainer spiked with soluble glycoprotein is shown in Figure 4.11a). This integrated device is user-friendly that allows one hand operation. About 1 ml

of blood was transferred automatically to the plasma separation stack. About 2 mL of PBS was pipetted to the chase buffer well to flush plasma out of the collection pads, whereupon it rehydrated the conjugate pads and flowed to the nitrocellulose LF detection strips. The strips were scanned 25 min after introduction of blood sample. The test line intensity was uniform in all the eight strips (Figure 4.11b)). The test line results show that the eight-channel device can separate and collect plasma that contains sGP marker from a blood sample and detect by sandwich immunoassay on downstream lateral flow strips.

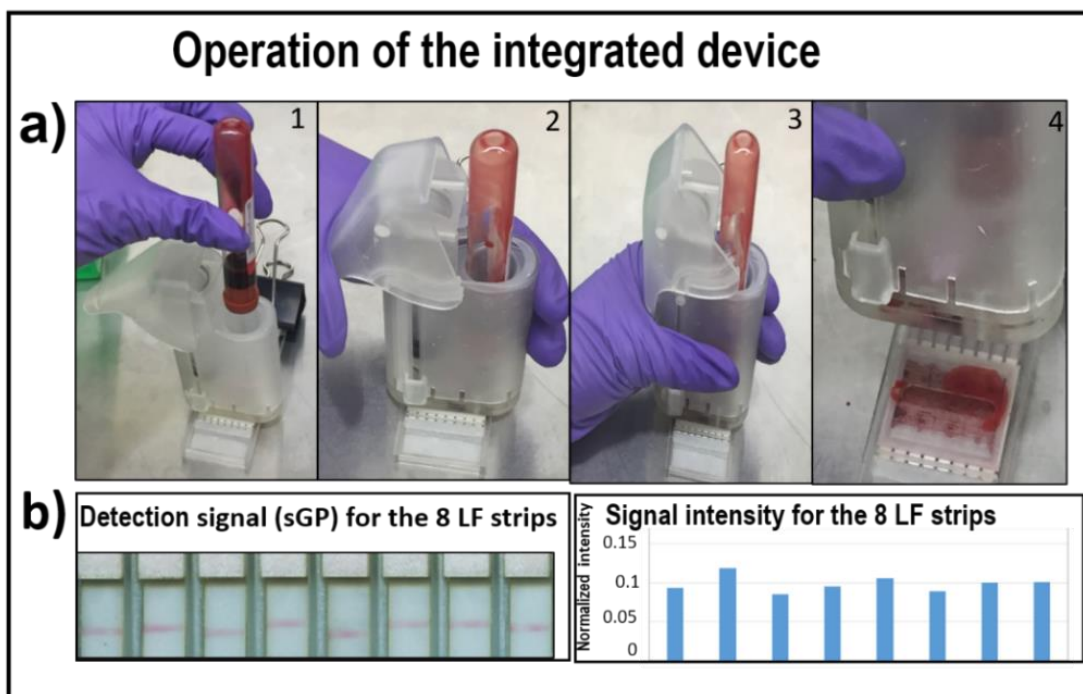


Figure 4.11. Integration of blood acquisition module with 8 channel LF detection cartridge. a) Sample-to-result operation of the integrated 8-channel device with blood acquisition from a vacutainer. Step 1, insert vacutainer, Step 2, pull lever to the body of the device, Step 3, push the lever further to deliver blood to the LF cartridge, Step 4 the blood flows into the 8-channel LF cartridge. b) Scanned photo of test lines for the sGP target and signal quantification of each channel.

Conclusion

We performed a proof-of-principle sample-to-result test to demonstrate a user-friendly blood acquisition module with an integrated 2DPN 8-channel LF device. The module delivered blood equally to the 8-channel device and detected Ebola glycoprotein markers. Ebola VLPs spiked into

blood was used to demonstrate plasma separation, VLP lysis, and detection of membrane-bound glycoprotein GP1/2 in a prototype device. The total operation time was 25 minutes. Overall, the device can be safely operated, is autonomous, disposable, and applicable to POC in low-resource settings. The device can multiplex with eight different protein markers from a single blood sample in a vacutainer. The vacutainer is the most common blood storage device in many clinical settings and would certainly also be so in a US domestic and worldwide hospital setting.

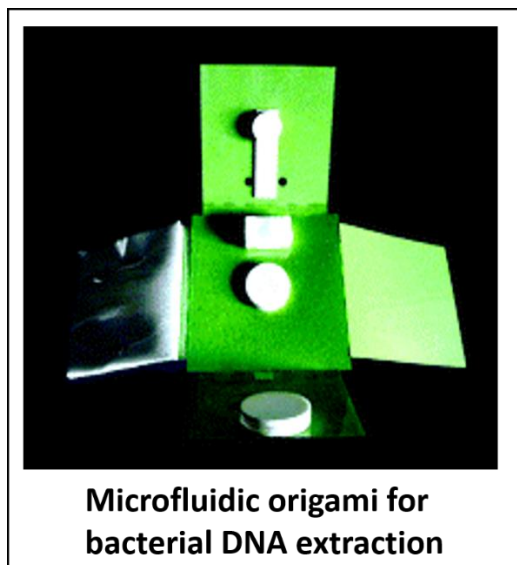
4.3 A paper-based microfluidic origami device for nucleic acid extraction

This section is based on the paper ¹³⁶

A low cost point-of-care viscous sample preparation device for molecular diagnosis in the developing world; an example of microfluidic origami

Anupama Govindarajan, Sujatha Ramachandran, Genevieve Vigil, Paul Yager and Karl Bohringer

Reproduced from *Lab Chip*, 2012, 12, 174-181 with permission from the Royal Society of Chemistry.



Reproduced from *Lab Chip*, 2012, 12, 174-181 with permission from the Royal Society of Chemistry.

I designed the experiment and together with Anupama Govindarajan conducted the work and analyzed the data. Together with the other authors discussed the results and wrote the paper.

Cite this: *Lab Chip*, 2012, **12**, 174

www.rsc.org/loc

PAPER

A low cost point-of-care viscous sample preparation device for molecular diagnosis in the developing world; an example of microfluidic origami†

A. V. Govindarajan, S. Ramachandran, G. D. Vigil, P. Yager and K. F. Böhringer*

Received 11th July 2011, Accepted 21st October 2011

DOI: 10.1039/c1lc20622b

The lab-on-a-chip concept has led to several point-of-care (POC) diagnostic microfluidic platforms. However, few of these can process raw samples for molecular diagnosis and fewer yet are suited for use in a resource-limited setting without permanent electrical infrastructure. We present here a very low cost paper microfluidic device for POC extraction of bacterial DNA from raw viscous samples—a challenge for conventional microfluidic platforms. This is an example of “microfluidic origami” in that the system is activated by folding; demonstrated here is room temperature cell lysis and DNA extraction from pig mucin (simulating sputum) spiked with *E. coli* without the use of external power. The microfluidic origami device features dry reagent storage and rehydration of the lysis buffer. We demonstrate DNA extraction from samples with a bacterial load as low as 33 CFU ml⁻¹. Extraction times, starting from the raw sample, have been optimized to about 1.5 h without the use of external power, or to within 1 h using an oven or a heater block. The fabrication of this paper microfluidic device can be translated into high volume production in the developing world without the need for a semiconductor clean room or a microfabrication facility. The sample preparation can be performed with the addition of just the sample, water, ethanol and elute buffer to the device, thus reducing chemical hazards during transport and handling.

Introduction

The development of nucleic acid amplification tests (NAATs) has opened the doors for highly specific molecular diagnosis and personalized medicine. These tests are currently available in advanced healthcare facilities and are limited in their distribution by their cost and by the lack of point-of-care (POC) sample preparation systems. Simple sample preparation will bring down the cost of molecular diagnosis and make it more accessible. Our goal is two-fold: i) to develop an extremely inexpensive, self-contained, disposable, portable nucleic acid extraction device and ii) to use it to demonstrate extraction of bacterial DNA from a viscous sample matrix, which presents a challenge for conventional microfluidic devices.

We describe here the development of a simple paper microfluidic platform for sample preparation. Sample preparation is the first step to nucleic acid-based diagnosis; our long-term goal for the technology shown in this paper is to simplify this complex process such that the cost of nucleic acid extraction will eventually be less than US\$2 per patient.

Since the lab on paper review article¹ published in 2008, low cost paper diagnostics,^{2–13} including those based on enzyme-

linked immunosorbent assay (ELISA)², sequential reagent delivery,³ multiplexed bioassays,⁸ and the integration of paper microfluidics with commercial electrochemical readers¹⁴ have been emerging for diagnostic applications in the developing world. Such devices must be inexpensive, rugged, lightweight, and independent of supporting infrastructure.¹⁰ Despite advances in conventional and paper microfluidic technology, the lack of development in sample preparation systems has led to there being few lab-on-chip^{15–19}/lab-on-paper^{5,6} systems that can extract nucleic acids (NA) from raw samples.

We describe our sample preparation platform as an example of “microfluidic origami” because it is fabricated from a stack of flat polymer sheets and paper, and is activated by folding. Demonstrated here is room-temperature cell lysis and DNA extraction from pig mucin (simulating sputum) spiked with *E. coli* without the use of external power.

A preliminary version of this platform without dry reagent storage was presented at the IEEE International Conference on Microelectromechanical Systems.²⁰ This paper introduces an integrated POC platform that can be operated with the addition of just water, ethanol and elute buffer to the device. This low cost origami-based sample preparation method in combination with an existing or to be developed portable NAAT based system should yield a raw sample-to-result molecular diagnosis in less than 2 h. As a stand-alone device, our approach enables storage of point-of-care extracted DNA for transport at room temperature to more centralized diagnostic facilities. This will be

University of Washington, Electrical Engineering, Campus Box 352500, Seattle, WA, USA 98195. E-mail: karlb@u.washington.edu; Fax: +1-206-543-3842; Tel: +1-206-221-5177

† Electronic supplementary information (ESI) available. See DOI: 10.1039/c1lc20622b

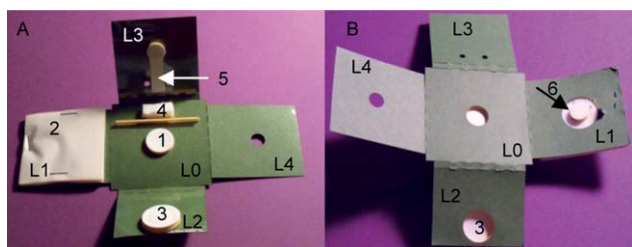


Fig. 1 Microfluidic origami device for point-of-care nucleic acid extraction. A. Front side, B. Backside, 1. DNA filter, 2. Waste absorption pad with Mylar backing, 3. Sample loading cup, 4. Lysis/wash buffer storage and rehydration pad, 5. Buffer transport channel, 6. Contact stack. L1...L4: Layers that fold above and below layer L0. Figure reprinted from Govindarajan *et al.*²

especially useful in the absence of reliable cold shipment or a portable NA amplification system—a typical situation in rural areas of the developing world. This work is the first step towards providing a low cost, low power alternative to a fully automated and portable sample preparation module of an integrated system like the Cepheid GeneXpert.²¹ The GeneXpert uses self-contained, single use, biosafe, microfluidic cartridges that feature ultrasonic lysis of the filter-captured organisms to release DNA.²²

The core idea of this microfluidic origami sample preparation device (Fig. 1) is sequencing complex chemical and physical processing steps through sequential folding of pieces of a flat substrate. This folding sequence puts different paper fluidic circuits in contact with new solvent and reagent sample pads, substituting capillary flow for pumps, and folding and unfolding for valve activation. This microfluidic origami device separates the process into steps on several layers (L0–L4) that fold above or below the central layer L0, which consists of the core elements—the DNA binding filter and a dry lysis buffer storage pad. The device in its present form is disposable and is designed as a single use, inexpensive device that can process one sample at a time.

Materials

Sample matrix and bacteria

Commercial mucin (M1778 mucin from porcine stomach, type III, bound sialic acid 0.5–1.5%, partially purified powder from Sigma-Aldrich) was used to simulate sputum. A sample of 20% (w/v) pig mucin in nuclease-free water resembled human sputum in viscosity, stickiness and color. However, the mucin can contain traces of *E. coli*. To ensure that the extracted and amplified DNA was from the bacterial cell lysis rather than the sample matrix, a transformed *E. coli* strain, XL1 blue transformed with plasmid DNA H127KSApuc18, was used to spike the mucin in our experiments.

Device fabrication and assembly

A single device fabrication (Fig. 2) took less than 30 min. The fabrication consists of stacking layers of paper, Mylar (Fraylock, Inc., San Carlos, CA, USA) and repositionable adhesive, followed by laser cutting. The approach of making both through

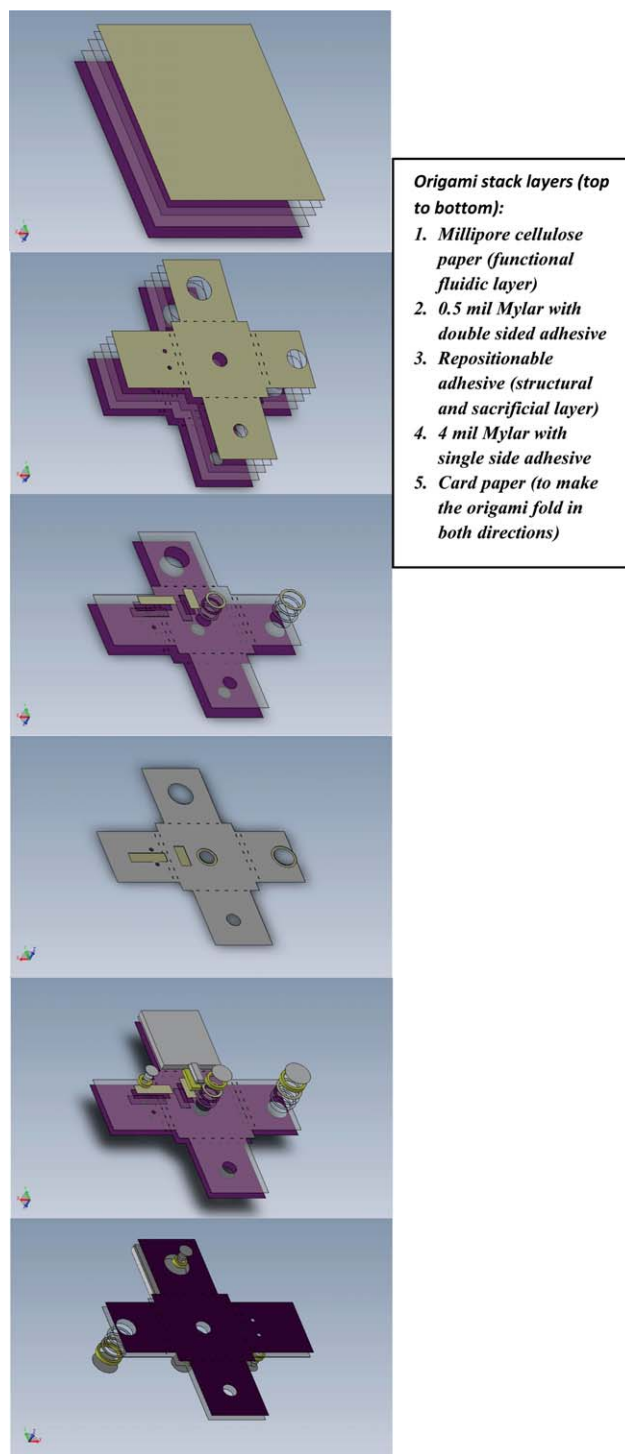


Fig. 2 Microfluidic origami NA extraction device fabrication. A. Stack layering, B. Stack through cuts, C. Stack partial cuts, D. Peeling between repositionable window decal and 4 mil Mylar layer to define paper fluidic channels on a non-wicking substrate. The repositionable adhesive film served both as a structural and sacrificial layer. After laser cutting with varying power, the repositionable film was peeled away from the substrate, leaving behind the entire stack in the lower power cut areas, E. Front side assembly of pre-cut parts (with laser cut 3M Scotch mounting tape, serving as spacer), F. Assembling pre-cut parts on backside. Laser cut 3M Scotch mounting tape and Millipore cellulose paper was used to form the sample-loading cup to accommodate larger sample volumes.

cuts and partial cuts (by varying the laser power) in combination with peeling of a repositionable adhesive layer presents a low cost alternative to the FLASH method¹¹ for defining paper fluidic channels on a non-wicking substrate. The stacking of layers of the origami from top to bottom was done by hand using a rolling pin to press the sheets together. The origami stack layers from top to bottom comprised of cellulose paper (Millipore, Billerica, MA, USA), 0.5 mil Mylar with double-side adhesive, repositionable adhesive layer (RoyalBrites window decals, Norwalk CT), 4 mil Mylar with single side adhesive and card paper to enable bidirectional folding.

The entire stack was placed in a laser cutting machine (M-360 laser engraving and cutting system, Universal Laser Systems Inc, Scottsdale AZ, with a 35 watt CO₂ laser). The device was laser cut using a single AutoCAD mask with higher power for the through cuts (power = 40, speed = 10, dpi = 1000, 2 passes) and lower power (power = 28, speed = 10, dpi = 1000, 1 pass) for the partial cuts. The units for the laser cutter settings are (power = % of max. power, *i.e.* 35 watt, speed = % of max. speed, *i.e.* 26.5 in s⁻¹, spatial resolution in dots per inch (dpi)).

Partial cuts were made from the top through the repositionable adhesive layer. After laser cutting, the repositionable adhesive layer was peeled from the bottom Mylar and card paper substrate. This left the entire stack (Millipore cellulose paper - card paper) in the regions that were cut with the lower power, and only the substrate (card paper and bottom Mylar layer) in the remaining areas. With this method we were able to fabricate fluidic channels on a non-wicking substrate down to a width of 1 mm.

The remaining parts of the origami device were laser cut and assembled by hand. The adhesive and spacers were formed by laser cutting 3M Scotch mounting tape (3M, St. Paul, MN, USA) (power = 40, speed = 10, dpi = 1000, 3 passes). Millipore cellulose paper was used to form the base of the sample-loading cup and the contact stack, bound by the 3M Scotch mounting tape for the sides of the cup and the contact stack. The Millipore cellulose paper was laser cut with parameters power = 10, speed = 10, dpi = 1000, 3 passes. The DNA capture filter was formed from Fusion 5 membrane (Whatman Inc., Florham Park, NJ) (laser cut with power = 7, speed = 7, dpi = 1000, 1 pass). The waste absorption pad (highly absorbent sterile sponge from Dukal Corporation, Hauppauge NY, catalog# 6125) was hand cut in 2'' × 2'' squares. The waste absorption pad was stapled onto the origami device on layer L1, with a contact stack placed in the center so that the waste absorption pad maintains capillary contact with the DNA binding filter. The dry reagent storage pad was made from hand cutting an absorbent 100% pure cotton non-woven fabric (Webril Handi-Pads from Fiberweb, Simpsonville, SC).

Dry lysis buffer storage

For dry reagent storage, wet lysis buffer (composition: 4.5M guanidinium thiocyanate, 50 mM MES (2-(4-morpholino)-ethane sulfonic acid) pH 5.5, 20 mM EDTA, 1% N-lauryl sarcosine (sodium salt), 5% Triton X-100 and 0.25M NaOH, developed in house) was pipetted onto the buffer storage pad. The pad was weighed after addition of the wet lysis buffer, dried in a vacuum oven at 50 °C for about 4 h and stored in a 45 °C

incubator until needed (to simulate high temperature environments in the resource limited settings). The last step of device assembly includes placing the dry lysis buffer storage pad on the origami device using 3M Scotch mounting tape.

In our laboratory, the fabrication and the operation of the microfluidic origami device were performed in different dedicated spaces with the idea of translating the device production and operation to the developing world while keeping the associated costs to a minimum. We discuss these conditions and make recommendations for high-volume production in a separate section on avoiding contamination.

Experimental

Microfluidic origami device operation

The operation of the microfluidic origami device for NA extraction is described in Fig. 3. (Please also refer to the supplemental video†). The procedure is modified from our earlier presentation²⁰ to include rehydration of dry stored lysis buffer. First a fresh DNA binding filter was placed on the microfluidic origami device and the waste containment pad with the contact stack (on L1) was folded below the filter. Next, the dry lysis buffer storage pad (on L0) was rehydrated with nuclease-free water (*please note that the supplemental video shows rehydration off the origami, however we have performed several instances of rehydration on the origami device itself*). The difference in the weights of the buffer storage pad after addition of the wet buffer and after drying was used to calculate the volume of water to be added for rehydration. Approximately 490 µl of water was added per 900 µl of wet lysis buffer for rehydration. The dry lysis buffer was rehydrated for approximately 5 min. The raw sample (*E. coli*-spiked mucin) was then loaded into the sample loading cup (on layer L2, that folds directly above the filter). Next, the buffer transport channel (made of Millipore cellulose paper on L3) was folded above L2. The transport channel made contact with the rehydrated lysis buffer storage pad and the raw sample that was loaded into the cup. A contact stack was included in the design of the transport channel to ensure that the lysis buffer reached the bottom of the sample loading cup, as the viscous sample “decongested” (dissolved with no visible mucin chunks in the sample loading cup) during lysis.

The lysis reagents flowed through the temporary fluidic pathways without having to move the sample laterally through the device, thus maximizing the DNA extraction efficiency. At this point, complete (but as-yet-unoptimized) lysis of the sample takes roughly 30 min. A weight was placed on the device in its closed form during lysis to ensure contacts and capillary wicking through layers L0–L3. L4 is reserved for integration of future functionality and was not in use here. After lysis, the weight was removed and the layers were unfolded to expose the DNA binding filter on L0, with the waste containment pad still folded beneath it. Since this is a paper device, the used layers L2 and L3 and the unused L4 layer were at this point cut off and discarded in biohazard waste. This was done to facilitate ease of operation and safety from exposure to harsh chemical residues that resulted from chemical lysis. The DNA binding filter was then washed with 100% ethanol to remove the protein and other non-nucleic acid debris that could be bound to the filter. After

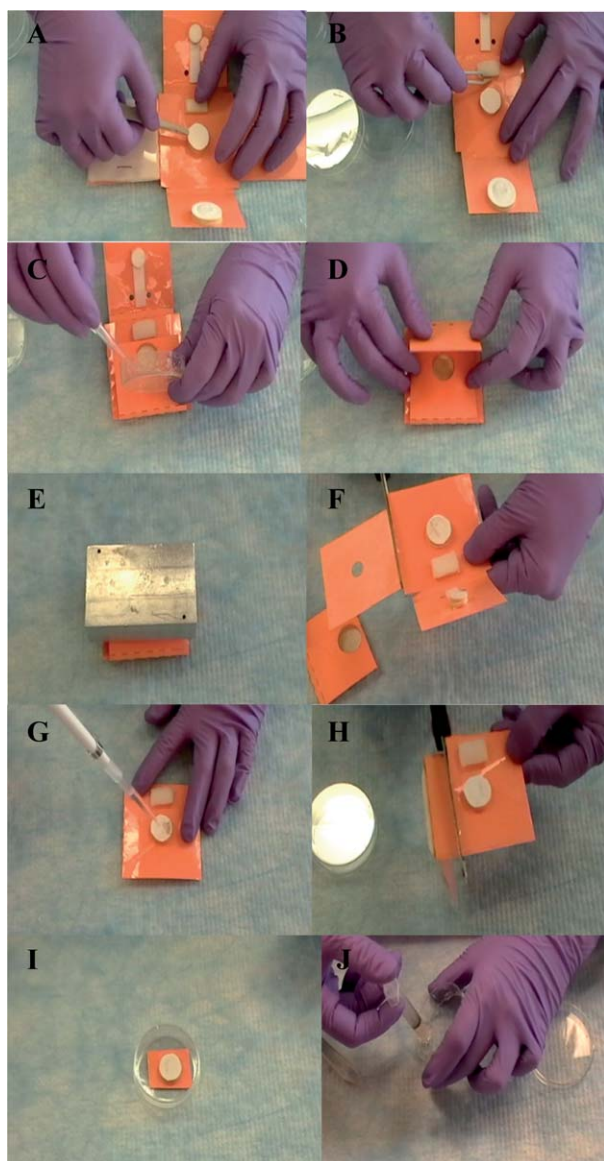


Fig. 3 Microfluidic origami operation: raw sample - DNA extraction 1. Place fresh DNA binding filter on origami device (A). 2. Fold waste absorption pad below the filter and place lysis buffer storage pad/rehydrate buffer (B). 3. Fold sample loading cup above DNA binding filter and load sample into the cup (C). 4. Fold buffer transport channel (D). 5. Place weight on closed microfluidic origami device to ensure contact and capillarity during lysis operation (~ 30 min) (E). 6. Unfold origami and cut and discard used/unwanted layers (F). 7. Wash DNA capture filter directly with 100% ethanol (G). 8. Cut off waste absorption pad (H). 9. Dry the DNA capture filter, e.g. on benchtop (I). 10. Elute DNA from filter in low salt solution (J). Note: The microfluidic origami is a low cost disposable device designed to process one sample per use. Gloves were changed after each use. Please refer to the supplemental video.†

the ethanol wash the filter was left to dry (for example, at room temperature).

DNA elution and PCR analysis

After drying, the filter with the bound dry DNA was transferred with a pair of sterile tweezers into a sterile syringe. A 150 μl

volume of low salt elute buffer (0.01 M Tris buffer, pH 8) was introduced into the syringe and siphoned up and down, past the DNA filter, using a sterile petri dish at the bottom. The filter was allowed to soak in the elute buffer in the syringe for 5 min before the extracted DNA was collected and stored in a nuclease-free Eppendorf tube, ready for amplification by polymerase chain reaction (PCR). The elutants from the microfluidic origami contained both plasmid and genomic DNA (extracted by a common procedure) that were amplifiable by a conventional benchtop PCR machine (Perkin Elmer Cetus DNA Thermal Cycler).

We used *malB* gene amplification product of 86 bp as a marker for *E. coli* genomic DNA. For genomic DNA amplification the forward and reverse primers were EC3F: 5'-GCCGATGCC AAATCGTCAG-3' and EC3R: 5'-GGCGAATACCCAGC GACAT-3'. The PCR used for amplifying genomic DNA incorporated an initial heat step at 95 °C for 3 min followed by 38 cycles of 95 °C for 10 s, 60 °C for 10 s and 72 °C for 15 s. Forward and reverse primers used for the amplification of plasmid DNA were S29: 5'- TCC CAG TCA CGA CGT - 3' and S33: 5'- AGC CGA TAA CAA TTT CAC ACA GCA - 3'. The PCR thermal process for plasmid DNA consisted of an initial heating step at 96 °C for 2 min followed by 40 cycles of 96 °C for 1 min, 52 °C for 2 min and 70 °C for 3 min (to detect low bacterial loads). For samples spiked with undiluted bacterial culture, 27 cycles were sufficient for detection of the extracted plasmid DNA. The positive controls for PCR were Qiagen (Qiagen Inc. Valencia, CA, USA) extracts from the *E. coli* culture (genomic extraction control: QIAmp DNA Mini kit, plasmid extraction control: QIAprep Spin Miniprep kit). The positive controls were processed without mucin. The negative control was nuclease-free water. For the plasmid extraction the "mucin only" lane served as an additional negative control. PCR products were separated using agarose gel electrophoresis and were visible in UV light with ethidium bromide staining.

Bacterial load variation

The bacterial DNA extraction experiments to validate the functioning of our device were from *E. coli* cultures. The *E. coli* was grown overnight at 37 °C in a shaker bath in *Luria-Bertani* (LB) broth containing carbenicillin. *E. coli* cells containing the plasmid DNA H127KSApuc18 are resistant to carbenicillin. In order to test the lower limit of detection sensitivity with the microfluidic origami extraction platform, a fresh culture was grown overnight and was serially diluted in 10 fold steps. A sample of 20 μl of each dilution was plated on LB-agar plates (with carbenicillin) and grown overnight in a 37 °C oven to estimate the colonies grown on the plates. This was translated in terms of colony forming units per ml (CFU ml^{-1}) of the grown culture. 50 μl of each *E. coli* dilution was spiked in separate 250 μl aliquots of porcine mucin. Each of these spiked raw mucin samples was processed separately on a microfluidic origami device.

Avoiding contamination

The fabrication of the microfluidic origami based sample preparation device can be translated in high volumes to the

developing world without a microfabrication laboratory (referred to commonly as “cleanroom”) – a typical environment for the fabrication of most lab-on-a-chip systems. This cuts down significantly the associated costs in maintaining the specialized cleanroom equipment and environment (*e.g.* the particle count). For this work, the origami device was fabricated in a dedicated room that housed a laser cutter, an attached computer and a work bench for assembly. The work bench was cleaned with ethanol and isopropyl alcohol (IPA) prior to hand-assembling laser cut portions of the origami device. The DNA binding filter in particular was stored in a nuclease free Eppendorf tube, immediately after laser cutting the factory sealed and shipped Fusion 5 membrane (Whatman Inc., Florham Park, NJ). It was placed on the origami device just before operation. For more commercial type production and disease diagnosis, assembling the laser cut portions of the device in a laminar flow bench fitted with UV light and high-efficiency particulate air (HEPA) filters would significantly reduce bacterial contamination. During device operation, nuclease free Eppendorf tubes/containers and sterile disposable sample applicators/syringes/tweezers should be used for any intermediate sample or DNA binding filter handling. In our laboratory protocol our dedicated sample preparation space was wiped with ethanol and IPA before processing a batch of samples. A fresh disposable diaper pad was used below to contain any waste or possible spills. Tweezers/sample applicators were sterilized between samples by washing the tips with ethanol. Rinsing in DNase away, RNase away solutions (Invitrogen, Carlsbad, CA) prevented NA degradation. Personal protective equipment included gloves (to be changed for every sample), labcoats, goggles, hairnets and facemasks.

Results and discussion

The sample size used in this work was 300 μl of pig mucin spiked with *E. coli*. The origami-based POC sample preparation device is designed to accommodate larger viscous sample sizes that are readily available from the source and useful to detect lower or sparser bacterial loads. Sample volumes can be downscaled, the limiting factor of fluid flow being the minimum channel width achievable by our fabrication method, which is currently 1 mm. Reagent volumes are yet to be optimized, but we have observed that $2 \times 900 \mu\text{l}$ volumes of lysis buffer are sufficient to dissolve 300 μl of viscous pig mucin. To facilitate ease of manual operation and to accommodate realistically useful viscous sample sizes, our channel widths and lengths and filter and cup diameters are of the order of 1–3.8 cm. We use the term microfluidic because we rely on small-scale physical effects like capillarity and



Fig. 4 Extraction of plasmid DNA from raw sample at room temperature, after rehydration of dry stored lysis buffer on microfluidic origami device. Gel lane description given in Table 1.

have channel thicknesses and layer heights in the hundreds of μm range.

The lysis buffer dissolves mucin at room temperature without external power. It provides complete lysis of the *E. coli* bacterial cells and does not inhibit PCR. The presence of a specific 500 bp plasmid DNA band, seen after DNA extraction and amplification only in *E. coli*-spiked mucin samples and not in unspiked mucin samples (Fig. 4, Table 1) confirmed *E. coli* cell lysis and DNA extraction from the spiked mucin matrix using the microfluidic origami platform. Comparison between lanes 2–4 (extraction with rehydration of dry lysis buffer on the origami) and lane 5 (extraction with direct wet lysis on the origami) in Fig. 4 showed that there was no significant loss in detection due to the buffer rehydration process.

Fig. 5 (Table 2) shows the extraction and amplification of genomic (naturally occurring) DNA (malB gene of *E. coli*, 86 bp). For gel images in Fig. 4–Fig. 6 (Table 1–Table 3) note the concurrence in the DNA band “expected” and “seen” columns.

The microfluidic origami approach features a raw sample to DNA extraction time (lysis and wash time included) of about 1.5 h without the use of external power or between 45 min–1 h by drying (post lysis and wash) on a heater block at 50 °C or in an oven at 37 °C. In comparison, the raw-sample to extraction time using the FTA® cards⁵ is as follows: the raw sputum drying on the FTA® card takes 1 h, drying post washes takes another hour, washing with the proprietary FTA® purification reagent and the TE buffer is about 25 min.

Bacterial load variation

Plasmid instead of genomic DNA was used in this work to determine the limits of extraction and detection (after

Table 1 Lane description for Fig. 4

Lane	500 bp band expected	500 bp band seen
1. Qiagen kit extraction of plasmid DNA from <i>E. coli</i>	Yes (+ve control)	Yes
2., 3. Mucin + <i>E. coli</i> with dry lysis rehydration (load $\sim 10^6$ CFU ml^{-1})	Yes	Yes
4. Mucin + <i>E. coli</i> with dry lysis rehydration (load $\sim 10^4$ CFU ml^{-1})	Yes	Yes
5. Mucin + <i>E. coli</i> with wet lysis	Yes	Yes
6. Mucin only	No	No
7. Water only	No (-ve control)	No
8. 100 bp Invitrogen ladder		

Table 2 Lane description for Fig. 5

Lane	86 bp band expected	86 bp band seen
1. Qiagen kit extraction of genomic DNA from <i>E. coli</i>	Yes (+ve control)	Yes
2., 3. Mucin + <i>E. coli</i> with dry lysis rehydration (load $\sim 10^6$ CFU/ml)	Yes	Yes
4. Mucin + <i>E. coli</i> with dry lysis rehydration (load $\sim 10^4$ CFU/ml)	Yes	Yes
5. Mucin only (mucin is partially purified and may contain traces of <i>E. coli</i>)	Maybe	No
6. Water only	No (-ve control)	No
7. 50 bp Invitrogen ladder		

Table 3 Lane description for Fig. 6

Lane	CFU in sample from plating estimate	CFU ml ⁻¹ of mucin	500 bp band expected	500 bp band seen
1. Qiagen kit extraction of plasmid DNA from <i>E. coli</i> (undiluted culture)	+ve control		Yes	Yes
2. Mucin + <i>E. coli</i>	4200	1.4×10^4	Yes	Yes
3. Mucin + <i>E. coli</i>	485	1.6×10^3	Yes	Yes
4. Mucin + <i>E. coli</i>	25	83	Yes	Yes
5. Mucin + <i>E. coli</i>	12	40	Yes	Yes
6. Mucin + <i>E. coli</i>	10	33	Yes	Yes
7. Mucin + <i>E. coli</i>	22	73	Yes	Yes
8. Mucin only			No	No
9. Water only	-ve control		No	No
10. 100 bp Invitrogen ladder				

**Fig. 5** Extraction of genomic DNA from raw sample at room temperature, after rehydration of dry stored lysis buffer on microfluidic origami device. Gel lane description given in Table 2.**Fig. 6** Bacterial load variation for DNA extraction on the microfluidic origami device. Gel lane description given in Table 3.

amplification). This is because the mucin used in this work, derived from the porcine stomach, could possibly contain traces of *E. coli* and would therefore not serve as a good negative background for the bacterial load variation. We acknowledge that diagnosis in a real world setting would be done with genomic DNA and that a closer comparison to existing molecular diagnostic kits would result from using similar bacterial strains of the disease with similar copy numbers. Our goal in this paper is to introduce a low cost proof of concept platform for POC sample preparation leading to POC molecular diagnosis.

Fig. 6 (Table 3) is representative of the bacterial load variations in this work. Plasmid DNA bands (500 bp), (after PCR) were visible for the culture, a 10-fold culture dilution and a 100-fold culture dilution. The corresponding bacterial load in the spiked mucin sample as well as an estimate of the colony forming units (CFU) in the actual spiked viscous mucin sample is given in Table 3. These calculations were made from counting bacterial colonies on agar plates.

The concentration of *M. tuberculosis* bacteria in clinical sputum samples can vary from over 10^7 to less than 20 CFU ml⁻¹.²³ Though our present model is pig mucin spiked with *E. coli*, our longer-term goal is low cost, POC sample preparation for tuberculosis. We therefore compare our results with standards that are useful for culture-based tuberculosis diagnosis (10^1 – 10^3 bacilli ml⁻¹ of sputum). However, diagnosis of tuberculosis by culture method normally takes 8–12 weeks with additional time for disease subtyping in a national reference laboratory specialized for culturing tuberculosis bacilli from sputum samples. Added to this, culturing requires pretreatment of sputum. The fully automated Cepheid GeneXpert MTB/RIF protocol showed a 95% probability of detecting *M. tuberculosis* in samples containing a bacterial load of at least 131 CFU ml⁻¹ and was able to detect as few as 10 CFU ml⁻¹ in 35% of the samples^{22,24} with a raw sample to result time of less than 2 h.^{22,24} Our goal is to provide a very low cost, and yet effective means to molecular diagnosis that will make disease sub-typing an affordable reality in high disease burden, impoverished areas.

Our sample preparation method showed detection by molecular diagnosis for a bacterial load as low as 33 CFU of *E. coli* ml⁻¹ of raw mucin. This low cost, origami-based sample preparation method in combination with a portable NAAT-based system should yield a raw sample-to-result point-of-care diagnosis in less than 2 h.

Conclusions and future work

We have presented a low cost microfluidic origami device for viscous sample preparation leading to point-of-care (POC) molecular diagnosis. For this DNA extraction device, we set ourselves the following design constraints:

- 1) Tolerance to a viscous sample matrix (mucus or blood).
- 2) Access to intermediate device layers at different times during operation (in contrast to so-called programmable paper diagnostics¹²).
- 3) Ability to process raw samples in a POC setting (similar to other lab-on-paper approaches to sample preparation^{5,6}).
- 4) Dry reagent storage for cell lysis and penetrating a viscous sample matrix (similar to Guio's approach with FTA[®] cards⁵).
- 5) Raw-sample to DNA extraction time of about 1.5 h without the use of external power or within 1 h using an oven or heater block after the lysis and wash steps.
- 6) Addition of minimal and safe liquid reagents to the origami device to reduce chemical hazards during transport and handling (in contrast to the protocol described by Guio for the FTA[®] cards⁵ that requires the addition of a proprietary FTA[®] purification reagent and TE buffer, 10 mM Tris HCl, 0.1 mM EDTA pH 8.0, to the chemically impregnated lysis paper).
- 7) Low cost device made from paper, Mylar and adhesives.
- 8) Freedom from the need to interface with permanent electrical equipment (vortexer, centrifuge, controlled heater) or Proteinase K (a PCR inhibitor) normally used in NA extraction by commercial kits (e.g. Qiagen).

Our method offers the possibility of POC, room temperature, NA extraction, followed by room temperature storage of the extraction device for transport to more centralized diagnostic facilities. This will potentially reduce the biohazard concerns associated with the shipment of whole samples. Additionally it will eliminate the cost of the cold chain, and sample fixing in the absence of a portable PCR machine.

The fabrication and assembly of this microfluidic origami device takes less than 30 min and can be adapted for high volume production in the developing world without the expensive overhead of a semiconductor cleanroom or microfabrication laboratory facility—a typical environment for the fabrication of lab-on-a-chip devices. All materials used in the fabrication and in the formulation of the lysis buffer are commercially available. The current prototype produces about 150 µl of concentrated nucleic acid solution isolated from a raw sample, ready to be transferred manually to another instrument.

Our sample preparation method allowed detection by molecular amplification from a bacterial load as low as 33 CFU of *E. coli* per ml of mucin, which falls in the lower limit for culture-based diagnosis of Tuberculosis. This device holds promise for affordable, specific and sensitive POC detection of diseases like Tuberculosis, but we need to move from the *E. coli*-spiked porcine mucin model system to human sputum loaded with *M.*

tuberculosis, a much more refractory organism. We plan to approach this goal incrementally with the minimum of additional processes on or off the microfluidic origami device. Our origami based NA extraction device is designed to act as a low cost but yet effective front end to a portable NA amplification device. The design and working of the portable amplification and detection device is outside of the scope of this paper.

This particular microfluidic origami device is also being developed as a generic low cost, POC, nucleic acid extraction device for samples of varying viscosities (sputum-urine) and volumes (µl-ml) without the need of permanent electrical infrastructure. We envision that the next generation of microfluidic origami platforms will enable affordable molecular diagnosis and disease sub-typing in geographically dispersed regions with high disease burdens.

Acknowledgements

The authors would like to thank Prof. Patrick Stayton and Dr Richard To for use of the PCR machine, and for donating the transformed XL1-Blue *E. coli* strain and the primers for the plasmid amplification. We thank Dr Richard To, Dr Barry Lutz, Dr Elain Fu, Dr Paolo Spicar-Mihalic and Peter Kauffman for insightful discussions. The primers used in this work for genomic DNA amplification were from previous work done by the Yager group with Micronics, Inc. This work was supported in part by a gift from BigTec Labs, Bangalore, India to KFB and internal funding by the University of Washington to PY and KFB.

Notes and References

- 1 S. J. Sia and L. J. Kricka, *Lab Chip*, 2008, **8**, 1982–1983.
- 2 C.-M. Chenga, A. W. Matrinez, J. Gong, C. R. Mace, S. T. Phillips, E. Carrilho, K. A. Mirica and G. M. Whitesides, *Angew. Chem. Int. Ed.*, 2010, **49**, 4771–4774.
- 3 E. Fu, P. Kauffman, B. Lutz and P. Yager, *Sens. Actuators, B*, 2010, **149**, 325–328.
- 4 E. Fu, B. Lutz, P. Kauffman and P. Yager, *Lab Chip*, 2010, **10**, 918–920.
- 5 H. Guio, H. Okayama, Y. Ashino, H. Saitoh, P. Xiao, M. Miki, N. Yoshihara, S. Nakanowatari and T. Hattori, *Int. J. Tuberc. Lung Dis.*, 2006, **10**, 906–910.
- 6 S. R. Jangam, D. H. Yamada, S. M. McFall and D. M. Kelso, *J. Clin. Microbiol.*, 2009, **47**, 2363–2368.
- 7 P. Kauffman, E. Fu, B. Lutz and P. Yager, *Lab Chip*, 2010, **10**, 2614–2617.
- 8 A. W. Martinez, S. T. Phillips, M. J. Butte and G. M. Whitesides, *Angew. Chem., Int. Ed.*, 2007, **46**, 1318–1320.
- 9 A. W. Matrinez, S. T. Phillips, E. Carrilho, S. W. Thomas III, H. Sindi and G. M. Whitesides, *Anal. Chem.*, 2008, **80**, 3699–3707.
- 10 A. W. Matrinez, S. T. Phillips and G. M. Whitesides, *Proc. Natl. Acad. Sci. U. S. A.*, 2008, **105**, 19606–19611.
- 11 A. W. Martinez, S. T. Phillips, B. J. Wiley, M. Gupta and G. M. Whitesides, *Lab Chip*, 2008, **8**, 2146–2150.
- 12 A. W. Martinez, S. T. Phillips, N. Zhihong, C.-M. Cheng, E. Carrilho, B. J. Wiley and G. M. Whitesides, *Lab Chip*, 2010, **10**, 2499–2504.
- 13 J. L. Osborn, B. Lutz, E. Fu, P. Kauffman, D. Stevens and P. Yager, *Lab Chip*, 2010, **10**, 2659–2665.
- 14 N. Zhihong, F. Deiss, X. Liu, O. Akbulut and G. M. Whitesides, *Lab Chip*, 2010, **10**, 3163–3169.
- 15 C. J. Easley, J. M. Karlinsey, J. M. Beinvenue, L. A. Legendre, M. G. Roper, S. H. Feldman, M. A. Huges, E. L. Hewlett, T. J. Merkel, J. P. Ferrance and J. P. Landers, *Proc. Natl. Acad. Sci. U. S. A.*, 2006, **103**, 19272–19277.
- 16 S.-I. Han, K.-H. Han, A. B. Frazier, J. P. Ferrance and J. P. Landers, *Biomed. Microdevices*, 2009, **11**, 935–942.

- 17 J. W. Hong, V. Struder, G. Hang, W. F. Anderson and S. R. Quake, *Nat. Biotechnol.*, 2004, **22**, 435–439.
- 18 J. Kim, M. Johnson, P. Hill and B. K. Gale, *Integr. Biol.*, 2009, **1**, 574–586.
- 19 J. Min, J.-H. Kim, L. Youngsun, K. Namkoong, H.-C. Im, H.-N. Kim, H.-Y. Kim, N. Huh and Y.-R. Kim, *Lab Chip*, 2011, **11**, 259–265.
- 20 A. V. Govindarajan, S. Ramachandran, G. D. Vigil, P. Yager and K. F. Böhringer, presented at the 24th IEEE International Conference on Microelectromechanical Systems(IEEE MEMS'11), Cancun, Mexico, Jan 23–27, 2011, 932–935.
- 21 Cepheid, GeneXpert System, http://www.cepheid.com/media/files/brochures/GeneXpert%20Brochure_0112-04.pdf, accessed April 10 2011.
- 22 C. C. Boehme, P. Nabeta, D. Hillemann, M. P. Nicol, S. Shenai, F. Krapp, J. Allen, R. Tahirli, R. Blakemore, R. Rustomjee, A. Milovic, M. Jones, S. M. O'Brien, D. H. Persing, S. Ruesch-Gerdes, E. Gotuzzo, C. Rodrigues, D. Alland and M. D. Perkins, *N. Engl. J. Med.*, 2010, **63**, 1005–1015.
- 23 M. L. Joloba, J. L. Johnson, A. Namale, A. Morrissey, A. E. Assegghai, R. D. Mugerwa, J. J. Elner and K. D. Eisenach, *Int. J. Tuberc. Lung Dis.*, 2000, **4**, 528–536.
- 24 D. Helb, M. Jones, E. Story, C. Boheme, E. Wallace, K. Ho, J. Kop, H. R. Owens, R. Rodgers, P. Banada, H. Safi, R. Blakemore, N. T. Lan, E. C. Jones-Lopez, M. Levi, M. Burday, I. Ayakaka, R. D. Mugerwa, B. McMillan, E. Winn-Deen, L. Christel, P. Dailey, M. D. Perkins, D. H. Persing and D. Alland, *J. Clin. Microbiol.*, 2010, **48**, 229–237.

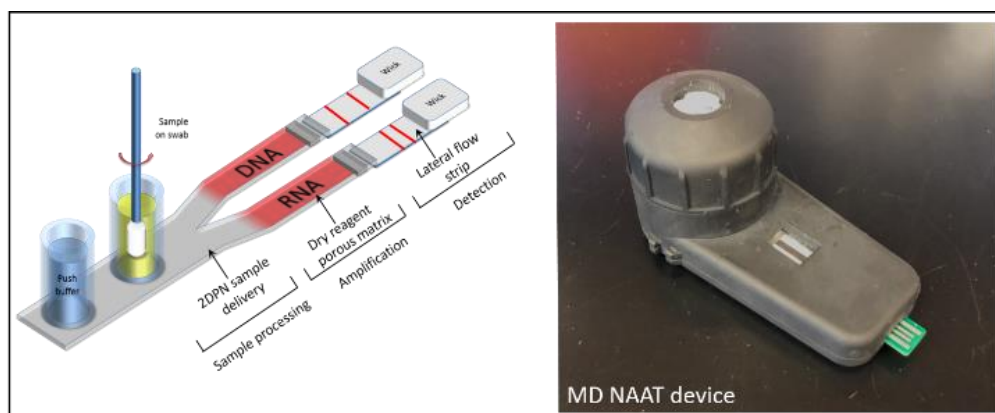
Chapter 5

5 Two-dimensional paper network for molecular diagnostics*

The following chapter is based on publication ¹⁴² in section 5.1 and a conference paper in section 5.2. The paper in 5.1 describes performing isothermal nucleic acid amplification (iSDA) ¹⁴³ (see **Appendix 11.3**) in porous matrices for DNA targets that can be easily incorporated into POC diagnostic devices. A long-term dry storage method of amplification reagents containing a polymerase and a nicking enzyme, four primers, dNTPs, and a buffer in a porous matrix is described. Reagents also included a capture probe and a streptavidin-Au label required for lateral flow (LF) detection after amplification, or a fluorescent probe used for real-time detection. The stability of the two enzymes, namely, nicking enzyme and polymerase, were independently studied with different sugar excipients. Two different ways to detect amplicons are described. 1) lateral flow detection with Au label (see **Appendix 11.4**) and 2) real-time fluorescence detection. Additional supporting material is given in **Appendix 11.2**.

The iSDA amplification method was embodied into an integrated 2DPN sample-to-result MAD NAAT device with onboard dry reagents for methicillin-resistant *Staphylococcus aureus* (MRSA) detection with real patient samples ¹⁴⁴ (see **Appendix 11.5**).

In section 5.2 a sample-to-result test for a Chlamydia target in the urine sample is demonstrated in a urinalysis system using an MD NAAT device with onboard dry reagents and operated by a pre-programmed USB-powered board with real-time fluorescence detection using a cellphone.



2DPN for nucleic acid amplification for POC

Figure courtesy Paul Yager

5.1 Long-term dry storage of enzyme-based reagents for isothermal nucleic acid amplification in a porous matrix for use in point-of-care diagnostic devices*

Sujatha Kumar, Ryan Gallagher, Josh Bishop, Enos Kline, Josh Buser, Lisa Lafleur, Kamal Shah, Barry Lutz, and Paul Yager

Reproduced from *Analyst*, 2020, 145, 6875-6886 with permission from the Royal Society of Chemistry.

I designed the experiment, conducted the work, and analyzed the data. Together with the other authors, I discussed the results, and I wrote the paper.

Cite this: *Analyst*, 2020, **145**, 6875

Long-term dry storage of enzyme-based reagents for isothermal nucleic acid amplification in a porous matrix for use in point-of-care diagnostic devices†

Sujatha Kumar, * Ryan Gallagher, Josh Bishop, Enos Kline, Joshua Buser, Lisa Lafleur, Kamal Shah, Barry Lutz and Paul Yager

Nucleic acid amplification test (NAAT)-based point-of-care (POC) devices are rapidly growing for use in low-resource settings. However, key challenges are the ability to store the enzyme-based reagents in dry form in the device and the long-term stability of those reagents at elevated temperatures, especially where ambient temperatures could be as high as 45 °C. Here, we describe a set of excipients including a combination of trehalose, polyethylene glycol and dextran, and a method for using them that allows long-term dry storage of enzyme-based reagents for an isothermal strand displacement amplification (iSDA) reaction in a porous matrix. Various porous materials, including nitrocellulose, cellulose, and glass fiber, were tested. Co-dried reagents for iSDA always included those that amplified the *ldh1* gene in *Staphylococcus aureus* (a polymerase and a nicking enzyme, 4 primers, dNTPs and a buffer). Reagents also either included a capture probe and a streptavidin-Au label required for lateral flow (LF) detection after amplification, or a fluorescent probe used for real-time detection. The reagents showed the best stability in a glass fiber matrix when stored in the presence of 10% trehalose and 2.5% dextran. The reagents were stable for over a year at ~22 °C as determined by lateral flow detection and gel electrophoresis. The reagents also exhibited excellent stability after 360 h at 45 °C; the assay still detected as few as 10 copies of *ldh1* gene target by lateral flow detection, and 50 copies with real-time fluorescence detection. These results demonstrate the potential for incorporation of amplification reagents in dry form in point-of-care devices for use in a wide range of settings.

Received 2nd June 2020,
Accepted 12th August 2020
DOI: 10.1039/d0an01098g
rsc.li/analyst

Introduction

Point-of-care (POC) devices that are accurate, robust, low cost, rapid, easy-to-use, equipment-free and disposable are in great demand for the diagnosis of diseases, especially in low-resource settings (LRS).^{1,2} However, the COVID-19 crisis has brought into sharp focus a great need to universally apply our tremendous gains in knowledge in molecular methods toward better POC diagnostics within the developed as well as developing worlds with high disease burden. Nucleic acid amplification tests (NAATs) are extremely sensitive methods for detecting DNA or RNA from pathogens and have relatively rapid turnaround times (getting results on the same day) compared to microbiological cultures or ELISA.^{3–8} Unfortunately, while NAATs aimed at POC for bacterial and viral infectious disease

diagnosis have been developed, they are instrumented and expensive because they either require thermal cycling and/or complicated optics for fluorescence readout.^{9–12} Examples of commercial POC instrumented diagnostic NAAT platforms include Cepheid GeneXpert, Abbott ID NOW, Credo Biomedical VitaPCR, Mesa Biotech Accula system, and Rapid Diagnostics Rapid MiniLab. They provide dry storage of reagents in cartridges, are rapid, and have high sensitivity but require trained users, need electricity, and are not affordable, limiting their use in low-resource settings.

There has been progress towards developing isothermal amplification systems in miniaturized microfluidic devices that are easy to use and suitable for LRS, but often at high prices and with varying levels of automation.^{13–16} A low-cost cartridge system with fluidic controls that executes isothermal amplification with lateral flow (LF) detection has recently been reported, but still requires a (portable) instrument.¹⁷ Paper fluidic devices have also been used for NAAT based testing as an inexpensive alternative to instrumented systems.^{18–20} All these systems, however, required fresh NAAT reagents to

Department of Bioengineering, University of Washington, 3720 15th Ave NE, Seattle, Washington, USA. E-mail: sujathar@uw.edu

† Electronic supplementary information (ESI) available: Fig. S1–S4. See DOI: 10.1039/d0an01098g

demonstrate the capability and did not address the dry storage of the reagents.

One of the key technical requirements for truly LRS-compatible NAAT-based POC systems is the ability to store dry reagents on the device. There are two main challenges. The first is the long-term stability of enzymes at elevated temperatures, especially for use in places where the ambient temperature could be as high as 45 °C. The most promising approach is to store all reagents except simple buffers in dry form in a way that limits exposure to oxygen. The subsequent challenge is uniform rehydration of the reagents within the device to achieve optimal performance. Overcoming these challenges would circumvent the need for the “cold chain” (continuous refrigeration from the point of manufacture to the point of use), which is inconvenient in any diagnostic product, and maybe too expensive and even unavailable in many LRS settings.

Methods for stabilizing proteins and enzymes in dry form using sugars and sugar alcohols are widely used in the pharmaceutical industry. The most common method of making solid proteins is lyophilization.²¹ Trehalose, a non-reducing disaccharide, can form protein-stabilizing glass and is the most common sugar used in the dry preservation of biomolecules.^{22–24} There have been a few reports on dry storage of PCR and isothermal amplification reagents, but they did not address long-term stability.^{25–30} A lyophilization method using Biolyph's patented technology for long-term dry storage for loop-mediated isothermal amplification was reported but did not include the primers.³¹ A direct blood dry LAMP system (CZC-LAMP) was applied to the diagnosis of malaria with different reagents dried separately in the lid and tube.³² In all the above studies, the dry reagents were in a tube, and the reactions carried out using an instrument. Short-term stability studies were reported for helicase dependent amplification (HDA) reagents in Whatman 1 chromatography paper stored at room temperature.³³ Similarly, reagents for isothermal reverse transcriptase recombinase polymerase amplification (RT-RPA) were freeze-dried onto cellulose pads and stored at room temperature.³⁴ Recently an autonomous microfluidic device with vitrified reverse transcription loop-mediated isothermal amplification reagents was reported with reagents stored dry up to three weeks at room temperature.³⁵ A sample-to-result integrated paper-based device with short-term reagent stability was also reported.³⁶ However, the stability of the reagents at elevated temperatures was not undertaken in any of these studies.

We previously reported successful long-term dry storage and stability of various reagents such as horseradish peroxidase (HRP)³⁷ and gold enhancement³⁸ reagents in a porous matrix and incorporated into an automated two-dimensional paper network (2DPN) fluidic devices for malarial antigen detection. An autonomous device with a combination of isothermal amplification and paper fluidics for NAAT with dry reagents stable at elevated temperatures holds great promise for an inexpensive POC diagnosis, especially for LRS settings. We reported an isothermal strand displacement amplification

(iSDA) method for a *Staphylococcus aureus* DNA target that uses two enzymes, namely a nicking enzyme and a polymerase, in combination with high specificity probes either for real-time fluorescence measurement or twin probes for lateral flow detection.³⁹ We have shown that speed, sensitivity, and specificity of iSDA make it a powerful method for point-of-care molecular diagnosis.

In this report, we describe a method for the long-term dry storage of the iSDA reagents, including probes with either a gold nanoparticle label for downstream lateral flow detection or a fluorescent probe for real-time detection in a porous matrix. The dry preservation of amplification reagents in a solid porous matrix could have high value for several applications with fluid connectivity especially in paper-based POC devices and applicable to low-resource settings, especially in hot climates where the ambient temperatures can be in the 40–45 °C range. We have also embodied this amplification method in an integrated 2-dimensional paper network (2DPN) sample-to-result device for methicillin resistant *Staphylococcus aureus* (MRSA) detection, the use of which could reduce the cost of diagnosis by eliminating the need for expensive instruments.⁴⁰

Experimental

Isothermal amplification in porous matrices

Porous matrices tested for iSDA compatibility included nitrocellulose FF80HP, cellulose CF5, Quartz QMA, Fusion 5, and Standard 17 Glass fiber (Std 17 GF). All these materials were purchased from GE Healthcare Life Sciences, Pittsburgh, PA. Each material was cut to size with a hole-puncher to hold 25 µl of fluid when saturated. Reagents specific for detection of the *Staphylococcus aureus ldh1* gene using iSDA (as noted in Toley *et al.*³⁹) contained 50 mM potassium phosphate buffer pH 7.6, 3.8 mM magnesium sulfate, 100 µM of each dNTP, 250 nM extension primer E1, 500 nM extension primer E2, 50 nM each of bumper primers B1 and B2, 8 units of WarmStart Bst 2.0 polymerase (New England Biolabs, Ipswich, MA) and 1.6 units of nicking enzyme Nt.BbvCI (New England Biolabs, Ipswich, MA). Primer and probe sequences for *ldh1* amplification have been previously published.³⁹

To test the compatibility of the porous matrices, about 20 µl of iSDA reagent solution containing 100 copies of purified methicillin-resistant *S. aureus* (MRSA) genomic DNA (ATCC, BAA-1556) was added to the different porous matrices; the porous matrix was placed in a Secure-Seal hybridization chamber (Electron Microscopy Sciences, Hatfield, PA). DNA solutions were replaced with pure water for no-template controls (NTCs) for each of the materials tested. The samples were incubated in a custom electric oven at 49 °C for 30 min, which has been shown to be sufficient for amplification of even single copies of the target sequence using iSDA (although a custom oven was used, any device capable of holding 49 °C for 30 min could be substituted). After amplification, the pads were placed in a 0.2 ml tube with a hole at the bottom, which

in turn was placed in a 0.5 ml tube, and centrifuged to collect the solution containing free amplicons. The amplicons were run on a gel electrophoresis system as described below.

Effect of leachates from porous matrices on iSDA

The effect of possible inhibitors contained in the leachates from the different matrices (listed in the previous section) on iSDA was tested. The materials were first incubated in clean water at 49 °C for 30 minutes and then centrifuged in a 0.45 μM filter spin column. The extracted fluid was used as a replacement for water in the iSDA reaction. The reactions were carried out in a tube in a thermocycler (CFX96, Bio-Rad Laboratories, Hercules, CA) with 100 copies of the MRSA genomic DNA. The amplicons were run on a gel electrophoresis system, as described below.

Lyophilization and long-term storage of iSDA and detection reagents

Several combinations of the formulation containing trehalose (Life Sciences Advanced Technologies, St Petersburg, FL), polyethylene glycol (PEG) (Hampton Research, Aliso Viejo, CA) and dextran (Sigma-Aldrich, St Louis, MO) were used for preservation of iSDA reagents (Table 1). The effect of the combinations of the excipients on the iSDA was first determined in a conventional tube reaction at 49 °C with MRSA genomic DNA using the thermal cycler. For lyophilization, the iSDA reagents specific to the *S. aureus* *ldh1* target were mixed with the different formulation given in Table 1. The mixtures also contained the lateral flow (LF) detection twin probes, including 10 nM of biotin probe (ELITechGroup, Bothell, WA) (5'-Biotin Phosphoramidite 10-5950-95, Glen Research, Sterling, Virginia, USA), and 20 nM of capture probe (ELITechGroup, Bothell, WA). We also included a 40 nm streptavidin-coated gold (Au) detection label (Innova Biosciences, Cambridge, UK) into the iSDA reagent mix by premixing one microliter of Au label (OD 10) with 10 nM of biotin detection probe for 5 min before adding to the iSDA reagents.

Standard 17 glass fiber (Std 17 GF) was laser-cut (VLS3.60, Universal Laser Systems, Scottsdale, AZ) to 20 mm × 5 mm strips having a fluid capacity of 40 μl. The Std 17 GF pads were incubated in 1% bovine serum albumin (BSA) containing 0.1% Tween 20 for one hour, drained of the solution, and dried overnight at 45 °C. An experimental setup for the lyophilization procedure is shown in ESI Fig. S1.† The BSA-coated Std 17 GF

pads were placed in a sterile 12-well polystyrene plate. The outer four wells contained a neodymium magnet. An aluminum plate with neodymium magnets embedded at the four corners was placed below the 12 well-plate, serving as a thermal mass to ensure the reagent pads in the well-plate remain frozen during lyophilization. The magnets held the aluminum and well plates together (ESI Fig. S1a†). About 35 μl of iSDA reagent containing Au label and the preservation mix was pipetted onto the pads. The entire apparatus, with samples loaded, was flash-frozen in liquid nitrogen, placed in a fast-freeze flask (Labconco, Kansas City, MO), and lyophilized overnight in a freeze-drying system (FreeZone 2.5 liter benchtop, Labconco, Kansas City, MO) operated at a temperature of -51 °C and vacuum pressure of 0.018 mbar (ESI Fig. S1b†). After lyophilization, each pad was individually transferred to 0.5 ml sterile tubes with a hole in the cap. Sets of four tubes along with 1 gram of silica desiccant (Delta Absorbents, Roselle, IL) were placed in a moisture barrier foil pouch (Ted Pella Inc., Redding, CA) and heat-sealed. The samples were stored at 22, 35, 40, or 45 °C for 360 h or stored at 22 °C for a year.

Amplification assay for iSDA preservation

The Std 17 GF pads containing the dry iSDA and detection reagents stored at varying temperatures for 360 h were taken out of dry storage and placed in a Secure-Seal hybridization chamber (Electron Microscopy Sciences, Hatfield, PA), rehydrated with 33 μl of water containing the MRSA genomic DNA template (10–200 copies) and incubated at 49 °C for 30 min in the aforementioned custom oven (ESI Fig. S1c†). For long-term storage study at 22 °C, the pads were periodically taken out of dry storage at 1, 2, 3, 6, and 12 months and iSDA performed with 100 copies of the genomic DNA template. After amplification, the pads were placed in a 0.2 ml tube with a hole at the bottom, which in turn was placed in a 0.5 ml tube and centrifuged to collect the amplicons and processed for lateral flow detection or gel electrophoresis.

Lateral flow detection of amplicons

Lateral flow detection of iSDA amplicons was by a twin probe method co-developed with our colleagues at ELITechGroup.³⁹ In short, a 3'-biotinylated detection probe hybridizes to the amplicon and binds a streptavidin-coated Au nanoparticle label. A chimeric pyranosyl DNA (pDNA)-DNA capture probe hybridizes by DNA independently to the amplicon and hybridizes by pDNA to an immobilized pDNA complement. A dipstick-style LF assay format was used for demonstrating the dry preservation of the iSDA reagents. Cardboard-backed nitrocellulose FF80HP (GE Healthcare, Waukesha, WI) striped with (1) a pDNA complement linked to T20 (twenty repeats of thymidine) and (2) a T20-biotin control line (provided by ELITechGroup, Bothell, WA), and attached to a cellulose wicking pad, was cut into ~5 mm-wide strips. For detection, 28 μl of the iSDA reaction mix containing amplicons was mixed with a solution of NaCl and Triton-X100 to give final concentrations of 0.6 M and 0.8%, respectively. The mixture

Table 1 List of preservation mix used for dry storage and stabilization of iSDA reagents

	Preservation mix for dry storage (w/v)
T	10% trehalose
TP	10% trehalose 1% PEG 8000
TD 70	10% trehalose 2.5% dextran (~70 kDa)
TD 500	10% trehalose 2.5% dextran (500 kDa)

was added into a 96-well deep well plate (VWR, Radnor, PA) and a detection strip placed into each well for 20 minutes. The LF strips were then imaged using the procedure described below.

Lateral flow image capture and quantification

Lateral flow strips were imaged wet using a flatbed scanner (Epson Perfection V700, CA, USA) in 48-bit RGB mode at a resolution of 600 dpi. The intensities in the region of interest (ROI) were quantified using ImageJ⁴¹ by measuring the mean green-channel intensity of each signal band and a background region within each strip. The assay signal was calculated as the background-subtracted intensity normalized to the full intensity range of the image.⁴²

Gel electrophoresis

PAGE analysis was conducted under denaturing conditions. A 2.2 μ L sample (from a 35 μ L reaction) was mixed with 6.8 μ L gel loading buffer II (Life Technologies, Carlsbad, CA) heated to 95 °C for 5 minutes, then kept on a cold block. About 7 μ L of this sample mix was loaded into pre-cast 15% Novex® TBE-Urea gels (Life Technologies). A 10 bp ladder (Life Technologies) was used as a marker. Electrophoresis was conducted in an XCell SureLock™ Mini-Cell Electrophoresis System (Life Technologies) at 160 volts for ~40 minutes using a 1 \times TBE running buffer. The electrophoresis cell was kept in a pre-warmed water bath at 70 °C to ensure that denaturing conditions were maintained throughout. After electrophoresis, gels were stained with 2 \times SYBR Gold® Nucleic Acid Gel Stain (Life Technologies) in 1 \times TBE for 20 minutes. Stained gels were imaged using a Gel Doc™ EZ System (Bio-Rad, Hercules, CA).

Real time fluorescence in porous matrix

An in-house method to monitor iSDA amplification in real time in the porous matrix was developed using a standard microplate reader (SpectraMax ID3, Molecular Device). Circular Std 17 GF pads with a fluid capacity of 13 μ L were laser cut to fit the wells of a black flat-bottomed 96 well plate (Greiner Bio-One). A minor-groove-binding (MGB) fluorescent Pleiades probe,⁴³ which has previously been described,³⁹ was used to monitor amplification in real time. In short, the DNA probe has fluorophore and a minor groove binder at the 5' end and a quencher at the 3' end. The fluorophore is quenched in the unbound state and fluoresces when hybridized to the target amplicon. About 200 nM red-emitting Pleiades probe (ELITechGroup, Bothell, WA) was mixed to the iSDA reagents with the excipients (Table 1) and added to the Std 17 GF pads placed in a black flat-bottomed 96 well-plate and lyophilized as previously described. The samples were stored at 22 or 45 °C for 360 h and reagents were rehydrated with water containing the MRSA genomic DNA (50–1000 copies). The well-plate was sealed with a PCR plate sealer (Bio-Rad, Hercules CA) and placed in the microplate reader set at 50 °C. Real-time kinetic measurement used the 593/650 nm excitation/emission setting, and fluorescence signals were acquired at 2-minute intervals.

Enzyme activity assay

The nicking enzyme Nt.BbvCI and WarmStart Bst polymerase 2.0 were separately lyophilized with the same formulations listed in Table 1, and tested for their activity after dry storage at different temperatures using enzyme-specific assays. The assays use reagent mixes of two components: an enzyme mix and a substrate/probe mix.

For the nicking enzyme activity assay, the 20 μ L enzyme mix contained 1.6 units of Nt.BbvCI, 100 μ M of each dNTPs, 50 mM potassium phosphate buffer pH 7.6, 3.75 mM magnesium sulfate, and one of the preservative mix (Table 1); and the 20 μ L substrate/probe mix contained 50 mM potassium phosphate buffer, the same preservative mix, and 188 nM substrate/probe. For this assay, the substrate/probe was a DNA hairpin labeled with a quencher and a fluorophore with a minor groove binder (MGB), provided courtesy of ELITechGroup. The substrate/probe mix, always freshly prepared, and enzyme mix, either freshly prepared or extracted from pads as described below, were added to alternating rows of a 96-well microplate. The plate was loaded onto a real-time thermal cycler (CFX96, Bio-Rad Laboratories, Hercules, CA) and equilibrated to 49 °C for 10 min. Each row of enzyme mixes was combined with the adjacent row of substrate/probe mixes using a twelve-channel pipette, and then the plate was immediately read for fluorescence in the FAM channel about every 17 s for ~25 min.

For the polymerase activity assay, the 20 μ L enzyme mix contained 8 units of WarmStart Bst 2.0 polymerase, 50 mM potassium phosphate buffer pH 7.6, 3.75 mM magnesium sulfate, and one of the preservative mix (Table 1); and the 40 μ L substrate/probe mix contained 50 mM potassium phosphate buffer pH 7.6, the same preservative mix, and 333 nM substrate, 333 μ M dNTPs, 1.25 μ M probes. For the polymerase activity assay, the substrate was a 90-nt, single-stranded DNA template (GCA CCG ATT TCC ACA GTT CTC CCG ACA CGC CCC TCA TAA ACA CAA TAC CAC CCA TTC ATT CCA AGC CAT ACC GAT TCC CAC AAA GCA TCT) with a 25-nt DNA primer (AGA TGC TTT GTG GGA ATC GGT ATG G), which were synthesized by Integrated DNA Technologies (Coralville, IA), and the probe was EvaGreen (Biotium). The substrate/probe mix was added to every other row of a 96-well microplate. The plate was loaded onto a real-time thermal cycler (CFX96, Bio-Rad Laboratories, Hercules, CA), and the template/primer substrate was annealed by heating to 95 °C for 2 min, then cooling to 25 °C. The enzyme was then added to interstitial rows, and the plate was equilibrated to 50 °C for 10 min. Each row of enzyme mixes was combined with the adjacent row of substrate/probe mixes using a twelve-channel pipette, and then the plate was immediately read for fluorescence in the FAM channel about every 22 s for ~25 min.

Enzyme mixes were either freshly prepared or rehydrated from lyophilized Std 17 pads with water and extracted by centrifugation in a 0.45 μ M filter spin column at 10 000g for 8 min. Enzyme activities were assayed in each preservative mix (Table 1); with fresh reagents, from pads with dry reagents on

the day of preparation; and from pads with dry storage at RT, 35 °C, 40 °C, and 45 °C after day 1 and day 15.

For the nicking activity assay, freshly prepared standard conditions used enzyme concentrations of 0 \times , 0.1 \times , 0.5 \times , 1.0 \times , and 2.0 \times the nominal amount of enzyme. For the polymerase activity assay, freshly prepared standard conditions used enzyme concentrations of 0 \times , 0.2 \times , 0.5 \times , 1.0 \times , and 2.0 \times the nominal amount of enzyme.

For analysis, a line was fit to the initial linear region of each curve while maintaining an R^2 value of greater than 0.985. The slope of this fit line was plotted vs. concentration to construct a k_{cat} vs. concentration calibration curve. A line was fitted to each data point in the same manner, and the slope was used to calculate the k_{cat} using the calibration curve. The 100% activity was determined by the calibration curve, which uses fresh reactions in the plate. The relative activity for each condition was calculated using three technical replicates, each from 5 dried pads.

Imaging of dried reagents in porous matrix

Std 17 GF pads containing iSDA reagents, 10% trehalose and 2.5% dextran and Au label were lyophilized as previously described. The lyophilized pads were set on a flatbed scanner (Epson Perfection V700, CA, USA) either dry or rehydrated with water, and scanned in 48-bit RGB mode at a resolution of 600 dpi.

For scanning electron microscopy, Std 17 GF pads with iSDA reagents containing 10% trehalose were either lyophilized or dried under vacuum using a centrifugal evaporator for 4 h (Genevac Inc., Gardiner, NY). All samples were Au/Pd sputtered (SPI Module Control, Structure Probe, Inc., West Chester, PA, USA) for 103 seconds, at a ~ 7 nm per minute deposition rate, leaving an estimated 12 nm Au/Pd coating. A FEI Sirion scanning electron microscope with a 5 kV beam and a spot size of 3 was used for imaging.

Results and discussion

The goal of this study was to develop a method for the long-term dry preservation of amplification reagents used in iSDA in a porous matrix that could be easily implemented in a POC NAAT platform for LRS settings. Porous materials were chosen as a matrix for drying the reagents since they are convenient to handle during drying and provided a format appropriate for integration with our 2D paper network-based POC MAD NAAT device, which has porous material connectivity for fluidic operations,⁴⁰ and a fluorescence-based MD NAAT device (Shah *et al.*, submitted). We included LF detection probes, and the Au-label in the iSDA reagent dry-down matrix itself, which could be applicable for an inexpensive colorimetric readout in POC device.⁴⁰ We also used real-time fluorescence kinetics as a tool to monitor iSDA performance after dry storage. Reagents for an iSDA reaction that targeted the *S. aureus ldh1* gene were selected for dry storage, and the limit of detection determined after rehydration.

We first tested iSDA assay compatibility with a variety of porous matrices. After the selection of a porous matrix, we tested a suitable drying and storage method. We then tested the stability of dry iSDA reagents, including the detection labels, in various preservation formulations by performing amplification in the porous matrix itself, followed by dipstick-style LF detection and gel electrophoresis. We also used a real-time fluorescence measurement in the porous matrix to assess the iSDA reagent stability. Furthermore, we separately tested the stability of the two enzymes (nicking enzyme and the polymerase) in dry storage in the porous matrix by using enzyme-specific activity assays. A range of temperatures of storage (22–45 °C) was studied for applicability to LRS, especially in hot climates where the ambient temperatures can be in the 40–45 °C range.

Porous matrix selection for iSDA assay

To select porous matrices that are compatible with iSDA, we first added the iSDA reagents directly to the native porous materials without any pre-treatment. We used a variety of porous matrices, including nitrocellulose (FF80), cellulose (CF5), quartz (QMA), Fusion 5, and Std 17 GF, and tested for the *ldh1* iSDA with 100 MRSA genomic copies in a custom oven. We found that, of this set, only Std 17 GF supported iSDA, and had sensitivity comparable to in-tube assay, as seen by gel electrophoresis (Fig. 1a). The target amplification products (100 and 120 bp) and the primer-dimer side products, as seen on the gel, are an indication of a successful iSDA. The other materials (nitrocellulose, cellulose, Fusion 5, and quartz) inhibited iSDA, as neither the *ldh1*-specific products nor the inevitable primer-dimer side products could be seen on the gel. We speculated two reasons for the failure of amplification in these materials; (1) that the materials had assay inhibiting compounds, or (2) the interaction of the enzymes with the surface of the materials rendered them inactive. To investigate the failure of amplification with those matrices, we tested the leachate from incubation of these materials in water in an in-tube iSDA with 100 MRSA genomic copies. We found that the leachate from the nitrocellulose, cellulose, and Fusion 5 significantly inhibited the assay, as seen by the very faint product-specific bands, compared to the strong control bands in the condition with clean water (Fig. 1b). Interestingly, for the quartz material, the leachate did not inhibit iSDA in the in-tube assay (Fig. 1b) compared to the in-material testing in Fig. 1a, possibly indicating that the surface of the quartz material inactivated or immobilized some or all of the reagents. These porous materials could support iSDA after washing away the inhibitors and/or blocking surfaces with protein coating, although we did not pursue these efforts. We used Std 17 GF as our material of choice for all the reagent dry storage studies.

Dry storage of iSDA reagents

Several formulations of preservatives involving combinations of trehalose, PEG, and dextrans (Table 1) were considered for stabilizing the iSDA reagents for dry storage. It was assumed

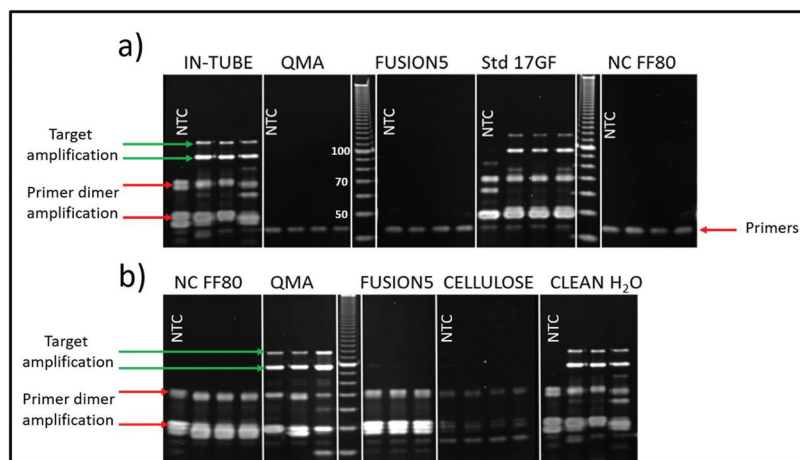


Fig. 1 (a) Denaturing PAGE image showing products of the *ldh1* iSDA assay in a few selected porous materials. Only Std 17 GF showed the targeted amplification product bands at ~100 and 120 nucleotides (green arrow) comparable to the assay as performed in-tube (conventional polypropylene tube). The inevitable primer dimer side products are indicated with a red arrow. Quartz (QMA), nitrocellulose (NC-FF80), and Fusion 5 totally inhibited amplification, including the primer-dimer side reactions. (b) Gel image showing the effect of leachate from porous materials on iSDA as performed in a tube. Leachate from NC-FF80, Fusion 5, and cellulose significantly inhibited iSDA as seen by very faint product-specific products, whereas the leachate from QMA did not affect the iSDA assay.

that the most unstable components of the amplification “master mix” would be the proteins: the nicking enzyme and the polymerase. The preservative formulations were initially tested for any adverse effect on iSDA by real-time amplification using a red-emitting fluorescent target-specific MGB probe in an in-tube assay with fresh reagents. The lift-off time of the reaction and the fluorescence levels serve as an indication of the performance of iSDA.³⁹ In the literature, PEG and dextran have been reported to act as crowding agents that enhance loop-mediated isothermal amplification (LAMP)^{44,45} and also to provide protein stabilization by volume exclusion.⁴⁶ We found that neither trehalose alone, nor in combination with moderate concentrations of the polymers, dextran and PEG, had any negative effect on iSDA when tested at 250 input copies of MRSA genomic DNA (Fig. 2). The lift-off time of the reaction (~7 minutes) and the fluorescence levels were comparable to the control sample without preservatives.

Next, we developed a freeze-drying method to store all the iSDA reagents in a Std 17 GF porous matrix. In addition, we were able to include the target-specific detection probes and the streptavidin-coated Au label into the iSDA reagent mix itself. The iSDA reagents, the detection probes, and the Au label in various preservation formulations (Table 1) were lyophilized in 5 mm × 20 mm Std 17 GF pads and stored at a range of temperatures (22–45 °C) for 360 hours. The pads were rehydrated, and iSDA assay performed within the matrix with 100 copies of MRSA genomic DNA followed by dip-stick style LF detection. The lateral flow detection of the iSDA amplicons was by a twin probe method co-developed with our colleagues at ELITechGroup and previously published.³⁹ In this paper, we used Au label instead of the blue latex beads for colorimetric detection. In this LF detection method, the twin probes hybridize with the amplicon and are captured by the test line *via* the complementary pDNA on the nitrocellulose. Any free probe

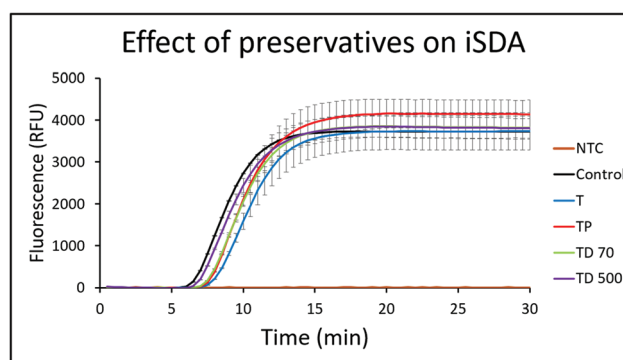


Fig. 2 Effect of combinations of preservatives on *ldh1* iSDA with 250 copies of MRSA genomic DNA measured by real-time fluorescence using the target-specific probe. The control sample was without any preservatives. Curves are mean of 3 replicates, and error bars are standard deviation. The preservatives did not have any negative effect on iSDA. The lift-off times of the reactions were nearly identical (~7 min), and the peak fluorescence levels were similar for all the formulations (T = 10% trehalose, TP = 10% trehalose + 1% PEG, TD70 = 10% trehalose + 2.5% dextran (~70 kDa), TD500 = 10% trehalose + 2.5% dextran (500 kDa) and NTC was a no-template control).

will flow downstream and bind to a biotin control line *via* streptavidin on the Au label.

An example of an LF detection strip with either a strong, medium, weak or negative amplification signal at the test line for the dry storage conditions with 100 genomic copy numbers is shown in Fig. 3a. Under the condition of the biotin probe and the streptavidin-Au label concentrations we used, a robust amplification gave us an intense test line signal with a very weak control line, and a negative amplification showed only an intense control line. Based on the stability of the iSDA reagents in different dry storage conditions, we saw a range of varying

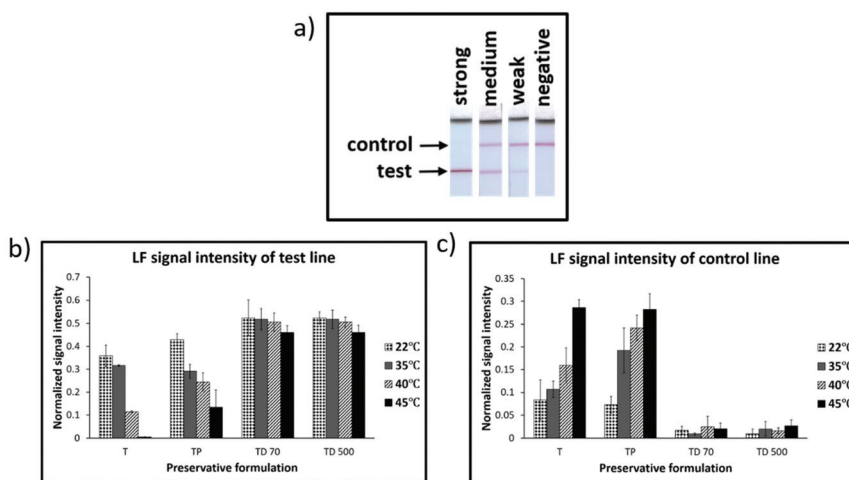


Fig. 3 Performance of *ldh1* iSDA of reagents stored dry in Std 17 GF for 360 h with different preservative formulations (Table 1), and range of temperatures. (a) Example of images of lateral flow (LF) detection strips showing strong, medium, weak, and negative amplification signal for *ldh1* iSDA with 100 genomic copies. (b) and (c) Normalized intensities of LF test line and control line, respectively. Excellent stability was achieved for formulations that contained both trehalose and dextran (TD 70 and TD 500), and at all temperatures of storage as indicated by strong signal intensities for the test line and a weaker control line. With trehalose alone (T), target amplification failed with storage at 45 °C, and amplification was weaker for 22, 35, and 40 °C (when compared to TD 70 and TD 500) as indicated by weaker signal intensity for the test line and stronger intensity for the control lines. Samples with both trehalose and PEG (TP) performed only slightly better than trehalose alone.

intensities for the test and the control line in an inverse relationship.

The signal intensities for the test and control line were measured for all conditions of dry storage (Fig. 3b and c). For formulations in which both trehalose and dextran were included, excellent stability was achieved at all temperatures of storage, including 45 °C, as indicated by strong signal intensities of the test line and a very weak control line. The test line signal intensity was comparable to iSDA with a fresh reagent for the 100 genomic copy number (ESI Fig. S2†). With trehalose alone, target amplification failed for storage at 45 °C, and amplification was weaker for 22, 35, and 40 °C (when compared to samples with trehalose and dextran) as indicated by weaker signal intensity for the test line and stronger intensity for the control lines. Samples with both trehalose and PEG performed only slightly better than trehalose. This inverse relationship of the control and test line intensities served as a qualitative measure for screening for iSDA reagent stability under different storage conditions. A similar relationship was seen when a LOD for *ldh1* iSDA using fresh reagents was performed with varying genomic copy numbers (ESI Fig. S2b†). At lower copy numbers, the signal intensity of the control line is stronger than the test line, and *vice versa* with increasing copy number. While the method for LF detection is very robust and sensitive, it gives us only a qualitative measure of reagent stability. Testing the stability of the reagents with real-time kinetics in terms of lift-off time and fluorescence levels gave us more quantitative results without the influence of excipients in lateral flow detection.

We included a target-specific red-emitting fluorescent probe instead of LF probes to monitor iSDA in real time after rehydration in the porous matrix using a plate reader to

compare the performance of different formulations at 22 °C and 45 °C storage. We found that the lift-off time of the iSDA assay for almost all conditions was within 15–18 minutes and comparable to fresh reagents in the porous matrix using 250 copies of MRSA genomic DNA (Fig. 4).

The peak fluorescence levels, however, varied for different formulations with the highest signal for formulations with trehalose and dextran. The trehalose only formulation did not amplify at 45 °C storage and performed poorly at 22 °C. Our results with fluorescence measurement directly matched the LF detection data presented in Fig. 3 for the formulations used for dry storage of iSDA reagents.

Interestingly, the peak fluorescence levels for dry stored conditions, especially for TP TD 70 and TD 500 (Fig. 4b and c), were higher than for iSDA with fresh reagents (Fig. 4a) in the porous matrix. We believe that this is due to non-uniform rehydration of reagents in the porous matrix, causing a concentration gradient. As a result, some areas in the matrix might have had robust amplification resulting in higher fluorescence measured locally, compared to the fresh reagents which are homogenous throughout the matrix. The result also agrees with additional unpublished data which suggests that the iSDA reaction is tolerant of a wide concentration range (0.5×–2.5× fold). While we do not get the spatial information of the amplification using the plate reader, support for this hypothesis has been addressed by fluorescence imaging in a submitted publication (Shah *et al.*).

Based on these results, we conclude that the addition of dextran to trehalose preserved the iSDA reagents better than other formulations at elevated temperatures in the Std 17 GF. In the literature, dextran has been reported to provide protein stability during freeze-drying.⁴⁷

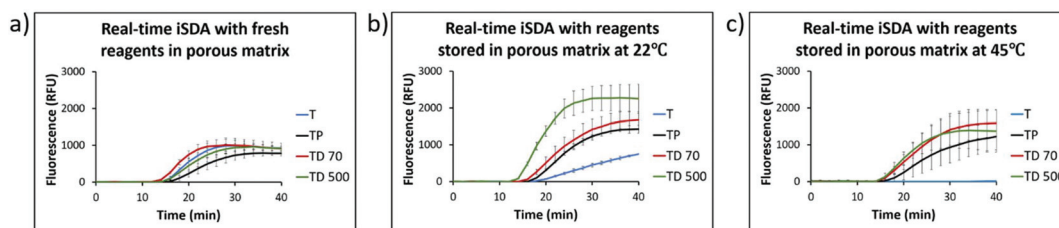


Fig. 4 Real-time fluorescence of iSDA in Std 17 GF for the *ldh1* target measured by plate-reader after rehydration in the porous matrix with different preservative formulations stored for 360 h. (a) With fresh reagents (b) with reagents stored at 22 °C and (c) with reagents stored at 45 °C. Curves are mean of 3 replicates, and error bars are standard deviation. The lift-off time of the reaction was within 15–18 minutes for all combinations of the preservatives. The peak fluorescence levels varied for different formulations with the highest signal for the formulation with trehalose and dextran. Trehalose only formulation did not amplify at 45 °C and performed poorly at 22 °C (T = 10% trehalose, TP = 10% trehalose + 1% PEG, TD70 = 10% trehalose + 2.5% dextran (~70 kDa), TD500 = 10% trehalose + 2.5% dextran (500 kDa)).

Enzyme activity

Another way to address the performance of iSDA at different storage conditions is to assess the stability of the two enzymes individually because they are likely the components of the amplification mixture most vulnerable to degradation. We, therefore, stored the nicking and the polymerase enzymes separately in Std 17 GF porous matrix under the same dry storage conditions as the iSDA reagents and used enzyme-specific assays to test the stability.

The results of the enzyme activity assays are shown in Fig. 5. The activity of polymerase does not appear to decrease appreciably over storage temperatures for all formulations except trehalose + PEG. The activity of the nicking enzyme does appear to decrease significantly over time at elevated temperatures. PEG was observed to be an overall detriment to storage for enzymes. The preservation of polymerase activity at 45 °C over time was expected as the optimal working tempera-

ture for the enzyme is listed as 65 °C. Loss of nicking enzyme activity during storage at 45 °C appears the likely candidate for the decrease of performance of iSDA over time. The decrease in activity at the elevated temperature over time of nicking enzyme was expected because the reported optimal temperature of the enzyme is 37 °C.

Limit of detection with dry stored iSDA reagents

Next, the limit of detection (LOD) for the iSDA reagents stored dry in Std 17 GF at 22 °C and 45 °C for 360 h with various formulations was determined by LF detection. From the LOD with fresh iSDA reagents (ESI Fig. S2a†), we determined that the linear range of the normalized signal intensity of the test line was below 100 copies. We, therefore, tested the *ldh1* iSDA performance in the range of 10–200 genomic copies for all the formulations stored at 22 °C and 45 °C. The normalized test line signal intensities for varying copy numbers are given in

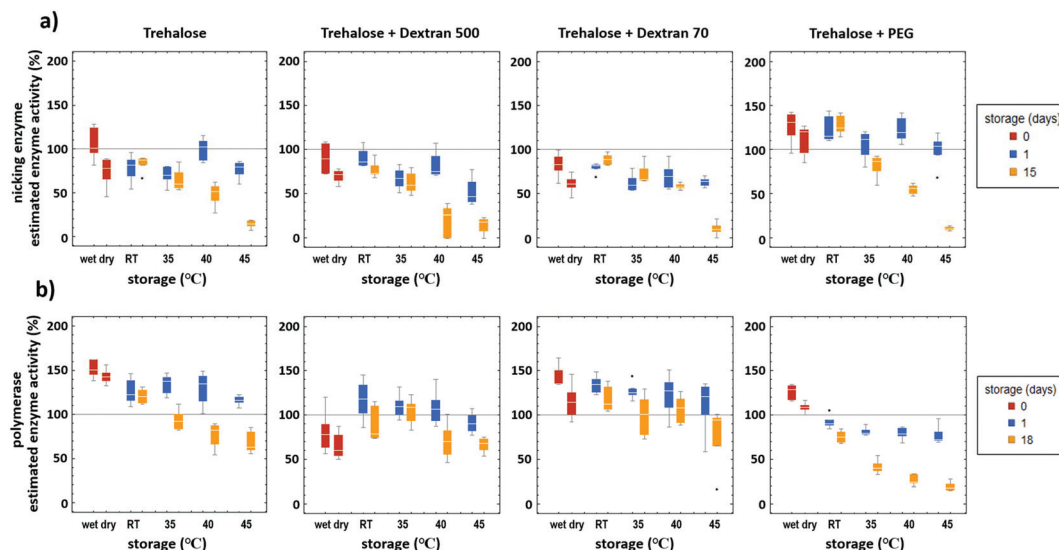


Fig. 5 Enzyme activity after dry storage in Std 17 GF with different preservation formulations (Table 1) and temperatures. The results are mean of 5 replicates, and error bars are standard deviation. (a) Nicking enzyme assay showed decreased activity at elevated temperatures of storage after 15 days. (b) Polymerase activity does not seem to decrease appreciably over storage temperatures except for formulation with trehalose and PEG. PEG was overall detrimental to the storage of both the enzymes.

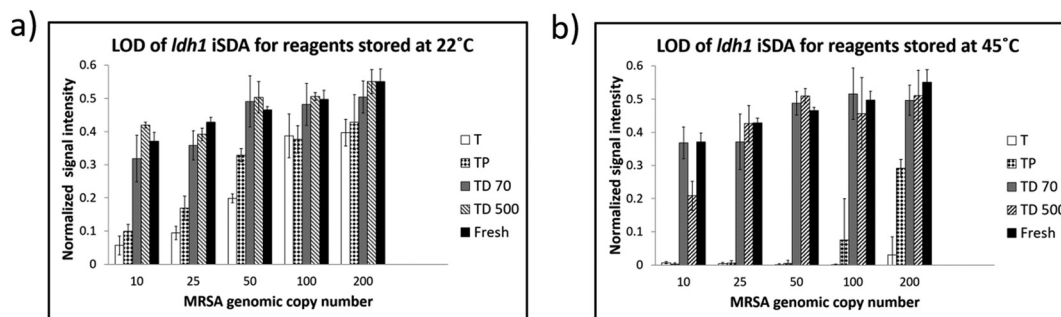


Fig. 6 LOD of *ldh1* iSDA with reagents stored dry in Std 17 GF at 22 °C and 45 °C for 360 h in different formulations of the preservatives. (a) Normalized intensity of the LF strip test line for samples stored at 22 °C. Samples with trehalose and dextran (TD 70 & TD 500) in the iSDA mix showed excellent stability down to 10 genomic copies. Samples with either trehalose only (T) or trehalose and PEG (TP) in the iSDA mix had diminishing signal intensity with decreasing genomic copy numbers. (b) Normalized intensity of the LF strip test line for samples stored at 45 °C. Excellent stability down to 10 copies was achieved for samples with trehalose and dextran (TD 70 & TD 500), whereas samples with trehalose (T) only or trehalose and PEG (TP) showed poor stability.

Fig. 6. We found that the samples stored in the presence of both trehalose and dextran showed excellent stability down to 10 copies of genomic DNA for both at 22 °C and 45 °C and comparable to fresh reagents (ESI Fig S2a†). For samples with trehalose only, or with trehalose and PEG, the test line signal intensities were lower below 50 genomic copies at 22 °C storage compared to TD 70 and TD 500 (Fig. 6a), and near zero for samples stored at 45 °C indicating poor stability (Fig. 6b).

We also tested the LOD for the *ldh1* iSDA by real-time fluorescence for the reagents stored in Std 17 GF with both trehalose and dextran (TD 500) at 22 °C and 45 °C for 360 h. We found that the lift-off time for all copy numbers (50–1000) was ~15 min (ESI Fig. S3†). The fluorescence peak intensities were a little higher for samples stored at 22 °C than 45 °C indicating slightly lower amplification efficiency at the higher storage temperature.

Long-term stability of iSDA reagents

To study the long-term stability in dry storage, the iSDA reagent mix and the Au label with 10% trehalose and 2.5% dextran (~70 kDa) were stored in Std 17 GF at room temperature (~22 °C) for one year. They were periodically tested by performing iSDA assay within the porous matrix with 100 copies of MRSA genomic DNA, and the amplicons detected by LF and gel electrophoresis. We found excellent stability of the iSDA reagents after one year of dry storage by LF detection and by gel electrophoresis (Fig. 7). The test line signal intensities on the LF strips were comparable to those with fresh reagents.

Our method of dry storage of isothermal amplification reagents in the porous matrix has several useful features. First, reagents stored in a glass fiber pad can be easily implemented for several applications with porous material fluid connectivity, especially in paper-based POC integrated systems. An image of the Std 17 GF pad with iSDA reagents lyophilized in the presence of 10% trehalose and 2.5% dextran before and after rehydration is shown in ESI Fig. S4a.† The glass fiber provides physical support during lyophilization, allowing passive spreading of the reagents across the matrix that allows rehy-

dration and amplification function without excessive variation in reagent concentration throughout the volume of the pad. We also compared scanning electron micrographs of reagents dried in Std 17 GF in the presence of 10% trehalose, either by vacuum drying or by lyophilization. In the lyophilized sample, the reagents migrate to the small features of the Std 17 GF and appear as dry sheets stretched across the void with high surface-area-to-volume ratio compared to the vacuum dried samples, where reagents appear as large clumps (ESI Fig. S4b†). Differences in freezing rate, handling time, vacuum, and time-temperature profiles could all contribute to the differential distribution of the reagents once dry. These two different drying conditions could be expected to perform differently in both how well reagents are preserved, along with how the dry structures enable imbibition and eventual dissolution once wet. We observed differences in wetting: the lyophilized pads tended to wet faster and more uniformly than the vacuum-dried pads (data not shown).

Second, we included all the detection reagents, including LF probes and Au label, with the amplification reagents mix for dry storage. This is an advantage when implemented in an inexpensive POC device with colorimetric LF readout, as it alleviates the need to store the detection label separately, and the complexity necessitated by subsequent rehydration and mixing detection chemistry with the amplicon.

Third, we were also able to include the target-specific fluorescent probe in the dry pads in our study: this facilitates real-time fluorescence imaging of amplification using mobile phone in POC integrated systems (Shah *et al.*, submitted). One potential disadvantage of our method is that scale-up requires creation of a specialized production facility for a specialized lyophilization procedure for the dry pads.

This method of dry storage of iSDA reagents along with the LF detection probes in the same mix has been incorporated into a sample-to-result instrument-free MAD NAAT device for the detection of MRSA from nasal swabs.⁴⁰ A modification of this device with a USB-powered printed circuit board, the MD NAAT device, with dry reagents including fluorescence detec-

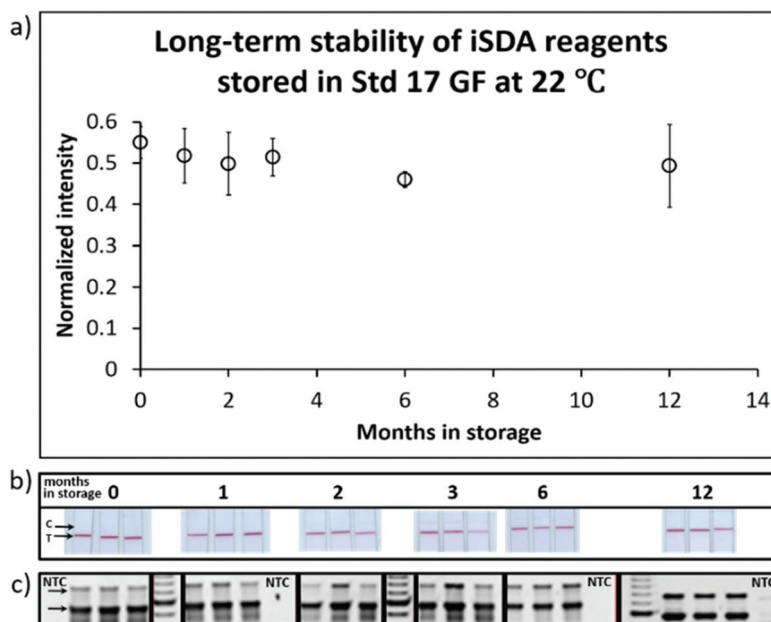


Fig. 7 Long-term iSDA reagent stability in the Std 17 GF. (a) Normalized intensity of the LF test line after dry storage at 22 °C at different times. (b) Images of lateral flow detection strips at various time points. "C" indicates the control line, and "T" is the test line for *ldh1* assay on the detection strips. (c) Corresponding gel images of the *ldh1* amplicon products (indicated by arrow) at various time points. NTC is no template control. The iSDA reagents in the presence of 10% trehalose and 2.5% dextran performed well after 12 months of dry storage, with signal intensities similar to that observed with fresh reagents.

tion with mobile phone imaging has been described in a submitted publication (Shah *et al.*). Our future publications will describe our progress in adapting this dry-down method to include reverse transcriptase for isothermal amplification methods for detection of RNA viruses such as SARS-CoV-2.

Conclusions

We developed a method for dry preservation of all reagents necessary for iSDA amplification and detection of DNA targets in a porous matrix. The reagents also included either fluorescence probes or Au-label probes for detection, thus eliminating the need to store them separately. We showed that the iSDA reagents retained a high level of activity after dry storage in a glass fiber matrix with trehalose and dextran at temperatures up to 45 °C. Lateral flow readout of iSDA produced consistently detectable colorimetric signals at 10 copies or above (visual readout by eye or by scanner), while fluorescence readout was reliably measurable at 50 copies or greater (fluorescence measurement in a plate reader). We demonstrated long-term stability of reagents up to one year at 22 °C. Our method for drying the reagents onto a glass fiber pad has the benefit of easy incorporation into POC devices, including conventional microfluidic or paper-based devices, especially in places where the ambient temperatures are in the 40–45 °C range. Further, we have demonstrated iSDA in a fully integrated 2DPN MAD NAAT device with dry reagents and successfully validated with real patient samples.⁴⁰ Dry preservation of amplification reagents in porous matrices

could be used for a variety of applications and has particular advantages for use in POC devices with LF detection or real-time fluorescence readout, portability, and ease-of-use in low resource settings.

Conflicts of interest

As of the date of this publication, Paul Yager has a nonpaying appointment as CSO of the UbiDX corporation. This work was performed before his association with the company.

Acknowledgements

Support for this project was provided through funding from DARPA DSO grant number HR0011-11-2-0007. We wish to acknowledge ELITechGroup, for collaboration on this grant and providing us with the iSDA assay reagents and probes, and their twin probe lateral flow detection technology. The authors thank Peter Kaufman for building the custom electric oven. SEM imaging and sputter coating work was performed at the University of Washington Nanotech User Facility (NTUF), a member of the NSF-sponsored National Nanotechnology Infrastructure Network (NNIN).

References

- 1 P. Yager, G. J. Domingo and J. Gerdes, *Annu. Rev. Biomed. Eng.*, 2008, **10**, 107–144.

- 2 R. Derda, J. Gitaka, C. M. Klapperich, C. R. Mace, A. A. Kumar, M. Lieberman, J. C. Linnes, J. Jores, J. Nasimolo, J. Ndung'u, E. Taracha, A. Weaver, D. B. Weibel, T. M. Kariuki and P. Yager, *PLoS Neglected Trop. Dis.*, 2015, **9**(5), e0003676.
- 3 E. A. Mothershed and A. M. Whitney, *Clin. Chim. Acta*, 2006, **363**(1–2), 206–220.
- 4 J. Ince and A. McNally, *Expert Rev. Med. Devices*, 2009, **6**(6), 641–651.
- 5 J. B. Mahony, *Clin. Microbiol. Rev.*, 2008, **21**(4), 716–747.
- 6 Y. Mori, H. Kanda and T. Notomi, *J. Infect. Chemother.*, 2013, **19**(3), 404–411.
- 7 O. Piepenburg, C. H. Williams, D. L. Stemple and N. A. Armes, *PLoS Biol.*, 2006, **4**(7), e204.
- 8 G. T. Walker, M. S. Fraiser, J. L. Schram, M. C. Little, J. G. Nadeau and D. P. Malinowski, *Nucleic Acids Res.*, 1992, **20**(7), 1691–1696.
- 9 D. Helb, M. Jones, E. Story, C. Boehme, E. Wallace, K. Ho, J. Kop, M. R. Owens, R. Rodgers, P. Banada, H. Safi, R. Blakemore, N. T. Ngoc Lan, E. C. Jones-López, M. Levi, M. Burday, I. Ayakaka, R. D. Mugerwa, B. McMillan, E. Winn-Deen, L. Christel, P. Dailey, M. D. Perkins, D. H. Persing and D. Alland, *J. Clin. Microbiol.*, 2010, **48**(1), 229–237.
- 10 S. Tanriverdi, L. Chen and S. Chen, *J. Infect. Dis.*, 2010, **201**(1), S52–S58.
- 11 A. V. Ritchie, I. Ushiro-Lumb, D. Edemaga, H. A. Joshi, A. De Ruyter, E. Szumilin, I. Jendrulek, M. McGuire, N. Goel, P. I. Sharma, J. P. Allain and H. H. Lee, *J. Clin. Microbiol.*, 2014, **52**(9), 3377–3383.
- 12 S. T. Douthwaite, C. Walker, E. J. Adams, C. Mak, A. V. Ortiz, N. Martinez-Alier and S. D. Goldenberg, *J. Clin. Microbiol.*, 2016, **54**(1), 212–215.
- 13 A. Niemz, T. M. Ferguson and D. S. Boyle, *Trends Biotechnol.*, 2011, **29**(5), 240–250.
- 14 P. J. Asiello and A. J. Baeumner, *Lab Chip*, 2011, **11**, 1420–1430.
- 15 M. Mahalanabis, J. Do, H. Almuayad, J. Y. Zhang and C. M. Klapperich, *Biomed. Microdevices*, 2010, **12**(2), 353–359.
- 16 C. H. Wang, K. Y. Lien, T. Y. Wang, T. Y. Chen and G. Bin Lee, *Biosens. Bioelectron.*, 2011, **26**(5), 2045–2052.
- 17 K. Roskos, A. I. Hickerson, H. W. Lu, T. M. Ferguson, D. N. Shinde, Y. Klaue and A. Niemz, *PLoS One*, 2013, **8**(7), e69355.
- 18 L. Magro, C. Escadafal, P. Garneret, B. Jacquelin, A. Kwasiborski, J. C. Manuguerra, F. Monti, A. Sakuntabhai, J. Vanhomwegen, P. Lafaye and P. Tabeling, *Lab Chip*, 2017, **17**(14), 2347–2371.
- 19 J. R. Choi, J. Hu, R. Tang, Y. Gong, S. Feng, H. Ren, T. Wen, X. J. Li, W. A. Bakar, B. Pingguan-Murphy and F. Xu, *Lab Chip*, 2016, **16**, 611–621.
- 20 N. M. Rodriguez, W. S. Wong, L. Liu, R. Dewar and C. M. Klapperich, *Lab Chip*, 2016, **16**(4), 753–763.
- 21 W. Wang, *Int. J. Pharm.*, 2000, **203**(1–2), 1–60.
- 22 L. M. Crowe, D. S. Reid and J. H. Crowe, *Biophys. J.*, 1996, **71**(4), 2087–2093.
- 23 M. F. Mazzobre, M. D. P. Buera and J. Chirife, *Biotechnol. Prog.*, 1997, **13**(2), 195–199.
- 24 S. Ohtake and Y. J. Wang, *J. Pharm. Sci.*, 2011, **100**(6), 2020–2053.
- 25 S. Lutz, P. Weber, M. Focke, B. Faltin, J. Hoffmann, C. Müller, D. Mark, G. Roth, P. Munday, N. Armes, O. Piepenburg, R. Zengerle and F. Von Stetten, *Lab Chip*, 2010, **10**(7), 887–893.
- 26 H. Al-Talib, C. Y. Yean, A. Al-Khateeb, H. Hasan and M. Ravichandran, *J. Microbiol., Immunol. Infect.*, 2014, **47**(6), 484–490.
- 27 A. L. Chua, H. T. Elina, B. H. Lim, C. Y. Yean, M. Ravichandran and P. Lalitha, *J. Med. Microbiol.*, 2011, **60**(4), 481–485.
- 28 S. Qu, Q. Shi, L. Zhou, Z. Guo, D. Zhou, J. Zhai and R. Yang, *PLoS Neglected Trop. Dis.*, 2010, **4**(3), e629.
- 29 J. Bell, A. Bonner, D. M. Cohen, R. Birkhahn, R. Yogev, W. Triner, J. Cohen, E. Palavecino and R. Selvarangan, *J. Clin. Virol.*, 2014, **61**(1), 81–86.
- 30 G. Y. Ang, C. Y. Yu, K. G. Chan, K. K. B. Singh and Y. C. Yean, *J. Microbiol. Methods*, 2015, **118**, 99–105.
- 31 Y. Chander, J. Koelbl, J. Puckett, M. J. Moser, A. J. Klingele, M. R. Liles, A. Carrias, D. A. Mead and T. W. Schoenfeld, *Front. Microbiol.*, 2014, **5**, 395.
- 32 K. Hayashida, K. Kajino, H. Simukoko, M. Simuunza, J. Ndebe, A. Chota, B. Namangala and C. Sugimoto, *Parasites Vectors*, 2017, **10**, 26.
- 33 P. Shetty, D. Ghosh, M. Singh, A. Tripathi and D. Paul, *RSC Adv.*, 2016, **6**, 56205–56212.
- 34 L. Magro, B. Jacquelin, C. Escadafal, P. Garneret, A. Kwasiborski, J. C. Manuguerra, F. Monti, A. Sakuntabhai, J. Vanhomwegen, P. Lafaye and P. Tabeling, *Sci. Rep.*, 2017, **7**(1), 1347.
- 35 E. A. Phillips, T. J. Moehling, K. F. K. Ejendal, O. S. Hoilett, K. M. Byers, L. A. Basing, L. A. Jankowski, J. B. Bennett, L. K. Lin, L. A. Stanciu and J. C. Linnes, *Lab Chip*, 2019, **19**, 3375–3386.
- 36 R. Tang, H. Yang, Y. Gong, M. L. You, Z. Liu, J. R. Choi, T. Wen, Z. Qu, Q. Mei and F. Xu, *Lab Chip*, 2017, **17**, 1270–1279.
- 37 S. Ramachandran, E. Fu, B. Lutz and P. Yager, *Analyst*, 2014, **139**(6), 1456–1462.
- 38 E. Fu, T. Liang, P. Spicar-Mihalic, J. Houghtaling, S. Ramachandran and P. Yager, *Anal. Chem.*, 2012, **84**(10), 4574–4579.
- 39 B. J. Toley, I. Covelli, Y. Belousov, S. Ramachandran, E. Kline, N. Scarr, N. Vermeulen, W. Mahoney, B. R. Lutz and P. Yager, *Analyst*, 2015, **140**(22), 7540–7549.
- 40 L. K. Lafleur, J. D. Bishop, E. K. Heiniger, R. P. Gallagher, M. D. Wheeler, P. Kauffman, X. Zhang, E. C. Kline, J. R. Buser, S. Kumar, S. A. Byrnes, N. M. J. Vermeulen, N. K. Scarr, Y. Belousov, W. Mahoney, B. J. Toley, P. D. Ladd, B. R. Lutz and P. Yager, *Lab Chip*, 2016, **16**, 3777–3787.

- 41 W. S. Rasband, ImageJ: Image processing and analysis in Java, *Astrophys. Source code Libr.*, 2012.
- 42 D. Y. Stevens, C. R. Petri, J. L. Osborn, P. Spicar-Mihalic, K. G. McKenzie and P. Yager, *Lab Chip*, 2008, **12**, 2038–2045.
- 43 E. A. Lukhtanov, S. G. Lokhov, V. V. Gorn, M. A. Podyminogin and W. Mahoney, *Nucleic Acids Res.*, 2007, **35**(5), e30.
- 44 K. Nose, K. Nagamine, J. Tokuda, J. Takino and T. Hori, *Yakugaku Zasshi*, 2013, **133**(10), 1121–1126.
- 45 K. Sasahara, P. McPhie and A. P. Minton, *J. Mol. Biol.*, 2003, **326**(4), 1227–1237.
- 46 A. Christiansen, Q. Wang, A. Samiotakis, M. Cheung and P. Wittung-Stafshede, *Biochem.*, 2010, **49**(31), 6519–6530.
- 47 W. Q. Sun and P. Davidson, *CryoLetters*, 2001, **22**(5), 285–292.

5.2 A sample-to-result urinalysis device for chlamydia detection at point of care

This section is based on a conference proceeding, “*A device for urine cell concentration, lysis, and nucleic acid amplification for Chlamydia detection at the point of care*”.

Steven Bennett, Sujatha Kumar, Erin Heiniger, and Paul Yager. *The 24th International Conference on miniaturized systems for chemistry and life sciences (MicroTas)*, virtual conference 2020.

Abstract

We report a novel, partially disposable chlamydia and gonorrhea diagnostic system that concentrates bacterial cells from a urine sample, and images the amplified DNA with a smartphone in real time. This diagnostic system was designed to be operated from sample to result with minimal end-user steps at the point of care (POC). We demonstrated the proof-of-principle of the system using urine spiked with cultured Chlamydia cells.

Introduction

Chlamydia trachomatis (CT) is a prevalent infection with significant impact on women’s health resulting in pelvic inflammatory disease, ectopic pregnancy, infertility and acute chronic pelvic pain. Current diagnostic tests for CT require up to 48 hours to process, and risk missed treatment due to lack of follow up. Attempts to date for point-of-care tests have suffered from inaccuracy. We previously developed a Multiplexible Autonomous Disposable Nucleic Acid Amplification Test (MAD NAAT) for the diagnosis of methicillin resistant *Staphylococcus aureus* (MRSA) infection from nasal swab ¹⁴⁴ and a compact, semi-autonomous disposable platform for sample lysis and nucleic acid amplification based on a single USB-powered printed circuit board MD NAAT ¹⁴⁵. Here, we demonstrate an integrated urine cell concentration device that acquires urine from a cup with a vacutainer, concentrates Chlamydia-infected cells onto a filter and transfers the cells into a disposable MD NAAT device. The MD NAAT device performs heat lysis of the cells and releases the DNA into a zone for isothermal amplification, and real time fluorescence detection acquired with a mounted smartphone ¹⁴⁵. The integrated MD NAAT device is run with a USB connection, is user-friendly and can be used at the POC for clinical testing in the doctor’s office.

Experimental

The diagnostic device is assembled by sealing dried reagent pads for iSDA for a chlamydia target assay (ElitechGroup, Bothel WA USA) prepared using the method developed in section 5.1¹⁴², and a valve in a laser-ablated acrylic tray, attaching the acrylic tray to a pre-programmed USB powered circuit board and enclosing these components within a 3D printed insulation. The cell concentration device is assembled by sealing a filter within a closed channel and attaching the filter to a cap that is used to transport the filter to the diagnostic device. Figure 5.1 shows the parts of the urinalysis system. Urine samples spiked with *Chlamydia*-infected cells were processed through the sample filtration unit and transferred to the MD NAAT device for heat lysis at $\sim 95^{\circ}\text{C}$. After lysis, the sample flowed into a porous glass fiber matrix containing dry reagents for the isothermal strand displacement amplification (iSDA) performed at 50°C . A red-emitting target-specific minor groove binding fluorescent probe (see **Appendix 11.3 Figure 11.2**) was used for real-time monitoring of the amplification.

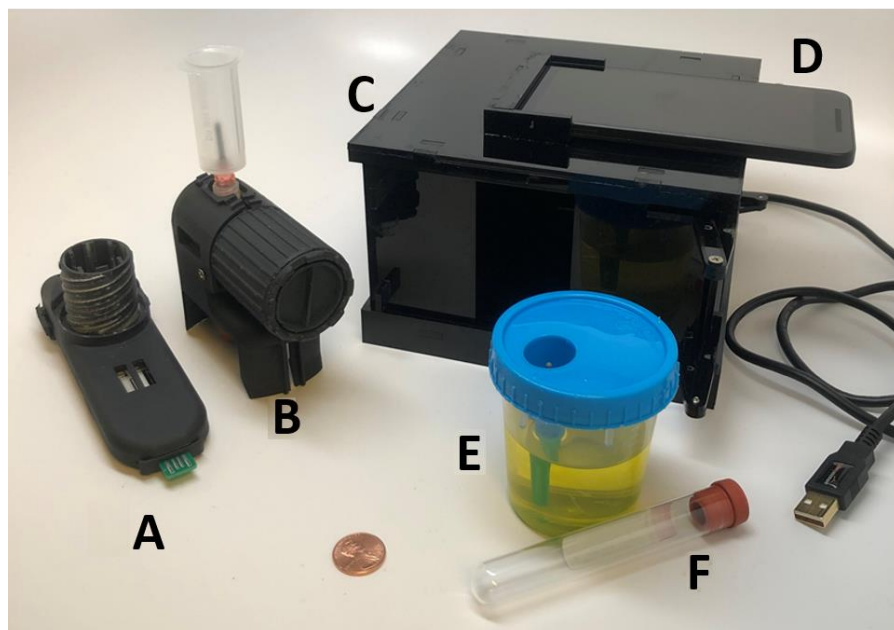


Figure 5.1: Photo of the complete urinalysis system. A) The diagnostic MD NAAT device. B) The urine sample filtration device. C) Mount for smartphone with built-in optical filters. D) Smartphone (Google Nexus 5X). E) Vacutainer compatible container with urine sample. F) 10 mL Vacutainer.

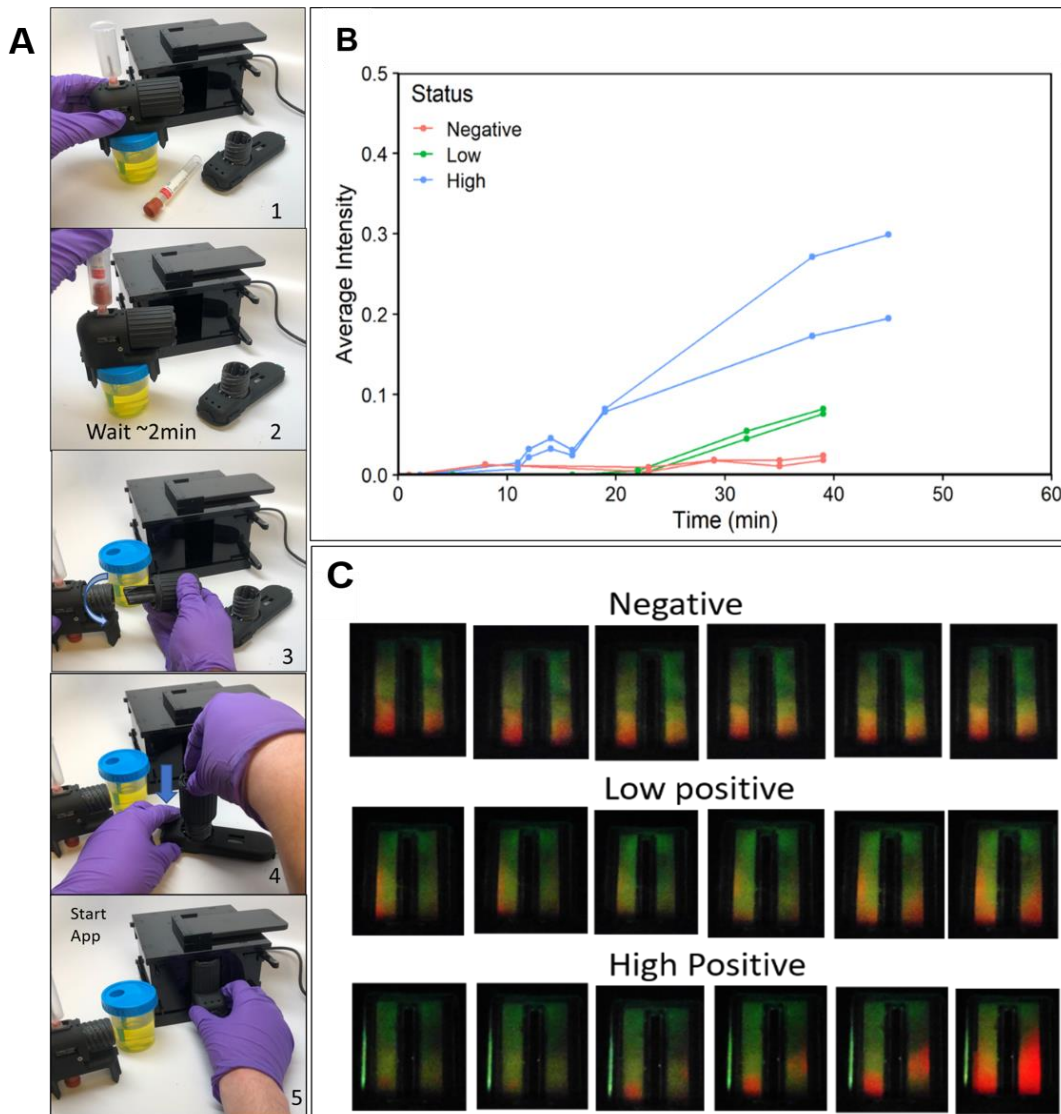


Figure 5.2. A) Demonstration of the user steps involved in the complete urinalysis system operation. 1) Attach concentration device to urine sample. 2) Insert vacutainer into concentration device, wait two min. 3) Unscrew cap of concentration device. 4) Screw cap onto diagnostic device. 5) Insert diagnostic device into the smartphone mount and start the image processing app on the smartphone. B) Real-time iSDA with red-emitting fluorescence probe for the *C. trachomatis* cryptic plasmid measured by cellphone in the integrated Urinalysis MD NAAT device. Urine samples were spiked with human tissue culture cells (the ratio of uninfected cells to cells infected with *C. trachomatis* varied between the different conditions), run through the urine filtration device, lysed, and amplified. C) Corresponding cellphone images of the real time fluorescence of the samples with negative, low (800 copies), and high (4×10^4 copies) of the *C. trachomatis* cells.

Results and discussion

We performed a proof-of-principle sample-to-result test to demonstrate a user-friendly urinalysis system for a sexually transmitted disease. The user steps are shown in Figure 5.2A). Urine samples spiked with *Chlamydia trachomatis* infected cells were successfully filtered through the unit and amplified in the MD NAAT device. Real-time amplification of the *Chlamydia* target showed differential intensity for the high- and the low-positive samples (Figure 5.2B)). The images of the corresponding time points are shown in Figure 5.2C). The total operation time was ~45 minutes. Overall, the device can be safely operated, is user-friendly, autonomous, partially disposable, and applicable for use at POC in a doctor's office.

Conclusion

An autonomous integrated disposable urinalysis device has broader applications at POC that could include rapid screening for markers, diagnosis of diseases, the staging of disease progression, and epidemiology.

Part II: Biomolecular motor-powered biosensing

*Dheere dheere re mana, dheere sab kuchh hoy,
maalee seenche sau ghada, rtu aae phal hoy.*

*- Kabir Das- mystic poet
15 th century
Language: Hindi*

Translation-

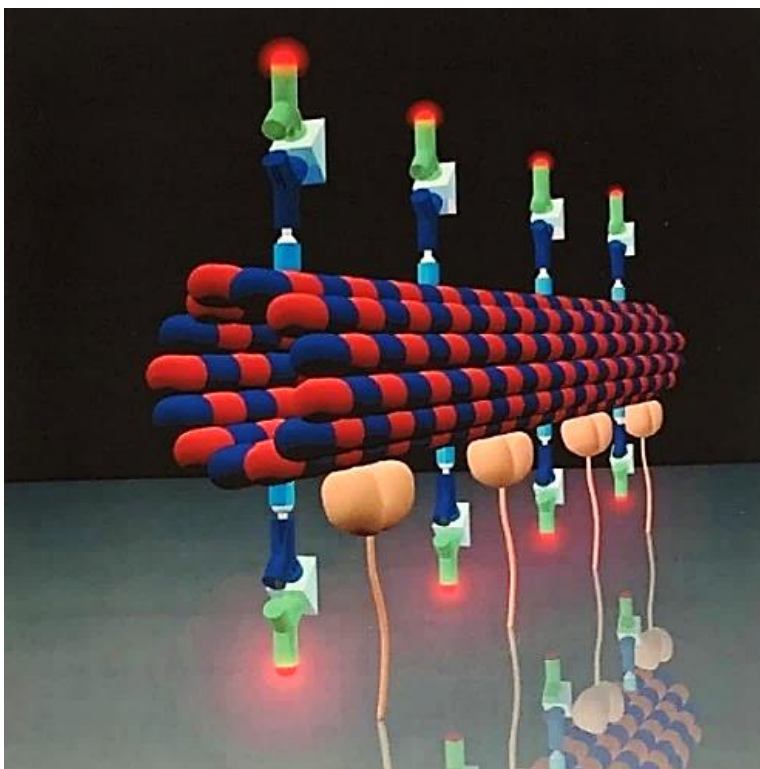
Being patient in the mind makes everything happen. Even if a gardener starts watering a tree with a hundred pots of water, fruits arrive only in season.

Chapter 6

6 Biomolecular motor-powered biosensing*

The following chapter is based on publication ¹⁴⁶ in section 6.1 and publication ¹⁴⁷ in section 6.2. In 6.1, the paper starts with an introduction to the use of kinesin motor proteins as a power source for *in vitro* active transport that can be used in an analytical device. An *in-situ* functionalization of microtubules with antibodies in building a “molecular shuttle” is described, and an immunoassay for a heart attack marker on the moving shuttle demonstrated. A method for enhancing the fluorescence signal by building multilayer structures using streptavidin- biotin linkages is elucidated.

In 6.2, the paper describes a method for the long-term dry storage of kinesin motor and complex protein assemblies on glass chip developed in 6.1. This technology leads to a nanoscale molecular biosensor entirely powered by motor protein and can be used at POC.



Model of kinesin-powered “molecular shuttle” (Cover picture- Small)

Reproduced cover picture from *Small*, 2006 2(3) with permission from Wiley and Sons

6.1 Selective loading of kinesin-powered molecular shuttles with protein cargo and its application to biosensing*

Sujatha Ramachandran, Karl-Heinz Ernst, George D. Bachand, Viola Vogel, and Henry Hess

Reproduced from *Small*, 2006 2(3), 330-334 with permission from Wiley and Sons

I designed the experiment, conducted the work, and analyzed the data. Together with the other authors discussed the results and wrote the paper.

DOI: 10.1002/sml.200500265

Selective Loading of Kinesin-Powered Molecular Shuttles with Protein Cargo and its Application to Biosensing**

Sujatha Ramachandran, Karl-Heinz Ernst,
George D. Bachand, Viola Vogel, and Henry Hess*

Molecular shuttles, nanoscale biomolecular-motor-driven transport systems, are a bioinspired alternative to pressure-driven fluid flow or electroosmotic flow in micro- and nano-fluidic systems.^[1] Significant progress has been made in directing the movement of such shuttles,^[2–6] in controlling their activation,^[7–9] and in loading some types of cargo. However, a generalized approach to selectively bind nanoscale cargo, such as proteins, viruses, or inorganic nanoparticles, to a molecular shuttle is a pressing concern for researchers interested in the technological applications of active transport, since it enables the design of a variety of analytical devices.

Here, we demonstrate that selective binding and subsequent transport of

target proteins can be achieved by assembling a multilayer structure consisting of streptavidin and biotinylated antibodies on a biotinylated microtubule, which can be transported by surface-immobilized kinesin motor proteins.

Taxol-stabilized biotinylated microtubules, tubular structures with a diameter of 25 nm and a length of several micrometers, have been previously used to transport a variety of streptavidin-coated cargoes, including microspheres,^[7] DNA,^[10] and quantum dots.^[11,12] The critical drawback of this approach is that the cargo has to be tagged prior to capture and transport with streptavidin or at least biotin, if a streptavidin bridge is employed.^[13] We have overcome this drawback by using streptavidin to immobilize commercially available biotinylated antibodies onto the biotinylated microtubules, thus permitting the capture of a wide range of targets. This technique complements the recently reported conjugation of cyclodextrin to microtubules via streptavidin, which permits the capture of selected chemical agents.^[14] Moreover, the resulting antibody-coated microtubule be-

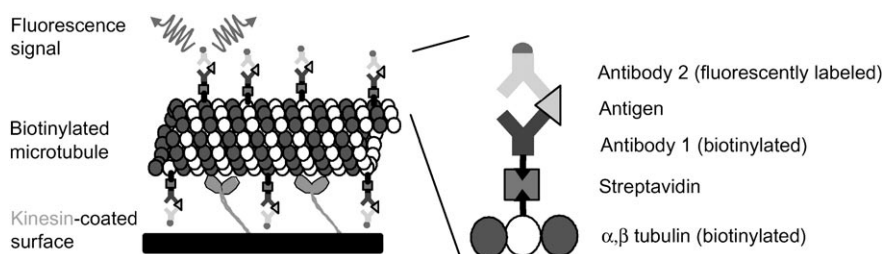


Figure 1. Biotinylated antibodies can be connected to biotinylated, taxol-stabilized microtubules via a streptavidin bridge, enabling specific capture of target antigens. A fluorescently labeled antibody can be used for double-antibody sandwich detection of antigens.

[*] S. Ramachandran
Department of Bioengineering, University of Washington
Seattle, WA 98195 (USA)
Dr. K.-H. Ernst
Molecular Surface Science Group
Swiss Federal Institute for Materials Science and Technology
(EMPA)
Dübendorf (Switzerland)
Dr. G. D. Bachand
Biomolecular Materials and Interfaces Department and
Center for Integrated Nanotechnologies
Sandia National Laboratories, Albuquerque, NM 87185 (USA)
Prof. V. Vogel
Department of Materials, ETH Zurich
Hönggerberg, 8093 Zürich, (Switzerland)
Prof. H. Hess
Department of Bioengineering, University of Washington
Seattle, WA 98195 (USA)
and
Department of Materials Science and Engineering
Rhines Hall 100, University of Florida
Gainesville, FL 32611 (USA)
Fax: (+1) 206-685-4434
E-mail: hhess@mse.ufl.edu

[**] We gratefully acknowledge financial support from the DARPA Biomolecular Motors Program, and the US Department of Energy, Office of Basic Energy Sciences, under grant DE-FG02-05ER46193.

comes a motile platform for established biosensing techniques, such as the double-antibody sandwich assay (Figure 1).

The challenge in this approach lies primarily in the assembly of a large supramolecular structure from more than ten thousand individual proteins, which are capable of cross-linking with each other in a variety of ways. While attempts to successively link streptavidin and antibodies to microtubules in solution proved unfruitful due to the difficulty of preventing unwanted crosslinking between microtubules and the difficulty of repeatedly purifying intact microtubules from a protein solution in high yield, we succeeded by exploiting the inherent affinity of microtubules to kinesin-coated surfaces. By immobilizing microtubules onto kinesin-coated surfaces, we were able to successively expose them to up to ten distinct solutions containing streptavidin, biotinylated antibodies, or buffer, and to observe the progress of the binding of proteins from solution to the microtubules in real time. In the following, details for the assembly steps and a demonstration of the selective binding of myoglobin (an important cardiac marker) are presented.^[15]

The initial coating of the kinesin-bound, biotinylated microtubules with streptavidin has to fill the available biotin binding sites completely in order to avoid unwanted cross-linking of microtubules with each other.^[16] Fluorescence measurements of the binding of streptavidin labeled with Alexa 594 as a function of time and initial streptavidin con-

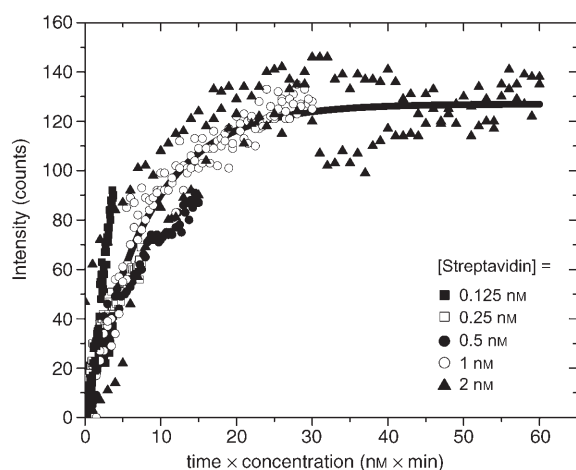


Figure 2. Time and concentration dependence of the binding of fluorescently labeled streptavidin from solution to surface-bound, biotinylated microtubules (MTs), as determined from a change in fluorescence intensity. Five streptavidin concentrations were used (0.125, 0.25, 0.5, 1, 2 nM). 99% of the biotin binding sites on the microtubules are filled after 40 min for a streptavidin concentration of 1 nM.

centration (Figure 2) show that the bimolecular reaction has a rate constant of $2 \mu\text{M}^{-1}\text{s}^{-1}$. The fit to the combined data assumes that an excess of streptavidin is available, so that the streptavidin concentration remains roughly constant throughout the reaction. While we do not know the exact concentration of accessible biotin binding sites (estimated at 100 pM), the fitted rate constant does not change substantially even if an initially equal concentration of available biotin sites and streptavidin is assumed.^[17]

Thus, a dosage of 8 nM streptavidin for 5 min leads to almost complete coverage of the binding sites. Moreover, since the reaction kinetics is not expected to change much for the subsequent reaction steps (biotinylated antibody binding, target capture, labeled antibody binding) due to the similar diffusion constants of the binding proteins, this dosage served as a benchmark for the next assembly steps.

The second step, binding of biotinylated antibodies to streptavidin-coated microtubules, is more difficult to observe in real time, since commercially available antibodies are either biotinylated or fluorescently labeled, but not both. We thus chose to confirm the successful attachment of the antibodies after completion of the reaction using two different approaches. Fluorescently labeled anti-mouse antibodies target the F_c regions of the biotinylated antibodies, and their binding indicates the presence of the biotinylated antibodies (Figure 3 A and B). Fluorescently labeled biotin targets unoccupied binding sites in the streptavidin coating, and the absence of biotin binding after dosing the streptavidin-coated microtubules with antibodies indicates that the coverage with antibodies is nearly complete (Figure 3 C and D).

The antigen-binding capacity of antibody-coated microtubules can potentially be enhanced by the assembly of a multilayer structure, since multiple biotinylation sites on the antibodies allow them to serve as scaffolds for additional streptavidin layers. Thus, structures resembling dendrimers can be assembled on the microtubules by alternating expo-

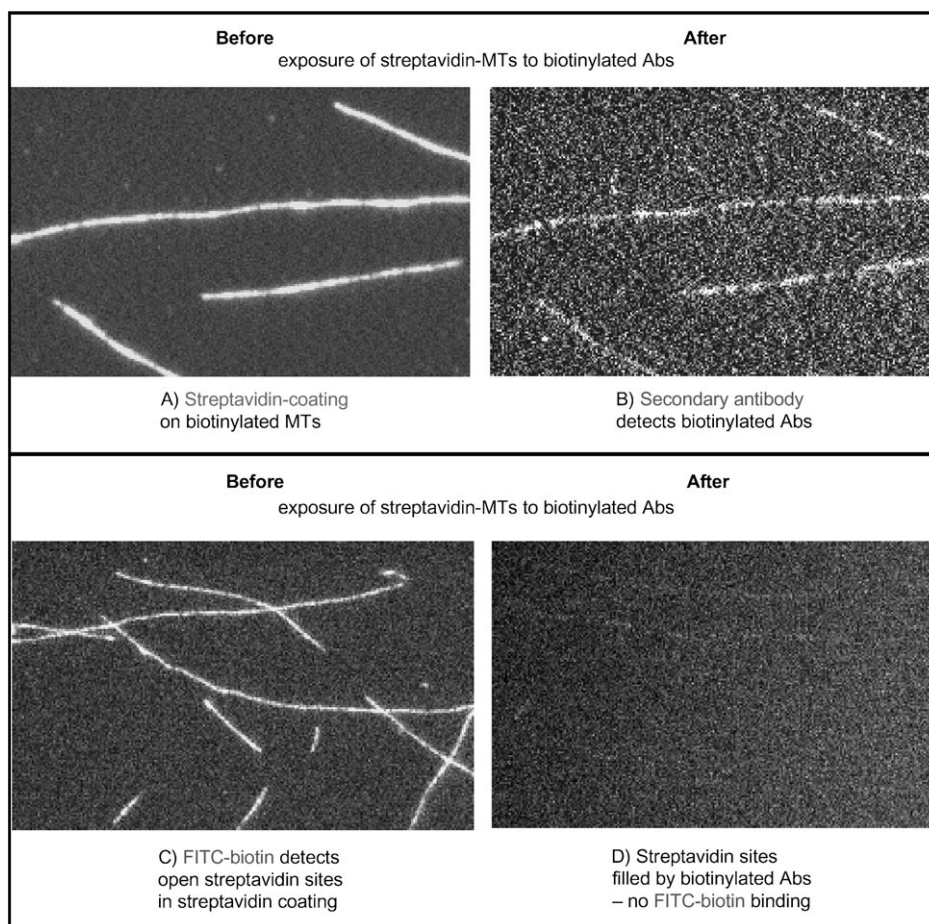


Figure 3. A) Fluorescent image of microtubules coated with streptavidin (fluorescently labeled with Alexa 594). B) After exposing the streptavidin-coated microtubules for 10 min to a 30 nM solution of biotinylated antibodies, we confirmed the successful attachment of antibodies through the co-localization of a FITC-labeled secondary antibody to the microtubules. C) Streptavidin-coated microtubules stained with FITC-labeled biotin, confirming that binding sites for biotin are available on the streptavidin coating prior to antibody attachment. D) Binding of FITC-labeled biotin is strongly suppressed after antibody binding, which demonstrates that almost all available streptavidin binding sites have been filled with biotinylated antibodies.

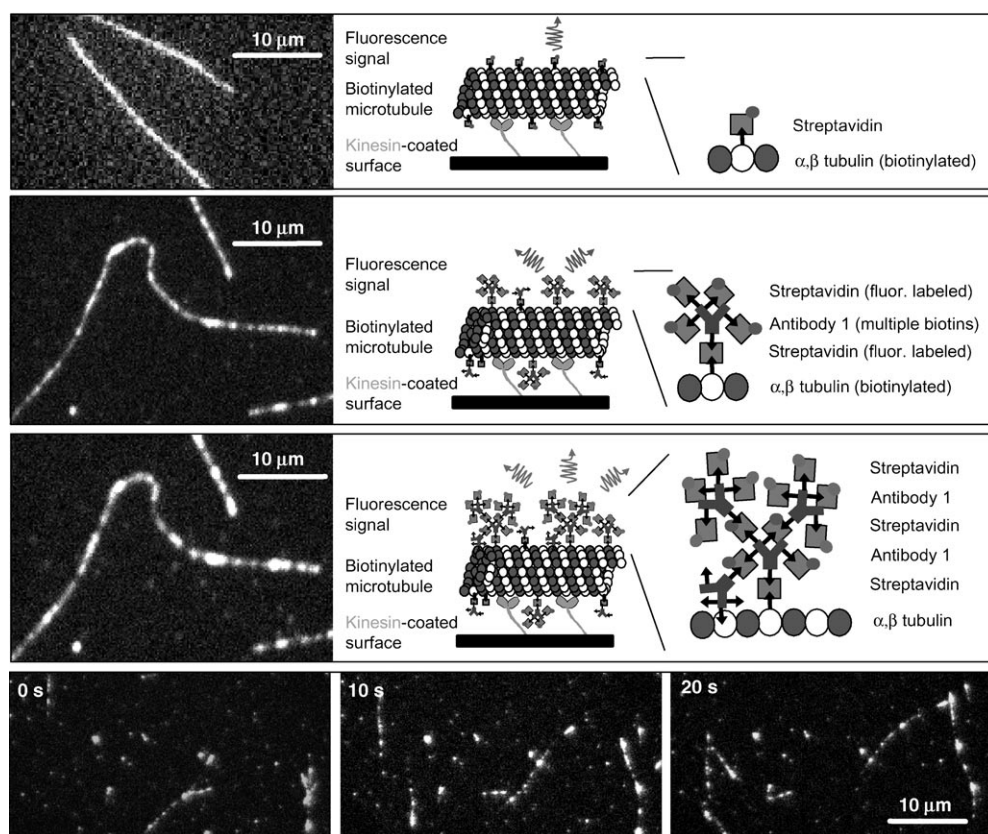


Figure 4. Multilayer structures assembled by alternating coatings of streptavidin and biotinylated antibodies (Abs). The top image shows the initial layer of Alexa 488-labeled streptavidin, the center image shows an Alexa 488-labeled streptavidin layer preceded by an unlabeled streptavidin layer and a biotinylated antibody layer, and the third row shows the same microtubule as the center image, but coated with an additional layer of antibodies and a layer of Alexa 594-labeled streptavidin (Alexa 594 imaged). The bottom row of images is a sequence (0 s, 10 s, 20 s) of images of microtubules moving despite being coated with three layers of streptavidin and two layers of antibodies (Alexa 594 imaged).

sure to streptavidin and biotinylated antibodies (Figure 4). The emerging speckle pattern along the microtubule axis points towards variations in dendrimer assembly caused by random variations in crosslinking activity along the microtubule. A detailed model for a similar process has been developed for the integration of fluorescently labeled tubulin subunits into growing microtubules.^[18] However, in order to explain the relatively strong speckle effect, a rather low density of potential binding sites has to be postulated. This is consistent with the low brightness of biotinylated microtubules coated with labeled streptavidin, but not with the biotinylation ratio of the biotinylated tubulin given by the manufacturer (one biotin site per tubulin heterodimer). Steric hindrance, in contrast, cannot explain the speckle pattern, since individual dendrimers with a size of less than 100 nm cannot be resolved with an optical microscope. An alternative explanation, namely that microtubules “phase separate” into biotinylated and biotin-free regions, has been suggested,^[11] and cannot be ruled out at this point. Remarkably, even the third layer seems not to affect the gliding of the structure on the kinesin-coated surface (Figure 4, bottom).

The capability of such antibody-functionalized microtubules to capture and transport specific antigens has been

confirmed by exposing the antibody-coated microtubule for 10 min to the antigen (myoglobin) at concentrations of 0.5, 1.0, and 2.0 nM, and tagging the captured myoglobin with a fluorescently labeled antibody (Figure 5A). Both, the biotinylated and the fluorescently labeled antibody have been chosen as a commercially available pair, which has been optimized for double-antibody-sandwich detection. Microtubules covered with the full double-antibody-sandwich structure move with a velocity that is not significantly different from bare microtubules (sandwich $707 \pm 80 \text{ nm s}^{-1}$; bare $724 \pm 50 \text{ nm s}^{-1}$ (mean \pm standard deviation); Figure 5B). Furthermore, we did not observe any change in appearance over a transport distance of 500 μm , which indicates that the double-antibody sandwich is reasonably stable. By measuring the fluorescence signal of the second antibody as function of the initial antigen concentration, we es-

tablished that the correlation between fluorescence output and antigen input is approximately linear as expected for these low dosages (Figure 2), suggesting that the structure can be used as a quantitative nanoscale immunoassay (Figure 5C).

The hallmark of the double-antibody sandwich assay is its selectivity, since it comprises two independent binding measurements. This is readily reproduced in our situation, where only the appropriate combination of capture and detection antibodies with the chosen antigen gives a strong fluorescence signal (Table 1). However, low selectivity of the antibody can result in cross-reactivity, as is the case for polyclonal anti-BSA.

It is intriguing that the filament geometry of a microtubule is very well suited to overcome limitations in the diffusive mass transport of the target to the nanoscale sensor.^[19] In addition, the ability of the sensing structure to actively move and explore the surface of a sample container in a directed^[20] or random^[21] fashion can be used to further concentrate the analyte at predetermined locations^[6] or at sites emerging from a self-organization process.^[16,22] By labeling the microtubule with a fluorescent dye of a different color from the dye attached to the detection antibody, one could

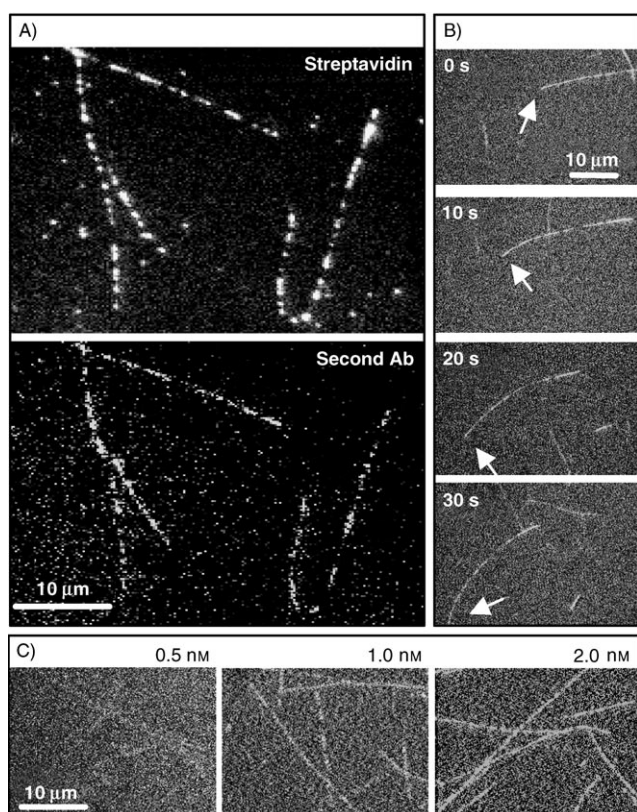


Figure 5. Fluorescence micrographs of microtubules with double-antibody sandwich structures based on the antigen myoglobin. A) The top image is of streptavidin (Alexa 594) coated microtubules, and the corresponding image of second-antibody (FITC) staining is below. B) Time-lapse images of kinesin-driven transport of microtubules with double-antibody-sandwich structures. C) Variation in the fluorescence signal of second antibody (FITC) with varying antigen concentration (0.5, 1.0, 2.0 nM from left to right). The brightness (after background subtraction) of the microtubules was 10, 24, and 39 counts, respectively, with a standard deviation of 5 counts.

Table 1. Selective binding of antigen to the antibody pair (capture (C) and detection (D)). The capture antibodies were biotin-labeled, and the detecting antibodies were FITC-labeled. The anti-BSA detecting antibody was polyclonal.

Antibody pair:	Antigen:	Antigen:
C – Capture	Myoglobin	BSA
D – Detection		
C – anti-myoglobin		
D – anti-myoglobin	28 ± 6	0 ± 2
C – anti-myoglobin		
D – anti-BSA (polyclonal)	12 ± 4	0 ± 2
C – anti-BSA		
D – anti-BSA (polyclonal)	0 ± 11	81 ± 10
C – anti-BSA		
D – anti-myoglobin	0 ± 6	0 ± 2

perform dual-color imaging^[23] to further improve signal detection via a co-localization measurement.

In conclusion, the functionalization of biotinylated microtubules with biotinylated antibodies via streptavidin

bridges permits the selective capture of proteins, and the subsequent detection of the capture event in double-antibody sandwich geometry. This strategy, which takes advantage of commercially available building blocks, significantly advances the field of molecular shuttles powered by biomolecular motors, since it enables the loading of all cargo types against which antibodies can be raised. The created structure is a remarkably complex, multifunctional supramolecular assembly.

Experimental Section

Kinesin and microtubule preparation: The expression and purification of *Drosophila melanogaster* conventional kinesin are described elsewhere.^[24] 20 μg of rhodamine or biotin-labeled tubulin (Cytoskeleton, Denver, CO) were polymerized into microtubules in BRB80 buffer (80 mM PIPES, 2 mM MgCl₂, 1 mM EGTA, pH 6.9) containing 4 mM MgCl₂, 1 mM GTP, and 5% DMSO to yield a final tubulin concentration of 3.2 mg mL⁻¹. After polymerization for 30 min at 37 °C, the microtubules were diluted 100-fold in BRB80 with 10 μM paclitaxel.

Construction of flow cells and motility assays: Flow cells were assembled using glass slides or cover slips as the bottom surface, a cover slip to cover the surface, and double-sided tape as spacer, creating a flow channel with a volume of about 20 μL. The kinesin gliding motility assay was performed according to a literature method.^[25] The surface of the flow cells were first pre-coated with a casein solution, which was replaced with a kinesin solution, and finally perfused with motility solution containing 3.2 μg mL⁻¹ biotin-labeled microtubules, 0.6 μg mL⁻¹ rhodamine-labeled microtubules, 10 μM ATP, and antifade solution (20 mM D-glucose, 20 μg mL⁻¹ glucose oxidase, 8 μg mL⁻¹ catalase, 1% dithiothreitol). The flow cells were washed twice with motility solution without microtubules to remove unbound microtubules and unpolymerized tubulin.

Streptavidin coating: After the wash steps to remove unbound microtubules, the flow cells were mounted on a microscope stage, and rhodamine-labeled microtubules were brought into focus. Varying concentrations of Alexa 594-labeled streptavidin (Molecular Probes) diluted in motility buffer without ATP were carefully exchanged into flow cells and images were captured every 30 s for 30 min at 500 ms exposures using an epifluorescence microscope (Eclipse TE200, Nikon) with a 100 W Hg lamp, a 60× oil objective (NA 1.4), a CCD camera (Roper Cascade 650), and image acquisition software (Metamorph, Universal Imaging Inc.). The exposure of the flow cell to excitation light was carefully controlled to minimize photobleaching. The intensity of bound fluorescent streptavidin was determined by measuring the average counts within a circle of 3.5-μm diameter centered on a microtubule, subtracting the average counts within a circle of the same size adjacent to the microtubule (background), and averaging the signal from three (Figure 2) or seven (Figure 5) different locations. The intensity value thus represents the average binding over a microtubule segment of 3.5-μm length. Importantly, the values also represent averages over the width of the microtubule (2–3 pixels). The method is designed to remove artifacts due to the pixelation of the image, which makes line-scans along narrow, curved objects somewhat arbitrary.

Antibody binding: About 8 nm of streptavidin (unlabeled or Alexa 594-labeled) was perfused into the flow cell and incubated for 5 min to cover all the biotin sites on the microtubules. After washing the flow cell twice, 30 nm of biotin-labeled anti-myoglobin monoclonal antibody (clone 4E2, Advanced Immunochemicals Inc.) was introduced into the flow cell, incubated for 5 min and washed twice. Then, the flow cells were incubated for 5 min with either 60 nm FITC-labeled biotin (Antibodies Incorporated) or 60 nm of FITC-labeled goat anti-mouse polyclonal antibody (Immunology Consultants Laboratory, Inc), washed twice, and imaged.

Multilayer structures: The biotinylated microtubules were first coated with 8 nm unlabeled streptavidin for 5 min, washed twice, and incubated with 30 nm of biotinylated antibody for 5 min. After two washes, the flow cell was incubated with 16 nm of Alexa 594-labeled streptavidin for 5 min to cover the biotin sites on the antibody, followed by two washes. Further, streptavidin sites on the antibody were coated with a second layer of biotinylated antibody (30 nm for 5 min), washed twice, and followed by addition of a third layer of Alexa 488-labeled streptavidin (30 nm for 5 min). After two washes, images of microtubules coated with Alexa 488- and Alexa 594-labeled streptavidin were acquired at 500-ms exposures.

Antigen binding and detection: The microtubules bound with biotinylated anti-myoglobin antibodies were incubated with varying concentrations of human cardiac myoglobin (0.5–8 nm) (Advanced Immunochemicals Inc.) for 10 min and washed twice. A second anti-myoglobin monoclonal antibody (clone 7C3, Advanced Immunochemicals Inc.) labeled with FITC dye was perfused into the flow cell at a concentration of 30 nm and washed twice after 5 min. The images of microtubules coated with FITC-labeled antibodies were taken at 2 s exposures. For studying the motility of microtubules coated with a double-antibody sandwich structure, the final wash solution contained 1 mM ATP.

Selectivity: To determine the selectivity of the antigens, combinations of monoclonal/polyclonal anti-myoglobin and anti-BSA antibodies as capture and detecting antibodies were used. The microtubules were first coated with 30 nm biotinylated monoclonal anti-BSA (Lab Vision Corporation) or anti-myoglobin antibodies as described earlier. Myoglobin or BSA antigens were used at a concentration of 8 nm, incubated for 10 min and washed twice. About 30 nm FITC-labeled sheep anti-BSA polyclonal antibodies (Immunology Consultants Laboratory, Inc.) or FITC-labeled anti-myoglobin monoclonal antibodies was perfused into the flow cell, incubated for 5 min, and washed twice with motility buffer without ATP. Images were taken at 2 s exposures, and di-thiothreitol was omitted from the antifade system for the BSA experiments.

The intensity of bound fluorescent detection antibody was determined by measuring the average counts within a circle of 3.5- μ m diameter centered on a microtubule at 15 different locations, averaging over these 15 locations, and subtracting the average of 15 background locations near those microtubule-centered regions. The entry in Table 1 is zero if no microtubules can be located due to negligible fluorescence. In this case the error is calculated as the square root of twice the standard error of the mean of the average counts within a circle at 15 random locations. In the other cases, the error is calculated as the square-

root of the sum of the squares of the standard error of the mean of the average counts at the 15 microtubule locations and 15 background locations.

Keywords:

biomolecular motors • biosensors • kinesin • microtubules • molecular shuttles

- [1] H. Hess, V. Vogel, *Rev. Mol. Biotech.* **2001**, *82*, 67.
- [2] Y. Hiratsuka, T. Tada, K. Oiwa, T. Kanayama, T. Q. Uyeda, *Biophys. J.* **2001**, *81*, 1555.
- [3] J. Clemmens, H. Hess, J. Howard, V. Vogel, *Langmuir* **2003**, *19*, 1738.
- [4] H. Hess, C. M. Matzke, R. K. Doot, J. Clemmens, G. D. Bachand, B. C. Bunker, V. Vogel, *Nano Lett.* **2003**, *3*, 1651.
- [5] S. G. Moorjani, L. Jia, T. N. Jackson, W. O. Hancock, *Nano Lett.* **2003**, *3*, 633.
- [6] J. Clemmens, H. Hess, R. Doot, C. M. Matzke, G. D. Bachand, V. Vogel, *Lab. Chip* **2004**, *4*, 83.
- [7] H. Hess, J. Clemmens, D. Qin, J. Howard, V. Vogel, *Nano Lett.* **2001**, *1*, 235.
- [8] G. Mihajlovic, N. M. Brunet, J. Trbovic, P. Xiong, S. von Molnar, P. B. Chase, *Appl. Phys. Lett.* **2004**, *85*, 1060.
- [9] Y.-Z. Du, Y. Hiratsuka, S. Taira, M. Eguchi, T. Q. P. Uyeda, N. Yumoto, M. Kodaka, *Chem. Commun.* **2005**, *16*, 2080.
- [10] S. Diez, C. Reuther, C. Dinu, R. Seidel, M. Mertig, W. Pompe, J. Howard, *Nano Lett.* **2003**, *3*, 1251.
- [11] G. D. Bachand, S. B. Rivera, A. K. Boal, J. Gaudio, J. Liu, B. C. Bunker, *Nano Lett.* **2004**, *4*, 817.
- [12] M. Bachand, A. M. Trent, B. C. Bunker, G. D. Bachand, *J. Nanosci. Nanotechnol.* **2005**, *5*, 718.
- [13] Y. Z. Du, Y. Hiratsuka, S. Taira, M. Eguchi, T. Q. P. Uyeda, N. Yumoto, M. Kodaka, *Chem. Commun.* **2005**, *40*, 2080.
- [14] K. A. Kato, R. Goto, K. Katoh, M. Shibakami, *Biosci. Biotechnol. Biochem.* **2005**, *69*, 646.
- [15] W. W. Chu, R. S. Dieter, C. K. Stone, *Wis. Med. J.* **2002**, *101*, 40.
- [16] H. Hess, J. Clemmens, C. Brunner, R. Doot, S. Luna, K.-H. Ernst, V. Vogel, *Nano Lett.* **2005**, *5*, 629.
- [17] L. Pauling, *General Chemistry*, W. H. Freeman and Company, San Francisco **1947**.
- [18] C. M. Waterman-Storer, E. D. Salmon, *Biophys. J.* **1998**, *75*, 2059.
- [19] P. E. Sheehan, L. J. Whitman, *Nano Lett.* **2005**, *5*, 803.
- [20] J. Clemmens, H. Hess, R. Lipscomb, Y. Hanein, K. F. Boehringer, C. M. Matzke, G. D. Bachand, B. C. Bunker, V. Vogel, *Langmuir* **2003**, *19*, 10967.
- [21] H. Hess, J. Clemmens, J. Howard, V. Vogel, *Nano Lett.* **2002**, *2*, 113.
- [22] G. Theraulaz, E. Bonabeau, S. C. Nicolis, R. V. Sole, V. Fourcasie, S. Blanco, R. Fournier, J. L. Joly, P. Fernandez, A. Grimal, P. Dalle, J. L. Deneubourg, *Proc. Natl. Acad. Sci. USA* **2002**, *99*, 9645.
- [23] H. Hess, M. Antia, V. Vogel, *Rev. Sci. Instrum.* **2004**, *75*, 266.
- [24] D. L. Coy, M. Wagenbach, J. Howard, *J. Biol. Chem.* **1999**, *274*, 3667.
- [25] J. Howard, A. J. Hunt, S. Baek, *Methods Cell Biol.* **1993**, *39*, 137.

Received: July 29, 2005

Revised: October 10, 2005

Published online on January 10, 2006

6.2 Long-term storage of bionanodevices by freezing and lyophilization*

Raviraja Seetharam*, Yuuko Wada*, Sujatha Ramachandran*, Henry Hess and Peter Satir.

* **Equal author contribution**

Reproduced from *Lab Chip*, 2006 6, 1239-1242 with permission from the Royal Society of Chemistry

I designed the experiment, conducted the work for Figures 2-4, and analyzed the data. Together with the other authors discussed the results and wrote the paper.

Long-term storage of bionanodevices by freezing and lyophilization†

Raviraja Seetharam,‡^a Yuuko Wada,‡^a Sujatha Ramachandran,‡^b Henry Hess^c and Peter Satir*^a

Received 2nd February 2006, Accepted 12th June 2006

First published as an Advance Article on the web 3rd July 2006

DOI: 10.1039/b601635a

Successful long-term storage of a “smart dust” device integrating biomolecular motors and complex protein assemblies has been demonstrated using freezing or lyophilization, which implies that fabrication and application can be separated even for complex bionanodevices.

Introduction

The integration of biological nanomachines into micro- and nanodevices promises rapid advances in nanotechnology,^{1–5} since device development is not hampered by the lack of critical nanoscale components of man-made origin. A prominent example of this hybrid approach is the utilization of biomolecular motors, such as the motor protein kinesin, for the active transport of molecules and particles in micro-fabricated devices.^{6,7}

Proof-of-principle demonstrations of such hybrid devices have been quite successful in the laboratory, for example achieving the integration of a double-antibody-sandwich bioassay for virus particles⁸ or the heart-attack marker myoglobin⁹ onto a single, actively transported microtubule. However, real-world applications such as a “smart dust” type biosensor,¹⁰ require the long-term storage of fabricated devices before deployment and activation. The challenges in storing proteins within microfabricated structures are only beginning to be addressed,¹¹ and seem particularly large for our nanobionodevices (Fig. 1) which integrate fragile multimeric proteins and large protein assemblies, such as kinesin motors and microtubules. The lifetime of such devices at room temperature has been measured to be less than a day, and is primarily limited by the depolymerization of the microtubules even in the presence of stabilizing agents.¹² In addition, immobilized microtubule arrays retain their ability to support kinesin motor motility after freezing or lyophilization, which permits partial separation of device assembly from utilization.¹³ Conversely, the stability of myosin motors adhered to a surface has been investigated,¹⁴ and protocols to extend their lifetime have been developed.¹⁵

Our goal in this study was to completely separate device assembly from device utilization and extend the lifetime

hundred-fold, either by storing the devices at cryogenic temperatures or, preferentially, by lyophilization of the entire assembly. Despite extensive research, driven by the interest in protein pharmaceuticals, no “single, short, and mature pathway” to a stable, lyophilized protein formulation has emerged.¹⁶ We thus relied on established strategies¹⁷ and extensive experimentation to overcome the key challenges of stabilizing complex assemblies of proteins rather than monomeric proteins.

Materials and methods

Construction of flow cell

For experimental purposes, flow cells were assembled using a glass slide as the bottom surface (Fisher^{finest}[®], Premium) and

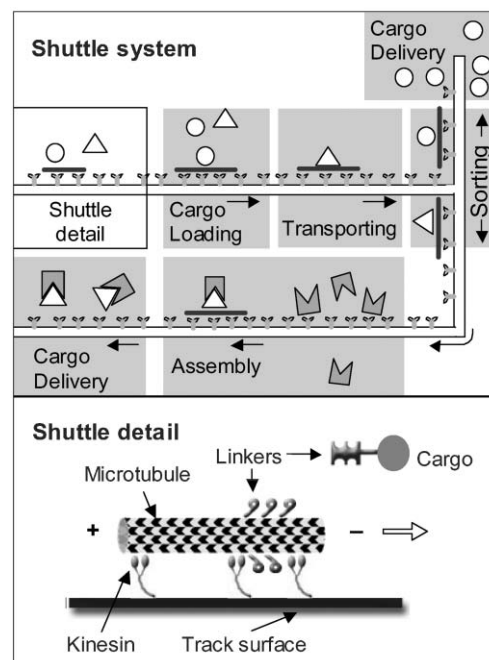


Fig. 1 A kinesin-powered molecular shuttle system is an example of a nanobionodevice, which employs fragile motor proteins and protein assemblies as active elements in a microfabricated structure. The shuttle system is envisioned to load, transport, sort, and assemble nanoscale building blocks (top). It utilizes surface-bound kinesin motor proteins to transport functionalized microtubules along fabricated tracks. Reproduced with permission from ref. 22. Copyright 2003, American Chemical Society.

^aDepartment of Anatomy and Structural Biology, Albert Einstein College of Medicine, 1300 Morris Park Ave., Bronx, NY, 10461, USA. E-mail: satir@aecom.yu.edu; Fax: +1 (1) 718 430-8996; Tel: +1 (1) 718 430 4062

^bDepartment of Bioengineering, University of Washington, Seattle, WA, 98105, USA. Tel: +1 (1) 206 616-3129

^cDepartment of Materials Science and Engineering, University of Florida, Gainesville, FL, 32611, USA. Fax: +1 (1) 352 846-3355; Tel: +1 (1) 352 854-3781

† Electronic supplementary information (ESI) available: Movie showing visualization of MT motility in a chamber reconstituted after 24 days storage at room temperature. Scale bar = 10 μm. See DOI: 10.1039/b601635a

‡ These authors contributed equally to this work.

a glass cover slip (Cover Glass, no. 1, Fisher Scientific) to cover the surface. Double-sided tape (Scotch^R, 3 M, about 75 μm in thickness) was used as a spacer to build a flow channel, with a volume of about 20 μl .

Kinesin and microtubule preparation

The expression and purification of the wild-type kinesin (KIF5) from *Drosophila melanogaster* were described elsewhere.¹⁸ *Thermomyces* kinesin (KIF1A) was also prepared using similar protocols.¹⁹ The prepared kinesin was placed in phosphate buffer (20 mM Sodium phosphate, pH 7), glycerinated (25%) and stored at $-30\text{ }^{\circ}\text{C}$. About 20 μg of biotin/rhodamine labeled tubulin (Cytoskeleton, Denver, CO, USA) was polymerized in BRB80 buffer (80 mM PIPES, 2 mM MgCl_2 , 1 mM EGTA, pH 6.85) containing 4 mM MgCl_2 , 1 mM GTP and 5% DMSO for 30 min at $37\text{ }^{\circ}\text{C}$. In some cases, PC tubulin prepared from calf brain was used for polymerization. For experiments with *Thermomyces* kinesin, only rhodamine labeled microtubules (MTs) were used. After polymerization the microtubules were diluted 100-fold in BRB80 containing 10 μM taxol for stabilization.

Motility assay

Motility assays were performed in flow cells. Flow cells were pre-coated with 0.5 mg ml^{-1} casein in BRB80 buffer for 5 min.¹⁸ The casein buffer was then replaced by BRB80 containing kinesin, 0.2 mg ml^{-1} casein and 1 mM ATP for 5 min. Motility solution containing rhodamine/biotin labeled MTs (32 nM), 1 mM ATP, oxygen-scavenging additives (20 mM D-glucose, 20 $\mu\text{g ml}^{-1}$ glucose oxidase, 8 $\mu\text{g ml}^{-1}$ catalase, 1% dithiothreitol) was then exchanged in the flow cell and kept for 5 min. The flow cells were sequentially flushed twice with motility solution without MTs to remove glycerol if present, and unbound MTs. For experiments with *Thermomyces* kinesin, 100 mM trehalose (Fluka, Sigma-Aldrich) was added to the BRB80–kinesin containing solution.

To the flow cells containing biotin labeled MTs, a mixture of unlabeled and Alexa 594 labeled streptavidin (10 nM) in the ratio of 5 : 1 was added and allowed to stand for 5 min and then washed twice. In some experiments, about 30 nM of biotinylated anti-myoglobin monoclonal antibodies (clone 4E2, Advanced Immunochemicals Inc., Long Beach CA) was added to the flow cell for 5 min and washed twice. The motility assays were all performed at room temperature ($22\text{--}25\text{ }^{\circ}\text{C}$).

Images of MTs were captured using an epifluorescence microscope (Eclipse TE200, Nikon) with a 100 W Hg lamp, a 60 \times oil objective (NA 1.4) and equipped with a CCD camera (Roper Cascade) and image acquisition software (Metamorph, Universal Imaging Inc.) or Zeiss Axiolab^R microscope equipped with Photometrics CoolSNAPTM camera and image acquisition software (IP Lab, 3.5).

Snap freezing

Usually ten flow chambers were used in each experimental setup. One of the flow cells with the motility assay components was examined for MT motility and the remaining chambers were then snap-frozen in liquid nitrogen for about 1 min and

thawed at room temperature. They were immediately observed under the microscope for stability and motility of the MTs. Some flow cells were stored at $-80\text{ }^{\circ}\text{C}$ immediately after snap-freezing to study the effect of long-term storage. The flow cells that had anti-myoglobin antibodies bound to microtubules *via* streptavidin were tested for antigen binding (for details see ref. 9) after snap freezing. 8 nM myoglobin (Advanced Immunochemical Inc.) in motility buffer was added to the flow cells and washed after 5 min. A FITC-labeled second anti-myoglobin monoclonal antibody 7C3 (Advanced Immunochemicals Inc.) was added to the flow cell and washed twice. The flow cells were observed under the microscope for antigen binding.

Lyophilization

For lyophilization, the flow cells with all components were first snap-frozen in liquid nitrogen and immediately transferred to a holder (Labconco, 600 ml) and lyophilized (Freeze Mobile 6, Cryostar Industries, Inc) for 12–15 h. After lyophilization, the flow cells were stored at $-80\text{ }^{\circ}\text{C}$ or at room temperature. The lyophilized flow cells were reconstituted with distilled water or motility buffer at room temperature and observed under the microscope for reconstitution of motility.

Results

Snap freezing

The MTs in the flow cell were found to be stable after snap freezing the entire flow cell in liquid nitrogen (Fig. 2a) and to retain their motility (Fig. 2b), although they often became reduced in length. Snap-frozen MT stored at $-80\text{ }^{\circ}\text{C}$ retained their motility even after 2 days. However the velocity of MTs was slightly reduced probably because of lower ATP concentration due to hydrolysis during storage. The biotinylated MTs decorated with anti-myoglobin antibodies retained their antigen binding capacity after snap-freezing. To demonstrate

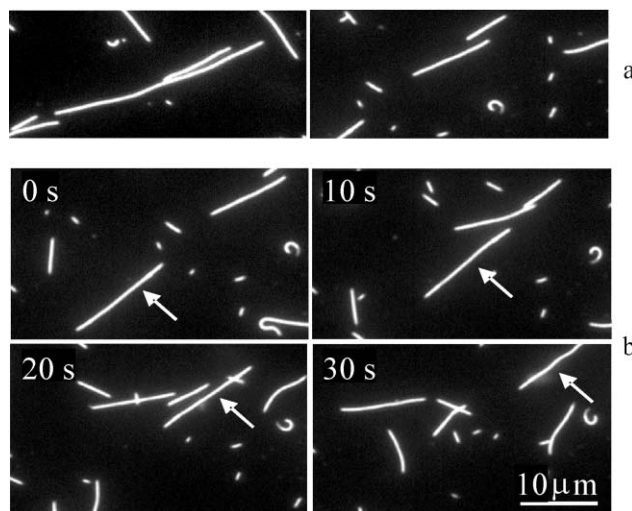


Fig. 2 a, Effect of snap freezing on microtubules. Left: Rhodamine-labelled MTs before snap freezing. Right: Rhodamine-labelled MTs after snap freezing. b, Motility of MTs immediately after snap freezing. Arrow shows a single microtubule.

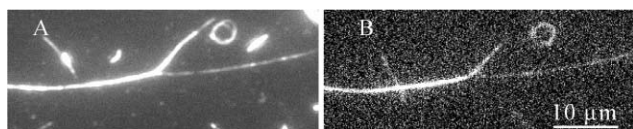


Fig. 3 Antigen binding and detection after snap freezing of flow cell containing biotinylated microtubules coated with anti-myoglobin. A, Microtubules coated with anti-myoglobin, snap-frozen in liquid nitrogen, thawed and detected by Alexa 594-labeled streptavidin. B, Myoglobin was added to the flow cell after thawing. Binding of myoglobin detected by FITC-labeled antibody.

this, the antigen (myoglobin) was added to the flow cell and detected by an FITC-labeled second antibody (Fig. 3). In comparison to rhodamine MTs, the biotinylated MTs were degraded to a lesser degree.

Lyophilization

In our first experiments we used flow cells constructed with whole cover slips (2×2 cm). Lyophilization was found to be non-uniform, giving a non-homogeneous distribution of MTs. Upon reconstitution of lyophilized flow cells with water or motility buffer, we could observe MTs but the motility was not retained. When smaller flow cells (1×2 cm or 0.7×2 cm) were used, we observed some areas with uniform distribution of MTs. Upon reconstitution of these flow cells with motility buffer (with ATP), in these areas $\approx 50\%$ or more MTs resumed their motility (Fig. 4). However, MTs were still degraded, becoming reduced in length from an average 3.13 ± 2.35 SD μm to small fragments (1.41 ± 0.67 SD μm), a significant difference ($p < 0.001$) rendering them less useful in detection devices. When reconstituted after lyophilization, chambers with *Thermomyces* kinesin stored at room temperature survived with areas of MT motility for at least 24 days; chambers with *Drosophila* kinesin retained MT motility for at least 40 days.

A final set of experiments employed trehalose as a cryoprotectant. In controls prior to snap freezing, the chambers were reasonably uniform and motility was high, usually between 40–85% (Fig. 5). After snap freezing, over 200 MTs were examined in duplicate chambers. In one chamber, motility averaged $27.0 \pm 6.1\%$; in the duplicate chamber, it averaged $46.9 \pm 24.6\%$ with a range from 15–77%,

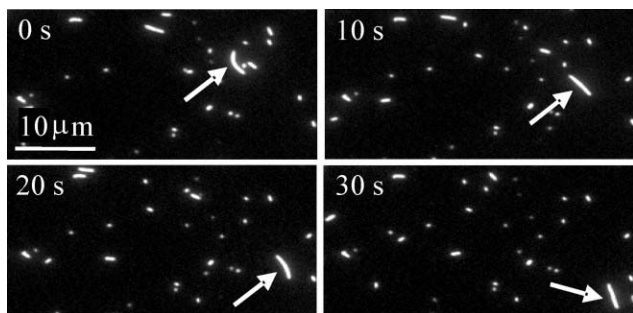


Fig. 4 Motility of microtubules after lyophilization in the flow cell, and reconstitution with fresh motility buffer containing ATP. When lengths are compared to Fig. 2b, note that many MTs have undergone degradation.

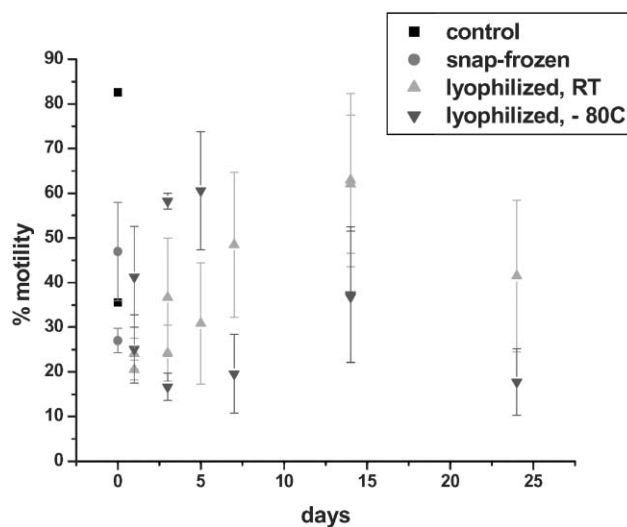


Fig. 5 Retention of MT motility with *Thermomyces* kinesin upon reconstitution with motility buffer + ATP, after lyophilization. Two sets of experiments compare survival of motility after lyophilization (stored at room temperature \blacktriangle and -80°C \blacktriangledown). Each point represents measurements of multiple areas in duplicate chambers (at least 200 MTs.) Areas differ in % motility leading to the high SEMs. MTs are motile after at least 24 days of storage before reconstitution. Motility is similar to chambers measured before (\blacksquare) and after snap freezing (\bullet) prior to lyophilization.

indicating non-uniformity upon freezing. MT length was also non-uniform with lengths of $>10 \mu\text{m}$, but many small fragments. Many of the long MTs were motile. Therefore, MT motility from both chambers would potentially be usable in detection devices. Replicate chambers were then lyophilized, stored either at room temperature ($\approx 24^\circ\text{C}$) or at -80°C . At intervals the chambers were reconstituted with motility buffer with ATP. Again, over 200 MTs were examined in duplicate chambers. The chambers remained non-uniform with areas where MTs were severely degraded and motility was lost and other areas where lyophilization was successful in preserving both MT length and good motility. Where MTs retained their length, they moved with velocities of 0.38 ± 0.06 SD $\mu\text{m s}^{-1}$, similar to aliquots before lyophilization (0.36 ± 0.07 SD). Overall, motility was essentially the same in chambers stored at room temperature and at -80°C . Initially all chambers reconstituted with many areas of good motility, but after 5 day's storage, there were many areas with minimal motility. Fig. 5 shows that average motility at 14 days remains above 30%, but with considerable variability both from chamber to chamber and even in different areas of the same chamber.

Discussion

We have succeeded in constructing a self-contained, chemo-mechanical, non-electrical, MT–kinesin driven system that can be lyophilized and stored for long periods of time and then rehydrated to restore activity. When the system is set up with trehalose, MT stability and length are largely preserved after reactivation and MTs move with the normal range of velocities. Uniformity of lyophilization improves MT motility and preserves MT length, but with the test chambers that we

have initially employed, uniformity throughout the chamber is not achieved and different parts of the chamber behave differently with respect to both MT length preservation and % motility. Nevertheless small chambers performed better than larger. In the best cases, MTs longer than 10 μm are preserved and % motility is nearly 50% and sometimes more. The non-uniformity of preservation is a difficulty that needs to be overcome, but the percentage motility even in these chambers would permit their use in detection devices such as smart dust sensors. Before lyophilization, we see variations in the percent motility in controls, but this increases substantially during snap freezing. The variability upon reconstitution after lyophilization is nearly the same as that seen after snap freezing, suggesting that variability is introduced by the freezing process and would be diminished if freezing could be improved. It would be useful to study the design of chambers and techniques where snap freezing could be eliminated and direct lyophilization resulted in uniform preservation of MT length and activity.

Restoration of MT motility does not depend so far on the type of kinesin used as the biomotor, although a wider sampling of the kinesin superfamily¹⁴ should produce variations in MT velocity and direction, if desired. Although we have used ATP as the energy source, and usually reactivated with buffers containing ATP, the chamber can be prepared for lyophilization incorporating ATP or perhaps caged ATP and rehydrated with distilled water. After rehydration MTs will move in the presence of ATP or movement can be triggered when needed, by UV irradiation with caged ATP.^{20,21}

Our demonstration that MT motility is retained after lyophilization can be considered an advance for designing and manufacturing a chamber, which provides a mechanical structure compatible with the stabilization process and exhibits uniform lyophilization, ease of loading and surface properties compatible with MT motility. This prototype could then be manufactured *en masse* and deployed when needed at distances and times far from the point of manufacture.

Conclusion

Flow chambers retained MT motility after snap freezing in liquid nitrogen. They needed no additional ATP when thawed immediately and observed under the microscope (Fig. 2a and b) or stored at $-80\text{ }^{\circ}\text{C}$ for 48 h. Streptavidin coated biotinylated microtubules were also found to be stable and retain motility after snap freezing. In addition, the anti-myoglobin antibody bound to biotinylated microtubules *via* streptavidin retained its ability to bind to myoglobin, which was detected with a secondary FITC-labeled antibody (Fig. 3).

The lyophilization of glass flow cells for motility assays was also successful. Freezing introduced variability of MT preservation and motility but smaller flow cells had more

uniform distribution of microtubules. Lyophilized chambers retained MT motility after addition of fresh motility buffer with ATP (Fig. 4) or when reconstituted with water. The degradation of microtubules upon lyophilization was reduced when trehalose was used in the chamber.

These experiments demonstrate that complete bionanodevices integrating large protein assemblies, such as microtubules, as well as highly functional molecular machines, such as kinesin motors, can be stored for extended periods of time and returned to an active functional state by thawing or rehydration.

Acknowledgements

This work was supported by DARPA and AFOSR.

References

- 1 *Nanobiotechnology*, ed. C. M. Niemeyer and C. A. Mirkin, Wiley-VCH, Weinheim, 2004.
- 2 V. Vogel, *MRS Bull.*, 2002, 972–978.
- 3 J. J. Schmidt and C. D. Montemagno, *Annu. Rev. Mater. Res.*, 2004, **34**, 315–337.
- 4 R. K. Soong, G. D. Bachand, H. P. Neves, A. G. Olkhovets, H. G. Craighead and C. D. Montemagno, *Science*, 2000, **290**, 1555–1558.
- 5 N. H. Arata and H. F. Fujita, *Appl. Phys. Lett.*, 2006, **88**, 083902.
- 6 H. Hess and V. Vogel, *Rev. Mol. Biotechnol.*, 2001, **82**, 67–85.
- 7 H. Hess, G. D. Bachand and V. Vogel, *Chem.–Eur. J.*, 2004, **10**, 2110–2116.
- 8 G. D. Bachand, S. B. River, A. Carroll-Portillo, H. Hess and M. Bachand, *Small*, 2006, **2**, 381–385.
- 9 S. Ramachandran, K.-H. Ernst, G. D. Bachand, V. Vogel and H. Hess, *Small*, 2006, **3**, 330–334.
- 10 T. A. Schmedake, F. Cunin, J. R. Link and M. J. Sailor, *Adv. Mater.*, 2002, **14**, 1270–1272.
- 11 E. Garcia, J. R. Kirkham, A. V. Hatch, K. R. Hawkins and P. Yager, *Lab Chip*, 2004, **4**, 78–82.
- 12 C. Brunner, H. Hess, K.-H. Ernst and V. Vogel, *Nanotechnology*, 2004, **15**, S540–S548.
- 13 R. Yokokawa, Y. Yoshida, S. Takeuchi, T. Kon, K. Sutoh and H. Fujita, *IEEE Trans. Adv. Packag.*, 2005, **28**, 577–583.
- 14 M. Sundberg, J. P. Rosengren, R. Bunk, J. Lindahl, I. A. Nicholls, S. Tagerud, P. Omling, L. Montelius and A. Mansson, *Anal. Biochem.*, 2003, **323**, 127–138.
- 15 T. J. Grove, K. A. Puckett, N. M. Brunet, G. Mihajlovic, L. A. McFadden, P. Xiong, S. von Molnar, T. S. Moerland and P. B. Chase, *IEEE Trans. Adv. Packag.*, 2005, **28**, 556–563.
- 16 W. Wang, *Int. J. Pharm.*, 2000, **203**, 1–60.
- 17 S. D. Allison, M. C. Manning, T. W. Randolph, K. Middleton, A. Davis and J. F. Carpenter, *J. Pharm. Sci.*, 2000, **89**, 199–214.
- 18 D. L. Coy, M. Wagenbach and J. Howard, *J. Biol. Chem.*, 1999, **274**, 3667–3671.
- 19 G. Bachand, personal communication.
- 20 H. Hess, J. Clemmens, D. Qin, J. Howard and V. Vogel, *Nano Lett.*, 2001, **1**, 235–239.
- 21 D. Wu, R. Tucker and H. Hess, *IEEE Trans. Adv. Packag.*, 2005, **28**, 594–599.
- 22 H. Hess, C. M. Matzke, R. K. Doot, J. Clemmens, G. D. Bachand, B. C. Bunker and V. Vogel, *Nano Lett.*, 2003, **3**, 1651–1655.

Part III: Label-free biosensing

*Pothi padi padi jag mua pandit bhaya na koy
dai akshar prem ke, pade so pandit hoye*

*- Kabir Das- mystic poet
15 th century
Language: Hindi*

My interpretation-

Reading books does not make one a pandit (scholar)

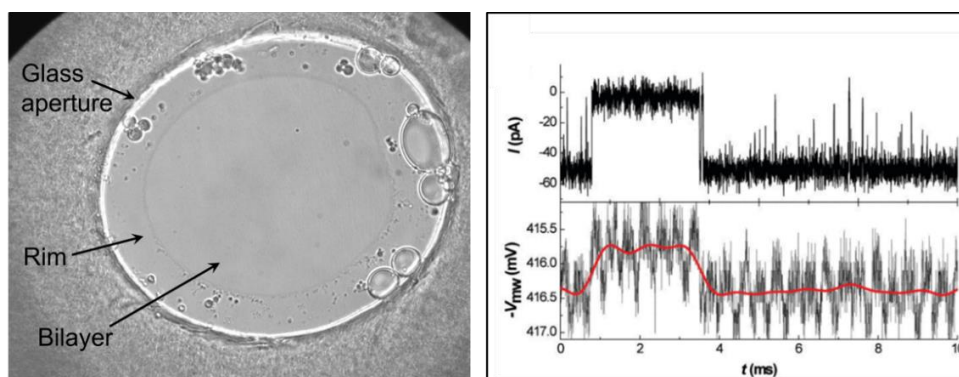
But, in the work you do with passion, you are the pandit!

Chapter 7

7 Electronic interface to biological pores in lipid bilayer for label-free biosensing*

The following chapter is based on two publications,¹⁴⁸ and ¹⁴⁹, in sections, 7.1 and 7.2 respectively. This chapter lays the groundwork for interfacing radiofrequency (RF) circuitry with biological pores in artificial lipid bilayer as a fast read-out technique for single-molecule real-time biosensing. The papers introduce the need for an ultra-broadband circuitry, in the MHz-GHz range, over the traditional patch-clamp recordings of ion channel currents in the dc regime. We first demonstrated the combination of transmission lines using micro stripline with an on-chip patch-clamp single-channel recording unit¹⁵⁰ (see **Appendix 11.6**).

In the two papers in the section 7.1 and 7.2, micro-coaxial probes were used to couple RF into the high-impedance channel in the lipid bilayer with Alamethicin (ALA) ion channels and α -hemolysin (α -HL) pore to study their response. The measurement results on the local interaction of an RF signal with single ion channels and pores are presented. In section 7.1, the rectification of the RF voltage and pumping of ions through the channel is presented. In section 7.2, the open-close state of the α -HL pore using β -cyclodextrin (β -CD), a channel blocker, is demonstrated by measuring changes in microwave-frequency transmission through the pore correlating simultaneously with conventional single-channel DC recordings.



Simultaneous recording of pore activity in a lipid bilayer direct current (top) and the RF transmission (bottom)

Reproduced from *Applied Physics Letters*, 2011, 99, 093105 with the permission of AIP publishing.

7.1 Radio frequency rectification on membrane bound pores*

Sujatha Ramachandran, Robert H. Blick, and Daniel W. van der Weide

Reproduced with permission from *Nanotechnology*, 2010 21 075201© IOP publishing

I designed the experiment, conducted the work, analyzed the results, and wrote the article together with other authors.

Radio frequency rectification on membrane bound pores

Sujatha Ramachandran, Robert H Blick¹
and Daniel W van der Weide

Electrical and Computer Engineering, University of Wisconsin-Madison, Madison,
WI 53706-1691, USA

E-mail: blick@engr.wisc.edu

Received 7 October 2009, in final form 23 December 2009

Published 18 January 2010

Online at stacks.iop.org/Nano/21/075201

Abstract

Probing the interaction of biological systems with radio frequencies holds great promise for research and drug screening applications. While a common assumption is that biological systems do not operate at radio frequencies, we find that currents due to ion transport through channels and pores in cell membranes are in the pA to nA range. These values translate via the average current $\langle I \rangle = \langle n \rangle e / \tau_d = \langle n \rangle e f$ to frequencies in the range of 1 MHz–1 GHz, where $\langle n \rangle$ is the average number of ions transported and τ_d is the dwell time of the ions in the channel. It is thus desirable to have circuitry available which facilitates radio frequency spectroscopy of ion transport. This will yield real-time *in vitro* information on ion channel operation. Here we present measurements on the local interaction of a radio frequency signal with single ion channels and pores. We find radio frequency rectification and pumping on the channels and pores embedded in suspended bilipid membranes, recorded in direct current measurements. This electromagnetic modulation can be used to probe the dynamics of ion channel conformational changes.

(Some figures in this article are in colour only in the electronic version)

1. Introduction

In studying the interaction of electromagnetic signals with biological systems the first consideration is to compare the Debye screening length of the molecule or protein under investigation in aqueous solution to the frequency of operation. For radio frequency (RF) signals this results in very strong attenuation due to the large dielectric constant of water ($\epsilon \sim 80$). This in turn requires higher signal power, heating the biological system. Hence, heating and rupture of membranes was found in previous work studying the effects of radio and microwave frequencies on ion channels in membranes [1–3]. Another hindrance is the low temporal resolution of probing single pore signals with bandwidths of ~ 10 kHz. This is due to the large access resistances (R) and membrane capacitance (C), leading to low time constants $\tau = RC$. We overcome these limitations by using micro-coaxial lines for delivering RF signals directly to ion channels and pore proteins embedded in suspended bilipid membranes, resulting in pumping of ions.

¹ Author to whom any correspondence should be addressed.

2. Ion channel preparation and measurement setup

The measurement setup is depicted in figure 1(a): a chamber combines a standard planar bilayer recording setup with a delrin cuvette for ion transport measurements on bilipid membranes with micro-coaxial lines. The chamber has a *cis*- and *trans*-side corresponding to drain and source contacts containing 1 M KCl and 10 mM HEPES (pH 7.3 in the total solution) in aqueous solution. The delrin cuvette has a ~ 200 μm pore onto which a lipid bilayer (1,2-diphytanoyl phosphatidyl choline in decane) is painted. This technique leads to the formation of a 4 nm thin phospholipid bilayer in the center of the pore spanning approximately 5 μm . Under optical inspection with a microscope the thicker rim can be clearly identified [4]. These membranes are ideal model systems, since they only contain phospholipids and no other proteins, which make them more stable for voltage–current recordings over a long period of time. The DC contacts (Ag/AgCl-wires) are simply dipped into the solution (*cis*-side grounded), similar to a standard membrane patch measurement [5]. A patch clamp amplifier Axopatch 200 B (Axon Instruments, Inc., Union City,

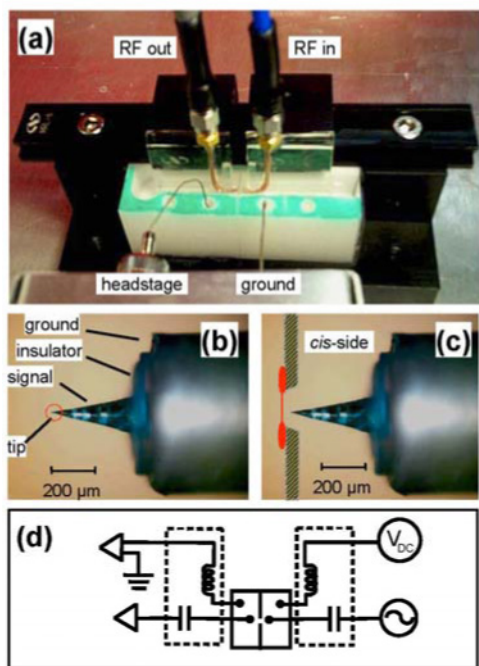


Figure 1. Experimental setup: (a) measurement chamber within a Faraday cage. Two coaxial lines enter from the top, feeding the micro-coaxes in the chamber (RF in/out). The direct current through the membrane is probed via Ag/AgCl-wires dipped into the *cis*- and *trans*-chambers. (b) Close-up of the micro-coax tip showing electrodes, insulating layer, and outer conductor. The whole micro-coax is coated with an insulator (parlylene). (c) Configuration in the experiment where the micro-coax is placed as close as possible at the suspended membrane, which is sketched spanning the aperture. (d) Circuit diagram for the AC/DC combination.

CA) was used for all the direct current measurements shown. The currents were low-pass filtered with a built-in four pole Bessel filter at 1 kHz and sampled at 10 kHz by computer with a Digidata 1320 analog-to-digital converter. The AC contacts (RF micro-coaxes) are brought in from the sides on optical reels to allow for exact positioning close to the suspended bilipid membrane. The alignment procedure is critical for this measurement, since it will determine the coupling efficiency of the coax line. The RF generator used was a Hewlett-Packard synthesizer (HP 83650A) generating a sinusoidal continuous wave excitation.

The whole chamber is mounted in a Faraday cage to achieve optimal shielding from spurious electromagnetic radiation. In figure 1(b) a magnified image of a typical micro-coax is depicted: the outer conductor is separated by a standard dielectric from the inner conductor, which tapers down to a tip of radius just below $1 \mu\text{m}$. The whole coax tip, which is immersed into the ionic solution of the *cis*-side chamber, is covered by parlylene to avoid surface potentials interfering with the DC measurement. Finally, the coax tip is mounted and positioned close to the bilipid membrane, about $10\text{--}15 \mu\text{m}$ away, as sketched in figure 1(c). The thicker edges and thin center of the membrane indicate the typical thinning process of painted membranes. In figure 1(d) an equivalent circuit is given: as seen, the two AC lines are DC blocked allowing the measurement of direct RF transmission. However, in the data

discussed here we focus on AC excitation and DC detection, i.e. only one micro-coax is brought to action.

3. Results on ion channels

The measurements were conducted in a fashion that first defined a stable bilayer and in a second step took current recordings of the insertion of the channel forming proteins. Only then was the RF signal switched on at a specific frequency and power level. We investigated two types of membrane proteins: Alamethicin (ALA), a fungal peptide which forms a voltage-gated ion channel [6], and α -Hemolysin (α -HL), which is a pore forming agent [7]. At a current level for ALA and α -HL of $20\text{--}50 \text{ pA}$ the ion transfer times correspond to values around $(1/100)\text{--}(1/300) \text{ MHz}^{-1}$.

For calibration purposes we first painted a bilipid membrane across the $200 \mu\text{m}$ aperture and recorded the direct current versus time trace shown in figure 2(a). The insulation resistance of the pure membrane is of the order of $16 \text{ G}\Omega$ (a bias of -40 mV is applied). Switching the RF source on we found a strong crosstalk signal, which decayed with a typical time constant of about 1 s . With a sinusoidal RF signal at 800 MHz the membrane resistance is reduced to about $8 \text{ G}\Omega$, as seen on the right-hand-side of figure 2(a). The time constant corresponds to the discharging time of the membrane, taking the membrane resistance of $R_m = 8 \text{ G}\Omega$ in the on-state and a calculated membrane capacitance of $C_m = 137 \text{ pF}$, we now find a time constant of $\tau_m = R_m C_m \sim 1 \text{ s}$. For calculations we assumed the membrane dielectric constant to be $\epsilon_m \sim 2$ [4] and a circular geometry of the membrane layer with diameter $200 \mu\text{m}$. After this initial spike the current relaxes to a non-zero value, already indicating an effective bias across the membrane. Although the power of the RF signal is comparatively high, with about $P = -15 \text{ dBm}$, we find only minimal heating effects, as evident in the increase of the DC current signal noise, indicated by the pairs of arrows (left and right) seen in the broadening of the current versus time trace.

The initial measurements were performed on ALA: these peptides were added to the *cis*-chamber and can be inserted into the membrane by a small DC bias voltage, due to their dipole moment of $\sim 75 \text{ D}$. In the membrane ALAs can combine in different numbers and form ion channels, as sketched in figure 2(b). Depending on the number of peptides, current through the ion channel scales accordingly to the cross sectional surface. These channels are only temporarily stable, i.e. their formation depends on the Brownian motion of the peptides in the membrane. The resulting current under a bias voltage of -20 mV is shown in figure 2(c). On the left side the typical ALA recording is found with predominantly smaller channels forming. After switching the RF signal on at 800 MHz and relaxation of the current spike we find a strongly enhanced current level. This already is a clear indication of an effective increase in DC bias by the RF voltage. This voltage enhances the current through the membrane by pumping the ions more effectively and increasing channel formation. We found several frequencies (between 750 and 850 MHz) at which the current through the pores could be increased, but best coupling was achieved at a frequency of

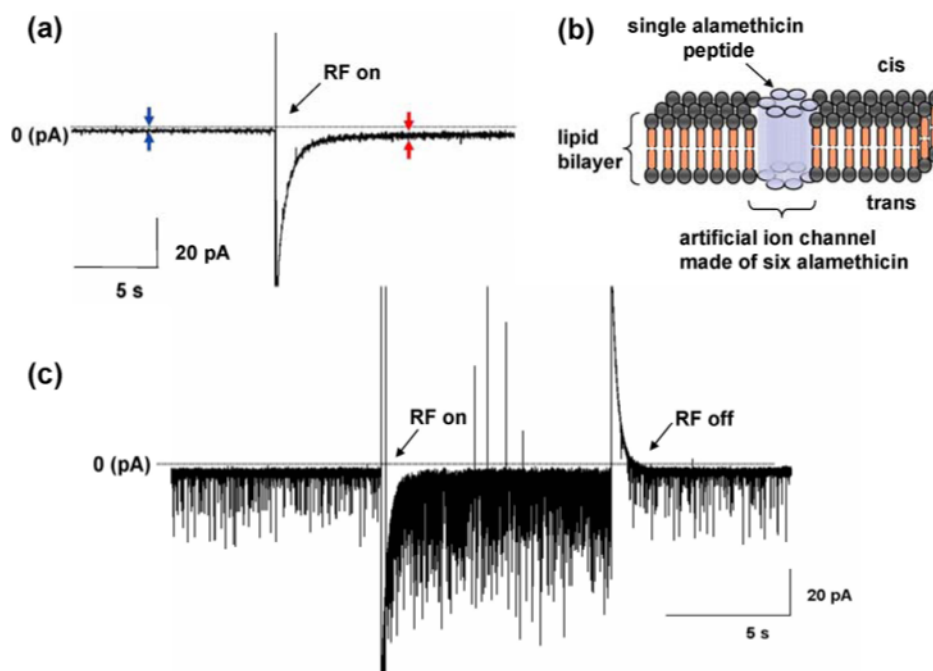


Figure 2. (a) Calibration measurement with a suspended bilipid membrane painted over a $200\ \mu\text{m}$ opening. Shown is the current versus time recording before and after the radio frequency (RF) signal at 800 MHz is turned on. This indicates a very good electrical insulation of the *cis*- and *trans*-side and minimal heating. (b) Sketch of six alamethicin peptides inserted into the suspended lipid bilayer. These peptides conjugate and form channels of different sizes. (c) Recording under $-20\ \text{mV}$ DC bias and 800 MHz applied. The RF signal is rectified and enhances the formation and current level of alamethicin channels, i.e. ions are more effectively pumped through the membrane.

800 MHz. All measurements were executed at this frequency. This is due to the geometry of the conducting elements and the dielectrics of the measurement cell, i.e. the location of the DC lines, the coaxes, the chip, the pore and membrane, and the aqueous solution in the chamber. Importantly, the RF signal at 800 MHz is faster and able to reverse (or pump) the flow of ions through the channels and pores with dwell times of $1/100\text{--}1/200\ \text{MHz}^{-1}$.

In figure 3 the measurements are repeated for different DC bias values: in (a) the conditions are identical except that the bias is inverted to $+20\ \text{mV}$. The ALA peptides are inserted into the membrane and show the typical current spikes. However, when the RF signal is turned on, ion channel formation is knocked off. Only after the excitation is again turned off do the ALA channels form again with the typical current trace. In figure 3(b) the measurements are repeated with zero bias applied. At zero bias no ALAs are inserted into the membrane and consequently no current spikes are obtained. Switching the RF signal on induces ion channel formation with an average channel current corresponding to an effective bias of about $-25\ \text{mV}$. So far, we can conclude that the application of an appropriate RF modulation corresponds to an effective DC voltage, which is applied to the membrane. This can be interpreted as rectification of the AC at the highly resistive bilipid membrane junction.

Conventionally, the term rectification refers to the conversion of an electromagnetic AC signal to a DC voltage across a junction. The junction's *IV*-characteristic has to be nonlinear of some form, which is the result of asymmetric barrier resistances and capacitances such as in a Schottky

diode. In DC measurements on ALA it was shown by Woolley *et al* [8] that the *IV*-relation of ALA is non-ohmic due to the electrostatic potential profile within this ion channel—this is also termed rectification. In more recent work by Siwy *et al* [9–11] asymmetric artificial nano-pores were fabricated in thin membranes. A similar rectification of ionic currents was found, being related to the asymmetry of the surface charges inside the nano-pore. Heins *et al* [12] finally have shown that this rectification effect can be enhanced by placing asymmetric molecular groups at the nano-pore. This so-called chemical rectification leads to a further increase of the non-ohmic response.

4. Results on pores

Obviously, the asymmetric potential along the ion channel or nano-pore determines the transport properties, i.e. the rectification effects should be reflected in the response to an AC excitation. This appears to be the case for the ion channel ALA. In order to determine how the potential and geometrical shape of the protein forming channel influences this rectification process and the resulting pumping of ions, other proteins have to be considered. Hence, we also employed the porin $\alpha\text{-HL}$ for the second line of experiments, which in contrast to ALA acts more like a DC resistor once inserted into the bilipid membrane [15, 16]. This is related to the fact that pores allow a constant flux of ions after insertion. There is no gating mechanism as for the ion channel ALA. Consequently, pores or *porins*, as they are sometimes called, lend themselves as a perfect 'calibration set'. Furthermore, it

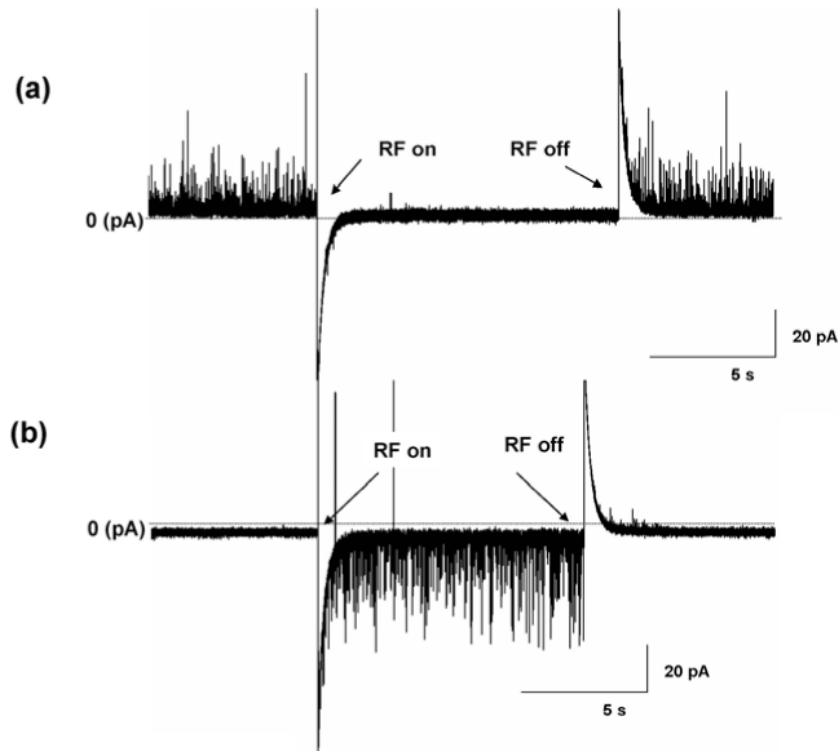


Figure 3. Bias variation on alamethicin under excitation: (a) At +20 mV bias the RF knocks off channel activity, leading to an effective pumping of ions against the bias. (b) RF triggers channel insertion at zero bias applied, i.e. rectification. Both results indicate rectification of the RF signal, since an effective DC voltage is present.

is important to note that α -HL is a protein, which possesses a highly asymmetric molecular structure, once inserted into the membrane (see figure 4(a)). The opening of the pore on the *cis*-side has a diameter of 2.9 nm, which widens into a mushroom-shaped vestibule of 4.2 nm in diameter and again narrows to an opening of 2 nm on the *trans*-side.

In figure 4(b) a simplified circuit diagram is shown: in parallel to the membrane resistance and capacitance we place a single α -HL pore with a resistance of $R_{\alpha\text{-HL}} = 1.1 \text{ G}\Omega$. Once α -HL is added to the *cis*-compartment of the setup it is inserted into the membrane with the head of the protein facing the RF signal and the current level rises to -35 pA under a bias of -40 mV . In figure 4(c) the direct current through the pore is shown with and without the RF signal. Evidently, switching the RF on results in a current spike, but with reduced relaxation time as compared to the ALA measurements (figures 2 and 3). This is related to the initial resistance of the system being an order of magnitude smaller $R_{\alpha\text{-HL}} \sim 1 \text{ G}\Omega < 9 \text{ G}\Omega \sim R_{\text{ALA}}$ and consequently $\tau_m \sim 100 \text{ ms}$. During RF emission the current through the pore is enhanced by 20 pA , indicating pumping of ions through the pore at a rate of $\tau = f^{-1} = 1/(800 \text{ MHz})$. This shows the possibility of real-time spectroscopy, i.e. the passage of single ions can now be resolved in the time domain. The current level of $|20 \text{ pA}|$ then translates to $n = I/(ef) = 0.16$ ions on average, which are pumped through the pore in each cycle of the RF signal ($f = 800 \text{ MHz}$). The increase by almost a factor of two in current again shows pumping of ions by the RF voltage. It is accompanied by a moderate increase in noise level.

A further test of AC rectification is given in figure 5 where we insert two α -HL pores. Naturally, this addition of a second resistance $R_{\alpha\text{-HL}}$ reduces the total resistance of the system to $0.5 \text{ G}\Omega$, while it increases the overall current through the membrane to -70 pA . This effect is seen in figure 5(a), where the two pores are monitored under -40 mV bias. After switching on the RF signal we again find the current spike. Now the RF signal increases the total current through the system to -110 pA , which is a linear offset of the α -HL I - V -characteristic expected. The subsequent relaxation process is accordingly even faster, at approximately 50 ms , than with a single pore. The determination of the actual pumping voltage induced by the RF voltage is depicted in figure 5(b): without the applied bias we find zero current through the pores, which changes once the RF is turned on. The total current through the two pores is -40 pA . From a linear extrapolation we find that an effective bias of $\sim |25 \text{ mV}|$ is induced by the RF voltage.

5. Theoretical background

So far the origin of the observed rectification process has not been sufficiently clarified. Considering, in a simplified model, the flux J_f of ions through an ion channel or pore it should follow in general the Nernst–Planck equation [13]

$$J_f = -\left(\frac{z\Gamma\Delta\phi}{\Re T}\right) \left(\frac{c_{\text{cis}} \exp\left\{\frac{z\Gamma\Delta\phi}{\Re T}\right\} - c_{\text{trans}}}{\exp\left\{\frac{z\Gamma\Delta\phi}{\Re T}\right\} - 1}\right), \quad (1)$$

where c_{trans} and c_{cis} are the ionic solution concentrations in the *cis*- and the *trans*-side, z is the valence of the ion, Γ

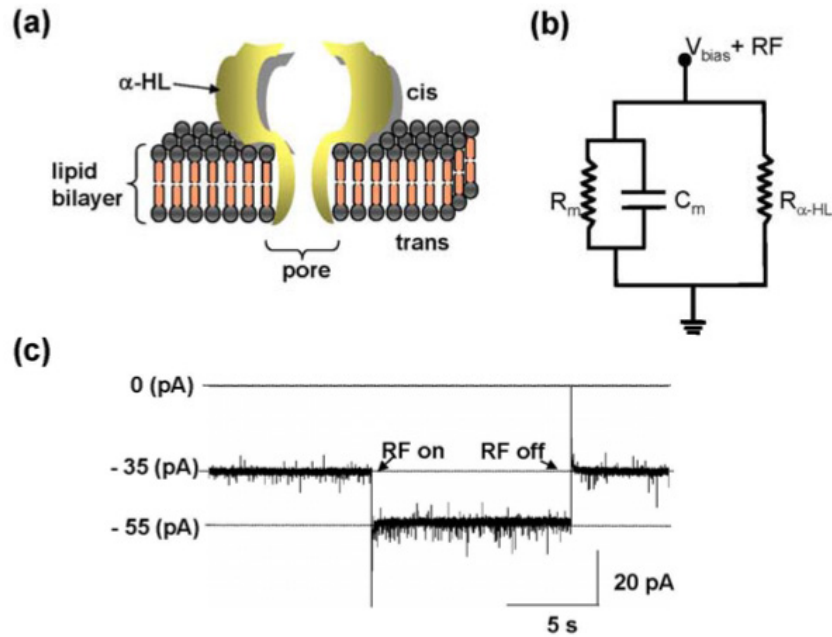


Figure 4. Measurements on a protein pore: (a) single α -HL after insertion into the bilipid membrane from the *cis*-side. The mushroom-like head of the protein faces the incoming RF signal. (b) Circuit diagram with membrane resistance and capacitance, R_m and C_m respectively, and the α -HL as a lumped resistor with $R_{\alpha\text{-HL}} \sim 1.1 \text{ G}\Omega$. (c) Current through a single α -HL pore with the standard level at -35 pA , which is enhanced to about -55 pA under RF pumping at -40 mV bias.

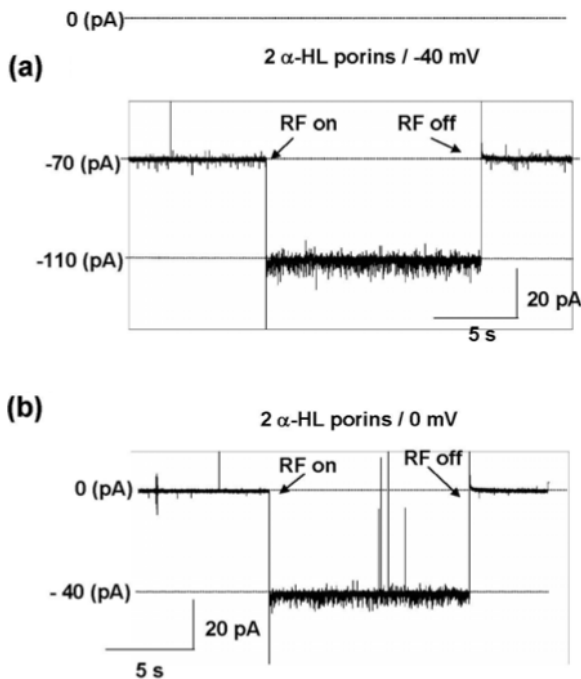


Figure 5. Measurements on two α -HLs inserted in the membrane: (a) as expected the current level is raised to -70 pA under a bias of -40 mV without RF and then further increased under RF excitation. (b) Same measurement at zero bias and 800 MHz RF signal, resulting in a current level of -40 pA , which corresponds to a rectified voltage of around $|25 \text{ mV}|$.

Faraday's constant, \Re the gas constant, and T the temperature. The potential gradient $\Delta\phi$ applied along the ion channel or pore in this approximation is assumed to be linear. Obviously,

equation (1) is a nonlinear relation for the flux based on the different salt concentrations in both reservoirs. The relation of ion flux to the direct current is given by $I = z\Gamma J_f$, where we quoted only one ion concentration for simplicity. However, in the measurements conducted here we adjusted the ion concentrations so that $c_{\text{trans}} = c_{\text{cis}}$. This leaves a linear relation for the channel current

$$I = z\Gamma J_f = -\left(\left[\frac{z^2\Gamma^2}{\Re T}\right]\Delta\phi\right) = R^{-1}V, \quad (2)$$

with the resistance R and assuming a linear potential drop $\Delta\phi(x) = V$, we find Ohm's law. Now rectification can only occur, if the potential along the channel $\phi(x)$ leads to a nonlinear potential drop, as is the case for ALA [8, 14] or if the nonlinearity is caused by an asymmetry of the molecular groups of the pore, as is the case for α -HL [15]. Hence, we can conclude that RF rectification occurs due to the combination of a channel's potential or shape asymmetry and the high overall junction resistance. In this case an effective DC voltage arises and ions are actively pumped through the channel.

This pumped current can now be applied as a spectrometric tool for studying the channels: the classical method to modulate the current through α -HL is to add a small molecule, such as β -cyclodextrin (β -CD) [15, 16]. This sugar component is ring-shaped with an outer and inner diameter of 1.5 and 0.78 nm , respectively. Hence, β -CD can propagate inside the pore, but is finally blocked at the neck of the α -HL, thus reducing the total current through the pore, as indicated in figure 6(a). For the measurements, we used the configuration with two α -HL pores as before, but now in the mode where one of the pores is blocked by β -CD (added to the *trans*-side). In this blocking mode the current through one

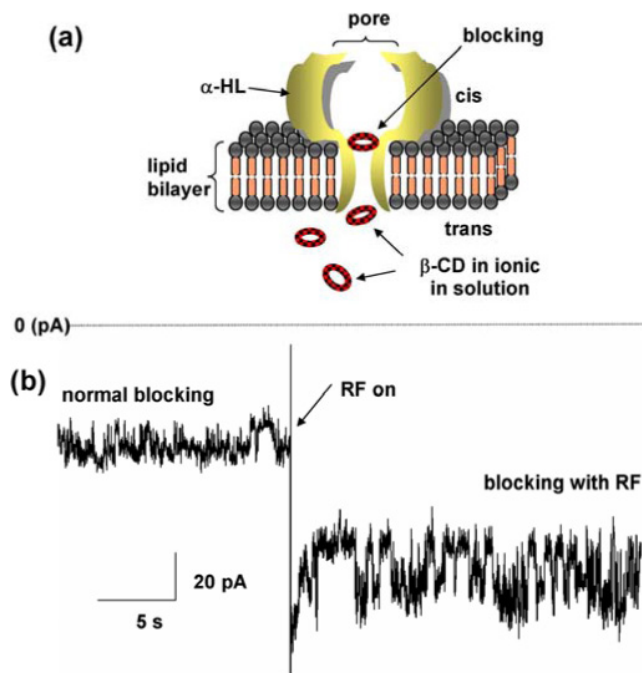


Figure 6. Modulation of current blocking in two α -HL porins using β -CD: (a) the ring-shaped sugar component β -CD is added to the *trans*-side of the solution. Its diameter allows it to enter the pore and reduce ion flux, due to the smaller neck diameter in the pore. (b) Two α -HL pores blocked with an increased current noise at -40 mV DC bias. After turning on the RF signal, ions are pumped more effectively through the pores with strongly increased noise level. This indicates direct mechanical modulation of the β -CD inside the pores—compare the pumped current in figure 5.

channel is reduced to about -15 pA while the other channel maintains a current of -35 pA. This yields a total average current of -50 pA, down from -70 pA in the open state of both channels (bias of -40 mV). Evidently, the current noise level is already increased, which can be attributed to the thermally induced motion of β -CD in the channel. Switching on the RF signal reveals a further increase in current noise and an average current around 100 pA. Assuming that one channel is not blocked, its current level increases under RF pumping from -35 to -55 pA, then the blocked channel's current is pushed up from -15 to -45 pA, almost to the open state. The important point in these measurements is that the RF signal gives a method at hand to modulate the channel current actively with which, in this case, the β -CD is 'wiggled' around. Further studies can now reveal the details of the *in vitro* interaction of β -CD with α -HL.

6. Conclusion

In summary we have shown that coated micro-coaxes can be applied successfully for delivering RF signals to ion channels and pores in bilipid membranes. The DC recordings revealed a very good seal resistance, which enabled RF recordings with an unprecedented signal-to-noise ratio. We find rectification of the RF voltage, with a resulting voltage which can be used for pumping ions through the channels. This method is shown to have potential for real-time spectroscopy on molecular channels and for drug screening applications.

Acknowledgments

We like to thank Hagan Bayley for providing the α -HL pores, Meyer Jackson and Sergey Bezrukov for helpful discussions. This work has been supported in part by the Defense Advanced Research Projects Agency under the MOLDICE grant.

References

- [1] Tyazhelov V V, Alekseyev S I and Grigorev P A 1979 *Biophysics* **23** 750
- [2] Sandblom J and Theander S 1991 *Bioelectromagnetics* **12** 9
- [3] Alekseev S I and Ziskin M C 1995 *Bioelectromagnetics* **16** 124
- [4] Katsaras J and Gutberlet T 2001 *Lipid Bilayers: Structure and Interactions* (Berlin: Springer)
Mueller P, Rudin D O, Tien H T and Wescott W C 1962 *Nature* **194** 979
- [5] Fertig N, Blick R H and Behrends J C 2002 *Biophys. J.* **82** 3056
- [6] Eisenberg M, Hall J E and Mead C A 1973 *J. Membr. Biol.* **14** 143
- [7] Gouaux E 1998 *J. Struct. Biol.* **121**, 110
- [8] Woolley G A, Biggin P C, Schultz A, Lien L, Jaikaran D C J, Breed J, Crowhurst K and Sansom M S P 1997 *Biophys. J.* **73** 770
- [9] Siwy Z, Gu Y, Spohr H A, Wolf-Reber A, Spohr R, Apel P and Korchev Y E 2002 *Europhys. Lett.* **60** 349
- [10] Siwy Z and Fulinski A 2002 *Phys. Rev. Lett.* **89** 198103
- [11] Siwy Z, Kosinska I D, Fulinski A and Martin C R 2005 *Phys. Rev. Lett.* **94** 048102
- [12] Heins E A, Baker L A, Siwy Z S, Mota M O and Martin C R 2005 *J. Phys. Chem. B* **109** 18400
- [13] Jackson M B 2006 *Molecular and Cellular Biophysics* (Cambridge: Cambridge University Press)
- [14] Mark S P 1991 *Prog. Biophys. Mol. Biol.* **55** 139
- [15] Gu L Q, Braha O, Conlan S, Cheley S and Bayley H 1999 *Nature* **398** 686
- [16] Gu L Q and Bayley H 2000 *Biophys. J.* **79** 1967

7.2 Direct microwave transmission on single alpha-hemolysin pores*

Sujatha Ramachandran, Daniel W. van der Weide and Robert H. Blick

Reproduced from *Applied Physics Letters*, 2011, 99, 093105 with the permission of AIP publishing.

I designed the experiment, conducted the work, analyzed the results, and wrote the article together with other authors.

Direct microwave transmission on single α -hemolysin pores

Sujatha Ramachandran, Daniel W. van der Weide, and Robert H. Blick^{a)}

University of Wisconsin-Madison, Electrical & Computer Engineering, Madison, Wisconsin 53706-1691, USA

(Received 1 April 2011; accepted 28 July 2011; published online 31 August 2011)

We integrated an ultra-broadband microwave circuit for direct sampling of single α -Hemolysin pores in a suspended bilipid membrane. Simultaneous direct current recordings reveal that we can monitor and correlate the radio-frequency transmission signal, with correspondence between open-close states of the direct current and the RF signals. This proves the ability of an RF-readout technique to perform real-time *in-vitro* recordings of pores. The technique thus holds great promise for research and drug screening applications, since the sampling rate of single channels can be drastically enhanced and the recording bandwidth allows for tracking the passage of single ions.

© 2011 American Institute of Physics. [doi:10.1063/1.3626586]

Information processing in biological systems is a highly complex task, which relies heavily on parallel processing. Due to this complexity, signal transduction times of cellular systems can afford to be fairly slow with 1–100 ms for action potentials,¹ as compared to current state-of-the-art semiconductor transistors operating in the sub-ns regime. This comparison can be pushed further, by analyzing how cellular currents are gated via ion channels embedded in cellular membranes. In contrast to semiconductor transistors, these “bio-transistors” reveal not only electrical gating, but are also sensitive to mechanical stress and to chemical gating effects.

An estimate for the frequencies at which these “bio-transistors” operate can be obtained by considering ion transport through channels and pores by a simple argument: one finds current levels of the order of some pA to some nA. These currents correspond to frequencies in the range of 1 MHz to 1 GHz, where assume for the current the relation $I = e \tau_d^{-1} = e f$. The time interval τ_d is the dwell time of the ions in the channel and f is the corresponding frequency. Consequently, one wants to have circuitry available with which radio frequency (RF) spectroscopy of ion transport can be traced on the ns-time scale. As a result such an approach can yield real-time recordings of ion channel operation.² In the following, we present high-bandwidth radio-frequency data on single α -hemolysin (α -HL) pores.^{3–5} This enhances the coupling strength and is compared to direct current recordings. In tracing transmission of the microwave signal and comparing this to the DC signal, we find a coincidence of the open and blocked states of the porin α -HL, as will be discussed below in detail.

For the interaction of electromagnetic signals with biological systems, the first consideration is usually to compare the Debye screening length λ_D in an aqueous solution to the frequency of operation. For electromagnetic radiation in the RF range, this results in very strong attenuation (the dielectric constant of water is $\epsilon \sim 80$). Typically measurements are then performed at higher power levels. This in turn leads to heating of the biological materials under investigation. Consequently, rupture of bio-membranes is most often found in previous

studies with radio and microwave frequencies on ion channels.^{6–8} Furthermore, one has to consider the large access resistance (R) and cross capacitance (C), leading to time constants ($\tau = RC$) which translate into very narrow measurement bandwidths ($BW = 1/\tau$) of below 100 kHz. These limitations can be overcome by using micro-coaxial lines for delivering the RF signal point blank to ion channels and pore proteins embedded in suspended bilipid membranes, leading to pumping of ions through the ion channels and pores, respectively. In earlier work, we have shown that applying an RF signal to single ion channels and pores leads to a rectified voltage, which in turn can pump ions through the molecular pore.⁹ In the present study, we are extending this method to perform true RF transmission recordings in which the applied RF signal is picked up by a second microcoax.

The measurement setup for being able to transduce the RF response of the pores embedded in bilipid membranes is depicted in Fig. 1. A Delrin cuvette chamber has two compartments, i.e., *cis*- and *trans*-side corresponding to drain and source contacts, which contain the aqueous ionic solution with a concentration of 1 M KCl, 10 mM HEPES (pH 7.5)

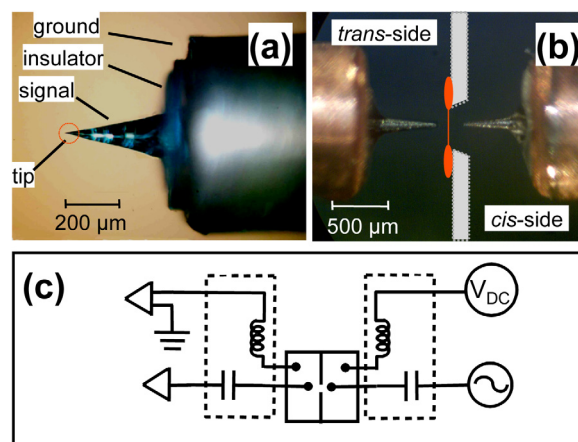


FIG. 1. (Color online) Measurement setup: (a) close-up of a micro-coaxial tip. The micro-coax is coated with a bio-compatible insulator. (b) Two micro-coaxes placed as close as possible on opposite sides of the suspended membrane for direct transmission measurements. The nanopore is placed in the bilipid membrane (sketched red line) between the two micro-coaxes. (c) Circuit diagram for the combined DC and RF measurements.

^{a)} Author to whom correspondence should be addressed. Electronic mail: blick@engr.wisc.edu. Tel./FAX: +1 (608) 262-1952.

for c_{cis} and c_{trans} . The compartments are separated by an insulating thin film with a 200 micron opening, onto which a lipid bilayer is painted. Planar lipid bilayer membranes were formed from 1,2-diphytanoyl phosphatidylcholine (DiPhyPC) in decane (Avanti Polar Lipids, Inc., Alabaster, AL) across the 200 micron orifice. The compartments were connected to an integrating patch clamp amplifier (Axopatch 200 B, Axon Instruments, Inc., Union City, CA) via a pair of Ag/AgCl electrodes in 0.5 M KCl, 1% agar bridges. The pore forming agent α -HL was then added to one side, the *cis*-chamber to a final concentration of 0.1 $\mu\text{g/ml}$. The *trans*-compartment was connected to the headstage of the amplifier, and the *cis*-compartment was held at virtual ground. The bilayer was held at varying positive and negative DC bias. Resulting currents were low-pass filtered with a built-in 4-pole Bessel filter at 1 kHz and sampled at 10 kHz with a Digidata 1320 A/D converter.

The AC contacts (RF micro-coaxes) are brought in from the sides on optical rails to allow for exact positioning close to the suspended bilipid membrane. The alignment procedure is critical for this measurement, since it determines the coupling efficiency of the coax-line. We were able to bring the coaxes as close as 10 microns to the suspended bilipid membrane. The RF generator used was a Hewlett-Packard synthesizer (HP 83650A) generating a sinusoidal continuous wave excitation. The whole chamber is then mounted in a Faraday cage to achieve optimal insulation from spurious electromagnetic radiation. In Fig. 1(a), a magnified image of a typical micro-coax is depicted: the outer conductor is separated by a standard dielectric from the inner conductor, which tapers down to a tip with tip radius just below 1 μm . Both coax-tips, which are immersed into the ionic solution of each side of the chamber, are covered with parylene to avoid surface potentials interfering with the DC measurement. Finally, the coax-tips are mounted and positioned close to the bilipid membrane, as sketched in Fig. 1(b). The thicker edges and thin center of the membrane indicate the typical thinning process of painted membranes. Signal coupling of the RF-lines was achieved by bringing them as close to each other as possible. In Fig. 1(c), an equivalent circuit is given: as seen the two AC lines are DC-blocked allowing the measurement of direct RF-transmission, avoiding cross-talk to the amplifier in the headstage.

The measurements were conducted as follows: we first defined a stable bilayer and in the next step took recordings of the insertion of the channel-forming proteins. Then the RF-signal was switched on at a specific frequency and power level. In these experiments, the mushroom-shaped top of α -HL is facing the *cis*-side. We found several frequencies at which the current through the pores could be increased, but best coupling in the present experiment was achieved at a frequency of $f = 788$ MHz. All measurements were executed at this frequency. This is due to the geometry of the conducting elements and the dielectrics of the measurement cell, i.e., the location of the DC-lines, the coaxes, the chip, the pore and membrane, and the aqueous solution in the chamber. At a current level of about -50 pA for α -HL, the ion transfer times correspond to of values around $(1/300)$ MHz $^{-1}$. Importantly, the RF signal at 788 MHz is larger and able to pump ions through the pore.

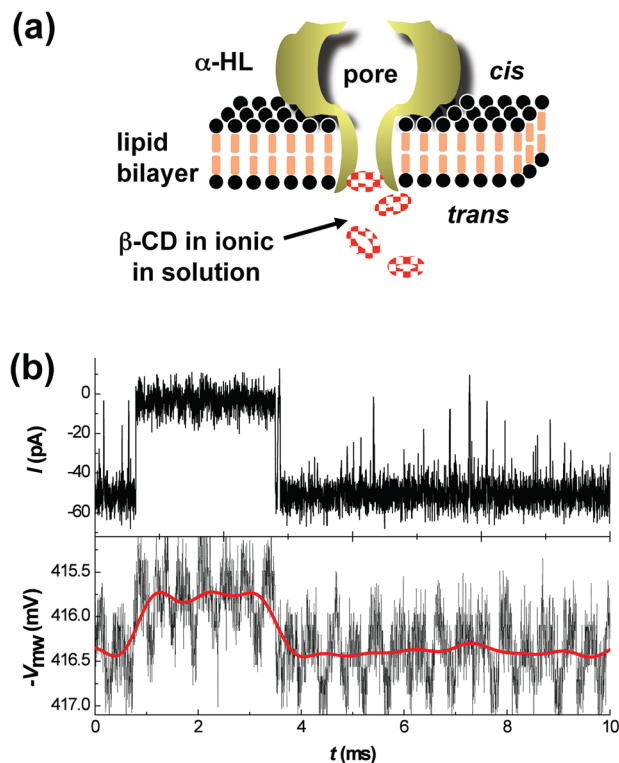


FIG. 2. (Color online) Measurements on a protein pore: (a) Single α -HL in combination with “blocker” β -cyclodextrin (β -CD). The β -CD fits into the pore, but cannot pass through it. It serves as a current modulation mechanism. (b) Comparison of DC recordings (top) and direct RF-transmission (bottom). As seen, the transmitted RF-signal at 788 MHz is tracing the conventional signal.

For calibration purposes of the absolute seal resistance, we first painted a bilipid membrane across the 200 μm aperture and recorded the direct current vs. time. The insulation resistance of the pure membrane is of the order of 16 G Ω (a bias of -40 mV is applied). The membrane capacitance was found to be of the order of $C_m = 137$ pF. The resistance of a single inserted pore is indicated as $R_{\alpha\text{-HL}}$. The typical resistance of a single pore is $R_{\alpha\text{-HL}} = 1.1$ G Ω with a neck diameter of ~ 2 nm.

Although the power of the RF-signal is comparatively high with about $P = -15$ dBm, we find in the calibration measurements only minimal heating effects. In previous measurement, we found⁹ that the application of a radio frequency signal yields an effective pumping voltage of the order of some $|20|$ – $|40|$ mV by which ions are pumped through ion channels and molecular pores. Comparing the width of the current trace prior and after turning the RF-signal on, only a minimal increase is found. In addition, the current level returns to its previous level, once the signal is turned off. Hence, we are confident that we can safely apply an RF-modulation without damaging the membranes’ properties.

For the direct transmission measurements we report on here, we employed porin α -HL which in contrast to ion channels acts more like DC resistor once inserted into the bilipid membrane.^{3–5} This is related to the fact that the pores allow a constant flux of ions once inserted. There is no direct gating mechanism as for the ion channels. The classical method to modulate the current through α -HL is to add a small molecule, such as β -cyclodextrin (β -CD), as also indicated in

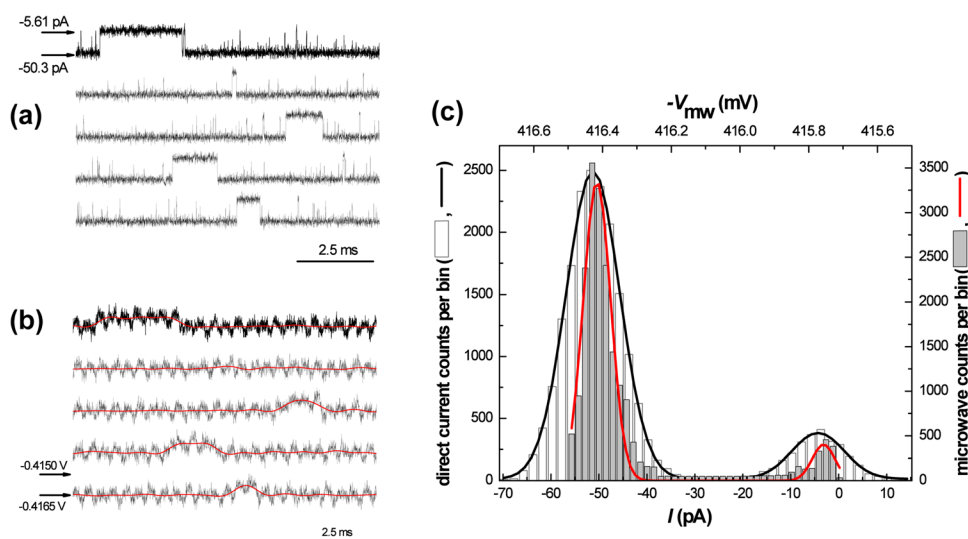


FIG. 3. (Color online) (a) Sampling the direct current through a single α -HL blocked by β -CD. (b) Corresponding RF-traces mapping the β -CD blocking events capacitively. (c) Summary of total measurements in a histogram: the solid black line shows a Gaussian distribution of the open and blocked events for the current bins. The red line shows the RF-signal bins for the corresponding events also as a Gaussian.

Fig. 2. This sugar component is ring-shaped with an outer and inner diameter of ~ 1.66 nm and ~ 0.7 nm, respectively. Hence, β -CD can propagate into the pore, but is finally blocked at the neck of the α -HL, thus reducing the total current through the pore, as shown in the upper trace of Fig. 2(a). For the measurements, we used the configuration with a single α -HL pore embedded into the membrane from the *cis*-side being blocked by β -CD from the *trans*-side. In this blocking mode, the current through the pore is reduced to about -5 pA. In the lower trace of Fig. 2(b), the microwave transmission of one micro-coax tip to the other is shown (see experimental geometry in Fig. 1(b)). The measurements are taken with a bandwidth of 3 MHz as compared to the DC data where we reduced the filter width down to 10 kHz. Hence, the RF-data trace is quite noisy. The RF-signal is averaged and finally represented by the red line. The capacitive coupling we estimate to be of the order of 50 aF. As seen, we find a correlation of the blocking events in the direct current and the RF-transmission.

Similar for standard DC recordings, we traced the opening/blocking events over longer time scales for analysis, as represented in Figs. 3(a) and 3(b). Obviously, the signal-to-noise ratio for the conventional recordings is still superior to the RF-traces. Nevertheless, we are able to pick up the small changes in capacitance, once the molecular pores are blocked. The summary of the measurements is depicted in the histograms of Fig. 3(c): it shows bins of *open* and *blocked* distributions for the case of DC recordings I and RF-transmission V_{mw} . As seen in the histogram for the DC-counts for the open channel show the expected Gaussian dis-

tribution. In contrast to this, the RF-counts obtained at a bandwidth of 3 MHz show a Gaussian with a much narrower distribution for the blocked as well as for the open state. At the current resolution, this is attributed to the filtering required for retrieving the RF-signal.

In summary, we have shown that the micro-coaxes can be applied for delivering and picking up RF-signals to molecular pores in bilipid membranes. We find direct transmission modulation in clear coincidence with direct current recording. This method provides evidence for the potential of real-time spectroscopy on single molecular channels and points towards future applications in high-throughput drug screening applications.²

This work has been supported in part by the Defense Advanced Research Projects Agency (DARPA) under the MOLDICE Grant (49620-03-1-03837). RHB likes to thank Meyer Jackson and Robert Pearce for detailed discussions.

¹M. B. Jackson, *Molecular and Cellular Biophysics* (Cambridge University Press, Cambridge, 2006).

²N. Fertig, R. H. Blick, and J. C. Behrends, *Biophys. J.* **82**, 3056 (2002).

³E. Gouaux, *J. Struct. Biol.* **121**, 110 (1998).

⁴L.-Q. Gu, O. Braha, S. Conlan, S. Cheley, and H. Bayley, *Nature* **398**, 686 (1999).

⁵L.-Q. Gu and H. Bayley, *Biophys. J.* **79**, 1967 (2000).

⁶V. V. Tyazhelov, S. I. Alekseyev, and P. A. Grigorev, *Biophys.* **23**, 750 (1979).

⁷J. Sandblom and S. Theander, *Bioelectromagnetics* **12**, 9 (1991).

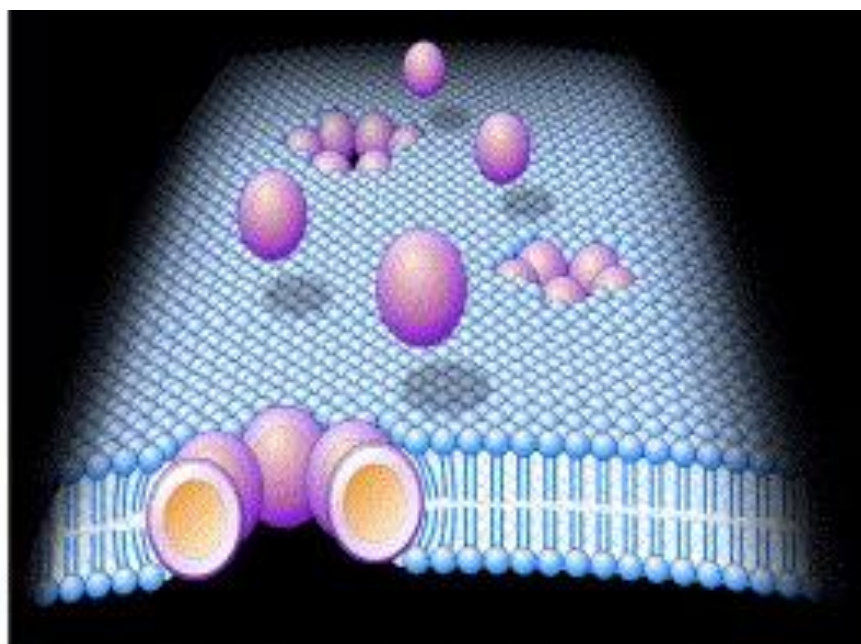
⁸S. I. Alekseev and M. C. Ziskin, *Bioelectromagnetics* **16**, 124 (1995).

⁹S. Ramachandran, R. H. Blick, and D. W. van der Weide, *Nanotechnology* **21**, 075201 (2010).

Chapter 8

8 Interaction of quantum dots with lipid bilayer membrane*

This chapter is based on the publication ¹⁵¹ and describes colloidal quantum dots initiating current bursts in lipid bilayers. The chapter starts with an introduction to applications of colloidal quantum dots (QDs) as fluorescent labels. Many of the applications of QDs in biology have been for cell staining. Hence their interaction with the cell membrane is of significant interest. The interactions of QDs with lipid membrane in an electric field using a planar lipid bilayer experimental setup was examined. Different voltage bias for different QD concentrations was tested. Pore formation with various sizes of QDs in the lipid membrane was calculated.



Mechanism of QD insertion into the lipid bilayer

Reproduced from *Applied Physics Letters* 2005, 86, 083901 with permission from AIP publishing.

8.1 Current bursts in lipid bilayers initiated by colloidal quantum dots*

Sujatha Ramachandran, George L Kumar, Robert H Blick, Daniel W Van Der Weide

Reproduced from *Applied Physics Letters* 2005, 86, 083901 with permission from AIP publishing.

I designed the experiment, conducted the work, and analyzed the data. Together with the other authors I discussed the results and wrote the paper.

Current bursts in lipid bilayers initiated by colloidal quantum dots

Sujatha Ramachandran, George L. Kumar, Robert H. Blick,^{a)} and Daniel W. van der Weide
*LMSE-Laboratory for Molecular Scale Engineering, Electrical and Computer Engineering,
 University of Wisconsin-Madison, Wisconsin 53706*

(Received 13 August 2004; accepted 20 December 2004; published online 17 February 2005)

Inorganic semiconductor nanocrystals, also called quantum dots, have recently attracted considerable interest as fluorescent labels. We report that CdSe QDs initiate current bursts in lipid bilayer membranes upon application of a bias voltage. The current bursts observed resemble those produced by the peptaibol class of antibiotics such as alamethicin and trichorzins. The current fluctuations are dependent on the bias voltage and on the concentration of the quantum dots applied to the membrane. Our data suggest that quantum dots with dipole moments similar to alamethicin are influenced by an external electric field, which creates a torque resulting in the insertion into the lipid membrane. We predict that at least three quantum dots are required to form a pore due to aggregation that leads to a macroscopic conductance. © 2005 American Institute of Physics. [DOI: 10.1063/1.1862752]

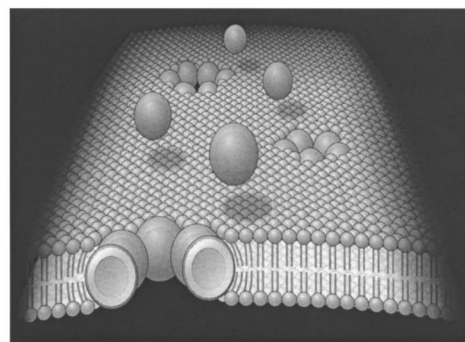
Inorganic semiconductor nanocrystals, also called colloidal quantum dots (QDs), are useful fluorescent labels for staining cells. Because of their size dependent color, their resistance to photobleaching, and size scale of less than 10 nm, they are becoming popular in many interesting biomedical applications ranging from intracellular tagging of biological molecules to applications such as tracking devices for neuronal receptors and as interfaces between nerve cells.^{1,2} Because many of the applications of QDs in cell biology involve interaction with lipid bilayer membranes, the behavior of QDs on these structures is of significant interest. We chose planar lipid bilayers as our study material since they form the basis of a simple model system for eukaryotic cell membranes where many ion channel and receptor activity studies have been conducted.³ A planar lipid bilayer is about 5 nm thick and composed of two layers of self-assembled amphiphilic lipid molecules such as phospholipids arranged so that their hydrocarbon tails face one another to form the hydrophobic core while their electrically charged polar heads face the aqueous solution on either side of the membrane [Fig. 1(a)].

In this letter, we study the behavior of colloidal QDs in planar lipid bilayers as indicated in Fig. 1(a) using electrical recording techniques.⁴ The QDs used in this study were colloidal CdSe nanocrystals. Three different QDs were used: (a) CdSe cores in toluene (Evident Technologies, Troy, NY), (b) Custom-made water-soluble CdSe cores with a ZnS shell coated with a polymer (Evident Technologies, Troy, NY), and (c) water-soluble streptavidin-conjugated CdSe cores with ZnS shell (Quantum Dot Corporation, Hayward, CA). To study their size QDs were deposited onto formvar free carbon film supported by a 300 mesh copper grid (Ted Pella, Inc., Redding, CA) and examined using a Philips CM120 transmission electron microscope operated at an accelerating voltage of 60 kV (300 000 \times). The average sizes of the QDs were: core CdSe QDs=(2.2 \pm 0.5) nm, water-soluble polymer coated CdSe/ZnS QDs=(3.2 \pm 0.5) nm, and the core/shell di-

ameter of water-soluble streptavidin-conjugated QDs = (5.7 \pm 0.8) nm.

Planar lipid bilayer membranes were formed from 1, 2-diphytanoyl phosphatidylcholine (DiPhyPC) in decane (Avanti Polar Lipids, Inc., Alabaster, AL) across a 200- μ m-diam orifice in a Delrin cuvette (Warner Instruments, Inc., Hamden, CT), separating two aqueous compartments containing 1 ml of 1 M KCl, 10 mM HEPES, at pH 7.5

(a)



(b)

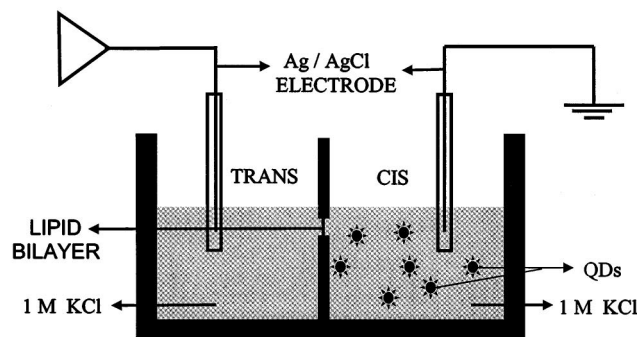


FIG. 1. (a) Suggested mechanism of QD insertion into the lipid bilayer membrane. When a membrane is polarized by an applied potential, QDs possessing a dipole moment insert into the membrane and form pores. (b) Schematic diagram of the measurement setup.

^{a)} Author to whom correspondence should be addressed; electronic mail: blick@engr.wisc.edu

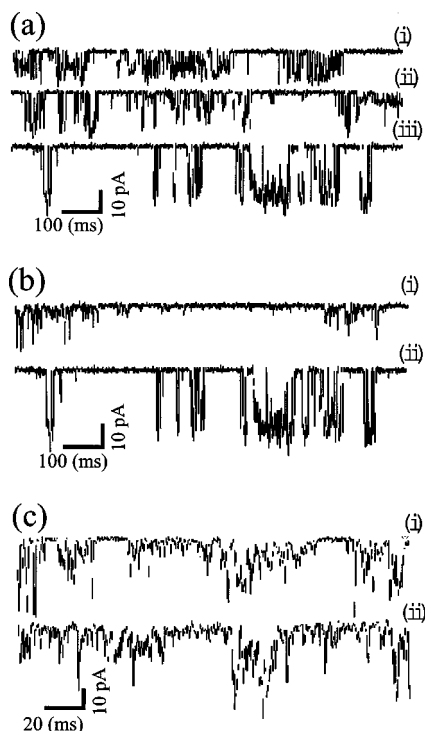


FIG. 2. Current fluctuations measured across the lipid bilayer in the presence of QDs. (a) Voltage-dependent current bursts in the presence of streptavidin-conjugated QDs at a concentration of 6 nM in a buffer containing 1 M KCl, 10 mM HEPES pH 7.5. Bias voltages are (i–iii) -30 , -40 , and -50 mV, respectively. (b) Current fluctuations under two different concentrations of streptavidin-conjugated QDs at a bias of -50 mV: (i) at 3 nM and (ii) at 6 nM. (c) Current bursts for (i–ii) 2.2 and 3.2 nm QDs, respectively, at -50 mV bias.

(23°C). A schematic diagram of the measurement setup is shown in Fig. 1(b). The compartments were connected to an integrating patch clamp amplifier (Axopatch 200 B, Axon Instruments, Inc., Union City, CA) via a pair of Ag/AgCl electrodes in 0.5 M KCl, 1% agar bridges. QDs of varying concentrations were added to the *cis* side of the chamber. The *trans* side was connected to the head stage of the amplifier, and the *cis* compartment was held at virtual ground. Resulting currents were low-pass filtered with a built-in four-pole Bessel filter at 1 kHz and sampled at 10 kHz by computer with a Digidata 1320 analog-to-digital converter. As a control, 5 nm streptavidin-conjugated gold particles (Ted Pella, Inc., Redding, CA), were added to the *cis* side to a final concentration of 3.4×10^{11} gold particles/ml to study their effects on the lipid bilayer in the presence of voltage bias ranging from 0 to 200 mV. No current was recorded for the gold particles.

Figure 2 represents the traces of current fluctuations measured across the lipid bilayer in the presence of the three different QDs used in our experiment. As shown in Fig. 2(a), we found a voltage dependent current flow through the membrane in the presence of streptavidin-conjugated CdSe/ZnS QDs on application of a negative voltage. Also, increasing the concentration of the QDs resulted in increased conductance [Fig. 2(b)]. Similar current bursts across the lipid bilayer were observed with the core CdSe and polymer-coated CdSe/ZnS QDs [Fig. 2(c)]. Although the current exhibits a stochastic pattern without discrete levels, the effect is repeatable at a given voltage and QD concentration. Figure 3 shows the current burst frequency distribution histograms

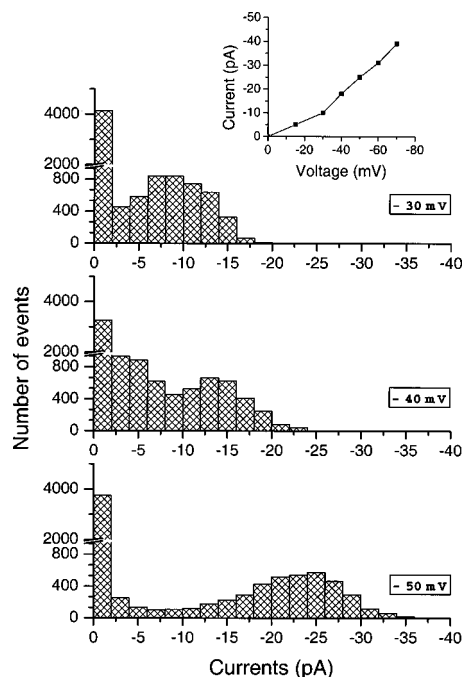


FIG. 3. Current burst frequency distribution histogram of streptavidin-conjugated QDs at varying voltage. Inset shows a current/voltage plot for the streptavidin-conjugated QDs.

and a current/voltage plot showing the ohmic nature of the current burst (plotted in the inset). Furthermore, we observed that reverse voltage bias did not elicit current bursts [Fig. 4(a)]. A control experiment using 5 nm streptavidin-conjugated gold particles failed to elicit current fluctuations [Fig. 4(b)].

Our data suggest: (I) QDs do not diffuse readily through the dielectric bilayer membrane, because the lipid bilayer forms a barrier to diffusion of ions and polar molecules larger than about 150 Daltons. (II) The current bursts we observe with QDs are very similar to alamethicin, a polypeptide antibiotic, which aggregates and forms voltage-dependent ion conducting pores in lipid membranes.⁵ It has been suggested that the alamethicin monomer is about 3.5 nm in length and carries a dipole moment of approximately 75 D units, which is responsible for the voltage-

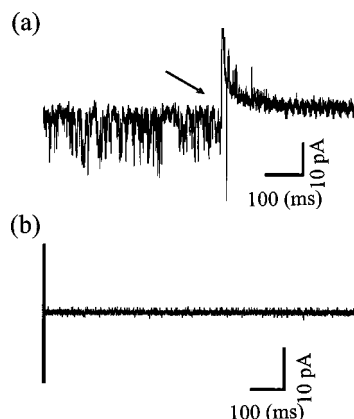


FIG. 4. (a) Reverse bias voltage trace of streptavidin-conjugated QDs. Arrow indicates reversing the bias voltage from -40 to $+40$ mV. No current bursts are seen with positive voltage bias. (b) Current trace in presence of streptavidin-conjugated gold nanoparticles (3.4×10^{11} gold particles/ml). Changing the bias in the range from -200 to $+200$ mV resulted in a similar zero-current trace.

TABLE I. Number of QDs required to form a pore and their respective pore diameters for a conductance of 500 pS (25 pA at 50 mV). Calculations were made on approximations used in the calculation of alamethicin pore.^a

	Diameter of QDs (nm)	Number of QDs required to form a pore	Diameter of pore (nm)
CdSe	2.2±0.5	3.04	0.36
CdSe/ZnS+ polymer	3.2±0.5	2.91	0.43
CdSe/ZnS+ polymer+ streptavidin	10–15 ^b	2.63 for 10 nm QD 2.57 for 15 nm QD	0.75 for 10 nm QD 0.92 for 15 nm QD

^aReference 9.

^bWhen streptavidin is not conjugated to QDs, the diameter is 5.7±0.8 nm (Quantum Dot Corporation, Hayward, CA).

dependent conductance.^{6,7} We can conclude that the QDs, having a permanent dipole moment⁸ similar to alamethicin, are influenced by an external electric field, which creates a torque on the QD dipole, forcing insertion into the lipid membrane [Fig. 1(a)]. (III) Because many voltage-dependent current bursts are observed in 1 s sometimes spaced a few milliseconds apart, it is possible that oligomeric aggregation of QDs forms pores leading to the macroscopic conductance we observe. In addition, we observe smaller current peaks that could be caused by single QDs embedded in the lipid membrane, which could cause a voltage-dependent flip-flop of lipids disrupting the membrane. We believe that the opening and closing of the channel occurs by random association and dissociation of QDs caused by disruptive forces of thermal agitation, and several other factors including surface tension of the lipid bilayer. Unlike peptide ion channels, which have defined structures and are attached to the membranes more stably, the QDs will only be weakly associated. This causes instability, and thus a nonstationary current flow is detected.

To determine both the “pore” size required for the macroscopic conductance observed and the number of QDs forming a pore [see Fig. 1(a)], we measured the conductivity of 1 M KCl at 23 °C, and found it to be $11.10 \times 10^4 \mu\text{S}/\text{cm}$. For an applied bias voltage of 50 mV and a current of 25 pA (for a large pore), we get a conductance of 500 pS. Assuming we have a very large pore in an uncharged membrane so that its conductivity is equal to that of 1 M KCl, we find the pore diameter responsible for a 500 pS conductance using $\sigma = G \times h/A$. Here, σ is the conductivity of bulk solution; G is the conductance; h is the height of the QD (=diameter of the QD as determined from electron microscopy), and A is the area ($=\pi r^2$, where r =pore radius) to get pore diameters (d_{pore}) of 0.36, 0.43, and 0.75–0.92 nm formed by the smallest to largest sizes of QDs, respectively (Table I). Based on electron microscopy data, and on the assumption that QDs are perfect spheres coming close together to form a pore, we find the number of QDs required to form a pore using the relation $d_{\text{pore}} = d_{\text{dot}} (1/\sin(\pi/N) - 1)$ with N being the number of QDs, d_{pore} =diameter of the pore formed by QDs and d_{dot} =diameter of the QD. We predict that a conductance of 500 pS results from three QDs assembling to form an electrolyte filled pore with diameters 0.36, 0.43, and 0.75–0.92 nm, depending on the diameters of the QDs used (see Table I). The values of pore sizes we calculate

correspond closely to the values that have been calculated for different “pore states” in alamethicin.⁹ Thus QDs appear to behave in a manner similar to alamethicin, aggregating to form pores capable of allowing ions to flow through the lipid bilayer. While an alamethicin pore is formed by peptide helices, and acts as a selectivity filter for most cations,¹⁰ a QD formed pore is not governed by helices and should therefore be nonselective.

Our demonstration that QDs elicit current bursts in synthetic membranes suggests that they could also do this in excitable cells such as neurons and muscles, or in any cell or organism with a bilayer membrane having an electrical potential (e.g., *Paramecium*, *Saccharomyces cerevisiae*, etc.). It would be of great utility to understand how QDs behave *in vivo* in excitable cells, especially because their use in tissue imaging is becoming widespread.

In summary, we have demonstrated that three different QDs elicit current fluctuations in artificial lipid bilayers. Our results show that these current bursts are voltage dependent and are due to the presence of a large permanent dipole moment of the QDs, which results in insertion into the lipid bilayer in the presence of an electric field. We believe that current fluctuations are due to formation of QD aggregates leading to pore formation as well as single dots breaking through the membrane leading to smaller current peaks. A collective event of such disruptions of the membrane would result in the pattern of current fluctuations we observe. Studying the gating mechanisms will be the next challenge.

The authors acknowledge support by a Vilas Associate award from the University of Wisconsin-Madison and the Office of Naval Research (ONR) (N00014-99-1-0717). The authors would like to thank Dr. Meyer B. Jackson (Department of Physiology, University of Wisconsin-Madison), and Ryan C. Toonen for their helpful suggestions.

¹P. Alivisatos, Nat. Biotechnol. **22**, 47 (2004).

²J. O. Winter, T. Y. Liu, B. A. Korgel, and C. E. Schmidt, Adv. Mater. (Weinheim, Ger.) **13**, 1673 (2001).

³R. Coronado, Annu. Rev. Biophys. Biophys. Chem. **15**, 259 (1986).

⁴P. Mueller and D. O. Rudin, Nature (London) **217**, 713 (1968).

⁵M. Eisenberg, J. E. Hall, and C. A. Mead, J. Membr. Biol. **14**, 143 (1973).

⁶R. Yantorno, S. Takashima, and P. Mueller, Biophys. J. **38**, 105 (1982).

⁷G. Schwarz and P. Savko, Biophys. J. **39**, 211 (1982).

⁸M. Shim and P. Guyot-Sionnest, J. Chem. Phys. **111**, 6955 (1999).

⁹W. Hanke and G. Boehm, Biochim. Biophys. Acta **596**, 456 (1980).

¹⁰R. O. Fox, Jr. and F. M. Richards, Nature (London) **300**, 325 (1982).

Chapter 9

9 Discussion

This dissertation detailed the designing and implementing of different challenging tools for use in point-of-care diagnostics and biosensing for low resource settings. They included:

- 1) Low-cost material for affordability
- 2) Performing multistep automated assay
- 3) Upstream processing of different samples
- 4) Incorporating signal enhancement for improved sensitivity
- 5) Long-term dry storage and stabilization of reagents
- 6) Minimal user steps for ease-of-use, and
- 7) Rapid detection time

The discussion for each specific aim of this dissertation was detailed at the end of their respective chapter papers. The following sections list the overall conclusions for the three parts of the thesis.

9.1 Low-cost paper-based POC Dx for infectious diseases

Two-dimensional paper network for multistep assays

Instrument-free 2DPN devices were efficiently designed with low-cost wicking materials like nitrocellulose, glass fiber, and cellulose encased in plastic laminate devices for use at POC. The porous materials were skillfully cut to the desired shape for the sequential delivery of reagents to the detection zone. The power of the 2DPN lies in its capability to perform automated multi-step processing with minimal user steps.

A foldable 2DPN card format that performed automated ELISA, including multistep processes such as rinse and signal amplification for a malarial assay within 15 minutes with a single user-activation step, was demonstrated. The sensitivity of the assay was comparable to the laboratory-based ELISA. The reagents were stored dry in porous glass fiber and incorporated into the 2DPN device. The long-term stability of dry reagents for ELISA in a porous matrix was remarkable. The

HRP-antibody conjugate and its substrate DAB retained a high activity level after long-term dry storage at 45°C. The method for drying the reagents onto a glass fiber pad has the benefit of easy incorporation into POC devices, including conventional microfluidic or paper-based devices. Dry preservation of enzyme-based signal amplification reagents could be used for various applications and has particular advantages for POC devices for enhanced sensitivity, portability, and ease-of-use in low resource settings.

Two-dimensional paper network for sample processing

Upstream sample processing to remove assay-interfering molecules was achieved using porous matrices with high binding efficiency for target specific “mop up” agents and easily integrated with 2DPN devices. An automated IgM assay with integrated IgG removal using a protein G coated membrane stack in a 2DPN foldable card was demonstrated as a serodiagnosis tool. This device format, with one user activation step, can be used for removal of a variety of assay interferents and is rapid, inexpensive, and appropriate for use in low-resource POC settings.

Sample processing steps like blood plasma separation and lysis of pathogens in the blood were easily implemented into 2DPN using porous materials capable of separating blood cells and cellulose materials impregnated with detergents, respectively. A user-friendly blood acquisition module demonstrated a proof-of-principle sample-to-result test with an integrated 2DPN 8-channel LF device. The module delivered blood equally to the 8-channel device. Ebola VLPs spiked into blood was used to demonstrate plasma separation, VLP lysis, and detection of membrane-bound glycoprotein GP1/2 in a prototype device. The total operation time was 25 minutes. Overall, the device can be safely operated, is autonomous, disposable, and applicable to POC in LRS and clinical settings worldwide.

A low-cost paper-based microfluidic origami device for viscous sample preparation was demonstrated, leading to POC molecular diagnosis. The origami device can be used as a generic low cost, POC, nucleic acid extraction device for samples of varying viscosities such as sputum or blood and volumes up to 1ml without the need for permanent electrical infrastructure.

Two-dimensional paper network for molecular diagnostics

Nucleic acid amplification in the porous materials has an advantage, as the porous matrix can be fluidically connected to the upstream sample input region and the downstream detection zone in

paper fluidic devices. A few porous materials were successful for an isothermal amplification assay (iSDA) **(see Appendix 11.3)** for MRSA target and preserved the enzyme-based reagents in the dry form up to one year at 22 °C, as well as at temperature up to 45 °C tested for 360 h. The reagents also included either fluorescence probes or Au-label probes for detection, thus eliminating the need to store them separately. Lateral flow readout of iSDA produced consistently detectable colorimetric signals at 10 genomic copies or above (visual readout by eye or by a scanner). In comparison, fluorescence readout was reliably measurable at 50 copies or greater. Our method for drying the reagents onto a glass fiber pad has the benefit of easy incorporation into POC devices, including conventional microfluidic or paper-based devices, especially in places where the ambient temperatures are 40–45 °C range. Dry preservation of amplification reagents in porous matrices could be used for various applications and has particular advantages for POC devices with LF detection or real-time fluorescence readout, portability, and ease-of-use in LRS settings. We demonstrated iSDA in a fully integrated sample-to-result 2DPN MAD NAAT device with dry reagents for MRSA DNA target and successfully validated with real patient samples¹⁴⁴ **(see Appendix 11.5)**. Real-time fluorescence in an MD NAAT device using cellphone imaging was also demonstrated¹⁴⁵.

Further, a sample-to-result test for a *Chlamydia trachomatis* target in the urine sample was demonstrated in an MD NAAT device operated by a pre-programmed USB-powered board with real-time fluorescence detection using a cellphone within 45 minutes. An autonomous integrated disposable urinalysis device has broader POC applications that could include rapid screening for markers, diagnosis of diseases, the staging of disease progression, and epidemiology without using expensive and bulky instruments.

The paper-based devices with incorporated tools lead to low-cost, sensitive, easy-to-use, portable devices with rapid detection time. They can be used for sample-to-result POC Dx in low resource settings, especially in hot climates where the ambient temperatures can be in the 40-45 °C range. Paper-based devices can be disposed of safely without posing a risk to the environment.

9.2 Biomolecular motor-powered biosensing

A kinesin motor-driven biosensor was built to transport complex molecules in an analytical device. Microtubules were successfully functionalized with antibodies via streptavidin-biotin bridges, and an immunoassay for a heart attack marker was demonstrated on the moving shuttle. The “molecular shuttle” can subsequently be transported to the detection zone by surface-immobilized kinesin motor proteins. This system would simplify the fluidic pathways without the need for pumps and valves typically used in microfluidic devices.

These bionanodevices integrating large protein assemblies and highly functional molecular machines were stored dry by lyophilization for extended periods and returned to an active functional state when needed by rehydration.

The nanoscale biomolecular-motor-driven transport systems developed here is an alternative to pressure-driven fluid flow in micro-and nanofluidic systems. Using commercially available building blocks significantly advances the field of molecular shuttles powered by biomolecular motors. It enables the loading of all cargo types against which antibodies can be raised for point of care applications or biosensing of warfare agents.

9.3 Label-free biosensing

RF interface to biological pores in lipid bilayer for label-free biosensing

Using radiofrequency bandwidths of at least 1000 times greater (MHz-GHz) than the current state-of-the-art patch-clamp technique would give a high temporal resolution for measuring ion channel activity. We first demonstrated the combination of transmission lines using micro stripline with on-chip patch-clamp single-channel recording unit (see **Appendix 11.6**).

Further, micro-coaxes were successfully applied for delivering and picking up RF signals to ion channels and pores in lipid bilayer membranes. Rectification of the RF voltage was observed, with a resulting voltage which can be used for pumping ions through the ion channels. Direct transmission modulation in clear coincidence with direct current recording was observed. We can thus monitor and correlate the radiofrequency transmission signal with corresponding open-close states of the ion channel. The method of interfacing radiofrequency (RF) circuitry with biological pores in artificial lipid bilayer can be used as a faster read-out technique for real-time sensing of

single molecules. Extending the dynamic range of standard patch-clamp measurements from the kHz to the GHz-range, one can observe a host of new phenomena, which include intermediate opening states of ion channels, the influence of noise, and possibly conformational changes resulting in current fluctuations. This method provides evidence for real-time spectroscopy potential on single molecular channels and points towards future applications in high-throughput drug screening applications. The label-free biosensing method developed in this thesis has the potential for rapid detection of pathogens at point-of-care in the near future without sample preparation or pretreatment.

Interaction of quantum dots with a lipid bilayer membrane

Many of the applications of QDs in biology have been for cell staining. Hence their interaction with the cell membrane was of significant interest. Voltage dependent current bursts were observed when QDs were applied to lipid bilayer due to the presence of a large permanent dipole moment in the QDs. It has been suggested that the QDs assemble and form pores on the lipid membrane. This phenomenon suggests that similar effects are likely to happen in excitable cells, such as neurons and muscles. It would be of great utility to understand how QDs behave in vivo in excitable cells, especially because their use in tissue imaging is becoming widespread. The interaction of the semiconductor colloidal quantum dots with a lipid bilayer can be used for probing living systems. The nanometer length scale of the QDs can sense and detect the state of biological systems and living organisms optically as well as electrically and can be expected to lead to entirely new types of biological sensors.

Overall conclusion

The challenges of REASSURED criteria set by the World Health Organization for point-of-care diagnostics (POC Dx), namely, **r**real-time connectivity, **e**ase of sample specimen collection, and **e**nvironment-friendliness, **a**ffordability, **s**ensitivity, and **s**pecificity, **u**ser-friendly, **r**apid and **r**obust, **e**quipment-free and **d**eliverable to the end-user can be achieved and universally applied with the tools developed in this thesis. In general, the work developed in this thesis can also be applied to the diagnosis of non-communicable diseases, biosensing for biological weapons, and in other resource-limited settings such as war zones. However, the COVID-19 crisis has brought into

sharp focus a great need to universally apply POC diagnostics within the developed as well as developing worlds with high disease burden during a pandemic.

10. Bibliography

1. Institute of Health Metrics and Evaluation, Human Development Network, The World Bank. *The Global Burden of Disease : Generating Evidence , Guiding Policy Sub-Saharan Africa Region Edition.*; 2013.
2. Bhutta ZA, Sommerfeld J, Lassi ZS, Salam RA, Das JK. Global burden, distribution, and interventions for infectious diseases of poverty. *Infect Dis Poverty*. 2014. doi:10.1186/2049-9957-3-21
3. Walensky RP, Wood R, Fofana MO, et al. The clinical impact and cost-effectiveness of routine, voluntary HIV screening in South Africa. *J Acquir Immune Defic Syndr*. 2011. doi:10.1097/QAI.0b013e3181fb8f24
4. Dowdy DW, O'Brien MA, Bishai D. Cost-effectiveness of novel diagnostic tools for the diagnosis of tuberculosis. *Int J Tuberc Lung Dis*. 2008.
5. Vassall A, van Kampen S, Sohn H, et al. Rapid diagnosis of tuberculosis with the Xpert MTB/RIF assay in high burden countries: A cost-effectiveness analysis. *PLoS Med*. 2011. doi:10.1371/journal.pmed.1001120
6. Price CP. Regular review: Point of care testing. *Br Med J*. 2001. doi:10.1136/bmj.322.7297.1285
7. Kosack CS, Page AL, Klatser PR. A guide to aid the selection of diagnostic tests. *Bull World Health Organ*. 2017. doi:10.2471/BLT.16.187468
8. Ventola CL. The antibiotic resistance crisis: causes and threats. *P T J*. 2015. doi:Article
9. Land KJ, Boeras DI, Chen XS, Ramsay AR, Peeling RW. REASSURED diagnostics to inform disease control strategies, strengthen health systems and improve patient outcomes. *Nat Microbiol*. 2019. doi:10.1038/s41564-018-0295-3
10. Whitesides GM. The origins and the future of microfluidics. *Nature*. 2006. doi:10.1038/nature05058
11. P. Y, G.J. D, J. G. Point-of-care diagnostics for global health. *Annu Rev Biomed Eng*. 2008.
12. Martinez AW, Phillips ST, Butte MJ, Whitesides GM. Patterned paper as a platform for inexpensive, low-volume, portable bioassays. *Angew Chemie - Int Ed*. 2007. doi:10.1002/anie.200603817
13. Shukla S, Leem H, Lee JS, Kim M. Immunochromatographic strip assay for the rapid and sensitive detection of salmonella typhimurium in artificially contaminated tomato samples. *Can J Microbiol*. 2014. doi:10.1139/cjm-2014-0223
14. Morales-Narváez E, Naghdi T, Zor E, Merkoçi A. Photoluminescent Lateral-Flow Immunoassay Revealed by Graphene Oxide: Highly Sensitive Paper-Based Pathogen Detection. *Anal Chem*. 2015. doi:10.1021/acs.analchem.5b02383
15. Kuang H, Xing C, Hao C, Liu L, Wang L, Xu C. Rapid and highly sensitive detection of

- lead ions in drinking water based on a strip immunosensor. *Sensors (Switzerland)*. 2013. doi:10.3390/s130404214
16. López-Marzo AM, Pons J, Blake DA, Merkoçi A. High sensitive gold-nanoparticle based lateral flow Immunodevice for Cd²⁺ detection in drinking waters. *Biosens Bioelectron*. 2013. doi:10.1016/j.bios.2013.02.031
 17. Zhao Y, Wang H, Zhang P, et al. Rapid multiplex detection of 10 foodborne pathogens with an up-converting phosphor technology-based 10-channel lateral flow assay. *Sci Rep*. 2016. doi:10.1038/srep21342
 18. Ching KH, He X, Stanker LH, Lin A V., McGarvey JA, Hnasko R. Detection of shiga toxins by lateral flow assay. *Toxins (Basel)*. 2015. doi:10.3390/toxins7041163
 19. Ang SH, Rambeli M, Thevarajah TM, Alias YB, Khor SM. Quantitative, single-step dual measurement of hemoglobin A1c and total hemoglobin in human whole blood using a gold sandwich immunochromatographic assay for personalized medicine. *Biosens Bioelectron*. 2016. doi:10.1016/j.bios.2015.11.045
 20. Vijayan T, Chiller T, Klausner JD. Sensitivity and specificity of a new cryptococcal antigen lateral flow assay in serum and cerebrospinal fluid. *MLO Med Lab Obs*. 2013.
 21. Schramm EC, Staten NR, Zhang Z, et al. A quantitative lateral flow assay to detect complement activation in blood. *Anal Biochem*. 2015. doi:10.1016/j.ab.2015.01.024
 22. Peter J, Theron G, Chanda D, et al. Test characteristics and potential impact of the urine LAM lateral flow assay in HIV-infected outpatients under investigation for TB and able to self-expectorate sputum for diagnostic testing. *BMC Infect Dis*. 2015. doi:10.1186/s12879-015-0967-z
 23. De Giovanni N, Fucci N. The Current Status of Sweat Testing For Drugs of Abuse: A Review. *Curr Med Chem*. 2013. doi:10.2174/0929867311320040006
 24. Carrio A, Sampedro C, Sanchez-Lopez JL, Pimienta M, Campoy P. Automated low-cost smartphone-based lateral flow saliva test reader for drugs-of-abuse detection. *Sensors (Switzerland)*. 2015. doi:10.3390/s151129569
 25. Martinez AW, Phillips ST, Whitesides GM. Three-dimensional microfluidic devices fabricated in layered paper and tape. *Proc Natl Acad Sci U S A*. 2008. doi:10.1073/pnas.0810903105
 26. Fu E, Lutz B, Kauffman P, Yager P. Controlled reagent transport in disposable 2D paper networks. *Lab Chip*. 2010. doi:10.1039/b919614e
 27. Fu E, Ramsey SA, Kauffman P, Lutz B, Yager P. Transport in two-dimensional paper networks. *Microfluid Nanofluidics*. 2011. doi:10.1007/s10404-010-0643-y
 28. Lutz B, Liang T, Fu E, Ramachandran S, Kauffman P, Yager P. Dissolvable fluidic time delays for programming multi-step assays in instrument-free paper diagnostics. *Lab Chip*. 2013. doi:10.1039/c3lc50178g
 29. Fu E, Liang T, Spicar-Mihalic P, Houghtaling J, Ramachandran S, Yager P. Two-

- dimensional paper network format that enables simple multistep assays for use in low-resource settings in the context of malaria antigen detection. *Anal Chem.* 2012. doi:10.1021/ac300689s
30. Yang X, Forouzan O, Brown TP, Shevkoplyas SS. Integrated separation of blood plasma from whole blood for microfluidic paper-based analytical devices. *Lab Chip.* 2012. doi:10.1039/c1lc20803a
 31. Byrnes SA, Bishop JD, Lafleur L, Buser JR, Lutz B, Yager P. One-step purification and concentration of DNA in porous membranes for point-of-care applications. *Lab Chip.* 2015. doi:10.1039/c5lc00317b
 32. Byrnes SA, Bishop JD, Yager P. Enabling lateral transport of genomic DNA through porous membranes for point-of-care applications. *Anal Methods.* 2017. doi:10.1039/c7ay00293a
 33. Byrnes SA, Buser JR, Kline E, Bishop JD, Wheeler MD, Yager P. An integrated sample preparation system for large volume processing at the point of care. In: *20th International Conference on Miniaturized Systems for Chemistry and Life Sciences, MicroTAS 2016.* ; 2016.
 34. Buser JR, Byrnes SA, Anderson CE, et al. Understanding partial saturation in paper microfluidics enables alternative device architectures. *Anal Methods.* 2019. doi:10.1039/c8ay01977k
 35. Cho IH, Seo SM, Paek EH, Paek SH. Immunogold-silver staining-on-a-chip biosensor based on cross-flow chromatography. *J Chromatogr B Anal Technol Biomed Life Sci.* 2010. doi:10.1016/j.jchromb.2009.07.016
 36. Horton JK, Swinburne S, O'Sullivan MJ. A novel, rapid, single-step immunochromatographic procedure for the detection of mouse immunoglobulin. *J Immunol Methods.* 1991. doi:10.1016/0022-1759(91)90135-3
 37. Zhang C, Zhang Y, Wang S. Development of multianalyte flow-through and lateral-flow assays using gold particles and horseradish peroxidase as tracers for the rapid determination of carbaryl and endosulfan in agricultural products. *J Agric Food Chem.* 2006. doi:10.1021/jf0531407
 38. Chun P. Colloidal Gold and Other Labels for Lateral Flow Immunoassays. In: *Lateral Flow Immunoassay.* ; 2009. doi:10.1007/978-1-59745-240-3_5
 39. Faulstich K, Gruler R, Eberhard M, Lentzsch D, Haberstroh K. Handheld and Portable Reader Devices for Lateral Flow Immunoassays. In: *Lateral Flow Immunoassay.* ; 2009. doi:10.1007/978-1-59745-240-3_9
 40. Mothershed EA, Whitney AM. Nucleic acid-based methods for the detection of bacterial pathogens: Present and future considerations for the clinical laboratory. *Clin Chim Acta.* 2006. doi:10.1016/j.cccn.2005.05.050
 41. Ince J, McNally A. Development of rapid, automated diagnostics for infectious disease: Advances and challenges. *Expert Rev Med Devices.* 2009. doi:10.1586/erd.09.46
 42. Mahony JB. Detection of respiratory viruses by molecular methods. *Clin Microbiol Rev.*

2008. doi:10.1128/CMR.00037-07
43. Y. M, H. K, T. N. Loop-mediated isothermal amplification (LAMP): Recent progress in research and development. *J Infect Chemother*. 2013.
 44. Piepenburg O, Williams CH, Stemple DL, Armes NA. DNA detection using recombination proteins. *PLoS Biol*. 2006. doi:10.1371/journal.pbio.0040204
 45. Walker GT, Fraiser MS, Schram JL, Little MC, Nadeau JG, Malinowski DP. Strand displacement amplification - an isothermal, in vitro DNA amplification technique. *Nucleic Acids Res*. 1992. doi:10.1093/nar/20.7.1691
 46. Helb D, Jones M, Story E, et al. Rapid detection of Mycobacterium tuberculosis and rifampin resistance by use of on-demand, near-patient technology. *J Clin Microbiol*. 2010. doi:10.1128/JCM.01463-09
 47. Tanriverdi S, Chen L, Chen S. A Rapid and Automated Sample-to-Result HIV Load Test for Near-Patient Application. *J Infect Dis*. 2010. doi:10.1086/650387
 48. Ritchie A V., Ushiro-Lumb I, Edemaga D, et al. SAMBA HIV semiquantitative test, a new point-of-care viral-load-monitoring assay for resource-limited settings. *J Clin Microbiol*. 2014. doi:10.1128/JCM.00593-14
 49. Douthwaite ST, Walker C, Adams EJ, et al. Performance of a novel point-of-care molecular assay for detection of influenza A and B viruses and respiratory syncytial virus (enigma minilab) in children with acute respiratory infection. *J Clin Microbiol*. 2016. doi:10.1128/JCM.02887-15
 50. Niemz A, Ferguson TM, Boyle DS. Point-of-care nucleic acid testing for infectious diseases. *Trends Biotechnol*. 2011. doi:10.1016/j.tibtech.2011.01.007
 51. Asiello PJ, Baeumner AJ. Miniaturized isothermal nucleic acid amplification, a review. *Lab Chip*. 2011. doi:10.1039/c0lc00666a
 52. Mahalanabis M, Do J, Almuayad H, Zhang JY, Klapperich CM. An integrated disposable device for DNA extraction and helicase dependent amplification. *Biomed Microdevices*. 2010. doi:10.1007/s10544-009-9391-8
 53. Wang CH, Lien KY, Wang TY, Chen TY, Lee G Bin. An integrated microfluidic loop-mediated-isothermal-amplification system for rapid sample pre-treatment and detection of viruses. *Biosens Bioelectron*. 2011. doi:10.1016/j.bios.2010.08.083
 54. Magro L, Escadafal C, Garneret P, et al. Paper microfluidics for nucleic acid amplification testing (NAAT) of infectious diseases. *Lab Chip*. 2017. doi:10.1039/c7lc00013h
 55. Choi JR, Hu J, Tang R, et al. An integrated paper-based sample-to-answer biosensor for nucleic acid testing at the point of care. *Lab Chip*. 2016. doi:10.1039/c5lc01388g
 56. Rodriguez NM, Wong WS, Liu L, Dewar R, Klapperich CM. A fully integrated paperfluidic molecular diagnostic chip for the extraction, amplification, and detection of nucleic acids from clinical samples. *Lab Chip*. 2016. doi:10.1039/c5lc01392e
 57. Hirokawa N. Kinesin and dynein superfamily proteins and the mechanism of organelle

- transport. *Science* (80-). 1998. doi:10.1126/science.279.5350.519
58. Visscher K, Schnltzer MJ, Block SM. Single kinesin molecules studied with a molecular force clamp. *Nature*. 1999. doi:10.1038/22146
 59. Coy DL, Wagenbach M, Howard J. Kinesin takes one 8-nm step for each ATP that it hydrolyzes. *J Biol Chem*. 1999. doi:10.1074/jbc.274.6.3667
 60. Lowe CR. Nanobiotechnology: Concepts, Applications and Perspectives. Edited by C. M. Niemeyer and C. A. Mirkin. *ChemBioChem*. 2004. doi:10.1002/cbic.200300180
 61. Schmidt JJ, Montemagno CD. BIONANOMECHANICAL SYSTEMS. *Annu Rev Mater Res*. 2004. doi:10.1146/annurev.matsci.34.040203.115827
 62. Soong RK, Bachand GD, Neves HP, Olkhovets AG, Craighead HG, Montemagno CD. Powering an inorganic nanodevice with a biomolecular motor. *Science* (80-). 2000. doi:10.1126/science.290.5496.1555
 63. Limberis L, Stewart RJ. Toward kinesin-powered microdevices. *Nanotechnology*. 2000. doi:10.1088/0957-4484/11/2/301
 64. Howard J, Hudspeth AJ, Vale RD. Movement of microtubules by single kinesin molecules. *Nature*. 1989. doi:10.1038/342154a0
 65. Dennis JR, Howard J, Vogel V. Molecular shuttles: Directed motion of microtubules along nanoscale kinesin tracks. *Nanotechnology*. 1999. doi:10.1088/0957-4484/10/3/302
 66. Moorjani SG, Jia L, Jackson TN, Hancock WO. Lithographically patterned channels spatially segregate kinesin motor activity and effectively guide microtubule movements. *Nano Lett*. 2003. doi:10.1021/nl034001b
 67. Hess H, Matzke CM, Doot RK, et al. Molecular Shuttles Operating Undercover: A New Photolithographic Approach for the Fabrication of Structured Surfaces Supporting Directed Motility. *Nano Lett*. 2003. doi:10.1021/nl0347435
 68. Kim T, Cheng LJ, Kao MT, Hasselbrink EF, Guo L, Meyhöfer E. Biomolecular motor-driven molecular sorter. *Lab Chip*. 2009. doi:10.1039/b900753a
 69. Diez S, Reuther C, Dinu C, et al. Stretching and transporting DNA molecules using motor proteins. *Nano Lett*. 2003. doi:10.1021/nl034504h
 70. Hess H, Clemmens J, Qin D, Howard J, Vogel V. Light-Controlled Molecular Shuttles Made from Motor Proteins Carrying Cargo on Engineered Surfaces. *Nano Lett*. 2001. doi:10.1021/nl015521e
 71. Bachand GD, Rivera SB, Carroll-Portillo A, Hess H, Bachand M. Active capture and transport of virus particles using a biomolecular motor-driven, nanoscale antibody sandwich assay. *Small*. 2006. doi:10.1002/sml.200500262
 72. Bachand GD, Hess H, Ratna B, Satir P, Vogel V. “smart dust” biosensors powered by biomolecular motors. *Lab Chip*. 2009. doi:10.1039/b821055a
 73. Sakmann B. Patch Clamp Techniques for Studying Ionic Channels in Excitable Membranes.

- Annu Rev Physiol.* 1984. doi:10.1146/annurev.physiol.46.1.455
74. Montal M, Mueller P. Formation of bimolecular membranes from lipid monolayers and a study of their electrical properties. *Proc Natl Acad Sci U S A.* 1972. doi:10.1073/pnas.69.12.3561
 75. Montal M. Reconstitution of channel proteins from excitable cells in planar lipid bilayer membranes. *J Membr Biol.* 1987. doi:10.1007/BF01872123
 76. Zakharian E. Recording of ion channel activity in planar lipid bilayer experiments. *Methods Mol Biol.* 2013. doi:10.1007/978-1-62703-351-0_8
 77. Allen TW, Andersen OS, Roux B. Energetics of ion conduction through the gramicidin channel. *Proc Natl Acad Sci U S A.* 2004. doi:10.1073/pnas.2635314100
 78. Hanke W, Boheim G. The lowest conductance state of the alamethicin pore. *BBA - Biomembr.* 1980. doi:10.1016/0005-2736(80)90134-0
 79. Schuster B, Pum D, Braha O, Bayley H, Sleytr UB. Self-assembled α -hemolysin pores in an S-layer-supported lipid bilayer. *Biochim Biophys Acta - Biomembr.* 1998. doi:10.1016/S0005-2736(97)00274-5
 80. Fertig N, Meyer C, Blick RH, Trautmann C, Behrends JC. Microstructured glass chip for ion-channel electrophysiology. *Phys Rev E - Stat Physics, Plasmas, Fluids, Relat Interdiscip Top.* 2001. doi:10.1103/PhysRevE.64.040901
 81. Suzuki H, Pioufle B Le, Takeuchi S. Ninety-six-well planar lipid bilayer chip for ion channel recording Fabricated by hybrid stereolithography. *Biomed Microdevices.* 2009. doi:10.1007/s10544-008-9205-4
 82. Favero G, Campanella L, Cavallo S, et al. Glutamate receptor incorporated in a mixed hybrid bilayer lipid membrane array, as a sensing element of a biosensor working under flowing conditions. *J Am Chem Soc.* 2005. doi:10.1021/ja042904g
 83. Uto M, Umezawa Y, Michaelis EK, Hu IF. Biosensor Development with a Glutamate Receptor Ion-Channel Reconstituted in a Lipid Bilayer. *Anal Sci.* 1990. doi:10.2116/analsci.6.221
 84. Gu LQ, Braha O, Conlan S, Cheley S, Bayley H. Stochastic sensing of organic analytes by a pore-forming protein containing a molecular adapter. *Nature.* 1999. doi:10.1038/19491
 85. Xie H, Braha O, Gu LQ, Cheley S, Bayley H. Single-molecule observation of the catalytic subunit of cAMP-dependent protein kinase binding to an inhibitor peptide. *Chem Biol.* 2005. doi:10.1016/j.chembiol.2004.11.013
 86. Provoda CJ, Lee KD. Bacterial pore-forming hemolysins and their use in the cytosolic delivery of macromolecules. *Adv Drug Deliv Rev.* 2000. doi:10.1016/S0169-409X(99)00067-8
 87. Panchal R, Smart M, Bowser D, Williams D, Petrou S. Pore-Forming Proteins and their Application in Biotechnology. *Curr Pharm Biotechnol.* 2005. doi:10.2174/1389201023378418

88. Legendre JY, Szoka FC. Cyclic amphipathic peptide-DNA complexes mediate high-efficiency transfection of adherent mammalian cells. *Proc Natl Acad Sci U S A*. 1993. doi:10.1073/pnas.90.3.893
89. Anrather D, Smetazko M, Saba M, Alguel Y, Schalkhammer T. Supported membrane nanodevices. *J Nanosci Nanotechnol*. 2004. doi:10.1166/jnn.2004.226
90. Rokitskaya TI, Antonenko YN, Kotova EA. The interaction of phthalocyanine with planar lipid bilayers. Photodynamic inactivation of gramicidin channels. *FEBS Lett*. 1993. doi:10.1016/0014-5793(93)80248-S
91. Nikolelis DP, Siontorou CG, Krull UJ, Katrivanos PL. Ammonium ion minisensors from self-assembled bilayer lipid membranes using gramicidin as an ionophore. Modulation of ammonium selectivity by platelet-activating factor. *Anal Chem*. 1996. doi:10.1021/ac950403v
92. Ito T, Sun L, Crooks RM. Simultaneous determination of the size and surface charge of individual nanoparticles using a carbon nanotube-based coulter counter. *Anal Chem*. 2003. doi:10.1021/ac034072v
93. Kasianowicz JJ, Brandin E, Branton D, Deamer DW. Characterization of individual polynucleotide molecules using a membrane channel. In: *Proceedings of the National Academy of Sciences of the United States of America*. ; 1996. doi:10.1073/pnas.93.24.13770
94. Butler TZ, Pavlenok M, Derrington IM, Niederweis M, Gundlach JH. Single-molecule DNA detection with an engineered MspA protein nanopore. *Proc Natl Acad Sci U S A*. 2008. doi:10.1073/pnas.0807514106
95. DeBlois RW, Wesley RK. Sizes and concentrations of several type C oncornaviruses and bacteriophage T2 by the resistive-pulse technique. *J Virol*. 1977. doi:10.1128/jvi.23.2.227-233.1977
96. Feuer BI, Uzgiris EE, DeBlois RW, Cluxton DH, Lenard J. Length of glycoprotein spikes of vesicular stomatitis virus and sindbis virus, measured in Situ using quasi elastic light scattering and a resistive-pulse technique. *Virology*. 1978. doi:10.1016/0042-6822(78)90344-6
97. DeBlois RW, Uzgiris EE, Cluxton DH, Mazzone HM. Comparative measurements of size and polydispersity of several insect viruses. *Anal Biochem*. 1978. doi:10.1016/0003-2697(78)90032-5
98. Uram JD, Ke K, Hunt AJ, Mayer M. Submicrometer pore-based characterization and quantification of antibody-virus interactions. *Small*. 2006. doi:10.1002/sml.200600006
99. Saleh OA, Sohn LL. Direct detection of antibody-antigen binding using an on-chip artificial pore. *Proc Natl Acad Sci U S A*. 2003. doi:10.1073/pnas.0337563100
100. Uram JD, Ke K, Hunt AJ, Mayer M. Label-free affinity assays by rapid detection of immune complexes in submicrometer pores. *Angew Chemie - Int Ed*. 2006. doi:10.1002/anie.200502862
101. Blake S, Mayer T, Mayer M, Yang J. Monitoring chemical reactions by using ion-channel-

- forming peptides. *ChemBioChem*. 2006. doi:10.1002/cbic.200500532
102. Shin SH, Luchian T, Cheley S, Braha O, Bayley H. Kinetics of a reversible covalent-bond-forming reaction observed at the single-molecule level. *Angew Chemie - Int Ed*. 2002. doi:10.1002/1521-3773(20021004)41:19<3707::AID-ANIE3707>3.0.CO;2-5
 103. Saleh OA, Sohn LL. Quantitative sensing of nanoscale colloids using a microchip Coulter counter. *Rev Sci Instrum*. 2001. doi:10.1063/1.1419224
 104. Lee S, Zhang Y, White HS, Harrell CC, Martin CR. Electrophoretic capture and detection of nanoparticles at the opening of a membrane pore using scanning electrochemical microscopy. *Anal Chem*. 2004. doi:10.1021/ac049147p
 105. DeBlois RW, Bean CP, Wesley RKA. Electrokinetic measurements with submicron particles and pores by the resistive pulse technique. *J Colloid Interface Sci*. 1977. doi:10.1016/0021-9797(77)90395-2
 106. Woodhouse G, King L, Wieczorek L, Osman P, Cornell B. The ion channel switch biosensor. *J Mol Recognit*. 1999. doi:10.1002/(SICI)1099-1352(199909/10)12:5<328::AID-JMR474>3.0.CO;2-5
 107. Oh SY, Cornell B, Smith D, Higgins G, Burrell CJ, Kok TW. Rapid detection of influenza A virus in clinical samples using an ion channel switch biosensor. *Biosens Bioelectron*. 2008. doi:10.1016/j.bios.2007.10.011
 108. Levis RA, Rae JL. Low-noise patch-clamp techniques. *Methods Enzymol*. 1998. doi:10.1016/S0076-6879(98)93017-8
 109. Benndorf K. Multiple levels of native cardiac Na⁺ channels at elevated temperature measured with high-bandwidth/low-noise patch clamp. *Pflügers Arch Eur J Physiol*. 1993. doi:10.1007/BF00375079
 110. Mayer M, Kriebel JK, Tosteson MT, Whitesides GM. Microfabricated Teflon membranes for low-noise recordings of ion channels in planar lipid bilayers. *Biophys J*. 2003. doi:10.1016/S0006-3495(03)74691-8
 111. Wonderlin WF, Finkel A, French RJ. Optimizing planar lipid bilayer single-channel recordings for high resolution with rapid voltage steps. *Biophys J*. 1990. doi:10.1016/S0006-3495(90)82376-6
 112. Uram JD, Ke K, Mayer ML. Noise and bandwidth of current recordings from submicrometer pores and nanopores. *ACS Nano*. 2008. doi:10.1021/nn700322m
 113. Chen C, Yemenicioglu S, Uddin A, Corgliano E, Theogarajan L. A CMOS enhanced solid-state nanopore based single molecule detection platform. In: *Proceedings of the Annual International Conference of the IEEE Engineering in Medicine and Biology Society, EMBS*. ; 2013. doi:10.1109/EMBC.2013.6609463
 114. Venta K, Shemer G, Puster M, et al. Differentiation of short, single-stranded DNA homopolymers in solid-state nanopores. *ACS Nano*. 2013. doi:10.1021/nn4014388
 115. Rosenstein JK, Wanunu M, Merchant CA, Drndic M, Shepard KL. Integrated nanopore

- sensing platform with sub-microsecond temporal resolution. *Nat Methods*. 2012. doi:10.1038/nmeth.1932
116. Wanunu M, Dadosh T, Ray V, Jin J, McReynolds L, Drndić M. Rapid electronic detection of probe-specific microRNAs using thin nanopore sensors. *Nat Nanotechnol*. 2010. doi:10.1038/nnano.2010.202
 117. Larkin J, Henley R, Bell DC, Cohen-Karni T, Rosenstein JK, Wanunu M. Slow DNA transport through nanopores in hafnium oxide membranes. *ACS Nano*. 2013. doi:10.1021/nn404326f
 118. Larkin J, Henley RY, Muthukumar M, Rosenstein JK, Wanunu M. High-bandwidth protein analysis using solid-state nanopores. *Biophys J*. 2014. doi:10.1016/j.bpj.2013.12.025
 119. Delsing P, Likharev KK, Kuzmin LS, Claeson T. Time-correlated single-electron tunneling in one-dimensional arrays of ultrasmall tunnel junctions. *Phys Rev Lett*. 1989. doi:10.1103/PhysRevLett.63.1861
 120. Bylander J, Duty T, Delsing P. Current measurement by real-time counting of single electrons. *Nature*. 2005. doi:10.1038/nature03375
 121. Geerligs LJ, Anderegg VF, Holweg PAM, et al. Frequency-locked turnstile device for single electrons. *Phys Rev Lett*. 1990. doi:10.1103/PhysRevLett.64.2691
 122. Facer GR, Notterman DA, Sohn LL. Dielectric spectroscopy for bioanalysis: From 40 Hz to 26.5 GHz in a microfabricated wave guide. *Appl Phys Lett*. 2001. doi:10.1063/1.1347020
 123. Hefti J, Pan A, Kumar A. Sensitive detection method of dielectric dispersions in aqueous-based, surface-bound macromolecular structures using microwave spectroscopy. *Appl Phys Lett*. 1999. doi:10.1063/1.124825
 124. Olapinski M, Manus S, George M, Brüggemann A, Fertig N, Simmel FC. Detection of lipid bilayer and peptide pore formation at gigahertz frequencies. *Appl Phys Lett*. 2006. doi:10.1063/1.2159571
 125. Misakian M, Kasianowicz JJ, Robertson B, Petersons O. Frequency response of alternating currents through the *Staphylococcus aureus* α -hemolysin ion channel. *Bioelectromagnetics*. 2001. doi:10.1002/bem.77
 126. Ervin EN, Kawano R, White RJ, White HS. Simultaneous alternating and direct current readout of protein ion channel blocking events using glass nanopore membranes. *Anal Chem*. 2008. doi:10.1021/ac7021103
 127. Bruchez M, Moronne M, Gin P, Weiss S, Alivisatos AP. Semiconductor nanocrystals as fluorescent biological labels. *Science (80-)*. 1998. doi:10.1126/science.281.5385.2013
 128. Gerion D, Pinaud F, Williams SC, et al. Synthesis and properties of biocompatible water-soluble silica-coated CdSe/ZnS semiconductor quantum dots. *J Phys Chem B*. 2001. doi:10.1021/jp0105488
 129. Chan WCW, Nie S. Quantum dot bioconjugates for ultrasensitive nonisotopic detection. *Science (80-)*. 1998. doi:10.1126/science.281.5385.2016

130. Parak WJ, Gerion D, Zanchet D, et al. Conjugation of DNA to silanized colloidal semiconductor nanocrystalline quantum dots. *Chem Mater*. 2002. doi:10.1021/cm0107878
131. Parak WJ, Gerion D, Pellegrino T, et al. Biological applications of colloidal nanocrystals. *Nanotechnology*. 2003. doi:10.1088/0957-4484/14/7/201
132. Wu X, Bruchez MP. Labeling cellular targets with semiconductor quantum dot conjugates. *Methods Cell Biol*. 2004. doi:10.1016/s0091-679x(04)75007-4
133. Parak WJ, Pellegrino T, Plank C. Labelling of cells with quantum dots. *Nanotechnology*. 2005. doi:10.1088/0957-4484/16/2/R01
134. Ramachandran S, Fu E, Lutz B, Yager P. Long-term dry storage of an enzyme-based reagent system for ELISA in point-of-care devices. *Analyst*. 2014. doi:10.1039/c3an02296j
135. Ramachandran S, Peltier J, Osborn J, et al. Integrated assay with sample processing: Paper-based device for IgM detection. In: *Proceedings of the 16th International Conference on Miniaturized Systems for Chemistry and Life Sciences, MicroTAS 2012*. ; 2012.
136. Govindarajan A V., Ramachandran S, Vigil GD, Yager P, Böhringer KF. A low cost point-of-care viscous sample preparation device for molecular diagnosis in the developing world; An example of microfluidic origami. *Lab Chip*. 2012. doi:10.1039/c1lc20622b
137. McKenzie KG, Lafleur LK, Lutz BR, Yager P. Rapid protein depletion from complex samples using a bead-based microfluidic device for the point of care. *Lab Chip*. 2009. doi:10.1039/b913806d
138. Huang S, Abe K, Bennett S, et al. Disposable Autonomous Device for Swab-to-Result Diagnosis of Influenza. *Anal Chem*. 2017. doi:10.1021/acs.analchem.6b04801
139. Phan JC, Pettitt J, George JS, et al. Lateral Flow Immunoassays for Ebola Virus Disease Detection in Liberia. *J Infect Dis*. 2016. doi:10.1093/infdis/jiw251
140. Hu J, Jiang YZ, Wu LL, et al. Dual-Signal Readout Nanospheres for Rapid Point-of-Care Detection of Ebola Virus Glycoprotein. *Anal Chem*. 2017. doi:10.1021/acs.analchem.7b02222
141. Murin CD, Fusco ML, Bornholdt ZA, et al. Structures of protective antibodies reveal sites of vulnerability on ebola virus. *Proc Natl Acad Sci U S A*. 2014. doi:10.1073/pnas.1414164111
142. Kumar S, Gallagher R, Bishop J, et al. Long-term dry storage of enzyme-based reagents for isothermal nucleic acid amplification in a porous matrix for use in point-of-care diagnostic devices. *Analyst*. 2020. doi:10.1039/d0an01098g
143. Toley BJ, Covelli I, Belousov Y, et al. Isothermal strand displacement amplification (iSDA): A rapid and sensitive method of nucleic acid amplification for point-of-care diagnosis. *Analyst*. 2015. doi:10.1039/c5an01632k
144. Lafleur LK, Bishop JD, Heiniger EK, et al. A rapid, instrument-free, sample-to-result nucleic acid amplification test. *Lab Chip*. 2016. doi:10.1039/c6lc00677a
145. Shah KG, Kumar S, Singh V, et al. Two-Fluorophore Mobile Phone Imaging of Biplexed

- Real-Time NAATs Overcomes Optical Artifacts in Highly Scattering Porous Media. *Anal Chem.* 2020. doi:10.1021/acs.analchem.0c02000
146. Ramachandran S, Ernst KH, Bachand GD, Vogel V, Hess H. Selective loading of kinesin-powered molecular shuttles with protein cargo and its application to biosensing. *Small.* 2006. doi:10.1002/sml.200500265
 147. Seetharam R, Wada Y, Ramachandran S, Hess H, Satir P. Long-term storage of bionanodevices by freezing and lyophilization. *Lab Chip.* 2006. doi:10.1039/b601635a
 148. Ramachandran S, Blick RH, Van Der Weide DW. Radio frequency rectification on membrane bound pores. *Nanotechnology.* 2010. doi:10.1088/0957-4484/21/7/075201
 149. Ramachandran S, Van Der Weide DW, Blick RH. Direct microwave transmission on single α -hemolysin pores. *Appl Phys Lett.* 2011. doi:10.1063/1.3626586
 150. Kim HS, Ramachandran S, Stava E, Van Der Weide DW, Blick RH. Radio-frequency response of single pores and artificial ion channels. *New J Phys.* 2011. doi:10.1088/1367-2630/13/9/093033
 151. Ramachandran S, Kumar GL, Blick RH, Van Der Weide DW. Current bursts in lipid bilayers initiated by colloidal quantum dots. *Appl Phys Lett.* 2005. doi:10.1063/1.1862752

11. Appendix

11.1 Supporting information to chapter 3, section 3.1

Long-term dry storage of an enzyme-based reagent system for ELISA in point-of care device

Sujatha Ramachandran, Elain Fu, Barry Lutz, and Paul Yager

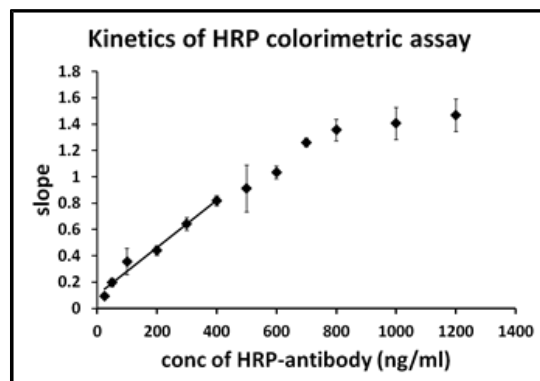


Figure S.1. Initial rate of reaction for varying concentrations of HRP-antibody. An HRP concentration of 200 ng/ml, which is in the linear range was chosen for subsequent kinetic measurements in the colorimetric assay.

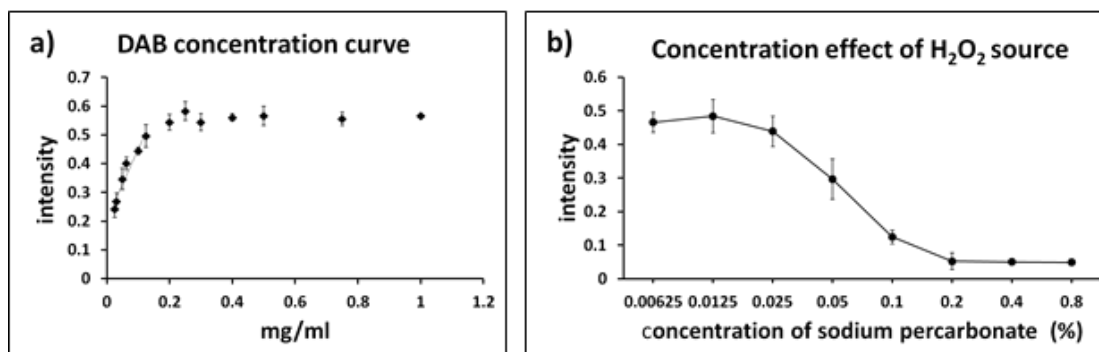


Figure S.2. Optimum range for diaminobenzidine and hydrogen peroxide. a) Plot showing the concentration of DAB vs. signal in the dipstick assay. This was used to determine a concentration within the linear range that would allow a sensitive measure of degradation. Based on this, 0.125 mg/ml was chosen for dry storage testing. b) Plot showing the effect of concentration of hydrogen peroxide source in the dipstick assay. Concentrations higher than 0.05% have an inhibitory effect on the enzyme system. A concentration of 0.025% form of sodium percarbonate was used for all dipstick immunoassays.

11.2 Supporting information to chapter 5, section 5.1

Long-term dry storage of enzyme-based reagents for isothermal nucleic acid amplification in a porous matrix for use in point-of-care diagnostic devices

Sujatha Kumar, Ryan Gallagher, Josh Bishop, Enos Kline, Josh Buser, Lisa Lafleur, Kamal Shah, Barry Lutz, and Paul Yager

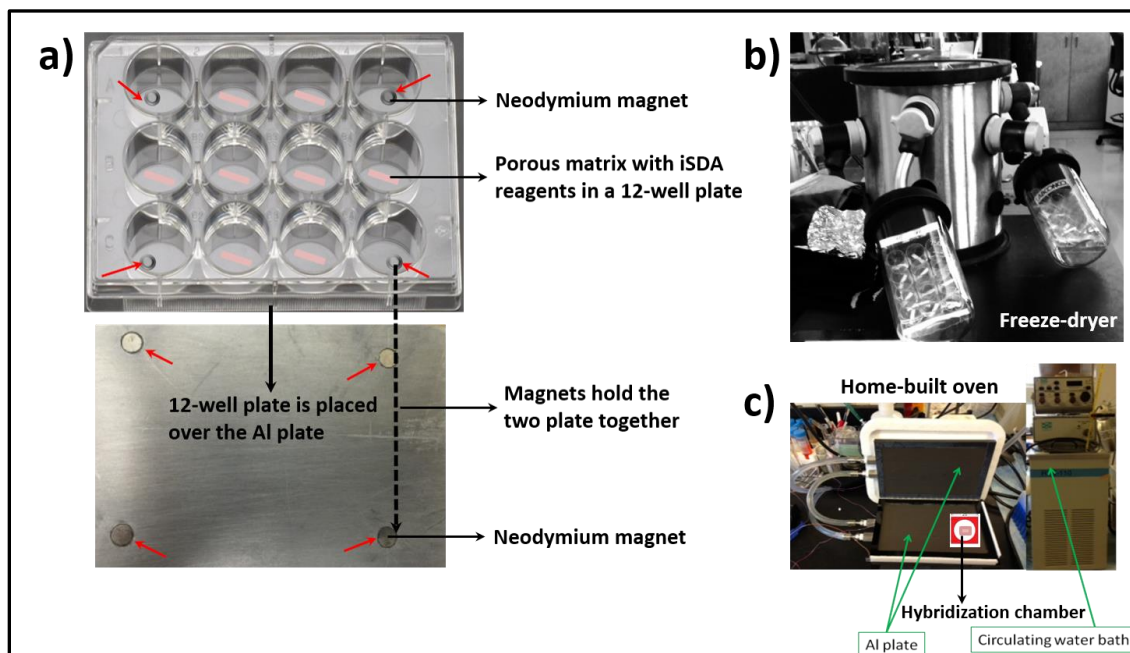


Figure S1. Experimental setup for lyophilization, and amplification in a porous matrix. a) 12-well plate containing iSDA reagent pads and magnets (red arrows) is placed over an aluminum (Al) plate with four magnets embedded in the corners (red arrows). The magnets hold the plates together during flash-freezing in liquid nitrogen. b) Lyophilizer with well plates inside a fast-freeze flask c) custom-built oven for performing iSDA in the Secure-Seal hybridization chamber.

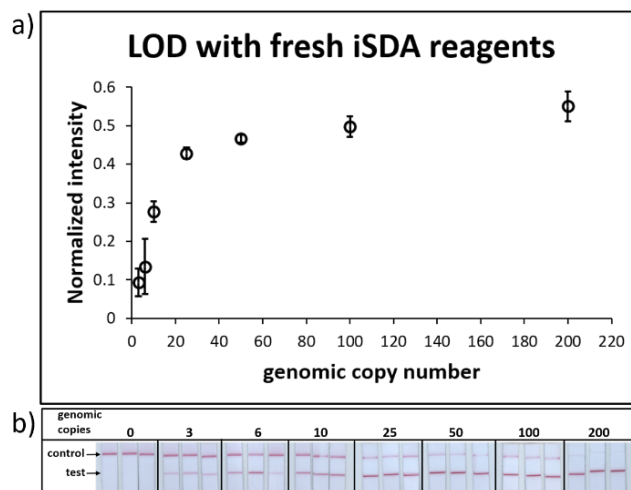


Figure S2. Limit of detection (LOD) for *ldh1* iSDA with fresh reagents in Std 17 GF. a) Chart showing signal intensities of the LF strips test line for a range of MRSA genomic copies and shown below, b) corresponding LF strip images at varying genomic copy number. Note the signal intensities of control line increasing with decreasing copy number.

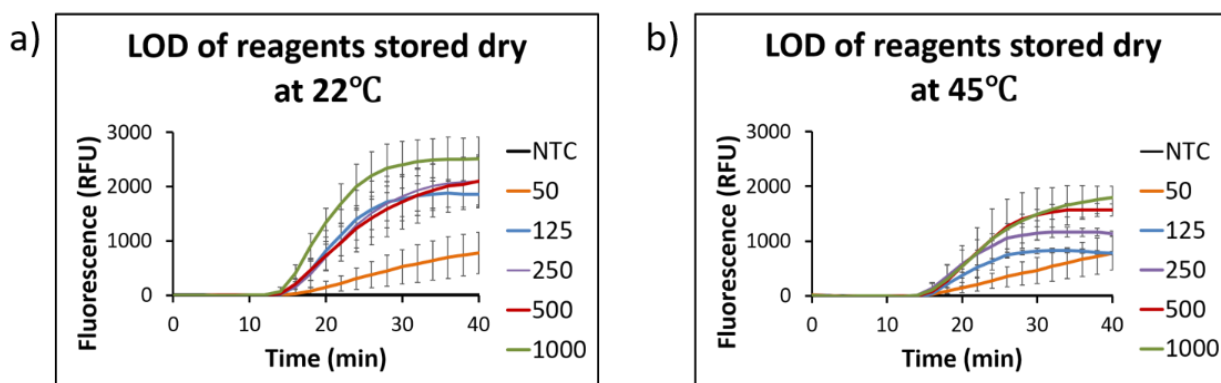


Figure S3. LOD of *ldh1* iSDA with reagents stored in Std 17 GF for 360 h storage in the presence of trehalose and dextran (TD 500) measured by real-time fluorescence at a) 22 °C and b) 45 °C. Curves are mean of 3 replicates, and error bars are standard deviation. The lift-off time for all copies was ~15 minutes; however, the peak fluorescence for 22 °C was higher than 45 °C, indicating lower amplification efficiency at higher temperature storage.

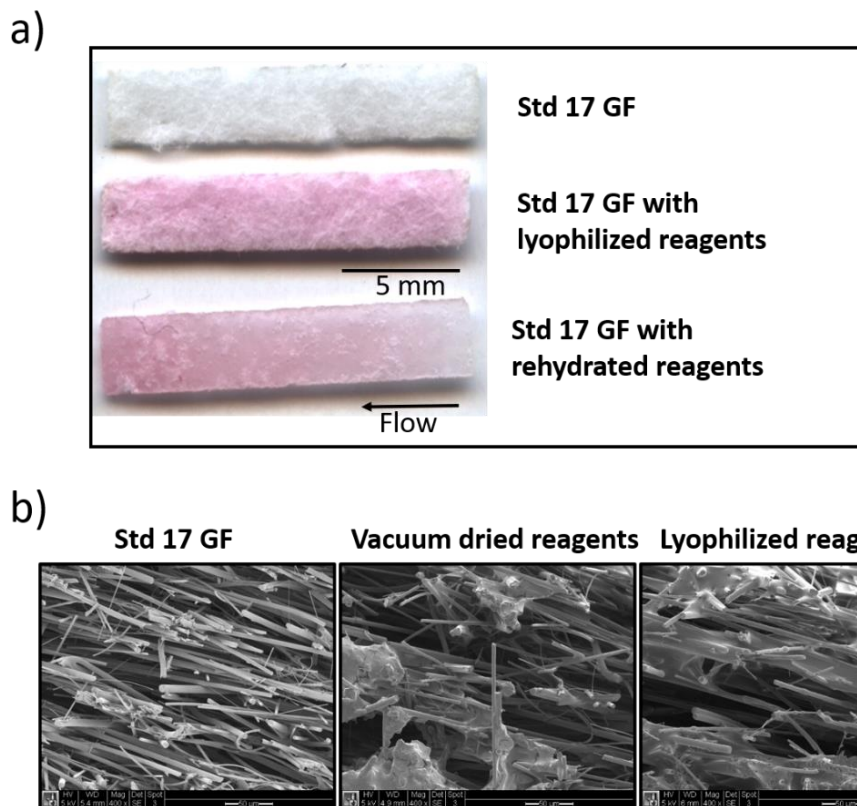


Figure S4. Images of dried reagents in porous matrix a) Flatbed scanned images of Std 17 GF. Lyophilized reagents in Std 17 GF appear uniform across the glass fiber pad. Rehydrated pad shows reagent spread without excessive variation in reagent concentration as visualized by the Au label. b) Scanning electron micrographs of Std 17 GF (scissor-cut cross-section) as received from the manufacturer, iSDA reagents in Std 17 GF dried by vacuum centrifugal evaporator and by lyophilization. Pore features in Std 17 GF are observable over a large length scale ($\sim 1\text{-}50\ \mu\text{m}$) with a range of fiber diameters. Reagents dried by vacuum appear as large clumps and seem to have a low surface area to volume ratio. In the lyophilized sample, the reagents migrate to the small features and appear as dry sheets stretched across the void with high surface area to volume ratio compared to the vacuum-dried sample.

11.3 Molecular mechanism of isothermal strand displacement amplification (iSDA)

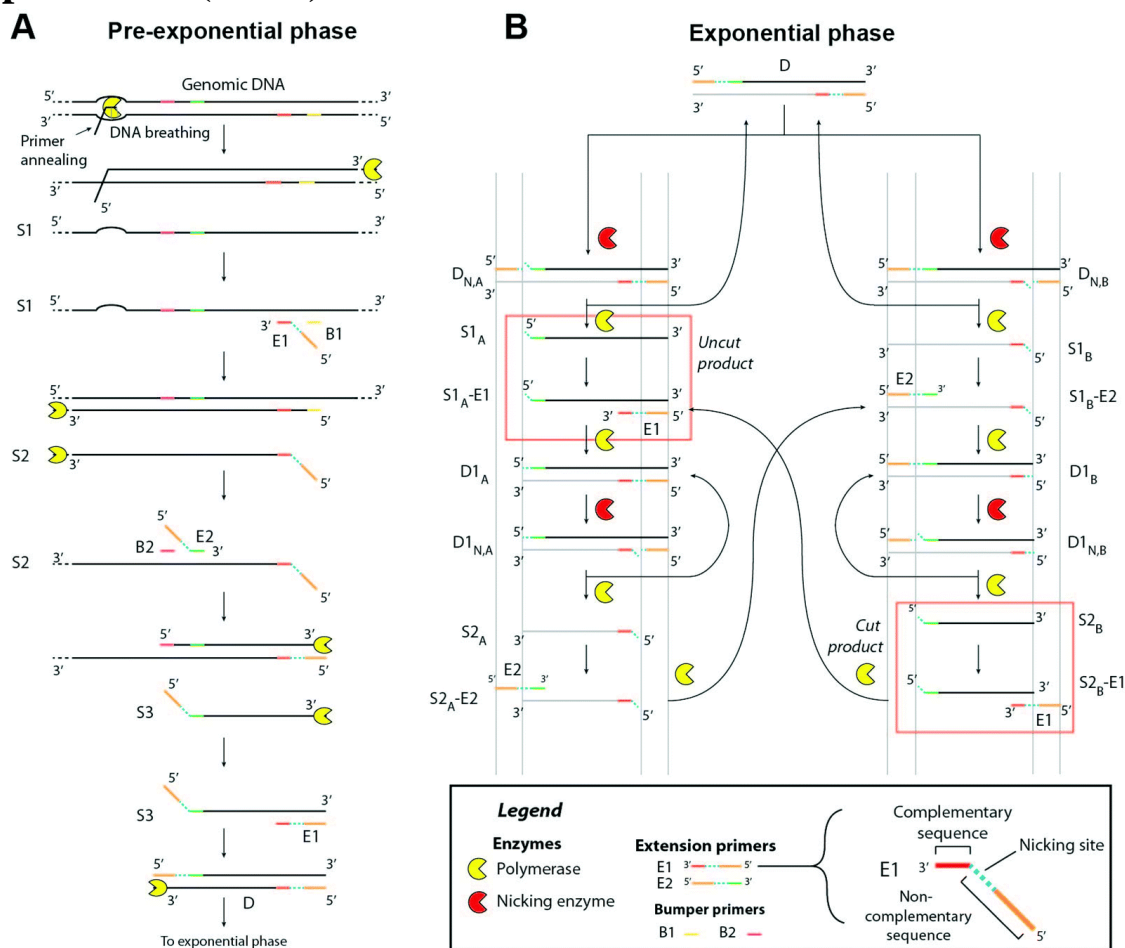


Figure 11.1 Proposed molecular mechanism of iSDA. There are two main stages: pre-exponential (A) and exponential (B). (A) In the pre-exponential phase, a primer invades the double-stranded DNA at a breathing site. The primer is extended by a polymerase, displacing a single strand, S1, which initiates a cascade of subsequent steps involving annealing and extension of two primer pairs (E1, E2, B1, B2), ultimately generating a double-stranded product, D, which has nicking sites (dotted blue sequence; see legend) on both strands. (B) The exponential phase initiates from species D and involves a set of nicking and extension reactions. The complementary strands of D are denoted by black and grey color. Nicking followed by extension and displacement from the two nicking sites in D generates single stranded products, SA1 and SB1. SA1 and SB1 bind to their corresponding complementary primers and their extension produces double-stranded products DA1 and DB1, respectively, each having a nicking site on one strand. Nicking and extension from these sites generates single strand products SA2 and SB2, respectively. Finally, the corresponding complementary primers anneal to SA2 and SB2 and their extension also regenerates DA1 and DB1. Legend shows the different regions of primer E1. Primer E2 has similar regions.

(Reproduced from *Analyst*, 2015, 140(22):7540-9 with permission from the Royal Society of Chemistry)¹⁴³.

iSDA is orchestrated by two enzymes: (i) a nicking enzyme, Nt.BbvCI, that creates a single stranded nick in the double-stranded DNA sequence 5'-CC[^]TCAGC-3' at the location marked by '^', and (ii) DNA polymerase, *Bst* 2.0 WarmStart, that has strong 5'→3' strand displacement activity but lacks 5'→3' exonuclease activity. There are two pairs of primers: a pair of flapped primers or extension primers, E1 and E2, and a pair of bumper primers, B1 and B2. The flap, a portion of the 5' end of extension primers, is not complementary to the target sequence and these non-complementary sequences contain the sequence recognizable by the nicking enzyme, *i.e.* a nicking site (Figure 11.1).

There are two phases of amplification: pre-exponential (Fig 11.1A) and exponential (Fig. 11.1B). Pre-exponential amplification starts with genomic DNA (lacking an Nt.BbvCI nicking site in the *ldh1* gene) and generates a double-stranded product with nicking sites on both strands. Only the polymerase is utilized in this phase; the nicking enzyme does not participate. A primer anneals to a DNA breathing site in genomic DNA (holding it open) and is extended by the polymerase to displace a single strand, S1 (Fig. 11.1A). Primers E1 and B1 then bind to S1. The extension of E1, followed by extension of B1, displaces another single strand, S2, the 5' end of which has the same sequence as primer E1 (Fig. 11.1A). Primers E2 and B2 now bind to S2 and in a similar manner, their extension displaces a single strand, S3, the 5' end of which has the same sequence as primer E2 (Fig. 11.1A). The 3' end of S3 is fully complementary to E1. E1 then anneals to S3 and its extension produces a double-stranded product, D, which has a nicking site on both strands (Fig. 11.1A). This concludes the pre-exponential phase and creates the double-stranded product with nicking sites at both ends needed for exponential amplification.

The exponential phase of the reaction involves synchronous action of the nicking enzyme and polymerase (Fig. 11.1B). The nicking enzyme can act on both nicking sites in D, producing nicked products DN,A and DN,B (Fig. 11.1B). The polymerase extends these nicked strands in the 5'→3' direction to regenerate D and displace single strands, S1A and S1B. Hybridization probes are designed for the sense strand, S1A. Sense and antisense strands are color coded black and grey, respectively, in Fig. 11.1B). S1A and S1B then anneal to primers E1 and E2 and their extension generates double strands, D1A and D1B, respectively (Fig. 11.1B). D1A and D1B have only one intact nicking site. Nicking and extension from these sites regenerate D1A and D1B and produces two new single strands, S2A and S2B. Note that hybridization probes can detect S2B, but not S2A. Primers E1 and E2 then bind to S2B and S2A to regenerate the intermediate species, S1A-E1 and S1B-E2, respectively, thus completing the loop. Multiple cycles of these reactions lead to exponential amplification. Detectable products of two different lengths are generated: uncut products, S1A and S1A-E1, and cut products, S2B and S2B-E1. For the *ldh1* iSDA assay, the uncut and cut products, S1A and S2B, are 121 and 101 bases long, respectively.

In order to detect amplicons using hybridization probes, it is necessary to generate single-strand products. Note that S1A, S2 A, S1B, and S2B have long complementary sequences. If the left and right reaction cascades in Fig. 11.1B, initiating from DN,A and DN,B, respectively, generate equimolar products, these single strands will preferentially anneal to each other and not to the probes. To allow detection by hybridization probes, in this embodiment of iSDA, a lower (and hence) limiting concentration of primer E1 is used to generate more S2B than S2A. Depending on the probe type used, detection can be conducted using two methods: (a) real-time fluorescence detection, or (b) lateral flow detection.

Appendix 11.3 is based on the publication *A Rapid and Sensitive Method of Nucleic Acid Amplification for Point-of-Care Diagnosis*. Toley BJ, Covelli I, Belousov Y, Ramachandran Sujatha, Kline E, Scarr N, Vermeulen N, Mahoney W, Lutz BR, Yager P, Isothermal Strand Displacement Amplification (iSDA): Reproduce from *Analyst* 2015, 140(22):7540-9 with permission from the Royal Society of Chemistry.

11.4 Schematic of lateral flow detection for isothermal strand displacement amplification (iSDA) amplicon product

The method of lateral flow detection illustrated below was used in Chapter 5-2DPN for molecular diagnostics in section 5.1 and 5.2.

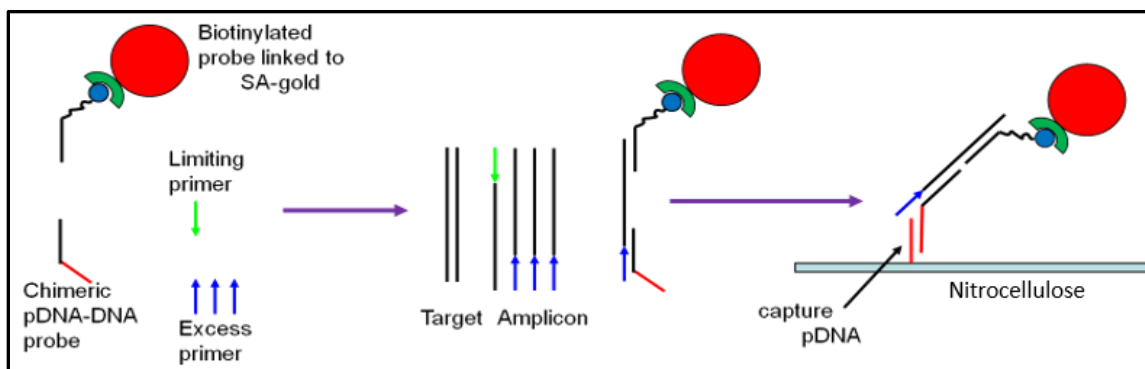


Figure 11.2 Schematic of the lateral flow detection using twin probes. The high specificity of LF detection is achieved by using two probes that target two different regions of the amplicon. The detection probe is biotinylated at the 3' end and conjugates with streptavidin-coated Au beads to produce a visible signal. The capture probe is a hybrid 5'-pDNA-DNA probe. The DNA portion of the probe hybridizes to the amplicon, and the pDNA portion hybridizes to a complementary pDNA surface capture probe.

11.5 Rapid, instrument-free, sample-to-result nucleic acid amplification test

The prototype illustrated here is the first fully integrated sample-to-result diagnostic platform for performing nucleic acid amplification tests that requires no permanent instrument or manual sample processing¹⁴⁴. The multiplexable autonomous disposable nucleic acid amplification test (MAD NAAT) is based on two-dimensional paper networks (2DPN) (Figure 11.3 and 11.4), which enable sensitive chemical detection normally reserved for laboratories to be carried out anywhere by untrained users. All reagents are stored dry in the disposable test device and are rehydrated by stored buffer. The paper network is physically multiplexed to allow independent isothermal amplification of multiple targets; each amplification reaction is also chemically multiplexed with an internal amplification control (IAC). The total test time is less than one hour. The MAD NAAT prototype was used to characterize a set of human nasal swab specimens pre-screened for methicillin-resistant *Staphylococcus aureus* (MRSA) bacteria (Figure 11.5). The lowest input copy number in the range where the MAD NAAT prototype consistently detected MRSA in these specimens was $\sim 5 \times 10^3$ genomic copies (~ 600 genomic copies per bplexed amplification reaction).

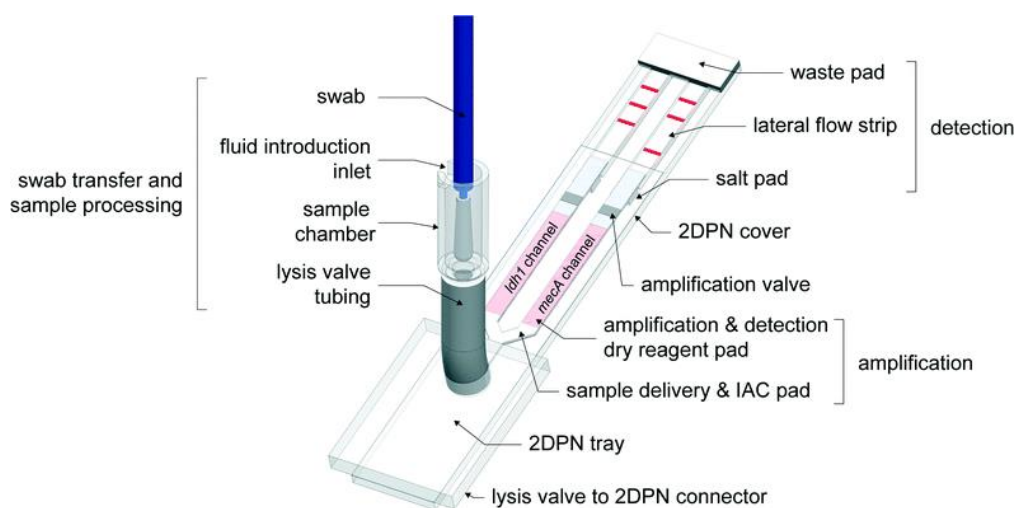


Figure 11.3. Fluid flow path of the prototype. Sample introduction and processing are performed in a sample chamber. The processed sample is delivered by an automated valve to a two-dimensional paper network (2DPN), where it is split into two physical channels (more channels are possible). Isothermal amplification and lateral flow (LF) detection with gold nanoparticles are also performed in the 2DPN. (Reproduced from *Lab Chip*, 2016, 16(19):3777-87 with permission from the Royal Society of Chemistry).

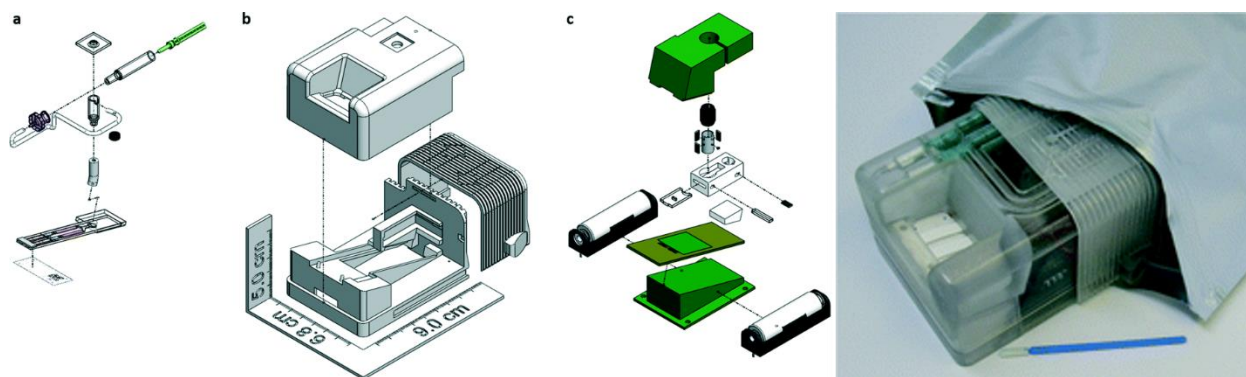


Figure 11.4. Exploded view of the MAD NAAT prototypes (left). (a) Fluid path components, including fluid storage and introduction syringe, sample chamber, and 2DPN. (b) Housing components: base, lid, and slider. (c) Supporting components, including electronics, valves, batteries, and insulation. Device prototype (right). (Adapted from *Lab Chip*, 2016, 16(19):3777-87 from The Royal Society of Chemistry).

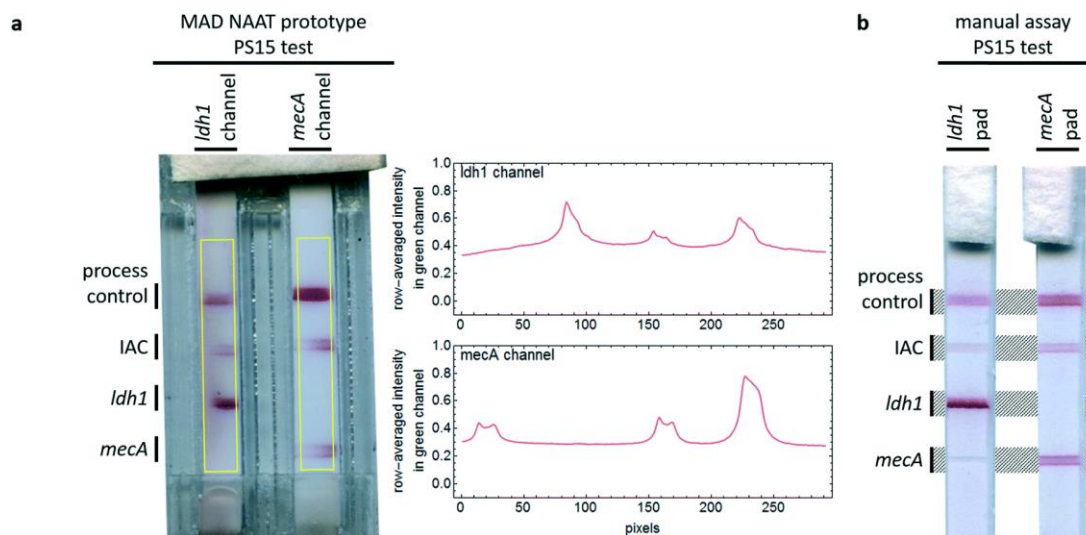


Figure 11.5. Sample-to-result demonstration with samples from human nasal swab specimens. LF strip data for tests on a sample from PS 15, which was positive for MRSA. (a) MAD NAAT prototype test. Two channels amplified and detected *ldh1* with IAC (left) and *mecA* with IAC (right). (b) Manual assay test, which confirms results of the MAD NAAT prototype test. (Adapted from *Lab Chip*, 2016, 16(19):3777-87 from The Royal Society of Chemistry).

Appendix 11.5 is based on the publication *A rapid, instrument-free, sample-to-result nucleic acid amplification test*. Lafleur LK, Bishop JD, Heiniger EK, Gallagher RP, Wheeler MD, Kauffman P, Zhang X, Kline EC, Buser JR, Kumar S, Byrnes SA, Vermeulen NM, Scarr NK, Belousov Y, Mahoney W, Toley BJ, Ladd PD, Lutz BR, Yager P, *Lab chip* 2016, 16(19):3777-87.

11.6 Measurements using radiofrequency micro-strip transmission line

Micro-strip transmission line sandwiched with on-chip patch-clamp unit

The results of the first attempts to funnel electromagnetic power to ion channels at MHz-GHz frequencies using micro-strip transmission line are presented here using the α -hemolysin (α -HL) pore in lipid bilayer¹⁵⁰. A micro-strip transmission line (TL) set-up sandwiched with an on-chip patch-clamping unit was designed. The schematic of the device is shown in Figure 11.6a).

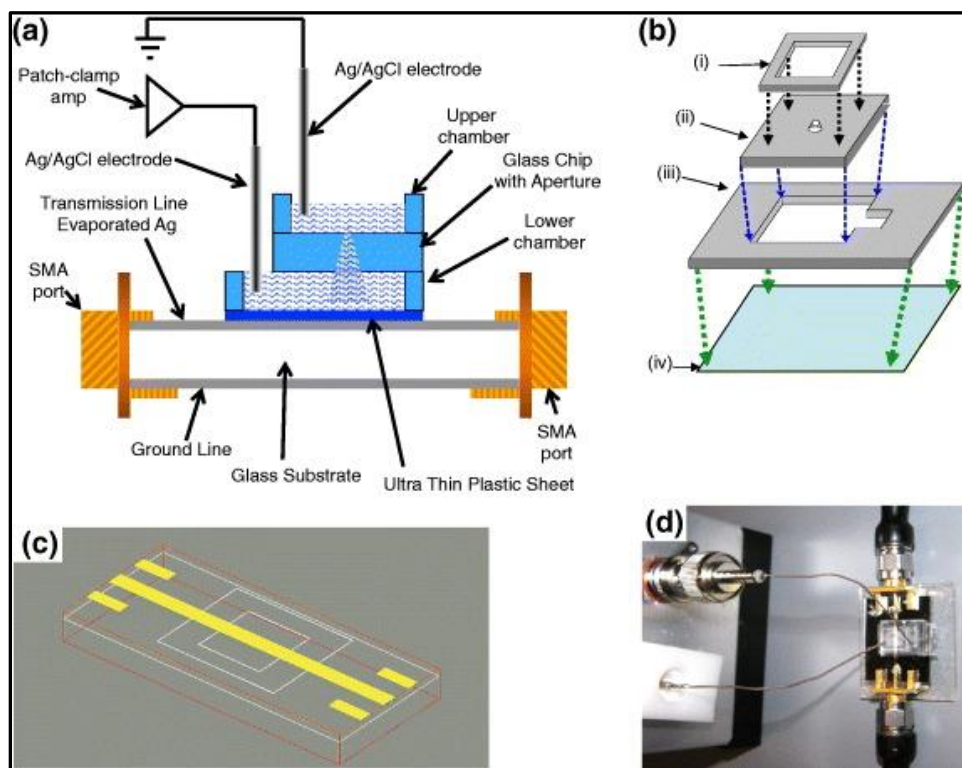


Figure 11.6. Micro-strip line/patch-clamp setup. (a) Schematic view of the micro-strip line/on-chip patch-clamp setup: (b) Exploded view of the on-chip setup: the 'upper chamber' (i) is glued on a micromachined glass chip (ii), which in turn is placed on the 'lower chamber' (iii). This on-chip patch-clamping unit is placed on a very thin electrically insulating plastic sheet (iv). The whole device is finally fixed on to a micro-strip line fabricated on a glass slide. (c) Micro-strip line circuit (yellow) with additional grounding pads for the SMA connectors (short yellow stubs). The back of the circuit is covered by a thin metal layer serving as ground potential. Standard finite-element packages are used to solve for the electromagnetic modes supported by this TL. (d) The two SMA connectors on the top and bottom enable connection to the standard microwave gear, while the Ag/AgCl dc connectors are directly dipped into the solution. (Adapted from *New Journal Physics* 2011, 13, 093033 doi:10.1088/1367-2630/13/9/093033 with permission).

The device consists of an on-chip patch-clamp unit made of glass coverslip placed on top of a TL defined on the glass as well. In Figure 11.6b), the assembly of the on-chip unit is shown in an exploded view: the cis- and trans-chambers made of PDMS sandwiched the glass-chip containing a laser-drilled aperture. This whole on-chip unit was then placed on top of the micro-strip protected from direct contact with the TL with a very thin insulating plastic sheet. The micro-strip line geometry is shown in an aerial view in Figure 11.6c). The TL, which is evaporated silver, has no direct electrical contact with the solution in the lower chamber. The coupling to the TL was purely capacitive. The central area marked by gray boxes indicates the region where the on-chip unit is positioned. The final measurement setup is shown in Figure 11.6d): the dc contacts made from Ag/AgCl wires were dipped into the solution, similar to a standard membrane patch measurement.

The on-chip unit's cis- and trans-sides corresponded to the upper and lower chambers and contained 1 M KCl and 10 mM HEPES pH 7.3 in aqueous solution. The glass chip was first treated with trimethoxy silane around the aperture to render it hydrophobic. A planar lipid bilayer was then formed from 1,2-diphytanoyl phosphatidylcholine (DiPhyPC) in decane (Avanti Polar Lipids Inc., Alabaster, AL) by painting across the ~ 150 μm aperture of the glass chip. This technique leads to the formation of ~ 4 nm thick phospholipid bilayer in the center of the aperture.

A patch-clamp amplifier Axopatch 200 B (Axon Instruments, Union City, CA) was used for all the direct current measurements. The trans compartment was connected to the headstage of the amplifier, and the cis compartment for held at virtual ground. The RF ports were attached to the circuit via SMA connectors, and a network analyzer (Agilent E5071B) was applied to drive the circuit. The whole chamber was mounted in a Faraday cage to achieve optimal shielding from spurious electromagnetic radiation. After the formation of a stable bilayer, a pore-forming protein α -hemolysin was added to the cis side chamber. Current recordings of a single pore inserted into the bilayer were taken by applying a bias DC voltage. The currents were low-pass filtered with a built-in four-pole Bessel filter at 1 kHz and sampled at 10 kHz by computer with a Digidata 1320 analog-to-digital converter. Only then was the RF signal switched on at a range of 100 MHz–1 GHz at moderately low power levels, and the S_{21} parameter measured.

Microwave circuit

In Figure 11.7, a diagram of our microwave circuit with a characteristic impedance is given. The transmission line (TL) is driven by a synthesizer and coupled to a junction circuit with a characteristic impedance Z_j . This junction is required in order to couple the 50 Ω TL impedance to the actual high-impedance molecular pore with the load (L) impedance Z_L . Essentially, the junction can be thought of as an impedance matching unit, which enables the coupling of electromagnetic power into and out of the load. One could assume that is purely real, since the typical ion channel or pore dc resistance (R_L) is of the order of several G Ω . However, these 'bio-transistors' possess a finite capacitance C_{bt} and are embedded in a comparatively large cellular or lipid membrane C_m . Both these capacitances alter the impedance via the reactance $X_L = -1/(\omega C_L) = -1/(\omega(C_{bt} + C_m))$, i.e. $Z_L = R_L + j X_L$. Consequently, the matching condition $Z_j = \alpha Z_L$ or, more precisely, its physical realization is key to this work.

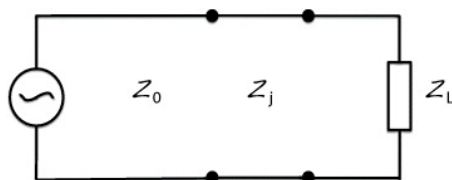


Figure 11.7. Circuit diagram of a transmission line with a characteristic impedance Z_0 , driven by a synthesizer and coupled to a junction circuit with a characteristic impedance Z_j . The actual high-impedance molecular junction possesses a load (L) impedance Z_L . From the engineering point of view, it is essential to optimize the coupling between the junction and the load to maximize the transmitted power. (Adapted from *New Journal Physics* 2011, 13, 093033 doi:10.1088/1367-2630/13/9/093033 with permission).

RF signal response to single pores on micro-strip transmission line

Early work on applying TLs for sampling protein binding and conformational changes^{123 122 124} featured the use of simple micro-strip lines onto which an analyte was added, thus changing the overall impedance of the device. We used lipid bilayer with a protein pore over the micro-strip TL for measuring the change in impedance. The lipid membranes themselves are ideal model systems since they contain no other proteins, which makes them more stable for voltage/current recordings over a long period of time. The resulting interaction specifically alters the effective dielectric constant and thus the characteristic impedance of the line. Consequently, the general aim of these measurements is to maximize the change in capacitance induced by the interaction of biological pore in close proximity to the TL. A major drawback of this method is a low sensitivity; that is, a

single molecular event causes only a minimal capacitive change. However, one can effectively sum over many events, i.e., obtain a rather 'global' picture and a fair signal-to-noise ratio (SNR). This then implies temporal averaging over many probably interrelated events.

As a first step, we combined the TL-based approach with an on-chip patch-clamp unit to probe the direct relation between the microwave spectra and the molecular events at the pore junction. In Figure 11.8, an example of TL measurements with α -HL is presented: the data are taken in the range of 100 MHz–1 GHz at moderately low power levels.

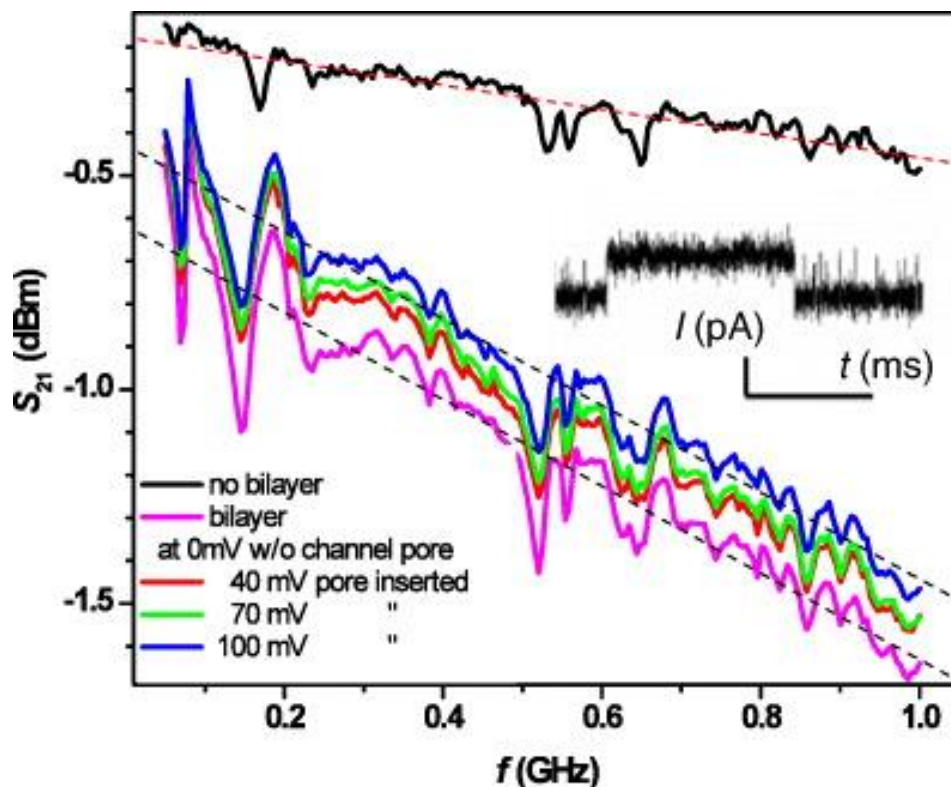


Figure 11.8. Transmission line measurements on the micro-strip and the on-chip patch-clamping unit. The S_{21} parameter versus the RF range of 100 MHz–1 GHz is given. The uppermost (black) trace shows the background when no lipid bilayer is painted on the glass chip. The colored traces below indicate the change once a bilayer forms for different dc bias voltages. The inset gives the dc recording from the integrated on-chip unit, revealing that pores do indeed penetrate the membrane. At about 40 mV, an α -HL is inserted into the membrane. The resulting current corresponds to exactly one α -HL being inserted. Note that the background is not calibrated, i.e., the visible resonances in transmission are due to interference and reflection of the RF signal. (Reproduced from *New Journal Physics* 2011, 13, 093033 doi:10.1088/1367-2630/13/9/093033).

The uppermost trace gives the transmitted power without a painted bilayer defined in the on-chip unit. The individual peaks that can be identified are due to resonances within the circuit and are evidently not caused by the phospholipids. It would have been possible to calibrate the whole setup and thus 'remove' these resonances. However, this would have led to the impression that a painted bilayer causes the rich spectrum, as given in the colored traces.

Nevertheless, there is a strong variation in overall signal attenuation once the bilayer forms over the aperture, i.e., the S_{21} amplitude is strongly reduced towards 1 GHz. This formation we can follow in simply recording the dc resistance of the aperture using the on-chip patch-clamp setup. The relevant change in the microwave signal is its enhanced attenuation towards the 1 GHz mark. This is to be expected since the presence of the phospholipid also enhances the dielectric losses. As noted before, we performed simultaneous dc recordings of the aperture resistance. From this, we were able to trace bilayer formation and the insertion of α -HL pores into the membrane. A single α -HL pore has a standard dc current level at -35 pA at -40 mV bias. As an example, the inset of Figure 11.8 shows the dc versus time of a blocking event, i.e., we added β -cyclodextrin to observe a modulation of the current through the pore. Apparently, we can monitor pore-blocking events in the dc signal at 40 mV. This is possible since we are simultaneously recording the dc signal while tracing the ac response of the entire circuit. We can conclude that the blocking of α -HL pores leaves a signature in the overall ac response. However, this shift in the global response happens to be only gradual.

Evidently, our results suggest that it is possible to combine an RF circuit with a dc circuit in order to correlate local single-pore events with 'global' TL characteristics. This approach is suitable as a testing ground for RF components as high-throughput screening tools. However, it only delivers a correlation but does not entail the full temporal domain. It is thus desirable to enhance the coupling capacitance to the microwave circuit that, in turn, provides real-time recordings with sub-microsecond resolution. In the ideal case, one would achieve capacitive coupling to single events, tracing the resulting impedance variations. One possible approach to achieve this is described in the next section, where we present the first measurements of single channels and pores using specially fabricated micro-coaxes.

Appendix 11.6 is based on the publication *Radio-frequency response of single pores and artificial ion channels*. Hyun S Kim, Sujatha Ramachandran, Eric Stava, Daniel W Van Der Weide, Robert H Blick. *New Journal Physics* 2011, 13, 093033 doi:10.1088/1367-2630/13/9/093033.

Risk and safety statement

The following is a list of potentially hazardous chemicals with their respective hazards and safety instructions. The classification is carried out according to the Globally Harmonized System (GHS) of classification and labeling of chemicals

Compound	Chemical Abstracts Service number	Hazard statement	GHS Hazard	Precautionary Statement
3,3'-Diaminobenzidine (DAB)	91-95-2	H302, H319 H341, H350	GHS07, GHS08	P201 - P301 + P312 + P330 - P305 + P351 + P338 - P308 + P313
3,3',5,5 tetramethylbenzidine (TMB)	54827-17-7	H226, H301, H311 H331, H319, H370	GHS02, GHS08	P210 - P280 - P301 + P310 + P330 - P302 + P352 + P312 - P304 + P340 + P311 - P305 + P351 + P338
Carbenicillin	4800-94-6	H226, H317, H334	GHS02, GHS08	P210 - P233 - P240 - P280 - P303 + P361 + P353 - P304 + P340 + P312
Decane	124-18-5	H226 - H304	GHS02, GHS08	P210 - P301 + P310 + P331
Dimethyl sulfoxide	67-68-5	H227	GHS07	P210; P280
Dithiothreitol (DTT)	3483-12-3	H302 - H412	GHS07	P273 - P301 + P312 + P330
Ethanol	64-17-5	H225; H315 H320; H335; H335	GHS02 GHS07	P210; P261; P305 + P351 + P338
Ethidium Bromide	1239-45-8	H302 - H330, H341	GHS06, GHS08	P201 - P301 + P312 + P330 - P304 + P340 + P310
Ethylenediaminetetraacetic acid (EDTA)	60-00-4	H319	GHS07	P305 + P351 + P338
Ferrous Sulphate	7782-63-0	H302 - H315 - H319	GHS07	P264 - P270 - P280 - P301 + P312 - P302 + P352 - P305 + P351 + P338
Guanidium thiocyanate	593-84-0	H302 + H312 + H332 - H314 - H412	GHS05, GHS07	P260 - P273 - P280 - P303 + P361 + P353 - P304 + P340 + P312 - P305 + P351 + P338 + P310
Hydrochloric acid (HCl)	7647-01-0	H290 H314	GHS05	P260; P280; P303 + P361 + P353; P305 + P351 + P338; P390; P501
Magnesium chloride	7786-30-3	H319	GHS07	P305 + P351 + P338
Paclitaxel	33069-62-4	H341 - H360FD, H371	GHS08	P201 - P308 + P311
N-lauryl sarcosine	97-78-9	H315 - H318, H330	GHS05, GHS06	P280 - P302 + P352 - P304 + P340 + P310 - P305 + P351 + P338 + P310
Sodium hydroxide	1310-73-2	H314; H402	GHS05	P260; P264; P273; P280; P301 + P330 + P331; P303 + P361 + P353; P304 + P340; P305 + P351 + P338; P310

Sodium percarbonate	15630-89-4	H272 - H302 - H318	GHS03, GHS05, GHS07	P220 - P280 - P305 + P351 + P338
Trimethoxysilane	2487-90-3	H225 - H319 - H330	GHS02, GHS06	P210 - P304 + P340 + P310 - P305 + P351 + P338
Tris	1185-53-1	H315; H319; H335	GHS07	P261; P280; P302 + P352; P305 + P351 + P338; P312; P403 + P233; P501
Triton X100	9002-93-1	H302 - H315 - H318 - H410	GHS05, GHS07, GHS09	P273 - P280 - P301 + P312 + P330 - P302 + P352 - P305 + P351 + P338 + P310

Acknowledgments

It was a warm summer afternoon in August. My younger son had just graduated from high school and was ready to leave home for college. I was walking along the corridor of the bioengineering department at the University of Washington, Seattle, to meet Prof. Paul Yager in his office when a thought occurred to me. I had worked with him for over a decade as a research scientist. My heart was pounding as I went into his office. I sat down, and as my heart skipped a beat, I told him I wanted to do a Ph.D. His immediate reply was yes, of course, you should pursue!

I met Prof. Robert Blick at the University of Wisconsin, Madison, for the first time while doing a silly experiment to see what effect coffee had on the ion channel I was working on. I could sense the sheer joy in his face when I showed the results of my investigation. While my coffee experiment was not publishable, his enthusiasm for all the other work I did led to a fruitful collaboration and future research direction. His appreciation for my work was genuine, and he often made me realize my potential I had not known myself. He instilled in me the confidence in presenting scientific data during the hours of discussions I had over coffee or lunch. Naturally, I approached him to be my supervisor, and he readily agreed. This dissertation would not have been possible without him, and I am deeply grateful for his help and support.

I wish to thank Prof. Paul Yager from the bottom of my heart for all the support and guidance he gave me throughout my research career. I am genuinely honored to have worked and contributed to his great mission in developing point of care diagnostics for low-resource settings and home-based tests. Above all, Paul trusted my ability to mentor numerous undergraduates and graduate students, manage different projects under different grants, and develop different skill sets. I am incredibly grateful to all my colleagues in Yager Lab who contributed to my growth as a scientist, especially Professors Barry Lutz and Elain Fu. I wish to thank Paolo Spicar-Mihalic for teaching me AutoCAD, laser cutting, and the protein spotter, and above all, for his friendship. Special thanks to Steven Bennett for building devices for the EbolaBox project and Urinalysis MD NAAT devices, Anupama Govindarajan on the Origami project, Josh Buser, Josh Bishop, Bhushan Toley, Enos Kline, Xiaohong Zhang, Peter Kaufmann, Lisa Lafleur and Caitlin Anderson on the MAD NAAT and EbolaBox projects. I wish to thank Kamal Shah for help with the cellphone imaging on the MD NAAT project and, listening to my lifelong research stories and all things philosophical.

Many thanks to my current lab members Erin Heiniger, Shichu Hwang, Kevin Jiang, Cara Brainerd, and Alexander Yan for making my day bright.

I want to thank Prof. Henry Hess immensely for introducing me to the beautiful world of biomolecular motors. It was a short but fun project, and I took great pride in developing the research.

I am grateful to Prof. Daniel van der Weide for giving me the complete freedom to begin a project from scratch at the University of Wisconsin. I did not know much about electrical engineering when I started the project but learned a lot during my research time. Since then, I have developed a deep passion for always venturing into the unknown.

Most of all, my husband George's unconditional love and patience made possible everything beautiful in life. Our boys Vikram and Raj have been the joy of my life as they took this journey together with me. My father-in-law was a wonderful person and the best grandpa at taking care of our children while pursuing my career. To my parents, Appa and Amma, thank you for all the love and support.

Declaration upon oath

I hereby affirm on oath that I have written this dissertation myself and that I have not used any aids other than those indicated. The submitted written version corresponds to the one on the electronic storage medium. I assure you that this dissertation was not submitted in a previous promotion procedure.

Signature: 

Date: 29-05-2021